STUDIES ON THE MECHANICAL BEHAVIOR OF FRP REINFORCED CONCRETE BEAMS USING ACOUSTIC EMISSION AND DIGITAL IMAGE CORRELATION

A thesis submitted

in fulfillment of the requirement for the award of degree

of

Doctor of Philosophy

Submitted by

Gaurav Sharma

Registration Number: 951602006

Under the Supervision of

Dr. Shruti Sharma
Professor, CED

Dr. Sandeep Kumar Sharma
Associate Professor, MED

DEPARTMENT OF CIVIL ENGINEERING
THAPAR INSTITUTE OF ENGINEERING AND TECHNOLOGY, PATIALA-147004

August-2021

DECLARATION

I, **Gaurav Sharma** hereby declare that the thesis titled, **"STUDIES ON THE MECHANICAL BEHAVIOR OF FRP REINFORCED CONCRETE BEAMS USING ACOUSTIC EMISSION AND DIGITAL IMAGE CORRELATION"** submitted to **Thapar Institute of Engineering and Technology**, Patiala in partial fulfillment of the requirement for the award of the degree of **Doctor of Philosophy** in **Civil Engineering** is a record of original and independent research work done by me during 2016-2021. This thesis has been conducted under the supervision and guidance of **Dr. Shruti Sharma,** Professor, Civil Engineering Department, Thapar Institute of Engineering and Technology, and **Dr. Sandeep Kumar Sharma,** Associate Professor, Mechanical Engineering Department, Thapar Institute of Engineering and Technology.

The work contained in this thesis has not been previously submitted to meet the requirements for a degree or diploma at this or any other higher education institution.

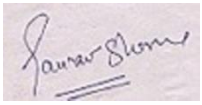

Gaurav Sharma
951602006

Date
17-01-2022

This is to certify that the above statement made by the candidate is correct to the best of my knowledge

CERTIFICATE

Certified that the work presented in this thesis titled **"STUDIES ON THE MECHANICAL BEHAVIOR OF FRP REINFORCED CONCRETE BEAMS USING ACOUSTIC EMISSION AND DIGITAL IMAGE CORRELATION"** which is being submitted by **Mr. Gaurav Sharma (Regd. No. 951602006)** in fulfillment of the requirements for the award of the degree of **Doctor of Philosophy** in the **Department of Civil Engineering, Thapar Institute of Engineering and Technology, Patiala, India**, is an authentic record of the research work carried out by him under our supervision and guidance.

The contents of this thesis, in full or in part, have not been submitted to any other Institute or University for the award of any degree or diploma.

Dr. Shruti Sharma
Supervisor
Professor
Civil Engineering Department

Dr. Sandeep Kumar Sharma
Supervisor
Associate Professor
Mechanical Engineering Department

ACKNOWLEDGEMENTS

First and foremost, I am beholden to the Almighty (**Lord Shiva**) and I bow before Him for his umpteen blessings and bestowing in me the girt and confidence to carry out the research work.

I wish to take the opportunity to express my acknowledgments to those whom without their assistance this dissertation work could not have been done.

I would like to express my sincere greatest appreciation and thanks to my research supervisor **Dr. Shruti Sharma,** Professor, Civil Engineering Department, and **Dr. Sandeep Kumar Sharma,** Associate Professor, Mechanical Engineering Department for offering me the opportunity to work on such a challenging subject. I feel blessed and proud to work with them. All of the guidance, insight, helpful advice and constant encouragement provided throughout the dissertation by them are greatly appreciated. I owe an unbelievable amount of gratitude to **Dr. Sandeep Kumar Sharma** for his prominent role in helping me to achieve one of the greatest accomplishments in my life.

I am honor-bound and profoundly thankful to the doctoral committee members **Dr. Prem Pal Bansal**, Professor and Head of Department, Civil Engineering Department, **Dr. Naveen Kwatra,** Professor, Civil Engineering Department, **Dr. Trishna Chaudhary**, Assistant Professor, Civil Engineering Department and **Dr. Rajeev Mehta**, Professor, Chemical Engineering Department, Thapar Institute of Engineering and Technology, for their valuable suggestions which helped me to improve further. I would like to express my gratitude to Mr. Varinder Sharma and Mr. Ramsimran for their constant help in the structures laboratory.

I would also like to express my gratitude to **Dr. A.B. Danie Roy** Assistant Professor Civil Engineering Department for timely advice and constant guidance. This journey would not have been possible without the constant support from my friends. First of all, I would like to thank my friend **Dr. Heaven Singh** for his consistent support throughout these years. I would like to thank my friends Mr. Hitesh Sharma, Mr. Devender Sharma, Mrs. Payal Sachdeva, Mr. Arunish Kumar, and Mr. Manreet Singh for making these years memorable. I would also like to thank my fellow research scholars Mr. Sunil Garhwal and Mr. Tarunbir Singh for their support.

Last, but not least, I am grateful to my parents, My father, **Sh. Ajit Sharma**, My mother, **Smt. Meenu Sharma** and my sister **Shaina Sharma** stood like a rock in my difficult times

and provide me full support. Their love, patience, persistent encouragement, and good virtuous understanding enabled me to complete this research work successfully.

Gaurav Sharma

ABSTRACT

Corrosion of steel reinforcement in Reinforced Concrete (RC) structures is one of the major challenges faced by the construction industry which severely limits the service life of structures. It is primarily caused by the penetration of aggressive ions like chloride and sulphates, which are either contributed from the concrete ingredients or by external agencies like de-icing salts, marine water, and atmosphere, etc. Several types of protective coatings like epoxy-coatings, biofilms, and galvanization, etc. have been suggested to protect the RC bars from corrosion. But these techniques only delay the onset of corrosion and do not prevent it completely. The use of non-corroding Fibre Reinforced Polymer (FRP) reinforcing bars in place of steel reinforcing bars in concrete offers a potentially good alternative in extreme environmental applications.

Glass Fibre Reinforced Polymer (GFRP) composites have extensive applications in various fields such as the aerospace and automotive engineering sectors. During the last two decades, there have been more novel applications for GFRP in the construction sector. GFRP composites have emerged as promising material that can be used in lieu of steel for Reinforced Concrete (RC) structures due to their high longitudinal tensile strength, excellent corrosion and fatigue resistant properties; and high stiffness to weight ratio. Furthermore, relevant design codes and guidelines have also been developed for the use of GFRP bars in RC structures. The behavior of structural members reinforced with GFRP bars is different than that of steel-reinforced concrete members due to the lower modulus of elasticity, brittle behavior, and sudden failure. The sudden brittle failure in GFRP RC structures necessitates the implementation of an effective and real-time health monitoring framework for assessing the structure's integrity, structural performance and crack evolution before the damage becomes catastrophic and disastrous.

In this research effort, to develop a damage monitoring methodology for GFRP reinforced concrete beams, their mechanical performance and structural behavior under flexure are first compared with the steel-reinforced beams. The load-deflection plot of steel reinforced and GFRP reinforced concrete beams show contrasting profiles. With increasing reinforcement ratio, steel-reinforced beams typically show an increase in ultimate load-carrying capacity, shrinking plastic zone with reduced ductility, and failure taking place at the much lower strains by steel yielding followed by concrete crushing. On the contrary, GFRP reinforced beams exhibit bi-linear load-deflection response up to the failure without any yielding and exhibit higher ultimate load-carrying capacities and deflections due to their

low elastic modulus as compared to steel reinforced beams indicating enhanced ductility and ultimate strength. During flexural loading of steel RC and GFRP RC beams, they are simultaneously subjected to Acoustic Emission (AE) and Digital Image Correlation (DIC) monitoring to investigate the initiation and progression of damage in these differently reinforced beams.

AE accurately determines the onset of cracking and monitors the development of micro-and-macro cracks in differently reinforced concrete beams using AE parameters like cumulative AE-hits and their amplitudes and Cumulative Signal Strength (CSS). GFRP reinforced concrete beams exhibit a larger number of cumulative AE hits of higher amplitudes as compared to steel reinforced beams due to their low elastic modulus and different bond characteristics. It is also well supported by the larger number of **Knees** (steep rise) in the CSS plots.

AE parameter of Average Frequency (AF) and Rise Angle (RA) plots can be used to predict the type of cracking in the RC beam. High AF and low RA values indicate pure bending cracks in steel-reinforced beams at the microcracking level, whereas low AF and high RA values point towards shear cracks in GFRP reinforced beams initially. At the macro cracking level, a marginal increase in RA and the drop of AF indicates flexure-failure by steel yielding followed by concrete crushing in steel-reinforced beams. On the other hand, in the GFRP-reinforced beams, a significant increase in AF value and a decrease in RA value indicate sudden shear failure followed by concrete crushing.

Similarly, Average Frequency (AF) and Rise Time (RT) signal values are averaged to distinguish the fracture behavior in RC beams. At the early stage of fracture analysis, high AF and shorter RT signal values indicate pure flexural cracks in steel RC beams, whereas low AF and longer RT signal values point towards shear cracks in GFRP RC beams. At the final stage of fracture analysis, a substantial shift from short to slightly longer RT signal indicates flexure-failure by steel yielding followed by concrete crushing in steel RC beams. On the contrary, a strong shift from longer to short RT signal and lower to high AF was observed in GFRP RC beams points towards sudden shear failure followed by concrete crushing.

Further, AE parameters of Average frequency (AF) and Duration (μs) with time show a significant drop in AF, and a jump in AE duration at the same time indicates critical failure points in steel RC and GFRP RC beams. These changes are better indicative of damage than the load-deflection plots. It is also observed that the moving average line of AF was high

and the duration line was low in the GFRP reinforced beams in comparison to the steel-reinforced beams. This is due to the fact that GFRP bars have lower elastic modulus and different bond characteristics and deflect more than steel bars, causing AE activity to accumulate leading to a high frequency of hits.

Along with AE monitoring which serves as an “ear”, DIC provides an “eye” to the damage monitoring strategy proposed in this work. DIC has the potential to serve as an online crack mapping tool in the form of surface strains and displacements and gives an indication much before the actual cracking is visible to the naked eye. It provides a mean for the exact localization of crack on the surface specimen using longitudinal surface strain (ε_{xx}) profiles. AE technique offers a qualitative insight into the damage process in concrete by studying variation in various AE parameters hits. The AE XY-events maps and DIC surface strain (ε_{xx}) profiles at different stages of damage in the steel and GFRP RC beams closely match with the actual cracked patterns observed in these differently RC beams.

Table of Contents

List of Figures

List of Tables

ACRONYMS AND ABBREVIATIONS

AE	Acoustic Emission
AFRP	Aramid Fibre Reinforced Polymer
AE	Acoustic Emission
AF	Average Frequency
BFRP	Basalt Fibre Reinforced Polymer
CI	Colour Intensity
CC	Cross Correlation
CFRP	Carbon Fibre Reinforced Polymer
CSS	Cumulative Signal Strength
FRP	Fibre reinforced polymer
GFRP	Glass Fibre reinforced polymer
DIC	Digital Image Correlation
RC	Reinforced concrete
MARSE	Measured Area under Rectified Signal Envelope
NDT	Non-Destructive Testing
RA	Rise Angle
P	Load
PAC	Physical Acoustic Corporation
RT	Rise Time
ε_{xx}	Longitudinal Strain along X-direction
HSC	High strength concrete
NSC	Normal Strength Concrete
TRC	Textile Reinforced Cement
SSD	Sum of Squared Difference
NCC	Normalised Cross Correlation
SS	Simply Supported
Δ	Mid-Span Deflection
4p	Four point

CHAPTER 1

INTRODUCTION

1.1 GENERAL

Reinforcing steel bar corrosion is now well acknowledged as one of the most prevalent and serious causes of concrete structure degradation worldwide **(Hansson, 1995; Raupach & Schiebl, 2001; El-Maaddawy, 2005 and Hawileh, 2011).** Traditional steel bars in Reinforced Concrete (RC) constructions are vulnerable to rust, which compromises the structure's safety and serviceability **(Batis, et al. 2005; Talakokula & Bhalla, 2014; Talakokula & Bhalla, 2015 & Alhozaimy et al. 2018).** Contaminants from the environment permeate the concrete cover and induce steel corrosion, decreasing strength, load-bearing capacity, lifespan, and cost of RC structures in humid conditions **(Almusallam et al. 1996; Paik et al. 2004; Frangopol & Tsompanakis 2014; Wang et al. 2015 and Dhawan et al. 2019).** The corrosion of rebars is caused by two primary mechanisms: chloride ion ingress and carbonation of reinforced concrete structures. When chloride ions enter concrete beyond the threshold value or when carbonation penetration overcomes the concrete cover, corrosion occurs in reinforced concrete structures, resulting in rebar delamination from the surrounding concrete **(Francois & Maso 1988 and Yoon, 2007).** It produces voluminous corrosion products having a volume 6-10 times that of the surrounding parent steel, which leads to the cracking and spalling of the surrounding concrete **(Castel et al. 2000; Ahmed et al. 2007; Ou et al. 2012 and Apostolopoulos et al. 2019).** Additionally, various environmental degradation factors such as moisture, chemical products, freeze-thaw, de-icing salts, and marine environments speed up the corrosion mechanism of steel bars in concrete assemblies **(Francois & Maso, 1988 and Yoon, 2007).**

The National Association of Corrosion Engineers (NACE) has highlighted the negative impact of structural component corrosion on the Indian economy **(Bhaskaran et al. 2005 and Raj et al. 2015).** The Indian government spends around 26.1 billion US dollars per year, or about 2.4 percent of the country's GDP, to safeguard infrastructure against corrosion **(Pardey et al. 2010).** Degradation failure is a major problem associated with coastal infrastructures in metro areas such as Mumbai, Bangalore, and Chennai, which occurs as an outcome of climate change and rising sea levels, resulting in deterioration of various kinds of infrastructures and their systems **(Valdez et al. 2016; Goldston et al. 2016 and Goldston et al. 2017).** The expense of maintaining and replacing highways, roads, bridges, and marine substructures in coastal locations is further in billions of dollars **(Pardey et al. 2010 and Koch, 2017).** To avoid

maintenance costs, many strategies and methods for delaying the onset and progression of corrosion in RC structures have been proposed. Commonly suggested methods include the use of stainless steel **(Gu & Meng 2016 and Rabi et al. 2019**) and epoxy-coated rebars **(Manning, 1998; Lee, 2004 and Lopez-Calvo et al. 2013)** in place of conventional steel bars, admixing corrosion inhibitors **(El-Hacha et al. 2010),** using self-healing compounds in concrete **(Stankiewicz et al. 2013 and Zhang et al. 2020)** and use of polymer concrete **(Fowler, 1999 and Allahvirdizadeh et al. 2011).** The use of stainless steel bars as reinforcement is not much effective as these bars are also prone to corrosion under a highly aggressive environment as well as they are costly **(Cope et al. 2013).** Epoxy-coated bars suffer from loss of adhesion with the surrounding concrete over a period of time (**Lopez et al. 2013)**. Corrosion Inhibitors in concrete decelerate the diffusion rate of the reactants by absorbing the ions at the concrete surface, which delays the corrosion initiation but does not fully prevent it **(Chigondo & Chigondo 2016 and Sehmi et al. 2020).** Some researchers have recently proposed using self-healing micro-capsules to protect metals against corrosion (**Stankiewicz et al. 2013; Giannaros et al. 2016 and Zhang et al. 2020).** After degradation, damage, or failure, these chemicals have the inherent ability to repair the substrate and restore functionality. However, this technique has practical challenges as the rupturing of self-healing-based micro-capsules takes place during the mixing of concrete. Apart from this, these specific techniques are not cost-effective and have scalability issues in structural applications.

Fibre-Reinforced Polymer (FRPs) composites reinforcement has been introduced in recent decades as an alternative and/or substitute material to replace traditional reinforcing steel in many civil engineering applications, hence alleviating the corrosion problem (**Alsayed, 1998; Triantafillou & Antonopoulos, 2000, Ascione et al. 2003; Mancusi and Spadea, 2010; Barris et al. 2012 Gudonis et al. 2013; Adam et al. 2015; Saleh et al. 2019 and Manalo et al. 2021).** Although various fibres such as asbestos, paper, or wood have been used in the past, the most common are aramid, basalt, carbon, and glass. Typically, thermoset resins such as polyester and vinylester, as well as thermoplastics such as nylon, polyethylene, and terephthalate, are used **(Hensher, 2016 and Abbood et al. 2021)** are used. Furthermore, in the aerospace, automotive, marine, and construction industries, FRPs are commonly utilized for structural applications as well as for repair and rehabilitation due to their most common being cost-effectiveness and high strength properties, Glass Fibre Reinforced Polymer (GFRP) bars or sheets **(Balendran et al. 2002).** Because of these benefits, FRP composites have been utilized as internal reinforcement in RC structures, bridges, piers, and external reinforcement

in modern construction and restoration of structures for strengthening and seismic upgrading **(Bonacci & Maalej, 2000; Pendhari et al. 2008** and **Amran et al. 2018).**

Being non-corrosive, GFRP composite bars offer numerous benefits, including electric and magnetic neutrality, convenience of handling, high strength/weight ratio high and longitudinal tensile strength. They also are simple to construct and can be tailored to meet specific performance requirements **(Goldston et al. 2016; Nanni et al. 2019; El-Hassan & Maaddawy 2019 and Abu-Obaida et al. 2020).** Wharves, box culverts, dry docks, sea walls, floating piers, facades, and retaining walls can all benefit from GFRP bars, which can be utilized in place of steel rebars under harsh exposure situations such as coastal environments **(Goldston et al. 2017).** Magnetic resonance imaging lodgings in hospitals, as well as bridge decks close to electronic toll plazas, are examples of RC constructions that prohibit the usage of steel bars, where it has been suggested to use GFRP as reinforcement in concrete **(Jakubovskis et al. 2014 and Goldston et al. 2016).** But there are some inherent issues in the practice of GFRP bars in concrete as external reinforcement which needs elaborate and detailed investigation and studies before it can be practically implemented and replace the conventional steel bars. The initial cost of GFRP bars is significantly higher than the cost of steel reinforcing bars. Because of its linearly elastic stress-strain behavior up to collapse and low elastic modulus, Glass FRP bars behave differently than traditional steel bars, resulting in a significant reduction in flexural rigidity (**El-Salakawy et al. 2003 and Ascione et al. 2010)**. Moreover, GFRP reinforced flexural members experience much larger deflection/deformations under service or loading conditions as compared to steel-RC flexural members **(Theriault & Benmokrane 1998; El-Salakawy et al. 2003; Ascione et al. 2010; Escorcio and Franca 2016 and Krasniqi et al. 2018).** Another important issue is the sudden failure in the form of rupturing of GFRP reinforcement, and it is recommended to design them as an over-reinforced to facilitate failure by concrete crushing (**ACI 2015).** Therefore, it is very essential to monitor the crack initiation and its progression initiation and progression of the cracking and failure mechanism in GFRP reinforced concrete beams.

In this research effort, the mechanical performance and behavior of steel RC & GFRP RC beams under flexure are investigated using the Acoustic Emission Technique (AE) and non-contact optical Digital Image Correlation (DIC) technique in conjunction with destructive testing. The joint approach provides complementary data from both the ear and the eye, aided by acoustic emission and digital image correlation, respectively. It is expected that the initiation and progression of the cracking and mode of failure in the beams will be characterized by

differently reinforced steel and GFRP concrete beams. AE and DIC are proposed to investigate and develop an advanced damage monitoring strategy to give an early warning of the onset and progression of damage.

1.2 AE AND DIC FOR MONITORING RC STRUCTURES

An effective and precise non-destructive approach is required to identify damage or cracks in concrete assemblies reinforced with conventional steel or GFRP bars at the early stages to ensure appropriate performance. In RC constructions, active NDT methods such as visual testing, infrared thermography, microwave, and ultrasonic testing have been employed **(Sharma et al. 2015 and Sharma et al. 2018)**. However, a passive NDT approach based on AE is presented in this study. The AE method has established itself as one of the most dependable and well-established NDT procedures **(Ohtsu and Tomoda, 2007; Ohno and Ohtsu, 2010 and Prem & Murthy, 2017)** for damage detection and monitoring, as well as damage progress in various reinforced concrete structures **(Providakis et al. 2014).** As compared to other non-destructive techniques, the AE approach offers two significant benefits.

i. It can provide important information about what is going on inside structures and
ii. It has the capacity to monitor online during structural services.

With the AE technique, it is possible to capture the damage process, when and where it occurs. It uses surface-mounted AE sensors to collect energy bursts in the form of elastic stress waves generated by fast energy release during RC structural deflection/deformation or crack propagation. In addition, the AE sensor transforms these transient elastic waves into an electrical signal **(Maji and Shah, 1998; Yun et al. 2010 and Verbruggen et al. 2015).** In the AE technique, various AE parameters are extracted and used to correlate to damage initiation, crack-growth, and progression in various kinds of infrastructures as well as localize and quantify it. In two ways, the AE approach is unlikely to vary from the rest of the non-destructive testing (NDT) procedures. The first distinction is related to the signal's origin. Rather than delivering energy to the item under investigation, this approach simply listens for the energy it emits. AE tests are frequently carried out on structures when they are in use, as this provides sufficient loading for flaws to propagate and acoustic emissions to occur. **(Ohtsu and Tomoda 2007; Prashanth & Kishen 2008; Ohno and Ohtsu 2010; Shah & Kishen 2012; Sharma et al. 2015; Prem & Murthy, 2017; Sharma et al. 2018; Burud & Kishen, 2020; Garhwal et al. 2021 and Burud & Kishen, 2021).** The efficiency of the AE approach to study and identify

structural behavior and failure patterns of steel-RC and GFRP-RC beams is attempted in this research effort.

The non-contact optical technique of Digital Image Correlation (DIC) has been proposed for detecting surface strain, displacement, or deformation in a variety of materials. **(Prashanth & Kishen 2008; Blaber et al., 2015 and Gribniak et al. 2017).** This approach is gaining popularity for studying crack development and material deformation being a low cost and a simple method to which gives an accurate solution. **(Shah & Kishen, 2012)** The positioning coordinates of digital images obtained from digital cameras before and after deformation are used in this approach to computing surface strains and deformations using cross-correlation or a least-squares function. **(Choi & Shah, 1997; Prashanth & Kishen 2008 and Bhowmik et al. 2019).** Furthermore, data on displacement and strain acquired during the load testing of a structure may be used to assess adherence to both strength; lifespan, and maintenance cost. This substantially improves the effectiveness of a structural evaluation and allows for more regular structural monitoring. **(Wang et al. 2005; Blaber et al., 2015 and Molina-Viedma et al. 2020).**

There are several DIC software's available but an open-source 2D-Ncorr platform is the most promising tool used by researchers for measuring surface displacements and strain at a lower price than high-end equipment and post-processing software **(Blaber et al. 2015 and Russ, 2016).** This study attempts to use this non-contact digital imaging technique to examine and assess the structural behavior and performance of steel RC & GFRP RC beams. A brief review of the AE and DIC methods is presented, as well as their current applications for the health monitoring of civil engineering structures is provided in **CHAPTER 3.**

1.3 GAPS IN RESEARCH AREA AND MOTIVATION

As GFRP reinforced concrete structures are expected to fail suddenly and are relatively brittle, monitoring the initiation and progression of cracking and fracture behavior is important in these structures. No work has been reported so far which investigates the flexural performance behavior and damage monitoring of GFRP reinforced concrete beams using non-destructive tools. Limited research evidence exists where investigators have used AE and DIC techniques for damage assessment to visualize crack propagation from invisible crack initiation to final fracture in plain concrete beams and specimens externally strengthened with Carbon Fibre Reinforced Polymer (CFRP) and Textile Reinforced Cement (TRC) sheets **(Alam et al. 2014; Verbruggen et al. 2014; Flansbjer & Limdqvist 2018 and Dai et al. 2019).**

However, sudden brittle failure in GFRP RC structures necessitates the implementation of an effective and real-time health monitoring framework for assessing the integrity of structures, performance, and crack evolution before the damage becomes catastrophic and disastrous. Hence it is important to understand the initiation and progression of cracking and damage in GFRP reinforced concrete beams under flexure. This would go a long way in developing NDT tools for RC structures irrespective of the reinforcement used. It is expected that a judicious combination of AE and DIC as recommended in this study would lead to damage and fracture evaluation in steel RC as well as GFRP RC beams. The basic premise of integrating the two advanced non-destructive and non-contact techniques is that while AE can effectively monitor volumetric and surface effects in the structure due to damage progression, it has limited visualization accuracy. DIC, on either hand, identifies deformations and gives complete field displacement maps of the monitored structures' surfaces **(Omondi et al. 2016 Sharma et al. 2020 and Sharma et al. 2021).** Both techniques when used simultaneously have the potential to lead to a comprehensive damage monitoring strategy for various kinds of RC structures utilizing steel or GFRP reinforcement.

1.4 OBJECTIVES OF STUDY

The use of GFRP as concrete structure reinforcement is a new topic of research in structural engineering that requires more exploration. The major objective of this study is to investigate the structural performance of behaviour of steel and GFRP reinforced concrete beams in flexure using advanced NDT tools of AET and DIC. The main objectives of the research can be outlined as below:

- Investigate and compare the behaviour of Steel Reinforced and FRP Reinforced Concrete Beams in flexure.
- Analysis of bending behaviour of Steel and FRP reinforced concrete beams using Acoustic Emission Technique (AET) for internal defect detection and Digital Image Correlation (DIC) for surface cracking.
- Characterization of the fracture process in Steel and FRP reinforced concrete beams using Acoustic Emission Technique (AET) and Digital Image Correlation (DIC).

1.5 ORGANIZATION OF THE THESIS

To accomplish the above-mentioned research goals and assess the problem definition and thesis structure has been broadly divided into as follows:

- The thesis is divided into **8 chapters** that cover all of the study goals. The information in this dissertation is organized into 8 chapters with **Chapter 1** being an introduction.
- A detailed review of the literature on the mechanical behaviour of GFRP RC beams is presented in **Chapter 2.** The review of recent literature about the application of AE and DIC for monitoring reinforced concrete structures is presented in **Chapter 3.**
- **Chapter 4** outlines the experimental program and methodology undertaken in this work. The details about the materials used, descriptions of the test specimens including steel and GFRP RC beam specimens, and experimental setup for flexural monitoring of steel and GFRP reinforced concrete beams are presented along with details of AE and DIC test set-ups.
- **Chapter 5** focuses on the comparison in the mechanical behaviour and structural performance of steel and GFRP reinforced concrete beams under flexural loading. The results of the load-deflection characteristics, failure modes, and the progression of visible cracking pattern, moment carrying capacity, energy absorption capacity, and pre-and-post cracking stiffness for two types of differently reinforced concrete beams have been compared in detail.
- **Chapter 6** presents the study of the bending behaviour of steel and GFRP reinforced concrete beams using AET for internal defect detection and DIC for surface cracking. Various AE parameters of cumulative AE hits, Average Frequency AF in (kHz), duration (μs), Rise Angle (RA), etc. along with Mid-point vertical displacement and surface strain in DIC have been used to study the variation in bending and failure pattern of steel RC and GFRP RC beams.
- **Chapter 7** examines the fracture monitoring of steel RC and GFRP RC beams, the results of cumulative AE hits, Cumulative Signal Strength (CSS), Amplitude, Average frequency, and Rise Time (RT), were utilized. Furthermore, the AE XY- plots and longitudinal surface strain (ε_{xx}) profiles are compared to real cracked images of steel and GFRP reinforced concrete beam specimens.
- Finally, **Chapter 8**, lists the major conclusions drawn from the work and research recommendations for the future.

CHAPTER 2

GFRP AS REINFORCEMENT IN CONCRETE

2.1 GENERAL

A number of studies on the flexural response of steel Reinforced Concrete (RC) structures under various types of loading have been undertaken in recent years **(Sumarac et al., 2003, Parvez & Foster 2012, Bodzak, 2019).** To overcome challenges of corrosion in steel-reinforced concrete structures, GFRP bars have been suggested in recent years as a potential and a viable solution commonly known as GFRP-RC structures **(Theriault & Benmokrane, 1998; El-Salakawy et al. 2003; Ascione et al. 2010 Gudonis et al. 2013 Escorcio and Franca, 2016; Krasniqi et al. 2018; Sharma et al. 2020 and Sharma et al. 2021).** Because of its non-corrosive properties, GFRP bars are ideal for use in coastal and marine environments **(Goldston et al. 2016 and Goldston et al. 2017).** Other important advantages include the high strength of tensile fiber, its non-conductive and non-magnetic, and it's lightweight and electrically and thermally properties.

This chapter covers the definition and characteristics of FRP, as well as an overview of the historical development of FRP as a reinforcing material in civil engineering projects and a review of some of the latest important works done in the use of GFRP bars as reinforcement in concrete structures.

2.2 FIBER REINFORCED POLYMER BARS

2.2.1 FRPs and their characteristics

Fiber-Reinforced Polymer (FRP) composites are made up of continuous fibers that are aligned and implanted in a resin matrix. Aramid, Basalt, Carbon, and Glass fibers can be used, and the resulting composites are designated for example AFRP, CFRP, and GFRP, respectively **(Yao et al. 2016 and Bazan et al. 2021).** The continuous fibres are embedded and bound by the polymer matrix, which is often a polyester, epoxy, or vinyl ester resin **(Hensher, 2016 and Abbood et al. 2021).** It also acts as a protective or shielding barrier for the fibers, reducing surface degradation throughout their service life. Thermosetting resins are a common form of polymeric matrix used in combination with fibers. Some of the most common thermosetting resins as presented in **Table 2.1**. The mechanical performance of the composite (FRP) will vary depending on the fiber quality, orientation, volumetric ratio, length, shape, adherence to a matrix, and manufacturing method **(Goldston et al. 2016).** The characteristics of these FRP kinds differ from those of steel in terms of modulus of elasticity and tensile strength **(Boyle and Karbhari 1994 and Benmokrane et al. 1996).** As demonstrated in **Fig. 2.1,** the tensile stress-strain conduct of FRP bars is linear-elastic till catastrophe for different types of fibers **(Nanni at al. 1993; Ascione et al. 2003 and Gudonis et al. 2013).** The tensile strength of FRP bars is often considerably higher than that of standard steel reinforcing bars. FRP bars are

particularly appealing for pre-stressed concrete applications due to their comparatively high tensile strength. However, the elastic modulus of these bars is lower than that of conventional steel bars **(Barris et al. 2012 and Goldston et al. 2017).** When compared to conventional steel bars, the modulus of elasticity of available GFRP and AFRP bars ranges from 20 to 25%, while that of CFRP bars ranges from 60 to 75 percent. **Fig. 2.1** depicts typical stress-strain curves for FRPs, reinforcing steel, and pre-stressing steel **ISIS, (2008).**

Table 2.1: Thermosetting Matrices' Characteristics ACI (2015)

Property	**Units**	**Matrix**		
		Polyester	**Epoxy**	**Vinyl Ester**
Density	(kg/m^3)	1200-1400	1200-1400	1150-1350
Tensile	(MPa)	34.5-104	55-130	73-81
Longitudinal Modulus	(GPa)	2.1-3.45	2.75-4.10	3.0-3.5
Thermal Expansion Coefficient	(10^{-6}/ °C)	55-100	45-65	50-75
Moisture Content	(%)	0.15-0.60	0.08-0.15	0.14-0.30

2.2.2 Advantages of FRP bars

The usage of FRP bars as interior reinforcement for engineering constructions has a number of advantages. When compared to typical steel reinforcement, the main advantage is that it is non-corrosive. It is most suited to extremely corrosive situations, such as bridge decks, when de-icing salts are present **(Goldston et al. 2016 and Goldstone et al. 2017).** When steel reinforcement is utilized in this sort of climate, it corrodes, producing financial and structural difficulties with maintenance and safety. Low weight-by-strength ratio, high longitudinal tensile strength, and non-magnetic characteristics are among the other benefits, which makes GFRP reinforcement useful in medical applications that employ MRI equipment **(Goldston et al. 2017).**

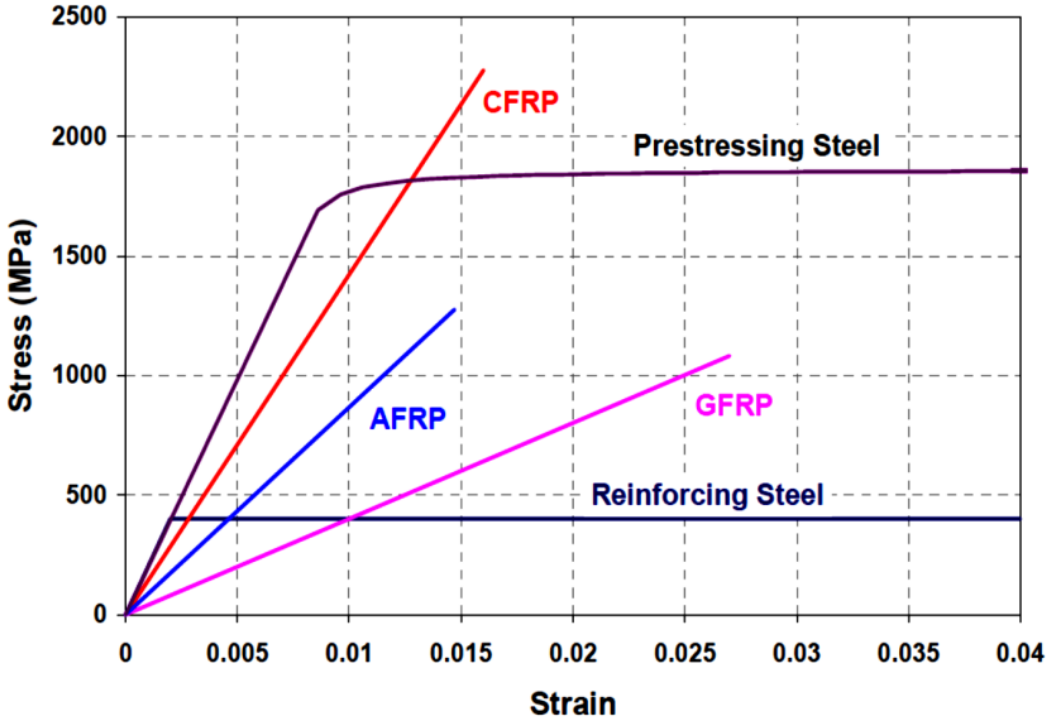

Fig. 2.1: Stress-strain conduct for FRP and reinforcing steel (ISIS, 2008)

2.2.3 Drawbacks of FRP reinforcing bars

One of the most significant disadvantages of all forms of FRP composites, including reinforcing bars, is their brittleness up-to collapse. FRP bar is acknowledged for being a non-ductile material that does not yield like typical steel reinforcement (**Sumarac et al. 2003)**. As a result, it is extremely difficult to bend FRP reinforcement on-site due to its lack of plasticity. The bending must be done by the manufacturer using specialist technology. Other drawbacks include the fact that the orientation of the fibers determines the reinforcing bar's strength. In comparison to the fiber direction, the longitudinal tensile strength is lower in the direction perpendicular to the fibers **(El-Salakawy et al. 2003 and Ascione et al. 2010).**

Similarly, FRP bars have a low elastic modulus, resulting in greater deflections and increased cracking in flexural components, producing serviceability issues. Finally, while the initial rate of FRP bar is greater than steel bar, the entire lifecycle cost of a building component reinforced with FRP bar is cheaper, as structures reinforced with FRP bars require much less maintenance **(Cadenazzi et al. 2019).** The benefits and drawbacks of FRP are summarised in **Table 2.2.**

Table 2.2: FRP Reinforcement Bars: Benefits and Drawbacks (Goldston et al., 2016).

Benefits	**Drawbacks**
Longitudinal tensile strength is high.	Depending on the matrix type and thickness of the concrete cover, it may be susceptible to fire.
Lightweight	In a wet environment, glass fibers have a low durability
Corrosion-resistant	Lower compressive/shear strength
Non-magnetic	Lower elasticity modulus
High service life/durability	Cannot be bent in the onsite
High fatigue tolerance	Before a brittle rupture, there is no yielding.
Minimum maintenance cost	UV rays cause degradation.

2.2.4 Historical development of FRP reinforcement

The increase of composites used in the defense sector following World War II in the 1940s, notably in the aeronautical, naval sectors, and military applications, is credited with the invention of FRP reinforcement **(Goldston et al. 2017).** It was known at the time to have a high strength/weight relation and to be non-corrosive, making it the longevity to the atmosphere and the corrosive properties of the sea and salty environment. The necessity for year-round maintenance grew as the National Highway (NH) systems expanded in the 1950s. De-icing salts were commonly used in these structures, and those exposed to salty atmosphere faced considerable corrosion, which became a serious problem and resulted in expensive maintenance costs. **ACI (2015)** examined galvanized coatings, electrostatic spray, fusion-bonded coatings, polymer-impregnated concrete, epoxy coatings, and glass FRP reinforcing bars. Until the late 1970s, when fiber-reinforced polymer reinforcing bar became commercially available, it was not considered a viable alternative.

GFRP bars were initially thought to be a feasible substitute to steel for polymer concrete reinforcement because they eliminated the need to deal with the conflict of thermal expansion characteristics between polymer concrete and steel. For specialized advanced technology in the 80s, the market wanted non-metallic reinforcement. The need for electrically non-conductive reinforcing was high in MRI medical tools installations (**Goldston et al. 2016).** As the benefits of FRP reinforcement became more increasingly recognized and demanded, new applications emerged, including seawall construction, power reactor bases, and electronics laboratories

(Goldston et al. 2017). Bridge degradation due to chloride-ion-induced corrosion has been a source of concern since the 1970s, and its impacts on America's aging bridges have been evident **(Frangopol & Tsompanakis 2014).** Furthermore, the discovery of corrosion in frequently used epoxy-coated reinforcing bars sparked curiosity in other corrosion-prevention techniques. FRP reinforcement was explored as a universal approach to solve corrosion issues in bridge decks and other constructions **(Boyle and Karbhari 1994 and Benmokrane et al. 1996).**

2.2.5 Field Applications

Japan had the greatest FRP reinforcement applications up to the mid-1990s, with over a hundred demonstration or commercial projects. The Japanese Civil Engineering Society incorporated fibre enhanced polymer design criteria in their recommendation for design and construction **(JSCE, 1997).** In the 2000s, China exceeded the US as the world's largest employer of composite reinforcement for new construction, with uses spanning from bridge decks to underground construction **(Feng, 2014 and Zhou & Zhang, 2019).** In 1986, Germany was the first country in Europe to employ FRP reinforcement, with the building of a pre-stressed FRP roadway **(Knippers and Gabler 2008** & **Lin et al. 2019).** Since the building of this bridge, platforms have been developed across Europe to promote FRP reinforcement research and usage **(Zyjewski et al. 2017).** The Canadian Highway Bridge Design Code allows FRP strengthening and a series of earlier FRP reinforced concrete constructions were established in Canada **(CSA 2012).**

In addition to that, Headingley Bridge in Manitoba included both Carbon FRP and Glass FRP reinforcement (**ACI 2015).** In 2006, the Floodway Bridge, which spans the Red River in Winnipeg, Manitoba, Canada, was finished. The bridge has sixteen spans, each measuring around 15 x 43 meters. Glass FRP bars are used to strengthen the concrete components above the girder. GFRP bars are used to strengthen all concrete parts above the girders. The project used 140000 kg of glass fiber reinforced plastic reinforcing bar, making it the world's largest non-metallic-reinforced concrete bridge. In addition, numerous bridges in Quebec, such as the Wotton Bridge in Wotton, feature GFRP bars in their decks. Three of the most well-known bridges in the area include the Magog Bridge on Highway 55 North, the Cookshire Eaton Bridge on Route 108, and the Val Alain Bridge on Highway 20 East. **(Salakawy et al. 2003).** Some of these bridges have been in use for over ten years with no evidence of GFRP reinforcement degradation **(Mufti et al. 2007).** As a result, the usage of GFRP bars has increased dramatically in Canada, where more than 200 bridge constructions have been completed positively. The Pierce Street Bridge in Lima, Ohio, was one of several

building applications and demonstration projects performed in the US and Canada to demonstrate the benefits of composite materials as revealed in **Fig. 2.2(a)** and the use of FRP bars in Ohio's Salem Avenue Bridge in 1999 **(Fig. 2.2 (b).**

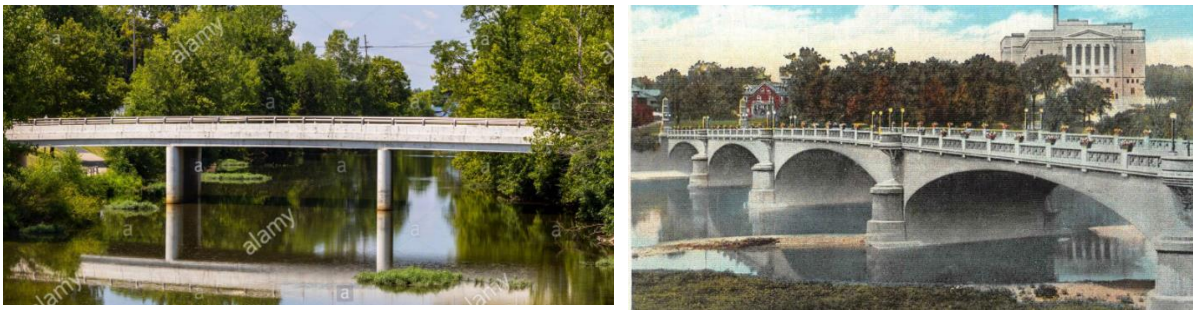

(a) **(b)**

Fig. 2.2 (a) Pierce Street Bridge in Lima, Ohio and (b) Dayton, Ohio's Salem Avenue Bridge (**Salakawy et al. 2003).**

2.3 DESIGN RECOMMENDATIONS FOR FRP REINFORCED STRUCTURES

Design guidelines have been produced globally in Japan due to the growing use of Fibre Reinforced Polymer (FRP) reinforcement **(JSCE 1997b)**, the USA **(ACI 2015),** Canada **(ISIS 2001; ISIS 2007; CSA 2002; CSA 2012**), Italy (**CNR 2006**) and Egypt **(HBNRC 2005).** The sequential order of the design codes available for concrete structures reinforced with FRP reinforcement is presented in **Table 2.3,** respectively.

Table 2.3: Sequential Order of Design Recommendations for Concrete Structures Reinforced with FRP Bars

S.No	Country	Publisher	Year	Guide/Recommendation
1	Japan	Japan Society of Civil Engineers/(JSCE)	1997	Recommendation for Design and Construction of Concrete Structures Using Continuous Fibre Reinforcing Materials
2	Canada	Intelligent Sensing for Innovative Structures/(ISIS)	2001	Reinforcing Concrete Structures with Fiber Reinforced Polymers
3	USA	American Concrete Institute/(ACI)	2005	Guide for the Design and Construction of Concrete Reinforced with FRP Bars
4	Egypt	Housing and Building National Research/(HBNRC)	2005	The Egyptian Code for the use of Fiber Reinforced Polymer in the Construction Fields

5	USA	American Concrete Institute/(ACI)	2006	Guide for the Design and Construction of Concrete Reinforced with FRP Bars
6	Italy	Advisory Committee on Technical Recommendations for Construction/(CNR)	2006	Guide for the Design and Construction of Concrete Structures Reinforced with Fiber-Reinforced Polymer Bars
7	Canada	Intelligent Sensing for Innovative Structures/(ISIS)	2007	Reinforcing Concrete Structures with Fiber Reinforced Polymers
8	USA	American Concrete Institute/(ACI)	2007	Report on Fiber-Reinforced Polymer (FRP) Reinforcement for Concrete Structures
9	Switzerland	The International Federation for Structural Concrete/(fib)	2007	FRP reinforcement in RC structures
10	Canada	Canadian Standards Association/(CSA)	2012	Design and Construction of Building Structures with Fibre-Reinforced Polymers
11	USA	American Concrete Institute/(ACI)	2015	Guide for the Design and Construction of Concrete Reinforced with FRP Bars

2.4 FRP REINFORCED STRUCTURES DESIGN AND CONSTRUCTION GUIDELINES

ACI (2015) has developed a guide for the design of concrete beams internally reinforced with FRP reinforcement bars, "**Guide for the Design and Construction of Structural Concrete Reinforced with FRP Bars".** According to this report, FRP reinforced concrete member design, particularly flexural capacity, may be estimated similarly to steel reinforced concrete member design. The technique for finding these parameters, including flexure requirements, is outlined in the handbook, which includes a beam design example (**ACI 2015),** makes the following assumptions:

- The strain in the concrete and the FRP reinforcement is proportional to the distance from the neutral axis (NA).

- In concrete, the maximum acceptable compressive strain (ε_{cu}) is 0.003.
- The tensile strength of concrete is negligible.
- Until failure, the tensile behavior of the FRP reinforcement is linearly elastic.
- Because FRP reinforcement and concrete have a perfect connection, the strain in the reinforcement bar is identical to the strain in the concrete at the same level.

Concrete crushing, FRP reinforcing bar rupture, and balanced failure are the 3 types of failure mechanisms for FRP RC specimens. (At ε_{cu} = 0.003, FRP tensile reinforcement reaches rupture strain at the same time as concrete crushing). The reinforcement ratio (ρ_f) and balanced reinforcement ratio (ρ_{fb}) determine the failure mode. If $\rho_f > \rho_{fb}$, the failure mode is governed by concrete crushing, whereas for FRP reinforcement rupture, $\rho_f < \rho_{fb}$. FRP RC specimens have a different suggested failure mode than steel RC specimens. Concrete crushing is favored over FRP bar rupture because if the reinforced FRP bars reach their strain for rupture (ε_{fu}), failure without precaution would be highly sudden and devastating. When compared to FRP reinforcement rupture, an over-reinforced FRP RC beam produces a more "ductile" reaction and exhibits some plastic behavior. Equations (2.1) and (2.2) may be used to compute the reinforcement ratio (ρ_f) and balanced reinforcement ratio (ρ_{fb}) for an FRP RC beam respectively.

$$\rho_f = \frac{Af}{bd} \tag{2.1}$$

$$\rho_{fb} = 0.85\,\beta 1 \frac{f'c}{f_{fu}} \frac{Ef \in_{cu}}{Ef \in_{cu} + f_{fu}} \tag{2.2}$$

ρ_{fb} =balanced reinforcement ratio and ρ_f = actual reinforcement ratio = $\frac{Ast}{bd}$ where A_{st} is the area of reinforcement provided in the tension phase, A_f = area of FRP tensile reinforcement, b = width of the beam, d = effective depth, $f'c$ = design characteristic concrete compressive strength, Ef = FRP elastic modulus, ε_{cu} = ultimate concrete strain, f_{fu} = tensile strength of the FRP and β_1 = stress block parameter. For concrete strength, the β_1 parameter is taken as 0.85 $f'c$ up to and including 28 N/mm^2. For concrete with a strength of more than 28 N/mm^2, β_1 is reduces at an amount of 0.05 for each 7 N/mm^2 up to $\beta 1$ = 0.65 (Equation (2.3). Henceforth, the stress block constraint should be within $0.65 \leq \beta_1 \leq 0.85$ (Equation (2.3).

$$\beta_1 = (0.85 - 0.05 \frac{(f'c - 28.0)}{7.0}) \geq 0.65 \tag{2.3}$$

The rectangular stress block may be utilized to calculate the nominal bending moment (M_n) in terms of the FRP reinforcement ratio (**Equation 2.4**) for an over-reinforced FRP RC beam ($\rho_f > \rho_{fb}$) as illustrated in **Fig. 2.3** and **Equation 2.4.**

$$M_n = \rho_f f_f \left(1 - 0.59 \frac{\rho f \, ff}{f'c}\right) bd^2 \quad (2.4)$$

Where ff = stress in the FRP reinforcement's under tension, which must be less than or equal to the tensile strength of the FRP reinforcement's (f_{fu}), and may be determined using **Equation 2.5.**

$$f_f = \left(\sqrt{\frac{(Ef\ \varepsilon cu)^2}{4}} + \sqrt{\frac{0.85\ \beta 1\ f'c}{\rho f}}\ E_f\ \varepsilon_{cu}\right) - 0.5\ E_f\ \varepsilon_{cu} \leq f_{fu} \quad (2.5)$$

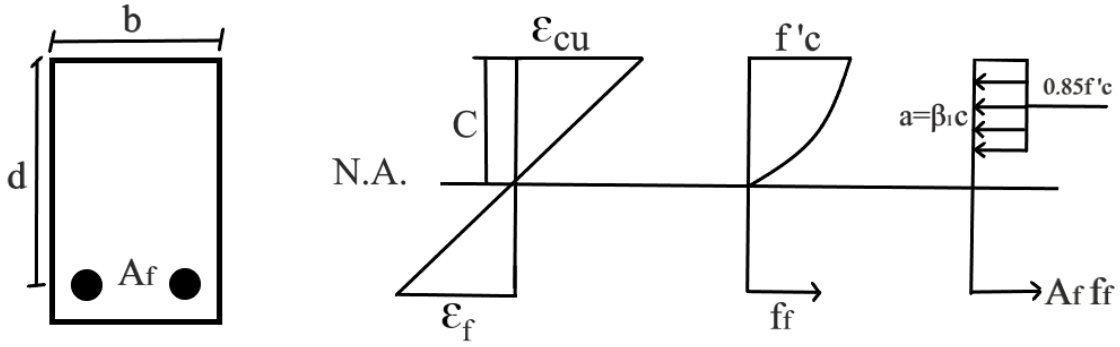

Fig. 2.3: Concrete Crushing's failure (ACI, 2015)

The rectangular stress block is impracticable for FRP rupture to regulate the design ($\rho_f < \rho_{fb}$) because the final strain in the concrete is unreachable. As a result, **(ACI 2015)** proposes a conservative and straightforward technique for calculating nominal bending resistance **(Equation 2.6).** When FRP reinforcement ruptures, the stress, and strain distributions are shown in **Fig. 2.4.**

$$Mn = A_f\ f_{fu} \left(d - \frac{\beta 1 cb}{2}\right) \quad (2.6)$$

Where cb is the distance between the compression fiber and the NA under balanced strain circumstances, which may be calculated using **Equation 2.7.**

$$c_b = \left(\frac{\varepsilon cu}{\varepsilon cu + \varepsilon fu}\right) d \quad (2.7)$$

Where ε_{fu} is the FRP tensile reinforcement's rupture strain.

As shown in **Fig. 2.4**, a balanced failure situation occurs when the concrete reaches the anticipated ultimate strain of 0.003 while the FRP reinforcing bars reach the rupture strain (ε_{fu}), that is, $\rho_f = \rho_{fb.}$

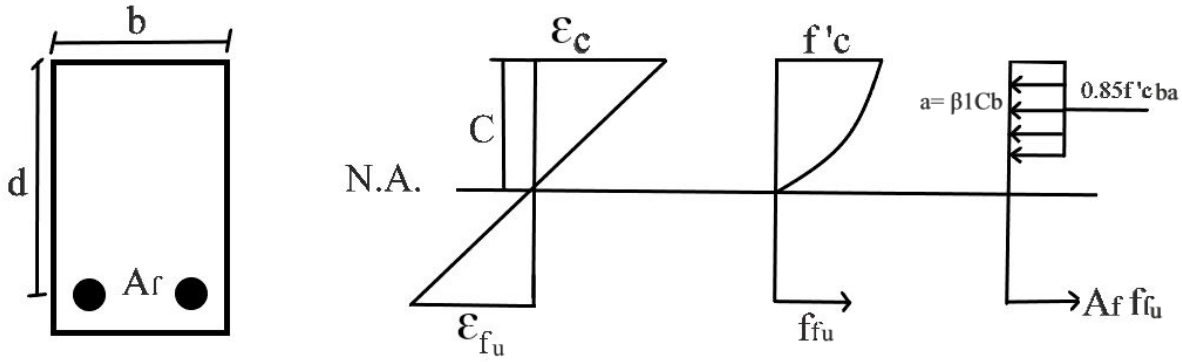

Fig. 2.4: Failure governed by FRP Rupture (ACI, 2015)

The rectangular stress block is unsuitable for FRP rupture to guide the design ($\rho f < \rho f b$), because the ultimate strain in the concrete ($\varepsilon cu < 0.003$) is unachievable. As a result, the **(ACI 2015)** proposes a conservative and simple method for calculating nominal bending resistance (**Equation 2.8**). When FRP reinforcement rupture dominates, the stress and strain distributions are seen in **Fig. 2.5.**

$$M_n = A_f f_{fu} \left(d - \frac{\beta 1\, Cb}{2}\right) \quad (2.8)$$

where cb is the distance between the extreme compression fiber and the NA under balanced strain circumstances, and it can be calculated using **Equation (2.9).**

$$C_b = \left(\frac{\varepsilon cu}{\varepsilon cu + \varepsilon fu}\right) d \quad (2.9)$$

Where ε_{fu} is the FRP tensile reinforcement rupture strain

As illustrated in **Fig. 2.5,** a balanced failure state occurs, when the concrete achieves the estimated ultimate strain value of $\varepsilon_{cu} = 0.003$ while the FRP reinforcing bars reach the rupture strain (ε_{fu}), which is $\rho_f = \rho_{fb}$.

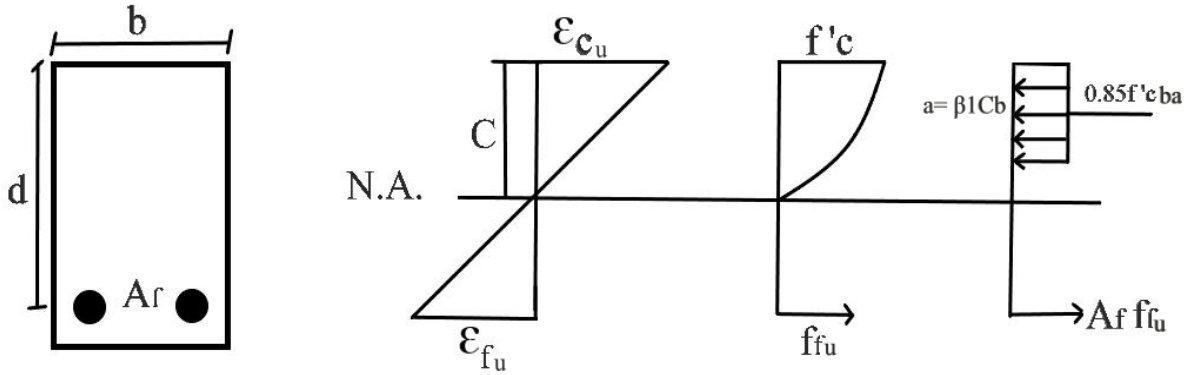

Fig. 2.5: Failure governed by Balanced Condition (ACI, 2015)

According to the concept of strength design **(ACI 2015),** says that the design flexural strength ($\emptyset Mn$) must exceed the factored moment (Mu): $\emptyset Mn \geq Mu$. Due to the variations in failure mode between GFRP-RC and steel RC components, a cautious strength reduction factor ($\emptyset$) in flexure is suggested. To compensate for the loss of ductility, the GFRP RC beams should have greater reserve strength. Thus to ensure $\emptyset Mn \geq Mu$, to calculate the necessary strength reduction factor, use equations (**2.10, 2.11, and 2.13**). Fig. 2.5 graphically shows Equation (2.9) as a function of the reinforcement ratio. Equation 2.10 for under reinforced section; Equation 2.11 for balanced and Equation 2.13 for over reinforced members. Where ρ_{fb} = balanced reinforcement ratio, ρ_f = actual reinforcement ratio.

$$\emptyset = 0.55 \; for \; \rho_f \; < \rho_{fb} \tag{2.10}$$

$$\emptyset = 0.3 + 0.5 \frac{\rho_f}{\rho_{fb}} \tag{2.11}$$

$$\emptyset = 0.65 \; for \; \rho_f \geq 1.4 \; \rho_{fb} \tag{2.12}$$

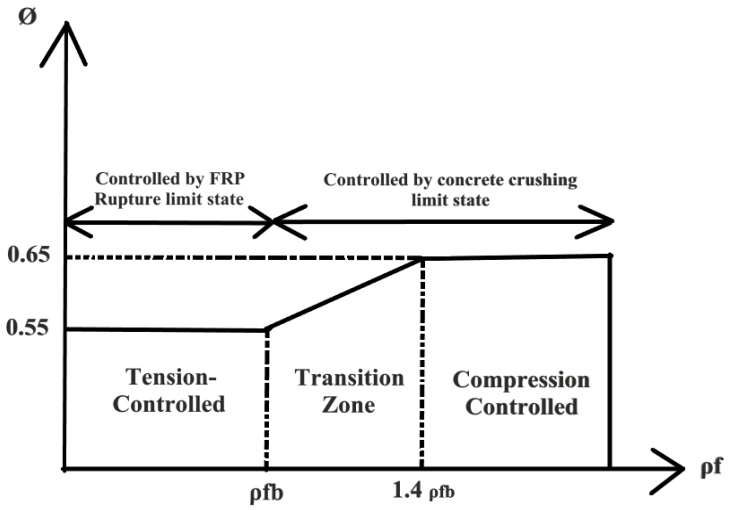

Fig. 2.6: Reinforcement Ratio and the Strength Reduction Factor (ACI, 2015)

The theoretical moment of resistance (Mth) in the case of a steel-reinforced concrete beam, on the other hand, is computed using the formula in Equation (2.13) **(ACI 2019).**

$$M_{th} = \rho_f \, f_y \left[1 - 0.59 \, \rho_f \, \frac{f_y}{f'_c} \right] bd^2 \tag{2.13}$$

Where M_{th} = theoretical bending moment resistance, ρ_f = reinforcement ratio, b= beam width, d= effective beam depth, f'c = Concrete compressive strength, f_f = stress in fiber reinforced polymer bar, and fy = steel reinforcement tensile strength.

For steel RC and GFRP RC beams, the M_{th}/M_{exp} ratio is less than 1. As a result, the strength reduction factor (Ø) for excessively reinforced GFRP RC beams is determined using equation (2.14) from **(ACI 2015).**

$$\emptyset = 0.65 \; for \; \rho_f \geq 1.4 \; \rho_{fb} \qquad (2.14)$$

$$\rho_{fb} = 0.85 \; \beta 1 \frac{f'c}{f_{fu}} \frac{Ef \in_{cu}}{Ef \in_{cu} + f_{fu}} \qquad (2.15)$$

Where ρ_{fb} = balanced reinforcement ratio, ρ_f = actual reinforcement ratio and
The strength reduction factor for under-reinforced steel-reinforced RC beams is 0.9 (**ACI 2019).**

2.5 RC MEMBERS REINFORCED WITH GFRP BARS - A REVIEW

A lot of research has been conducted on the performance of Simply Supported (SS) girders with internal reinforced with FRP bars under four-point bending. The previous study focused on the flexural behavior of FRP reinforced concrete beams with longitudinally reinforced **Glass Fibre Reinforced Polymers (GFRP)** reinforcing bars (**Sam & Swamy 2005, Chitsazan et al. 2010, Ascione et al. 2010, Goldston et al. 2016 and Goldston et al. 2017).** Furthermore, performance and reliability and deflection computation for FRP RC beams using latest methods for an effective moment of inertia are essential issues **(Al-Sunna et al. 2005, Rafi, & Nadjai 2011, Toutanji and Saafi, 2000)** incorporating the model supplied by FRP design suggestion **(ACI 2015)**, which is based on **(Bischoff et al. 2009)** research. Furthermore, there have been several kinds of research on the behavior of normal and high strength concrete with FRP bars, highlighting the impact of concrete strength on the performance of FRP RC beams. **(Theriaule and Benmokrane 1998).** The following section, which also contains a review of the research, discusses the flexural behavior, serviceability, and influence of normal concrete and high concrete strength on the performance of FRP reinforced concrete beams.

GFRP-RC beams have different flexural behavior than steel-RC beams. This is due to substantial mechanical and physical differences between GFRP and traditional steel reinforcing bars **(Ascione et al. 2010).** FRP is a linear-elastic material, whereas steel reinforcement is ductile, as previously stated. As a result, concrete crushing is the favored failure mechanism of FRP RC beams, as the beam exhibits some sort of "ductility" and plastic behavior before failure. The failure of FRP bars in tension can be catastrophic or disastrous occur without warning, thus it should be avoided **(Goldston et al. 2016).** As a result, the flexural design

philosophy was developed. FRP reinforced RC beams have a different concept than typical steel RC beams. For traditional steel-reinforced concrete beams, yielding steel before exceeding the moment capacity is critical because it provides ductility and failure warning. Consequently, the FRP design procedures specify that concrete crushing govern the design for FRP reinforced concrete beams. Furthermore, as compared to steel reinforced concrete beams, FRP reinforced concrete beams exhibit substantially greater deflections and fracture widths due to mechanical characteristics, largely due to the low elasticity modulus of FRP reinforcements **(Goldston et al. 2017)**. A substantial expanse of study has been done in this field by examining the flexural behavior of FRP reinforced concrete spiecemens subjected to four-point loading **(Alsayed 1998, Theriaule and Benmokrane 1998, Sam & Swamy 2005, Chitsazan et al. 2010, Ascione et al. 2010 Goldston et al. 2016 and Kumar and Sundaravadivelu 2017) and discussed briefly below:**

Alsayed (1998) examined the flexural conduct of 12 reinforced concrete beams subjected to 4p-bending, dividing them into four groups, each with three specimens of different material characteristics. The control specimens (group A) were made using typical steel reinforcement and were meant to fail due to the steel reinforcement yielding.

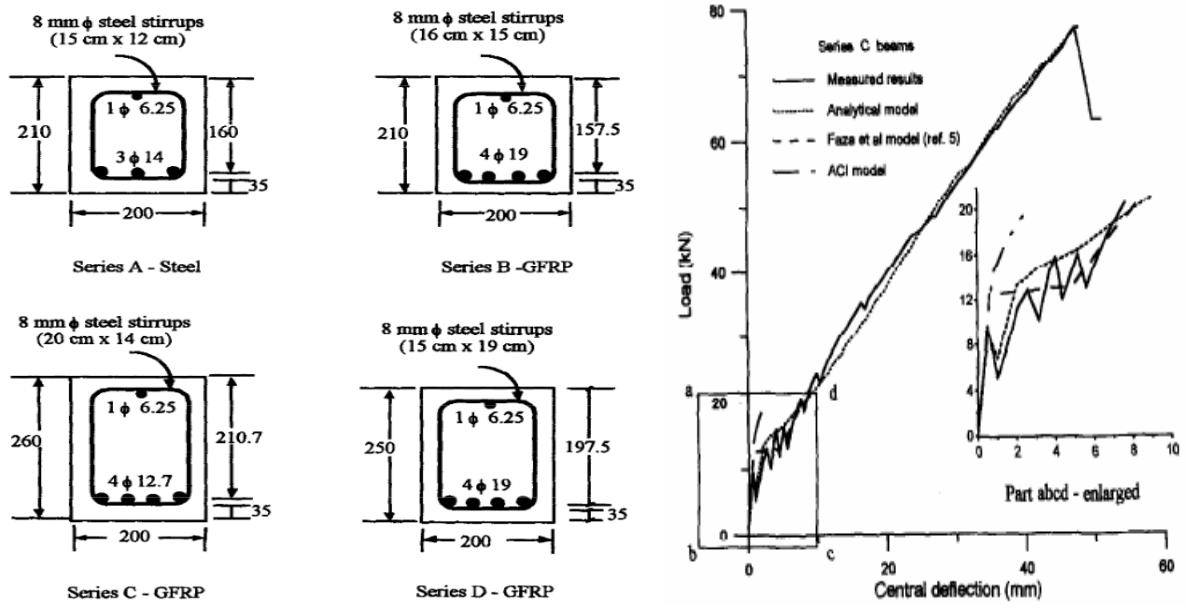

(a) **(b)**

Fig. 2.7: (a) Cross-Section and Reinforcement Details for Beams in series A, B, C, D and (b) P-∆ curve for Series C Beams (Alsayed, 1998)

The remaining 9 GFRP reinforced concrete beams (groups B, C, and D) were designed to be over-reinforced with GFRP reinforcement bars, with flexural strength judged to be comparable

to group one beams as shown in **Fig. 2.7(a)**. The beams in the corresponding group were made in the same way. The normal strength concrete (NSC) utilized was between 31 and 41 MPa. The results of the experiments revealed that GFRP reinforcement is a viable substitute for steel reinforcement. The GFRP reinforced concrete (Series C) beams' average load-deflection behaviour showed a bi-linear correlation as shown in **Fig. 2.7(b).** The authors observed a considerable reduction in load drop near the cracking threshold, which they ascribed to the low mechanical properties (elastic modulus) of the GFRP bar. The controlled specimens were constructed as under-reinforced initially and were demonstrated to fail due to steel reinforcement giving, followed by compression failure. On the contrary, concrete crushing was the cause of the collapse because all of the GFRP RC beams were designed to be over-reinforced.

Theriaule and Benmokrane (1998) studied twelve concrete beams reinforced with E- Glass FRP bar rods were tested under 4 point loading with two different longitudinal

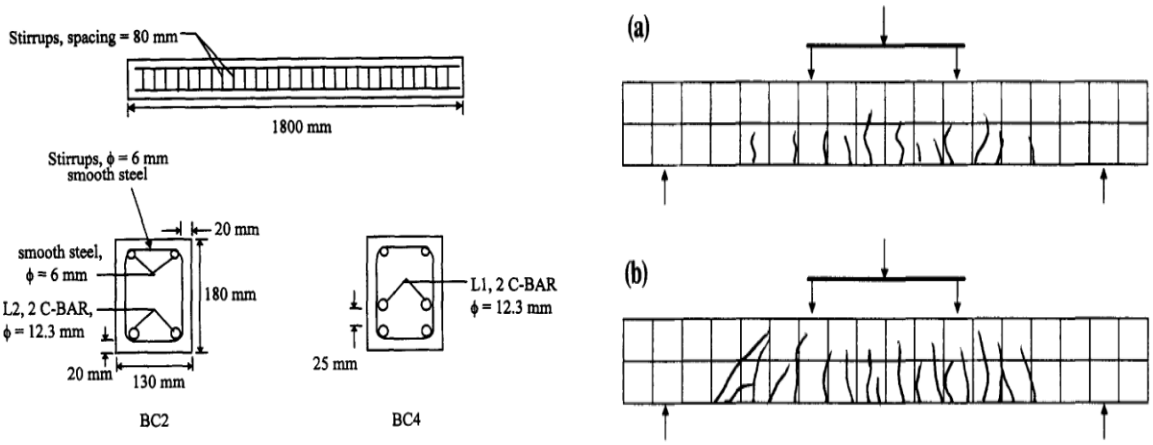

(a) **(b)**

Fig. 2.8: (a) Details of reinforcement and test specimen and (b) Cracking Pattern In BC4 and BC2 Specimen (Theriaule and Benmokrane, 1998)

reinforcement ratios of 1.16 percent and 2.77 percent are denoted as BC2 and BC4, respectively. The reinforcement ratio and concrete strength were two of the most important factors investigated in this research. Furthermore, the behavior of the beams was monitored before and after cracking to quantify fracture widths, crack spacing, mid-span deflections, and stresses, among other things. The ultimate moment capacity of the tested beams increases as concrete strength and reinforcement ratio increase, however, this increase is limited by the concrete compressive failure strain of over reinforced concrete beams Furthermore, when the

reinforcement ratio improves, the remaining crack width, crack spacing, mid-span deflections, and stresses decrease as revealed in **Fig. 2.8.**

Sam and Swamy (2005) studied the flexural behavior of RC beams measuring (0.15 x 0.255 x 2.4) m and strengthened with Glass FRP and stainless steel bars was evaluated under four-point loading**.** The load-carrying capacity, load-reinforcement strain, cracking, and mechanism of failure of RC beams were all examined by the author. The flexural behavior of the beam reinforced with Glass FRP bars differed from that of the beam reinforced with stainless steel bars, owing to the lower modulus of elasticity of the GFRP bars. Furthermore, the author discovered that the deflection of the GFRP RC beam was approximately 3 times that of the traditional RC beam at the identical load level.

Chitsazan et al. (2010) examined the flexural behavior of RC beams made of GFRP, looking at different types of failure, ultimate moment capacity, deflection, the load of the first crack, how to generate and expand cracks on the beam, and the position of the NA during loading for various GFRP bar ratios. On flexural behavior of concrete beams with GFRP, the author utilizes HSC mix instead of NSC mix and increases the effective depth across the width. The P-Δ plot of reinforced beams with FRP, according to the author, looks like a straight line with no failures. As a result, increasing concrete strength does not influence deflections. The author also noticed that in some GFRP-RC beams, particularly those composed of regular concrete mix, the NA rises due to the formation of fractures and that this process continues until ultimate loading. The NA then decreases until the beam ruptures completely and the GFRP-RC beams also exhibit elastic behavior as expected, with a large deflection shown to reverse after the load is removed.

Ascione et al. (2010) examine the research observations of ten beam specimens to see what properties of concrete specimens reinforced with Glass FRP bars and stirrups are peculiar. Experimental evidence and theoretical expectations are compared as represent in **Fig 2.9**. The author found that the moment-curvature relationship of Glass-FRP reinforced members is linear in both the pre-and-post-cracked phases; moreover, experimental results support the accuracy of the prediction formulas provided in CNR-DT 203/2006 for both deflections and crack width.

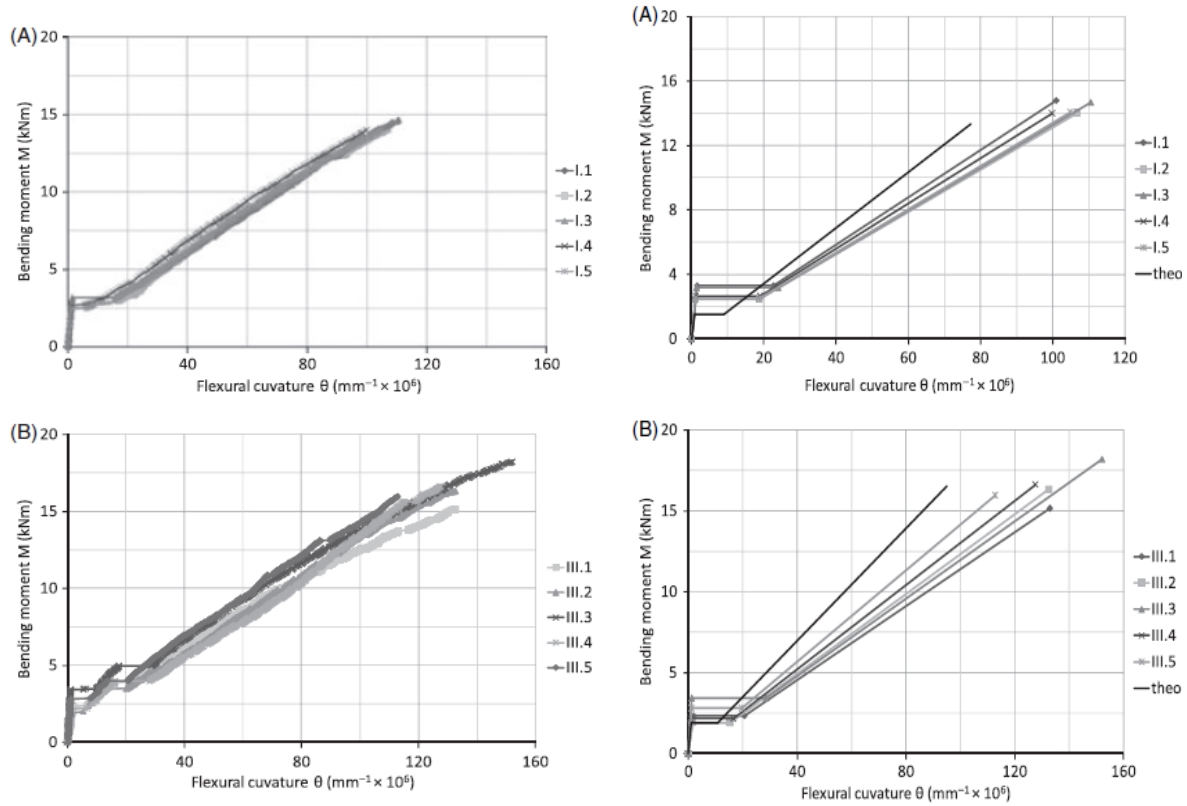

(a) **(b)**

Fig. 2.9: (a) Bending moment versus experimental flexural curvature and (b) Idealized bending moment versus experimental flexural curvature (Ascione et al. 2010)

RC beams strengthened by the reinforced GRP bars were examined by **Kalpana and Subramanian (2011)**, the key factors being the strengthening ratio (1.0, 1.6, and 2.4%) and concrete compressive strength; NSC and HSC (20, 40, and 60) MPa three specimens each. Glass FRP beams dimensions were 1.8 m in length with a rectangular cross-section of (0.2 x 0.25) m subjected to 4-point bending. Steel stirrups with an 8 mm diameter and a 100 mm c/c were utilized for shear reinforcement. The P-Δ behavior, failure mechanism, and fracture breadth at various load levels were also studied. The author found that improving the ultimate load-carrying capability of the GFRP-RC beams was more important than minimizing mid-span deflection. Furthermore, for reinforcing ratios of (1.0, 1.6, and 2.4) percent, increasing concrete strength from 20 to 60 N/mm2 increased load-carrying capacities by (53, 67, and 62) percent, respectively. By maintaining concrete strength constant, load capacity increases by increasing the GFRP reinforcement ratio, whereas decreases mid-span deflection with NSC (20 N/mm^2), between 3%-20%, compared to 2%-13% and 2%-7% for 40 N/mm^2 and 60 N/mm^2 HSC, respectively. When the GFRP reinforcement ratio was increased, while maintaining same

concrete strength, the load capacity is increased, while mid-span deflection decreased by 3%-20% with NSC (20 N/mm^2), compared to 2%-13% and 2%-7% for (40 and 60) N/mm^2 HSC, respectively.

Getzlaf et al. (2012) studied the flexural behavior of glass FRP reinforced concrete beams under 4 point loading. Sixteen GFRP RC beams were cast, reinforced with GFRP bars of various diameters, and the following factors were investigated: longitudinal reinforcement ratio (0.4-1.9%), failure mode (balanced, GFRP rupture, concrete crushing). The author utilises both normal and high strength concrete mixes (NSC = 41.4 N/mm^2, HSC = 80.9 N/mm^2). The GFRP-RC beams had a rectangular cross-section of 200 by 325 mm and a total length of 3620 mm. The GFRP-RC beams were intended to fail in three different ways: balanced, under-reinforced and over-reinforced. The impact of changing concrete compressive strength from NSC to HSC was studied and found to be significantly reliant on the longitudinal reinforcement ratio, according to the author. With a reinforcement ratio of 0.5 percent, the GFRP-RC beams were initially intended as under-reinforced (governs GFRP rupture). Furthermore, the author found that increasing concrete strength from 41.4 to 80.9 N/mm^2 only enhanced load-carrying capacity by 6%.

El-Nemr et al. (2013) studied the flexural behavior of twelve GFRP RC beams with normal and high strength, as well as two control specimens strengthened with conventional steel reinforcement. With cross-sectional characteristics of 0.2 m x 0.4 m and a total length of 4.25 m, the RC beams were easily supported and tested under 4-point loading. The author employs GFRP reinforcement with diverse external surface textures, such as sand coated and helically grooved. The NSC varied from 29 to 34 N/mm^2, whereas the HSC ranged from 59.1 to 73.4 N/mm^2. The major test parameters evaluated by the author were concrete compressive strength and reinforcement ratio. In comparison to NSC, the author found that GFRP-RC beams with HSC had a greater post-cracking rigidity. In comparison to the helically grooved, the sand-coated GFRP-RC beams had lower fracture widths. With both NSC and HSC, increasing the quantity of longitudinal reinforcement increased the load-carrying capability of the GFRP RC beams as shown in **Fig 2.10.** The flexural performance of 10 GFRP reinforced RC beams was analysed by **Adam et al. 2015** under 4-point loading. The FRP Glass RC beams had a rectangular cross-section of were 0.12m by 0.3 m rectangular and 2.8 m long and had shear reinforcement in form of 8mm diameter steel links spaced at 150 cm/c. The concrete compressive strength (three distinct classes, including NSC (25 and 45 N/mm^2) and HSC (70 N/mm^2), reinforcement-ratio, and material type were all investigated by the author (GFRP

reinforcement and steel reinforcement). The author discovered a bi-linear P-Δ up to catastrophe, with the crack section considerably reducing the whole stiffness of the Glass FRP reinforced concrete beams, resulting in greater deflections. Furthermore, as compared to the under-reinforced GFRP RC beams, the over-reinforced GFRP RC beams with the highest amount of tensile reinforcement showed some ductility before failure. In addition it has been found that the GFRP RC beam failure process is dependent on the tension reinforcement's ratio. Furthermore, raising concrete strength from 25 to 45 MPa (an 80 percent increase) decreased fracture width by 52 percent, compared to an 80 percent reduction when concrete strength was raised from 25 to 70 N/mm^2 (180 percent increase).

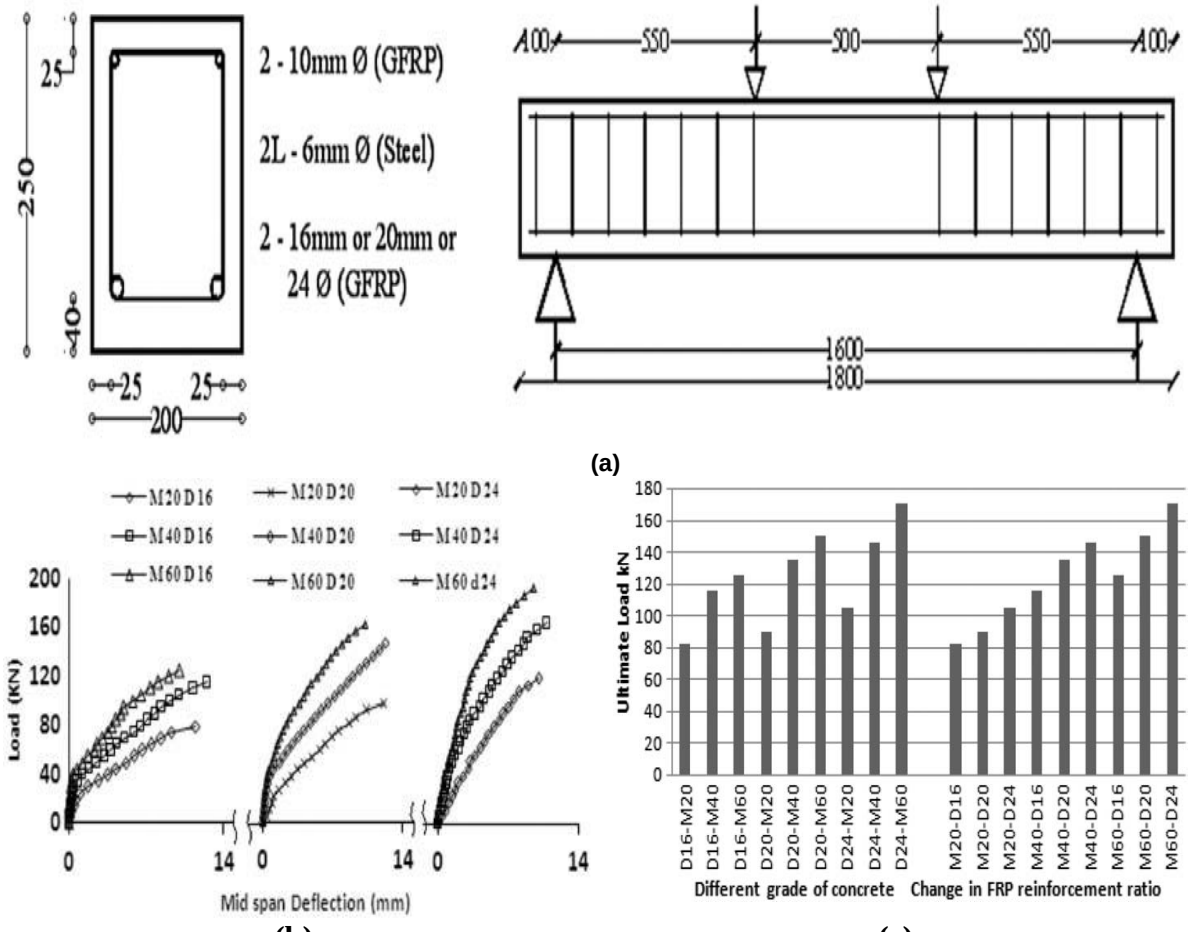

Fig. 2.10: (a) Cross-section detail and test setup of the beam (b) Midspan deflection of beams for varying grades of the concrete and (c) Ultimate load of GFRP beams (El-Nemr et al. 2013)

High Strength (HS) and Ultra High Strength (UHS) concrete beams reinforced with GFRP bars were studied by **Goldston et al. 2016.** Six beams were utilized in the experimental program to study the flexural behavior of Glass FRP RC beams under 3-point bending. The

impact of reinforcement ratio and concrete compressive strength (HSC and UHSC) on capacity, for load carrying, deflection, capacity for absorption of energy, stresses in the concrete and reinforcement, and failure mechanisms were examined by the author. The energy absorption capabilities of UHSC GFRP RC beams were shown to be greater for the same amount of tension reinforcement as HSC GFRP-RC beams, according to the author. Furthermore, the GFRP-RC beam's flexural capcacity was found to be conservative (load-carrying capacity was 36 percent under-predicted for both HSC and UHSC GFRP-RC beams). Furthermore, Glass FRP design guidelines for calculating deflection at the load-carrying capacity were found to be un-conservative (deflections for HSC GFRP-RC beams and UHSC GFRP-RC beams were under-predicted by an average of 10–22 percent).

The findings of experimental research into the impact of using GFRP bars as internal reinforcement on the behavior of concrete beams under four-point bending are presented by **Goldston et al. 2017.** The longitudinal reinforcement ratio, with reinforcement ratios of 0.5

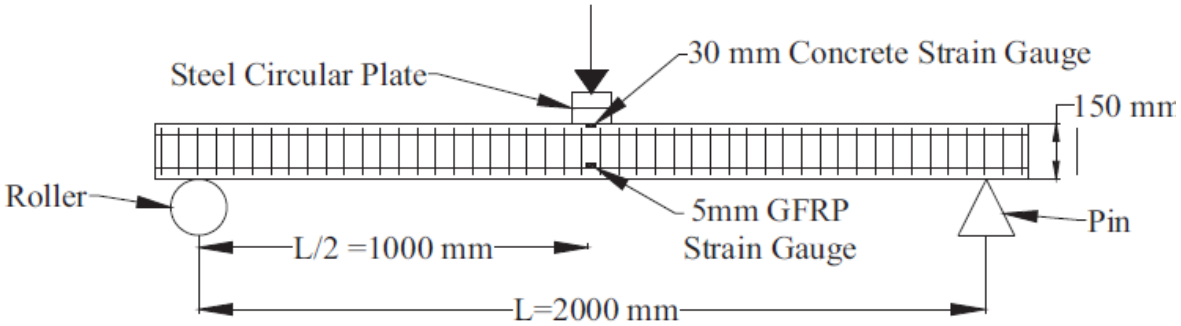

(a)

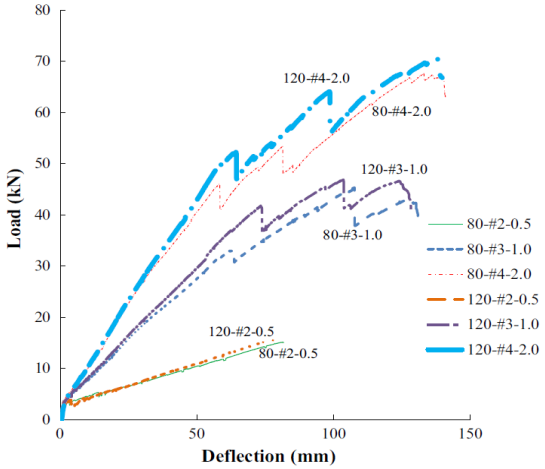

(b)

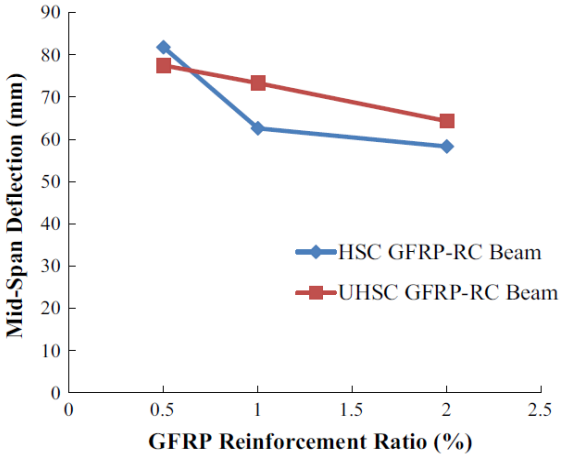

(c)

Fig. 2.11: (a) Schematic view of GFRP-RC beams (b) Load-midspan deflection behavior of GFRP-RC beams under static loading and (c) Effect of reinforcement

ratio and concrete strength on mid-span deflection at peak 1 load (Goldston et al. 2017)

percent, 1.0 percent, and 2.0 percent, and High Strength (HS) and Ultra High Strength (UHS) concrete compressive strength were the test variables. The P-Δ behavior of normal and high strength concrete GFRP RC beams showed a bi-linear response, with the first part of the response suggesting an un-cracked beam. The second part of the respondents indicated the cracking behavior of the GFRP-RC beam. Furthermore, before the whole breakdown, GFRP RC beams intended as over-reinforced with one percent and two percent reinforcement ratios exhibited symptoms of reserve capacity or "ductility." Furthermore, concrete strength was shown to have a stronger impact on lowering deflection and improving post-cracking bending stiffness. When concrete strength was increased with a greater reinforcement ratio (2.0 percent), mid-span deflection was reduced by 21%, compared to just 7.0 percent for a reinforcement ratio of 1.0 percent. On the other hand, regardless of the reinforcing ratio, increasing concrete strength from normal to high strength had no influence on experimental moment capacity as presented in **Fig 2.11. Krasniqi et al. (2018)** studied the flexural conduct of two steel and four GFRP RC beam specimens, under 4-point loading. The control specimens (series A) were made with conventional steel and a tension reinforcement ratio of 0.46 percent, while the remaining four GFRP-RC beams (series B and C) were made with GFRP reinforcement bars and reinforcement ratios of 0.19 percent and 0.46 percent, respectively. The influence of the GFRP bars' reduced modulus of elasticity was obvious in early fracture to start in the beams reinforced with GFRP compared to conventional reinforcement, according to the author. Furthermore, as compared to concrete members reinforced with conventional steel, RC beams reinforced with GFRP bars have 2.5 times higher deflections and 1.6 times wider crack widths. Furthermore, the GFRP-RC beams' failure is primarily caused by lower post-cracking stiffness and rebar-to-concrete matrix slip.

The flexural conduct of 8 GFRP RC beams under four-point loading was studied by **Saleh et al. (2019).** Rebars with diameters of 6.35 mm, 9.53 mm, and 12.7 mm were utilised, respectively with reinforcement ratios of 0.5%, 1.0%, and 2.0%. The energy Absorption Capacities and experimental load-deflection relationships were measured and evaluated. The author employed two design codes, ACI (2015) and CSA (2012), in relation to experimental data, for the flexural design of Glass FRP-RC specimens. The ACI-2015 predicted higher nominal loads, mid-span deflections at nominal loads, and energy absorption capacities than the CSA (2012) by a factor of 20 to 43. The nominal loads, mid-span deflections at nominal

loads, and energy absorption capacities predicted by the CSA (2012) were more conservative than those predicted by the ACI (2015). Furthermore, both ACI (2015) and CSA (2012) predicted values nearer to the experimental results for Glass FRP RC beams with high concrete compressive strength and tension reinforcement ratio with respect to maximum load, mid-span deflection and energy absorption capacity.

2.6 CLOSING REMARKS

This chapter focuses on the definition and characteristics of FRP, as well as a timeline of how FRP has been used as reinforcement in civil engineering projects throughout history. Design guidelines for FRP-reinforced beams are explained in depth. In addition, a comprehensive literature study on GFRP utilized in reinforced concrete members was conducted.

CHAPTER 3

AE AND DIC TECHNIQUES FOR DAMAGE MONITORING

3.1 GENERAL

The chapter analyses the effectiveness of sophisticated non-destructive testing (NDT) techniques such as the Acoustic Emission (AE) and Digital Image Correlation (DIC) for monitoring concrete structures. Acoustic Emission outperforms existing NDT methods in terms of monitoring dynamic deformation processes. Minor or significant fractures, bond failure, yielding, and other factors can cause material deformation. When a structure deforms, energy is released due to micro- and macro-cracking, resulting in a transient elastic wave known as "acoustic emission" that travels through the specimen. AE waves change in size and frequency with structural deformation may be readily captured by putting sensors on the structure surface. **(Ohtsu and Tomoda, 2007; Prashanth & Kishen, 2008 Sharma et al. 2015; and Burud & Kishen, 2021)**. DIC, on the either hand, is an optical and non-contact measuring technology that allows the displacement, deformation, and strain fields of a specimen's frontal surface to be determined under any loading condition **(Bruck et al. 1989, Wattrise et al. 2001; Shah and Kishen 2010; Blaber et al. 2015, Gribniak et al. 2017).** This approach is gaining popularity for studying crack development and material deformation being a low cost and a simple method to which gives an accurate solution **(Shah & Kishen, 2012).**

In the sub-categories of AE and DIC, the chapter discusses about the principal, equipment, various parameters, and methodology of these monitoring techniques.

3.2 ACOUSTIC EMISSION TECHNIQUE

3.2.1 Basic Principle

AE is the creation of elastic stress waves in a structure caused by a fast redistribution of stress or when a structure is subjected to an external stimulus such as a change in load, temperature, or pressure. Localized sources emit energy in the form of elastic-stress waves, which travel to the surface and are detected by a surface-momentum sensor **(Ohstu & Tomoda 2007; Yun et al. 2010; Sagar & Prasad 2012 and Gholizadeh et al. 2015).** This elastic stress wave propagates through the solid due to the energy released during the bending process **(Ohno**

& Ohno 2010 and Prem & Murthy 2017). The quantity of acoustic energy emitted is determined by the magnitude and velocity of the local deformation process.

In both extremely elastic and brittle materials, AE activity can be detected **(Sharma et al. 2018).** AE has been measured and recorded in a variety of materials, including, wood, polymers, and concrete **(Verbruggen et al. 2015).** With the aid of this approach, the maintenance team may be forewarned and repair work can be completed on time, saving money on repairs and extending the life of structures **(Barile et al. 2020).** This approach has been studied for almost sixty years, and various benefits and drawbacks have been identified, some of which are described below **(Ohno and Ohtsu, 2010).** The technique's advantages can be summarised as follows:

- The only non-destructive approach that allows for worldwide and passive monitoring of active faults.
- Using several sensors to locate the source of AE can help.
- Real-time measurements are possible.
- The signals are analyzed in detail to distinguish between real damage-related signals and background noise.

AE is the consequence of an irreversible process; therefore any loading profile cannot be used to confirm the presence of a source in a suspected location. This characteristic, while generally beneficial, can occasionally be a barrier in testing. The tendencies for signals to attenuate, as well as the removal of background noise, are both drawbacks of this acoustic method **(Ohtsu and Tomoda 2007 and Ohno and Ohtsu 2010).**

3.2.2 Types of AE waveforms

AE is described as brief elastic-stress waves caused by the fast release of energy during mechanical loading processes in a structure or material **(Ohtsu and Tomoda 2007; Ohtsu et al. 2011; and Verbruggen et al. 2015).** These transient elastic-stress waves

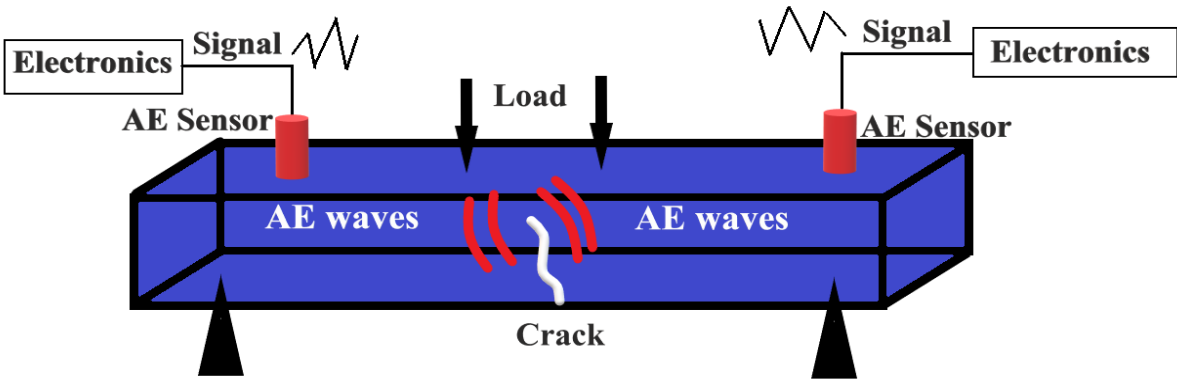

Fig. 3.1: Acoustic Emission Principle (Sharma et al. 2015)

propagate through the structure before being detected by acoustic sensors placed on the structure's surface. Electrical AE signals are converted from mechanical AE signals, which are then transformed into an electronic data set **(Sharma et al. 2015).** This data collection is further examined, and the collected data is graphed. The method of generating and recording acoustic emissions is depicted in **Fig. 3.1.**

In general, the following categories can be used to classify acoustic emission signals **Transient Signals (Bursts):** As illustrated in **Fig. 3.2,** these signals have a clear beginning and ending points that are distinct from background noise. They are frequently linked to crack propagation.

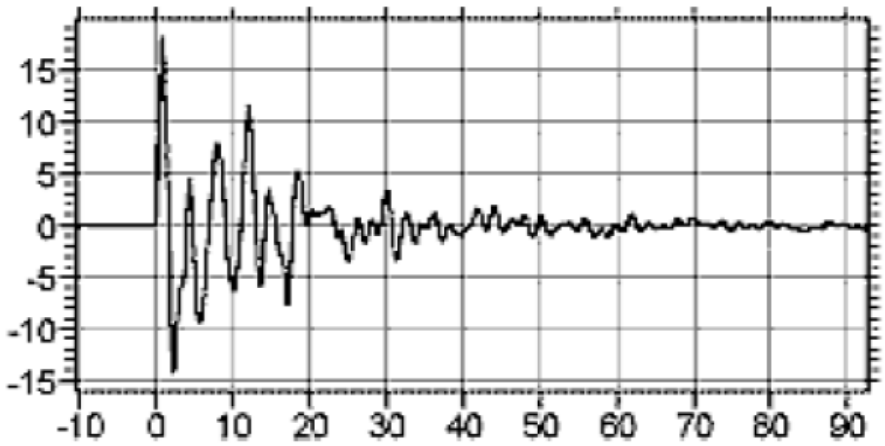

Fig. 3.2: Transient signal (Sharma et al. 2015)

1. **Continuous Signal:** These are never-ending waves with fluctuating amplitudes and frequencies, as the name implies. **Fig. 3.3** depicts a typical continuous signal pattern. For motions or dislocations, they are usually the AE response.

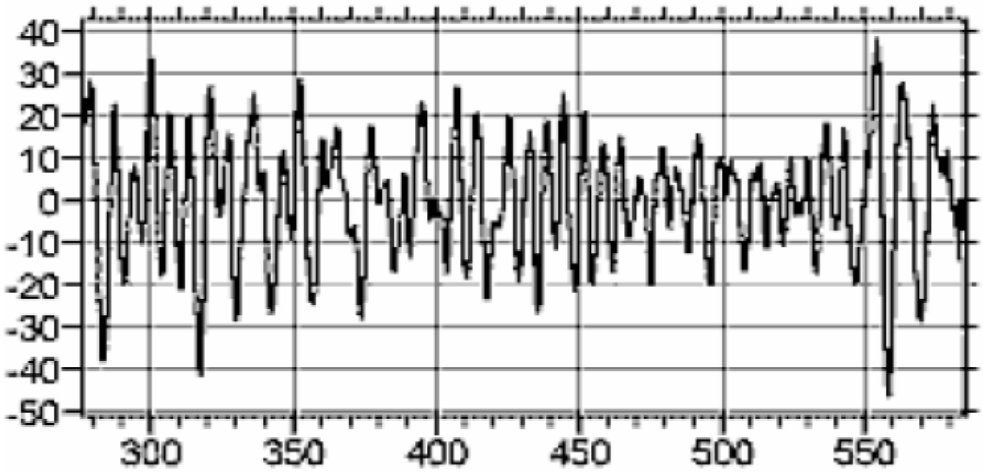

Fig. 3.3: Continuous signal (Sharma et al. 2015)

3.2.3 AE Set-up

The monitoring of AE is made feasible by a variety of equipment. Each component serves a specific purpose and is required for proper monitoring. This section includes a summary of each component:

- **AE Sensors: -** It is used to record AE signals and is placed on the surface of an RC structure. A piezoelectric transducer is often used to transform mechanical AE waves to electrical signals. In order to properly identify the source location, the sensors must be carefully placed at the appropriate location.

Fig. 3.4: Common types of AE sensors (www.googleimages.com)

- **Couplants and holders**: Various couplants are used to attach sensors to the surface of the item to be evaluated. These are mostly utilized to assist inside the efficient and complete

transmission of the source's acoustic waves. The AE sensors are generally mounted on the surfaces to be monitored using Vaseline cream and held in place using cello adhesive tape.

- **Pre-Amplifiers**: Pre-Amplifiers are used to provide gain in order to amplify signals to a less susceptible level and to filter and eliminate sound from locations outside the sensor's working range efficiently.
- **Data acquisition system:** Modern AE systems use computers and associated software to offer menu-driven parameter input and system control. All of the signals received at the sensor end are collected and stored by the acquisition system. The new generation method also offers a wide range of post-processing options.

3.2.4 AE signal parameters

Essentially, acoustic emission monitoring has two key characteristics: first, it can detect and record AE generated by a cause of damage, and second, it can pin-point the source of damage. Following the recording of AE waveforms, the detected signals are analyzed numerically and qualitatively to determine the properties of source acoustic emission. The features of AE sensors, the kind of damage source, and the distance between the source and the AE sensor are the three primary parameters that impact the recording of AE signals. Understanding an acoustic signal necessitates an understanding of certain fundamental terminology that is required to analyze and understand these indications. In **Fig. 3.5,** a typical signal is depicted.

- **Threshold**: A threshold is a predetermined voltage level that must be surpassed before an acoustic emission signal can be recognized and processed.
- **Hit:** A hit is a word used to describe when an AE transient is recognized and processed by an acoustic emission channel that is over the threshold value. The total number of AE strikes is recorded for all acoustic emission data. It also suggests that the material or structure has experienced some type of alteration.

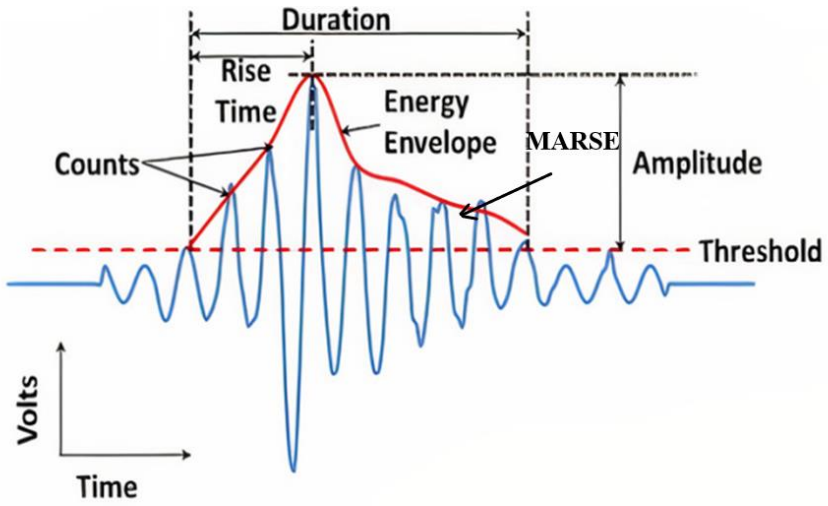

Fig. 3.5: Waveform of Acoustic Emission signal and various parameters (Dunn et al. 1984)

- **Arrival time:** The exact moment when a burst signal passes the detection threshold for the first time.
- **Peak Amplitude:** Throughout the course of the burst signal, the maximum absolute amplitude. The amplitude of the source event is related to its size.
- **Rise Time**: The period between the first threshold crossing and the burst signal's maximum peak amplitude is known as the rise time **(Ohtsu and Tomoda 2007).** This parameter is frequently used in problems requiring time-dependent processes like dynamic loading or structural vibration.
- **Signal Duration:** The time between the first and final time a burst signal surpassed the detection threshold. This parameter measures something similar to counts **(Sharma et al. 2015 and Sharma et al. 2018).** It's very handy for noise filtering and other signal qualifying applications.
- **Counts:** The nos. of times the amplitude of the signal surpasses the threshold value.
- **Absolute Energy:** Over the period of the acoustic emission packet, absolute energy is defined as the integral of the squared voltage signal divided by the reference resistance. This is the real energy of an AE-hit, and its units are attojoules. The only constraint of absolute energy is that it only covers digitized signal length; if the signal length is longer, the total recorded energy will be significantly lower than the true energy.
- **Event**: A single acoustic emission (AE) generates a transitory mechanical wave that travels in all directions in a medium. The AE wave is recognized when one or more AE sensors are struck. As a result, an event is defined as a collection of AE hits from a single source. The AE event is mostly used for source location with the aid of AE.

- **Signal-Strength (SS):** The term "signal-strength" (SS) is used to describe how damage evolves in structures. The word signal strength is defined by the Physical Acoustic Corporation (PAC) as the integral of the rectified voltage signal over the duration of the AE waveform packet, or the quantity of energy emitted by the material or structure. It is a direct function of the recorded Acoustic Emission (AE) signal's amplitude (db) and duration (us).
- **MARSE** (Measured Area of the Rectified Signal Envelope): The area under the envelope of the sensor's rectified linear voltage-time signal is measured. Because it is sensitive to both amplitude and duration, this quantity is chosen over counts. It's also less responsive to a threshold and operating frequency settings. As demonstrated in **Fig. 3.5,** MARSE is most suited for defining the total cumulative AE activity.

Several signal characteristics influence the accuracy of the data acquired using the collection equipment. The primary impacts include attenuation, which is defined as the loss of signal amplitude owing to material dampening, as well as the geometry of the material **(Archana et al. 2003).** The quantity of acoustic activity created is affected by wave velocity, shape, and material characteristics **(Sarfarazi, 1992).** The AE signature is affected by the kind of stress and rate of loading applied to the materials. Damage to materials, crack propagation, low temperature, and deformation are all connected to high AE, as are brittle fracture, anisotropy, heterogeneity, high strength, and high strain rate **(Ohstu & Tomoda, 2007 and Ohno & Ohstu, 2010).**

The advent of new signal processing methods has simplified the elimination of unwanted segments during the post-processing stage. When analyzing large constructions like bridges, advanced approaches may be required, including the use of extra transducers recognized as guard sensors. These extra transducers have logic that allows signals detected by these sensors to be disregarded **(Ohtsu and Uddin, 2008).**

3.2.5 AE Signal Analysis

Parametric Analysis (PA) and Waveform Analysis (WA) are two approaches for evaluating an acoustic emission signal to detect damage in RC structures **(Sharma et al. 2015).** PA is the process of extracting parameters from an AE signal and evaluating the amount of damage based on the features of the AE signal. Because it only deals with parameters concerning a certain threshold voltage and not the full acoustic emission signal, the parametric analysis approach has a fast recording and data storage speed. The WA approach involves immediately capturing the AE signal and determining the amount of damage based on the

behavior of the AE signal. The WA approach can distinguish between the AE signal waveform and noise and offer accurate results. But it requires a large amount of system memory for data storage and necessitates the temporary shutdown of the recording system while storing AE signals, resulting in a delay or interruption.

As a result, recording of AE signal parametric analysis is recommended in real-world situations where massive reinforced concrete structures must be monitored. At the same time, technicians should confirm that the monitoring system is functioning properly by capturing and analyzing AE signals.

3.2.5.1 Parametric Analysis (PA)

- It includes capturing acoustic emission signal characteristics to give both qualitative and quantitative damage evaluations in reinforced concrete (RC) structures. Hits, energy, counts, amplitude, and signal intensity are some of the most often utilized AE characteristics for qualitative damage estimation.
- **Cumulative AE-hit:** The regions of micro- and macro-cracks may be estimated using cumulative AE-hit. Higher AE activity or a greater number of AE strikes are associated with a higher crack evolution rate.
- **Cumulative Signal Strength:** The term "cumulative signal strength" states to the accumulation of each hit's signal strength over time, with an emphasis on the overall quantity of acoustic emission activity generated. This curve can be used to notice significant damage in a reinforced concrete structure that occurs suddenly or unexpectedly. The CSS curve's height of spikes, also known as the knee, shows the existence of micro and major macro cracks in RC structures.
- **Amplitude of AE hits:** The amplitude of AE impacts is proportional to the severity of the damage to the RC structure. Microcracks, which are generally formed in higher numbers, produce AE signals with lower or lower amplitude values (dB). Micro-cracks, on the other hand, provide a higher-amplitude AE signal when they are formed in small numbers.
- **Intensity Analysis:** This is an analytical approach that aids in determining the specimen's overall integrity as well as the structural relevance of the observed AE events. The parameter under consideration is **"signal strength,"** which is a distinctive AE signal waveform that includes both the amplitude and duration components. From the signal strength parametric data gathered during collection, two indices known as the **"Historic**

index" are calculated, demarcated as average signal strength among the largest numerical values of the signal; using the formula shown in **Equation 3.1.**

$$\mathbf{HI(t)} = \frac{\sum_{i=K+1}^{N}[S_i/(N-K)]}{\sum_{i=1}^{N}(S_i/N)} \quad (3.1)$$

Where HI (t) represents the historic index at time t, K represents the number of previous hits, S_i represents the signal strength at the i^{th} hit, and N represents the total number of hits.

Severity Index is the average signal-strength for a specific number of hits with the highest signal-strength is used to compute the Severity Index. It is represented as in **Equation 3.2.**

$$\mathbf{SI(t)} = \sum_{j=1}^{L}\left(S_j/L\right) \quad (3.2)$$

$S_I(t)$ = severity index at time t, L = number of hits with the highest signal intensity, and S_j = the signal strength at the j^{th} hit.

- **AF/RA value analysis**, using the raw AE signal parameters obtained from continuous Structural Health Monitoring (SHM) systems, several researchers have been able to identify, quantify, and locate various forms of damage in RC structures using AF/RA value analysis. For example, in RC constructions, the Average Frequency (AF) and Rise Angle (RA) values have been used to categorise distinct types of cracks **(Ohtsu et al. 2010).** This study shows that AE analysis can distinguish among tensile and shear cracks caused by external loads or forces on RC structures.
- **Average Frequency (kHz) and Duration (µs) analysis**, apart from Amplitude of AE-hits, Cumulative AE-hits, and AF/RA value analysis, valuable information can also be derived from Average Frequency (kHz) and duration (µs) of AE hits with time. For instance, a reduction in AF and substantial increases in AE duration at the same time can be seen as a good indicator of key failure sites in RC structures.
- **AF/RT plot analysis,** for damage quantification, AF/RT plot analysis uses the average frequency and rise time characteristics of AE signals. For example, in RC constructions, average frequency and rising time plot values have been used to distinguish distinct types of cracks (micro and macro) (Ohtsu, 2010). The author concluded that tensile cracking is indicated by a greater average frequency and shorter rise time, whereas shear cracking is indicated by a longer rise time and shorter average frequency. In RC constructions, there is a wide range of damage initiation and development, fracture classification (micro- and macro cracks), and failure mechanisms.

3.2.5.2 Waveform Analysis

The recording and analysis of acoustic emission signals, also known as Moment Tensor Analysis (MTA), is used to determine the amount of damage in RC structures. Processing techniques such as Fourier-Transform/(FT), Short Time Fourier Transform/(STFT), and Wavelet Transform/(WFT) can be used to analyze the recorded AE signal.

- **The Fourier-Transform/ (FT)** converted the acoustic emission signal from time to frequency domain, allowing the frequency components of the AE signal to be identified. However, the information or data detailing the time-of-occurrence of the AE signal is lost during this conversion. **Equation 3.3** is used to compute the Fourier-Transform/(FT) of a signal.

$$\mathbf{F(\omega) = \int_{-\infty}^{\infty} f(t) e^{-j\omega t}\, dt} \qquad (3.3)$$

- **Short-Time Fourier-Transform/(STFT)** By maintaining the time information as well as the frequency components of the AE signal, the STFT overcomes the limitations of the FT. The FT of the product of an acoustic emission signal and a window function is computed in STFT. First, at a specific moment, a fixed-size window is put over the AE signal, and the FT is determined. Second, the FT of this fixed-size window is computed and transferred to the next section of the AE signal. This procedure is carried out for the full AE signal. STFT has a fixed time and frequency resolution due to the settings window size. **Equation 3.4** is used to determine the signal's Short-Time Fourier-Transform/(STFT):

$$\mathbf{S(\omega) = \int_{W} f(t) s(t-\tau) e^{-j\omega t}\, dt} \qquad (3.4)$$

  where, $s(t-\tau)$ represents the window function centered at time τ and $S(\omega)$ represents the STFT of AE signal $f(t)$.

- **Wavelet-Transform/(WT)** By utilizing a variable window size for Fourier-Transform, Wavelet-Transform/(WT) overcomes the constraints of the Short-Time Fourier-Transform/(STFT) (FT). The frequency component of the AE signal determines the window size. A window with a short time interval is required for a low average frequency module, while a window with a short time interval is required for a high average frequency module. Splitting the acoustic emission signal into various levels with varying average frequencies and multiplying each level by an appropriate window size accomplishes this. **Equation 3.5** is used to determine a signal's continuous wavelet transform:

$$\mathbf{CWT(a,b)} = \frac{\mathbf{1}}{\sqrt{\mathbf{a}}}\int_{-\infty}^{\infty} \mathbf{f(t)}\Psi\left(\frac{\mathbf{t-b}}{\mathbf{a}}\right)\mathbf{dt} \quad (3.5)$$

Where, CWT (a,b) represents continuous WT of AE signal $f(t)$ and a and b are scaling and shift parameters of wavelet function of (t).

It is proposed that sensors be mounted on the concrete surface to monitor the flexural behavior of RC beams subjected to 4-point loading using the AE approach. The next section examines the current state of the AE approach for corrosion monitoring in RC structures.

3.3 REVIEW OF AET FOR DAMAGE MONITORING IN RC BEAMS

Maji and Shah (1988) studied the localization of cracks and movement of the Fracture Process Zone (FPZ) using the Acoustic Emission (AE) technique. Laboratory experiments were performed on plain-mortar and model-concrete specimens were subjected under direct tension and the rate of acoustic emission events and sources of AE activity were studied. The author reported that the before peak load (P_{peak}) was reached; all the recorded AE events were located near the notch. Furthermore, the author observed that a single peak load in plain-mortar specimen whereas multiple peak-load were observed in the model-concrete specimen. Moreover, the AE activity progressed during the strain-softening region with an increase in four-point loading. The FPZ was located using AE events and the location of the zone was confirmed with the location of the crack-tip evaluated by a modified Linear Elastic Fracture Mechanics (LEFM) model for plain-concrete and model concrete as well as by the microscopical observations.

Quyang et al. (1991) studied mode I, mode II and mixed-mode failure in pre-notched plain concrete beams specimens using the acoustic technique. Pre-notched plain concrete beams with an X-section of 0.037 m x 0.15m were tested in the lab under 4p-loading over a span of 375 mm. AE activity in pre-notched plain concrete beams loaded in flexure using four-point loading. The acoustic emission activity was represented as mode I-II, and mixed-mode using the AE seismic moment tensor demonstration. Moreover, the author also compared the observed visual cracking on the surface of the beams. For a mode-I macro

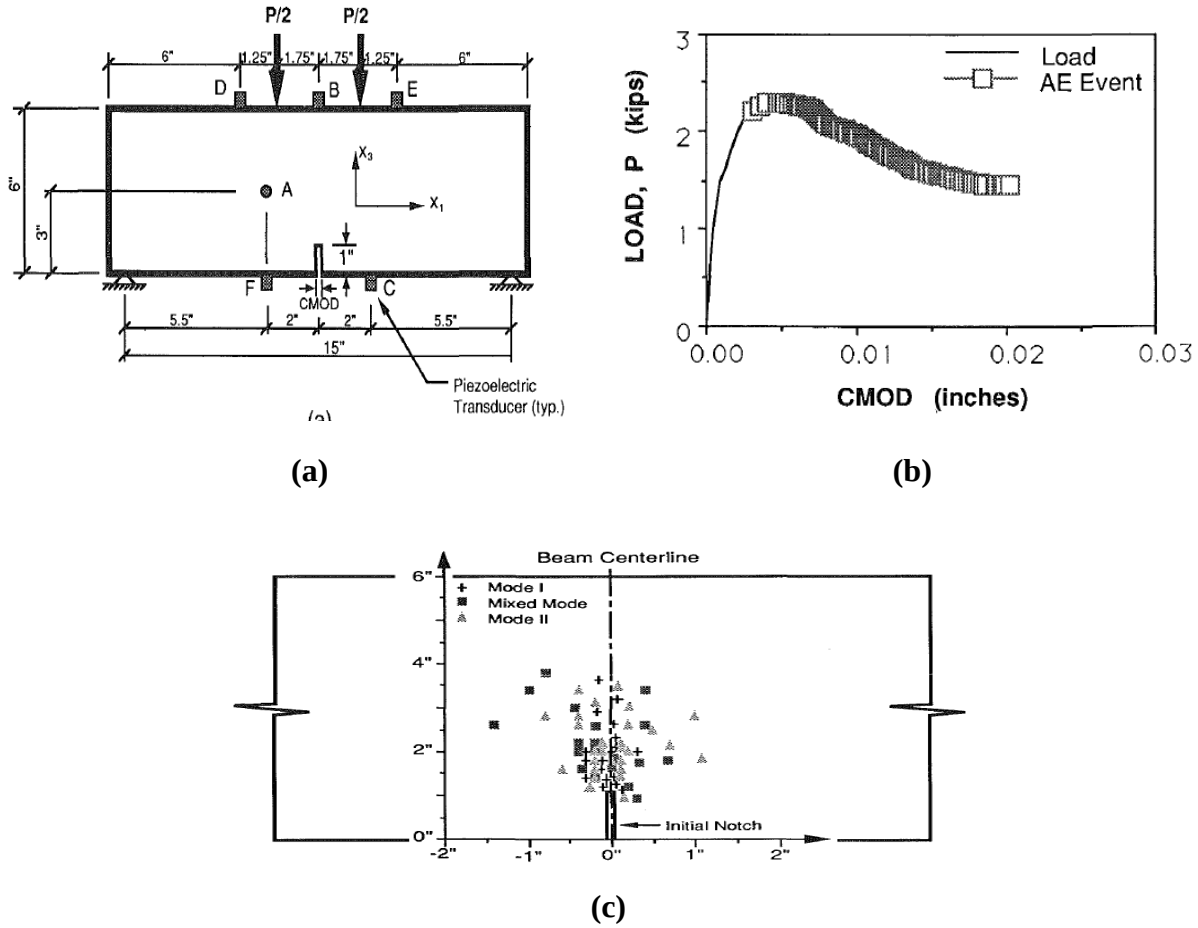

Fig. 3.6: (a) Geometry of Center-Notched Beam (b) Load-Crack Mouth-Opening Curve and Corresponding AE Events and (c) Locations and Fracture Modes of Microcrack for Center-Notched (Quyang et al. 1991)

crack (center-notched), the majority of the micro-cracking or micro-crack planes were in a direction normal to the tensile stresses, where micro-cracking was rather uniformly distributed for a mode-II and mixed-mode macro-crack (off-center notched). In the end, the author also concluded that acoustic emission could be used as a powerful technique for assessing the damage in concrete as shown in **Fig. 3.6.**

Zdunek et al. (1995) describe a technique for identifying early re-bar corrosion in reinforced concrete (RC) specimens exposed to cyclic salt exposure to initiate corrosion and monitored using an acoustic emission approach. The number of AE events increases in relation to micro-cracking of concrete owing to corrosion products build-up on re-bar, according to the author. Furthermore, a high amplitude of AE events was also observed due to micro-cracking in RC specimens. Moreover, when acoustic signals recorded by the two transducers were analyzed, a shift of ~ 10 micro-sec was observed which can help in finding the source location of AE events. Finally, the researchers noted that AE can identify the beginning of rebar corrosion early on.

Sagar et al. (2002) use the acoustic emission approach to describe a method for assessing damage in RC bridge beams exposed to incremental cyclic stress. The four-point loading tests were carried out on high-strength RC beams with the same reinforcement ratio (1.395%) but under three different loading circumstances (0.2115, 0.2052, and 0.1954). Three RC beams were tested, each with a depth of 0.3 m, a width of 0.15 m, and a span of 3.0 m. The concrete's compressive strength was 58 N/mm^2 after 28 days, and its tensile strength was 3.56 N/mm^2. The maximum size of coarse aggregate was 20 mm. The levels of damage indicated by AE data shift from minor to heavy damage levels as load cycles proceed, according to the author. As a result, the suggested revised criterion may be used to evaluate the damage of RC bridge beams. The author also investigates the relationship between AE activity and concrete and steel strain. Damage levels determined from maximum deflection and strain in steel and concrete are quite similar to the damage seen in RC beams, and flexure failure modes were created in RC beams.

Yun et al. (2010) used the acoustic emission approach to evaluate the damage of reinforced concrete beams reinforced with CFRP sheets. Five beams, each 200 mm x 300 mm in cross-section, were evaluated in the laboratory under 3-point loading across a span of 1700 mm. To serve as a reference, one of the beams was tested in its original state; the remaining 4 beams were evaluated after being reinforced using CFRP sheets glued to the tension face. Both the quantity of CFRP sheets and the number of construction imperfections were studied by the author in this investigation. For four levels of damage (I, II, III, and IV), the AE parameters in terms of AE event, amplitude, frequency, and duration time were analyzed based on initial crack, propagation, yielding of main bars, and fracture or rip-off of the CFRP sheets, and show clear differences in the different loading stages, depending on the active damage mechanism. The parameters of the average AE signal for beams reinforced with CFRP sheets, i.e., amplitude, frequency, and duration time, are in the range of 52–74 dB, 83-201 kHz, and 489-1099 μs when the crack is formed and propagated (damage levels I and II). The parameters of an average AE signal, i.e., amplitude, frequency, and duration time, were in the range of 72-89 dB, 172-230 kHz, and 891-2030 μs, respectively, when substantial fractures remained seen, major bars had surrendered (damage levels III and IV). Finally, the author found that when damage levels grow, the characteristic value of the AE signal tends to increase.

Shahidan et al. (2012) studied the damage classification of RC beam utilizing AE techniques. This method was utilized to determine the extent of damage as well as the kind of damage, such as tensile and shear crack motions at key zones inside an RC beam. Laboratory experiments are performed on one type of RC beam of concrete compressive strength 35

N/mm^2 having the overall dimension of 0.15 m wide, 0.25 m depth, and 1.9 m length along with tension reinforcement i.e. 1.33% against balanced-section. The RC beam would go through four stages of mechanical behavior before failure, according to the author. These four stages are (20%, 50%, 80%) ultimate load and ultimate failure. The results were presented using an AE signal waveform such as amplitude, rise angle, average frequency, and signal strength. The result indicates high AF and low RA values are observed which implies a low level of tensile cracking at the initial stages (20% and 50% of ultimate load) in the RC beam specimen. As the load increases towards the final failure low average frequency and high RA values are noticed which implies shear movements slowly increase through the final loading stage (ultimate failure).

Sagar and Prasad (2012) investigate an experimental study on damage assessment of RC beams subjected to progressive cyclic loading using the acoustic emission method. Three different depths of beams are examined in the laboratory, namely (150, 300, and 450) mm of grade M30 with 150 mm width and 3200 mm overall length of the RC beams specimen. The main parameter investigated in this article was relaxation ratio versus loading cycle. One notable outcome was observed for the relaxation ratio for specimens with depth 0.45 m, 0.3 m, and 0.15 m respectively. The ratio generally increases with the cycle number or in other words as damage increases. The trend changes when the load reaches about 70 percent, 75 percent, and 45 percent of maximum failure load respectively. Hence author concluded that the relaxation ratio could be a good parameter to identify the level of damage.

The AE approach was used by **Aggelis et al. (2013)** to investigate the mechanical performance of beams externally reinforced with Textile Reinforcement Cementitious (TRC) and CFRP (Carbon Reinforced Polymer) Strip. A 4-point bending test was performed on reinforced composite concrete beams with a total length of 2.5 m, a distance between the supports of 2.3 m, and height and breadth of 0.3 m and 0.2 m, respectively, a 4 point bending test was accomplished. The key parameters investigated in this article were Average Frequency (AF) versus Rise angle (RA). The author observed that the TRC beam withstands a 10% higher load than the CFRP reinforced beam. However, higher average frequency and lower rise angle value were observed in TRC Beam, which represents Flexure failure; on the other hand, lower average frequency and higher rise angle value were observed in the CFRP layer beam which represents the shear failure.

Verbruggen et al. (2015) investigated the structural analysis of Hybrid Composite-non carbon-reinforced beams and carbon-reinforced beams. In a laboratory test, AE analysis is used to monitor the failure of non-carbon reinforced and carbon-reinforced beams under four-point

loading. The main parameters investigated in this article were AF versus RT. The carbon-reinforced beams eventually failed in the GFR due to debonding, according to the author. A substantial shift from short to longer RT signals, as well as from high to lower AF was observed in the box's GFR.IPC layers. A tensile composite failure was observed for the non-carbon reinforced beams. On the other hand, the non-carbon-reinforced beams exhibit a distinct AE pattern throughout the whole experiment. A strong shift from longer to short RT signals and from lower to high AF was recorded. This behavior allows for real-time evaluation of the behavior, especially the dominant fracture mode, which is difficult to do with any other approach.

Prem and Murthy (2016) investigate the damage process of RC beams subjected to four-point loading. In a lab test, AE analysis is used to track the degradation of an RC beam under four-point loading. The study's major goal is to determine if AE monitoring can be used as an NDT approach in reinforced concrete structures. 3 types of reinforced concrete beams of grade M30 with overall dimensions of 0.1 m widths, 0.2 m depth, and 1.5 m length are tested in the lab against a balanced section with three different longitudinal tension reinforcements of 0.42, 0.64, and 0.93 percent and it is denoted as A, B, and C. There are 4 stages of mechanical behavior the beam would experience before the collapse, according to the author. Micro cracking, localized crack propagation, widespread flexural cracking, and damage localization are the four phases. The number of counts, cumulative absolute energy,

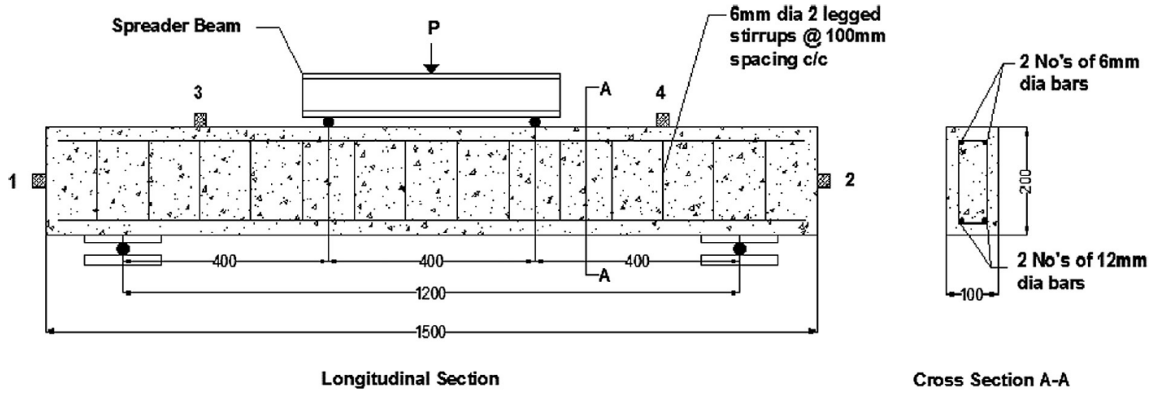

(a)

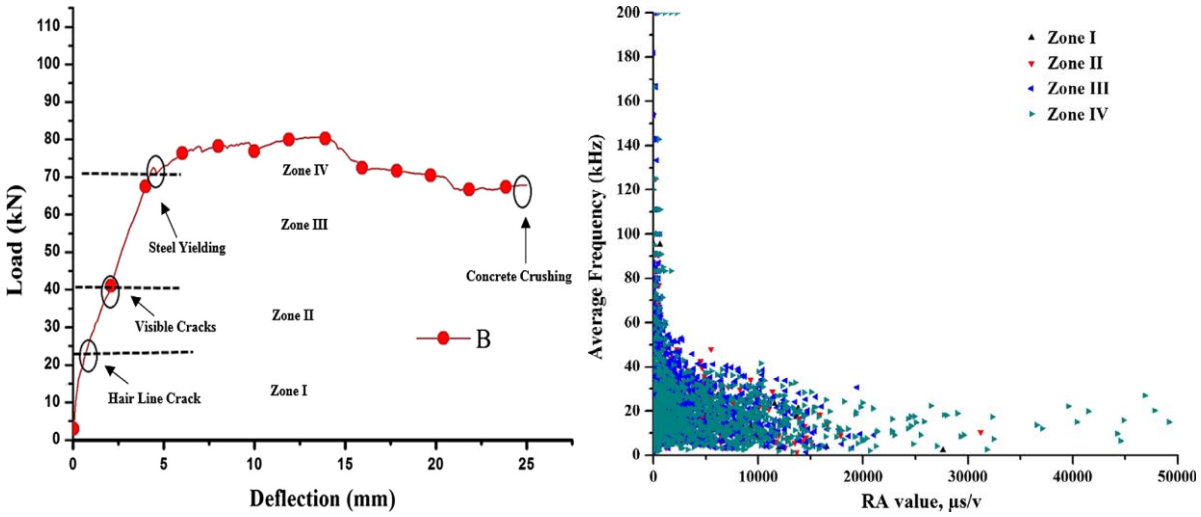

(b) **(c)**

Fig. 3.7: (a) Under four-point bending, a typical test setup and data collection system (b) Categorization of damage zones in RC beams under bending and (c) Relation between AF and RA value of B beams (Prem and Murthy 2016)

nos. of hits, and amplitude all rise as the damage level increases, as observed by the author. Furthermore, a moving average is used to do a parametric comparison between average frequency and rising angle value based on over 50 AE hits. By applying the present classification the A, B, and C RC beams are analyzed at each level of damage. Fig. 3.9(b) illustrates the damage zone classification of B beams under loading and **Fig. 3.9(c)** illustrates the relation between AF and RA values of B beams. The rate of increase differs from one AE parameter to another, having amplitude having the lowest rate. Frequency varies as well, and as the level of damage increases, it decreases. The effects of longitudinal steel on all AE parameters are nearly identical, the average and cumulative values of these parameters increase as the reinforcement ratio increases **(Fig 3.7).**

Corrado et al. (2017) used non-destructive techniques to assess the damage of an RC beam. The University of Salerno uses AE analysis to track the damage progress of an RC beam under load. Lab experiments are performed on one type of RC beam of concrete compressive strength 40.62 N/mm^2 having the overall dimension of 0.15 m wide, 0.2 m depth, and 2.0 m length along with tension reinforcement i.e. 1.12% against balanced-section. During a four-point loading test, mechanical and acoustic data were gathered using a loading technique that included multiple loading and unloading cycles. The Felicity ratio, SS, and CSS were all used to show the findings. When damage exceeds a 60% threshold, the Felicity ratio lowers to 0.7-0.75 according to the author. Signal Strength, on the other hand, has been studied and compared to

the cumulative signal strength. It was discovered that when the maximum load was reached, the CSS increased significantly and suddenly.

Sagar et al. (2017) studied the fracture monitoring of RC T-beam specimens that were put through an incremental cyclic load until they failed in bending. In a laboratory test, AE analysis is used to monitor the fracture monitoring of an RC beam under cyclic loading. Five RC flanged beams with a length of 3.2 meters and a span of 2.6 meters were tested out of which three flanged beam specimens each having 1.45 percentages of tension steel and a single specimen for test specimen containing 1.06 and 0.75 percentage of steel respectively. The total AE energy reported at the collapse of the specimen decreases as the reinforcement ratio increases, according to the author. Moreover, the author also observed that the slope of the line plotted between cumulative AE energy and time for a higher percentage of steel is less when compared with a lower percentage of steel. It might due to the fact that the reinforcement is more the specimen may behave more brittle and fails quickly.

The AE method is used by **Sutter et al. (2017)** to detect fractures in lightweight composite concrete beams that are reinforced with TRC and CFRP strips. The author investigated four hybrid design beams in this research. The 1st design is a TRC box with four glass fiber textile layers, while the 2nd has eight; both types are referred to as reference beams or plain beams. The 3rd is a traditional hybrid, with two CFRP strips of 2.4 mm within the TRC box and 50 mm concrete on top of the eight layers of thickness of the TRC box. The reference beams, also known as CFRP-reinforced hybrid beams, have two CFRP strips (2.4 mm) outside the TRC box and 50 mm concrete on top of the 8-layer TRC box. The main fracture parameters investigated in this research were AF v/s RT. The CFRP-reinforced hybrid beams emitted longer signals based on the AE waveform measured at low load stages. Strong fluctuations are observed in the hybrid concrete-TRC beams, although the average values of AE parameters indicate stronger shear fracture appearances. At low load stages, the plain reinforced concrete beam emits shorter signals, indicating that the proportion of de-bonding and cracking events is larger for the CFRP hybrid beams and lower for the plain beams. Strong variations are observed for plain beams, whereas average AE parameter values imply stronger tensile fracture characteristics.

Garhwal et al. (2020) used the passive AE approach to examine the P-**Δ** behavior of Glass FRP repaired corroded RC beams. In the laboratory, nine beams with concrete compressive strength of 35 N/mm^2 and a cross-section of 0.127 x 0.227 m were evaluated under 4-point loads across a span of 4.1 m. The flexural performance of one control specimen with a 0.5 percent tension reinforcement ratio was used by the author. Four RC beams had different levels

of corrosion (viz. C/0, C/10, C/20, C/30, and C/40). The four remaining damaged RC beam specimens (R/10, R/20, R/30, and R/40) were repaired using impressed current chloride (cl^-) induced corrosion and examined under 4p-bending. The key acoustic emission parameters explored were cumulative AE hits and amplitude versus time. According to the author, flexural testing of corroded reinforced concrete beams shows a drop in load-carrying

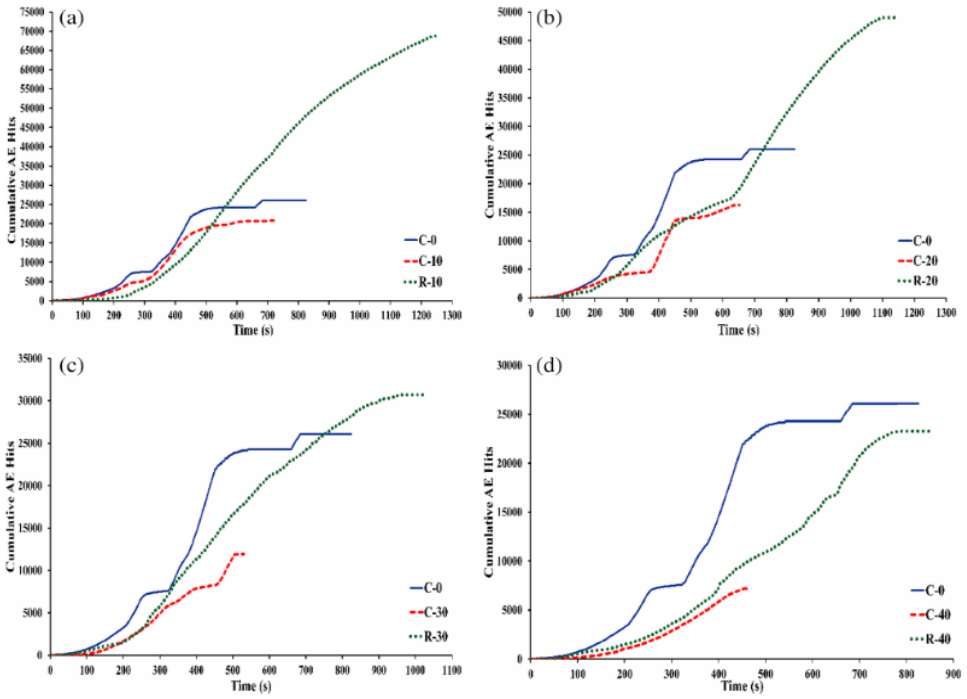

(a)

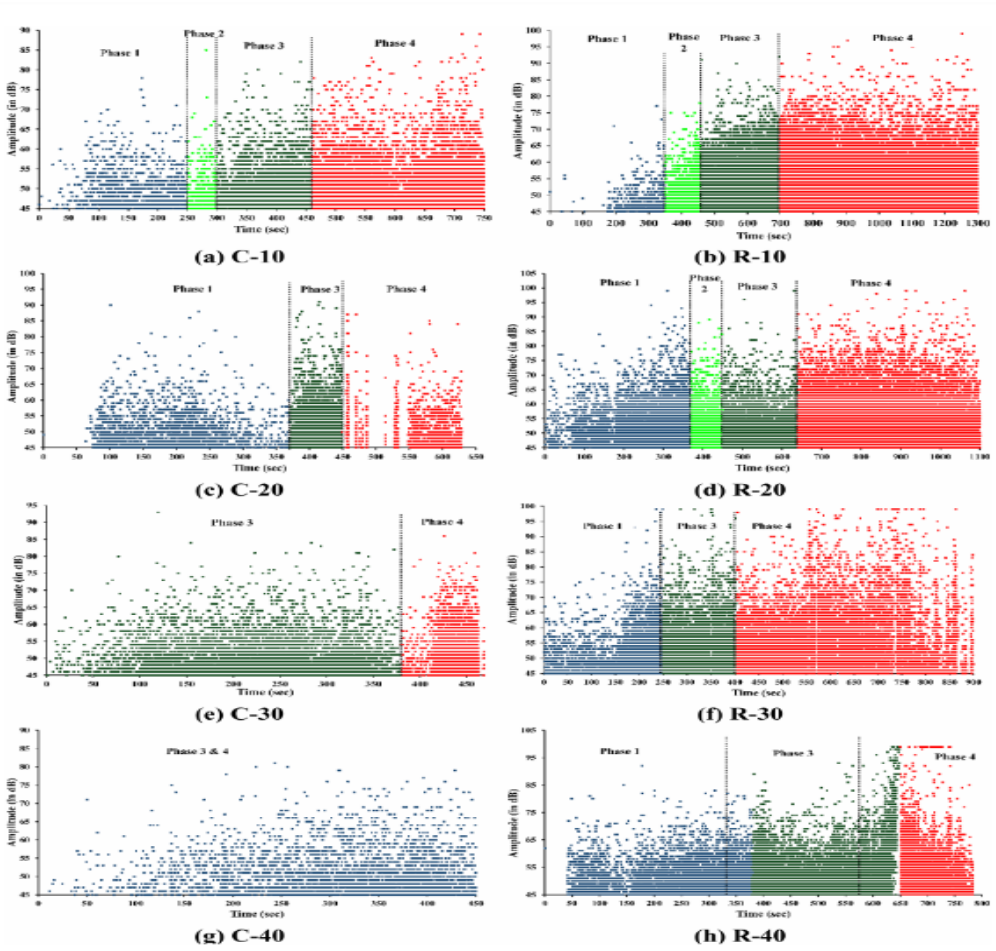

(b)

Fig. 3.8: (a) Cumulative Hits for corroded and repaired beams;(b) Amplitude of AE hits in corroded and repaired beams (Garhwal et al. 2020)

capacity as well as a decrease in deflection as corrosion levels increase. However, when the replicates of these corroded beams were repaired with micro-concrete and Glass (FRP) covering, substantial progress in the flexural properties of the corroded beams was found, indicating that strength and integrity were restored. Because of the attenuation of the recorded AE signals produced by pre-existing cracks, the authors noticed a substantial decline in cumulative acoustic hits and their associated amplitudes as corrosion levels increased, as well as depletion of distinct AE cracking phases. As illustrated in **Fig. 3.8**, the authors also concluded that AE monitoring has the benefit of detecting the beginning and progression of damage and fractures far before they become evident on the surface, making it more desirable and useful.

3.4 DIGITAL IMAGE CORRELATION (DIC)

DIC is an optical and non-contact measuring technology that allows the displacement, deformation, and strain fields of a specimen's frontal surface to be determined under any

loading situation **(Bruck et al. 1989, Wattrise et al. 2001; Shah and Kishen 2010; Blaber et al. 2015, Gribniak et al. 2017).** The structure of a digital picture will be defined in **Section 3.4.1** of this unit; the foundation of image matching algorithms can be established. The 2D-DIC approach will be described in **Section 3.4.2**, as well as the operational idea of the DIC measurement technique, which is how the information contained in a digital picture is utilized to monitor an object's deformation.

3.4.1 Structure of a digital image

The Color Intensity (CI) of a specific spot on the surface of an object of interest is collected by rectangular arrangements of individual picture elements, in digital photographs **(Choi & Shah, 1997).** Discrete pixels are not visible to the naked eye at

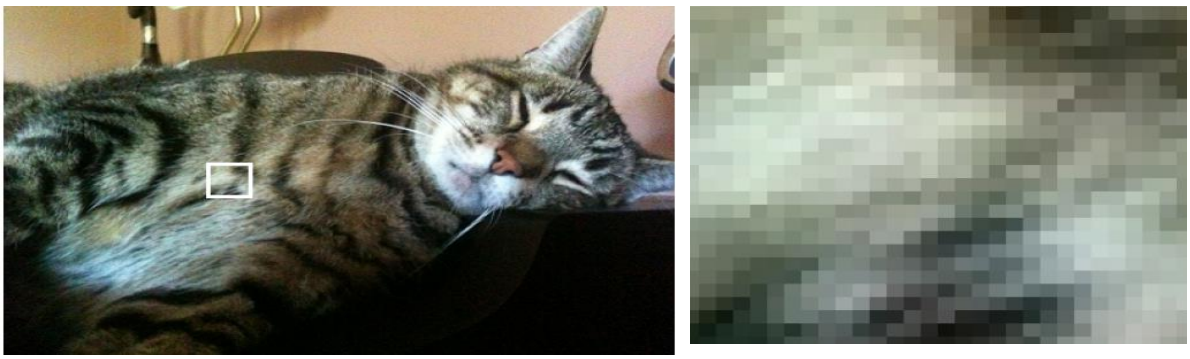

(a) (b)

Fig. 3.9: (a) Normal magnification digital image; (b) High magnification of a digital image (Wilbur, 2011)

normal magnification; but, as illustrated in **Fig. 3.9a,** In a digital photograph, the CI variations between neighboring pixels mix and appear as continuous, progressive color shifts. As seen in **Fig. 3.9b**, increased magnification demonstrates the discrete structure of the pixel array.

Color Intensity (CI) data is generally recorded as an 8-bit integer ranging from zero to 255 in each pixel of a picture **(Peterson, 2005 and Reichmann, 2011).** A value of 0 implies that there is no Color Intensity (CI), whereas 255 represents the highest intensity. The Red, Green, and Blue (RGB) color space, often known as the grey-scale color space, is the most popular color space utilized to capture digital pictures. Each pixel in the RGB color space has three layers of data, allowing each of the three color's intensity levels to be defined (**Wilbur, 2011**). Each CI matrix seems like a grey scale picture when presented separately; combining the 3 results in a full-color image, as illustrated in **Fig. 3.10.**

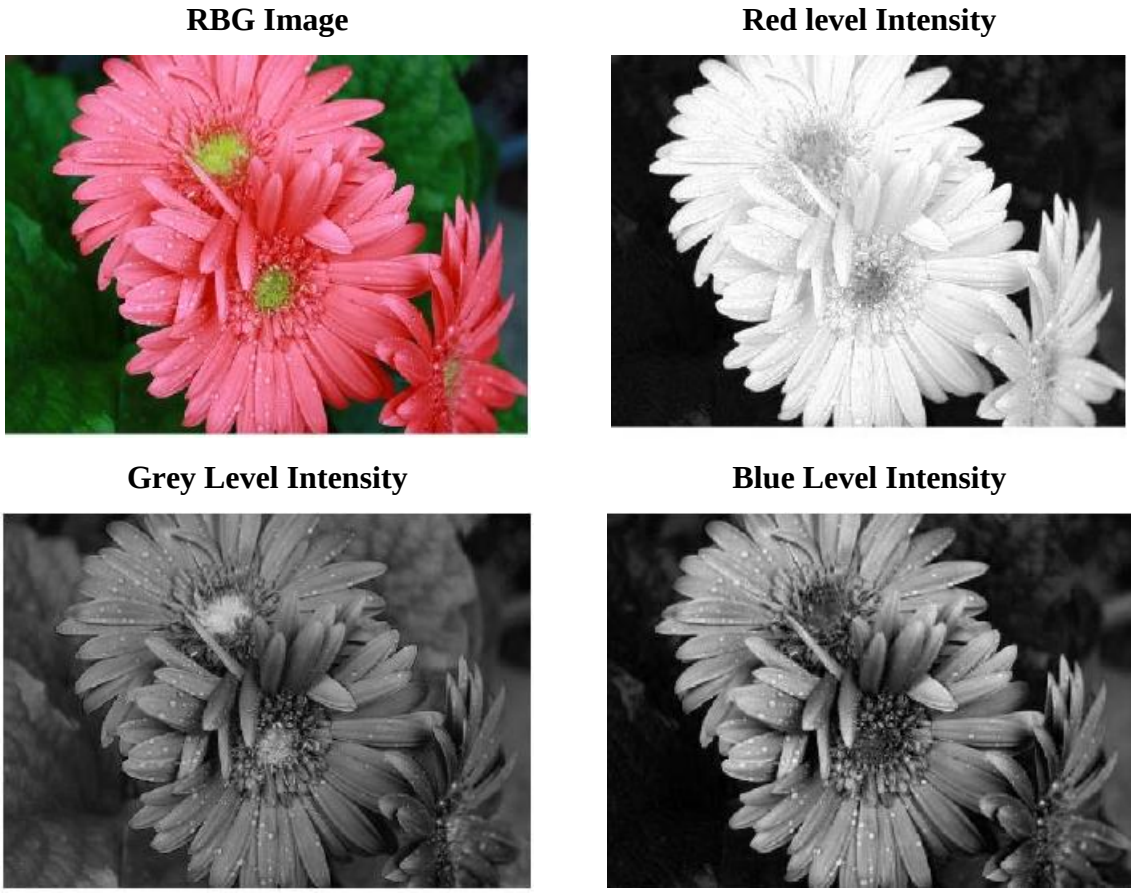

Fig. 3.10: RGB picture with all 3 color matrices shown and split into each colour matrix (Wilbur, 2011)

The two most popular color spaces utilized to capture digital images are the RGB color space and the grey-scale color space. (**Afifi & Ashour, 2012**). Each pixel in the RGB color space includes three layers of data, allowing the three colors' intensity levels to be adjusted. Each colur intensity matrix will appear as a greyscale image when presented individually. A full-colored image will be generated when all three are merged, as seen in **Fig. 3.10.** Grey digital pictures are often used by DIC since just a single layer of information representing the color information on the surface of an object is needed **(Maas and Hempel, 2006).** Grey pictures can be produced in one manner or another: by making measurements of the light intensity from the surface of an object or by scaling three RGB image CI arrangements to create a single "averaged" intensity matrix **(Stevens, 2007).** Both options are acceptable for the use of DIC as long as the digital images have adequate changes in the intensity values of each pixel.

3.4.2 2-D DIC

Although every pixel in a digital photograph represents a certain point CI on the forehead side of the object, the stressed deformation of the object can be detected by taking a series of digital images and comparison in two consecutive images of the CI values of the pixels **(Wilbur, 2011). Fig. 3.11** depicts the procedure for collecting DIC measurements.

The initial stages are to prepare the specimens and set up the experiment. A speckled arrangement of different black dots on a white backdrop is applied to the surface of the reinforced concrete specimen before testing. A 2D digital image of the specimen's frontal surface may be generated from grey scale digital images obtained during testing by one charge-coupled device camera. Testing can begin when the specimen preparation and experimental setup are completed. Prior to loading, a digital picture of the specimen is taken, as well as during each load that needs displacement data.

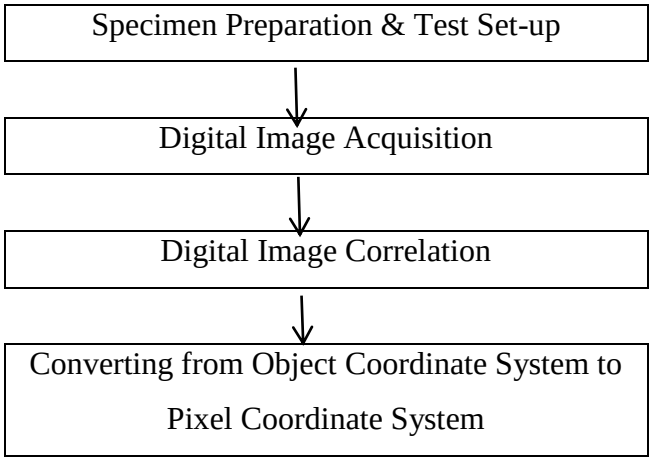

Fig. 3.11: The DIC process is depicted in a flowchart

Although only one digital image per load phase is required, taking many photographs to assure data gathering at each load step is preferred. As demonstrated in **Fig. 3.12a,** the initial stage in digital image processing is to define the Region of Interest (R.O.I) in the different digital picture that requires deformation measurement. Because each pixel's intensity only can vary from zero to 255, and photographs typically comprise millions of pixels, many pixels in a picture will have the same intensity value. As a result, as shown in **Fig. 3.12b**, the R.O.I. is organized into a grid of square selections with various pixel widths that will be used to search for correlations. **(Hild and Roux, 2006).**

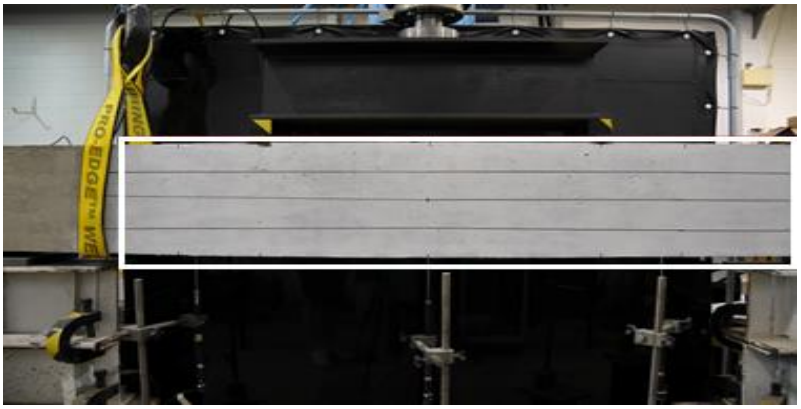

(a)

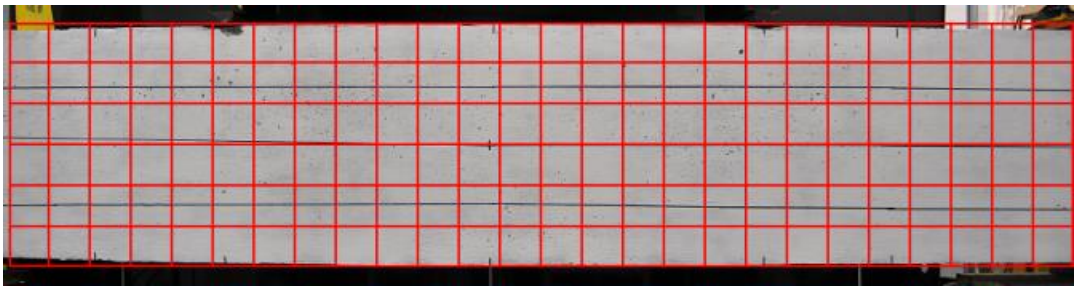

(b)

Fig. 3.12 (a) ROI selection in the sample image, and (b) Pixel sub-division of R.O.I (Hild and Roux, 2006).

Using a correlation criterion, every subset from the reference digital picture is identified in a digital picture of the deformed test specimen to compute the dislocation of the test sample at every load stage **(Pan et al. 2009).** For every subset in the deformed digital photo that the reference subset is compared to, a CC, SSD, or NSSD coefficient is often computed, and then the shift in the location of the subset between the two pictures is computed by identifying the maximum of the correlation coefficient matrix and computing the shift in the location of the subset between the two pictures, the displacements are calculated as shown in **Fig. 3.12 (Bruck et al. 1989).** These coefficients determine how comparable the two pixels being compared are. A pixel subset at its reference location is illustrated in **Fig. 3.13a**, and the same pixel subset following deformation is presented in **Fig. 3.13b.**

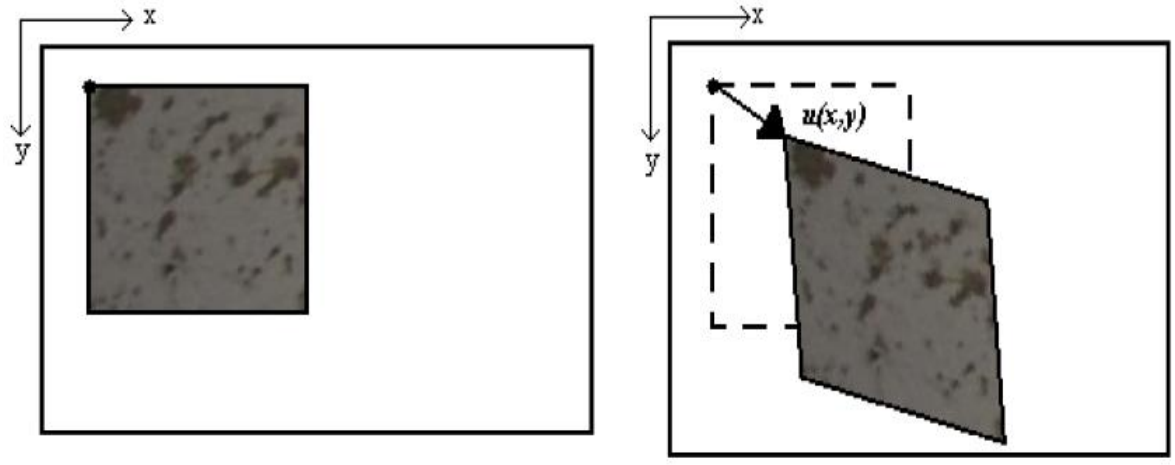

(a) **(b)**

Fig. 3.13: (a) Subset pixel illustration in position of reference and (b) after displacement (Bruck et al. 1989).

The displacement vector produced for each subgroup at this level of digital image processing does not adequately represent the test specimen's deformation. Even though the deformed digital image's subset is skewed, the displacement vector remains constant nevertheless of the distortion of the entire subset, as seen in **Fig. 3.14** below. This is because the correlation analysis ignores the translations and rotations of the subset that occur during

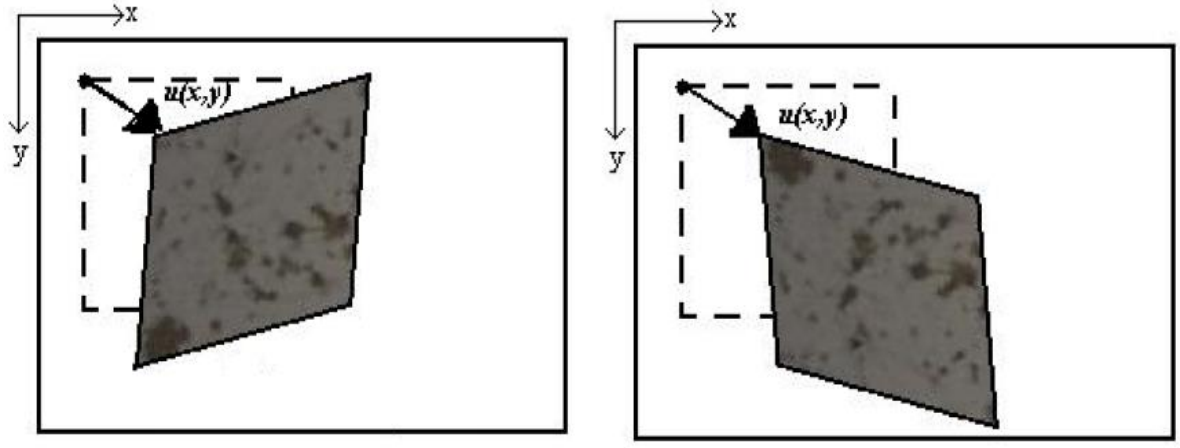

Fig. 3.14: Deformed subset with the same vector at two different places (Bruck et al., 1989).

loading and instead focuses on determining which subset in the deformed digital image has the closest CI distribution to the reference subset **(Bing, 2006).**

To obtain a test sample complete displacement profile, the displacement vectors obtained by correlation analysis must be interpolated. Some interpolation methodologies for sub-pixels that can be used to achieve varied degrees of precision include genetic algorithms,

intensity interpolation and correlation curve adjustment. **(Bing, 2006).** Because the members examined in the enclosed research will only be subjected to vertical forces, it is fair to infer that displacement will only occur vertically. The digital image of the body is described by a discrete function indicating the grey level of each pixel. The grey level value runs from 0 to 255, with 0 being black and 255 indicating white, and all numbers in between indicating various shades of grey **(Bruck et al. 1989).**

As illustrated in **Fig. 3.15,** the correlation computations are performed for a group of pixels known as a pattern. Inside a pattern, the deformation field is considered to be homogenous. The digital image of the body is a discrete function f(x, y), before deformation. The function f*(x*, y*) is transformed to a distinct function after deformation **(Bruck et al. 1989). Equation 3.6** expresses the theoretical relationship between the two discrete functions.

$$f^*(x^*, y^*) - f(x + u(x,y), y + v(x,y)) = 0 \qquad (3.6)$$

Where u(x, y) and v(x, y) indicate the pattern's displacement field, as illustrated in **Equation 3.6**.

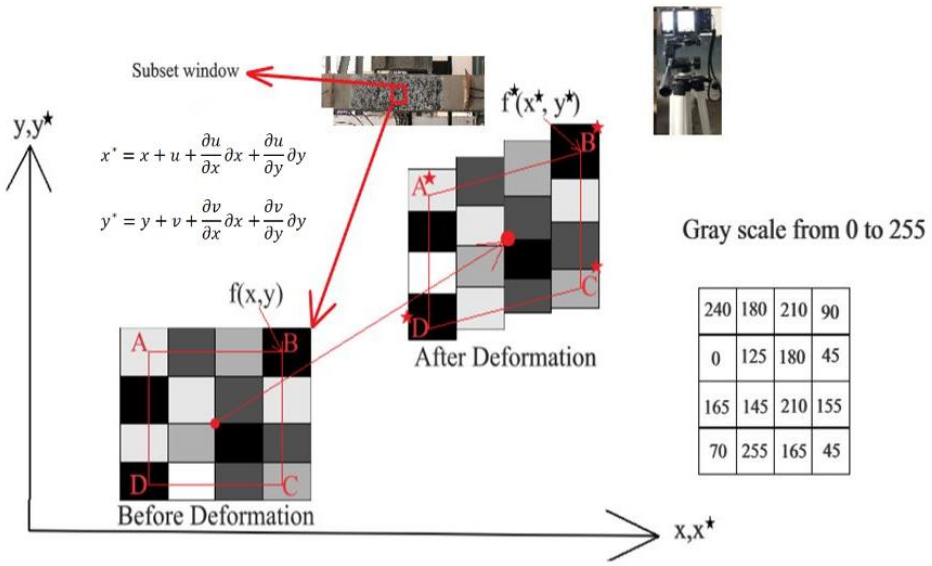

Fig. 3.15: Undeformed and deformed Pattern (Bruck et al. 1989).

Correlation is now simplified to the process of matching subsets of numbers in the two digital photo. **Equation 3.7** is used to determine the cross-correlation value, which evaluates how closely subsets match.

$$C = \frac{1 - \sum[f(x,y).f^*(x^*,y^*)]}{\sum f(x,y)^2 . \sum f^*(x^*,y^*)^2]^{1/2}} \qquad (3.7)$$

f(x, y) is the grey level value at coordinate (x, y) for an undeformed photo, while f*(x*, y*) is the grey level value at point (x*, y*) for a deformed photo in **Equations 3.8 and 3.9.** The coordinates (x, y) and (x*, y*) are connected by the deformation that happened between the capture of the two digital photos. If the object's motion is parallel to the image plane in respect to the camera, then they are related by;

$$x^* = x + u + \frac{\partial u}{\partial x}\delta x + \frac{\partial u}{\partial y}\delta y \tag{3.8}$$

$$y^* = y + v + \frac{\partial v}{\partial x}\delta x + \frac{\partial v}{\partial y}\delta y \tag{3.9}$$

The subset centers are displaced in the x and y-axis by u and v, respectively. The letters x and y represent the distances between both the subset's center and each point (x, y). Image correlation can be used to identify the values of coordinates (x, y), displacement (u, v), and derivatives. Detailed information about the DIC algorithms is available as open-source tools namely 2D-DIC code N-Corr **(Blaber et al. 2014)** operating in MATLAB **(Russ, 2016).**

3.5 REVIEW OF DIC FOR DAMAGE MONITORING IN RC BEAMS

Choi and Shah (1997) investigated the deformation of concrete subjected to compression testing is measured. The authors observed that the fractures patterns of concrete are very complicated; gages attached to the concrete specimens do not give an accurate reading. With the help of the non-contact (DIC) technique is applied to monitor the concrete fracture under compressive loads, so that gage readings are not disturbed while failure progresses. The study's major goal is to determine the viability of using DIC monitoring as a non-contact approach in concrete structures. Laboratory tests are performed on M20 grade concrete specimens with overall dimensions of 0.1 m width, 0.075 m height, and 0.075 m thickness. The prismatic shape of concrete specimens is necessary to give flat viewing frontal surfaces required for clear focusing during the digital-image grading. The author found that displacement contour maps profiles at various stages of loading were used to illustrate the development of non-uniform displacements in concrete. Authors also evaluate that with the help of this technique the cracks circumventing the aggregates and propagating parallel to the loading way in the concrete matrix.

Wattrisse et al. (2001) use the DIC method to perform an experimental investigation to evaluate damage in RC beams subjected to increasing cyclic stress. Laboratory experiments are performed on flat Mild steel specimens of size (77.4 x 13.9) mm. The author used a digital camera to collect surface pictures before and after the deformations, and DIC techniques were

used to estimate relative motions of the points identified at the surface of interest. Additionally, the obtained digital pictures were manually adjusted to improve image quality before being input into DIC software for examination on the surface of interest. The main parameter investigated in this article was strain lagrangian strain-rate measurement (ε_{xx}) versus tensile load. The author observed that the strain-rate measurements will provide information about the onset and development of the strain localization. The author also reported that as the rate of the tensile load is small lagrangian strain-rate measurement is also small and represents with light bluish color but as tensile load is increased on flat Mild steel specimen the lagrangian strain-rate is also increased and its represents with the dark red color.

In a static test on Saint-Marcel bridge, **Kuntz et al. (2007)** studied the mechanical response of a shear crack on the RC beam. A DIC analysis of displacements was used to evaluate the mechanical conduct of a shear crack in an RC beam in response to full load cycles in static load testing. According to the author's study of displacement data, the fracture behavior changes meaningfully with load order, in this case, truck heading and position as it passes the bridge. Furthermore, a single displacement sensor does not capture tangential displacement along a fracture; at the absolute least, two displacement transducers positioned at 90˚ to each other are required, according to the author. The correlation digital-image method gives you access to the whole displacement field, whereas two connected transducers can only provide one displacement vector. Furthermore, the final results' quality in terms of uncertainty is largely determined by the care done during the digital-image capturing step.

Shah and Kishen (2010) using the Digital Image Correlation (DIC) method and a three-bending test, the fracture characteristics for various concrete-concrete surfaces were investigated. Authors capture the digital images before loading (un-deformed stage) and at different stages of loading. For the DIC analysis, the open-source code 2D-Ncorr was utilized, and the simulations were run on a personal computer. Surface displacements, surface stresses, load point displacement, Crack Mouth Opening Displacements (CMOD), and crack tip location are all determined utilizing correlation algorithms on these digital images. Vertical displacements and CMOD calculated with DIC and those obtained with Linear Variable Differential Transducers (LVDTs) and clip gauge are quite comparable, according to the author. Furthermore, the DIC method is a feasible and cost-effective alternative to LVDTs, strain gauges, and clip gauges, according to the author. In the end, the author concluded that DIC methods can successfully assess crack-tip position and crack length, which is challenging and costly for concrete-like materials using conventional sensors as presented in **Fig. 3.16.**

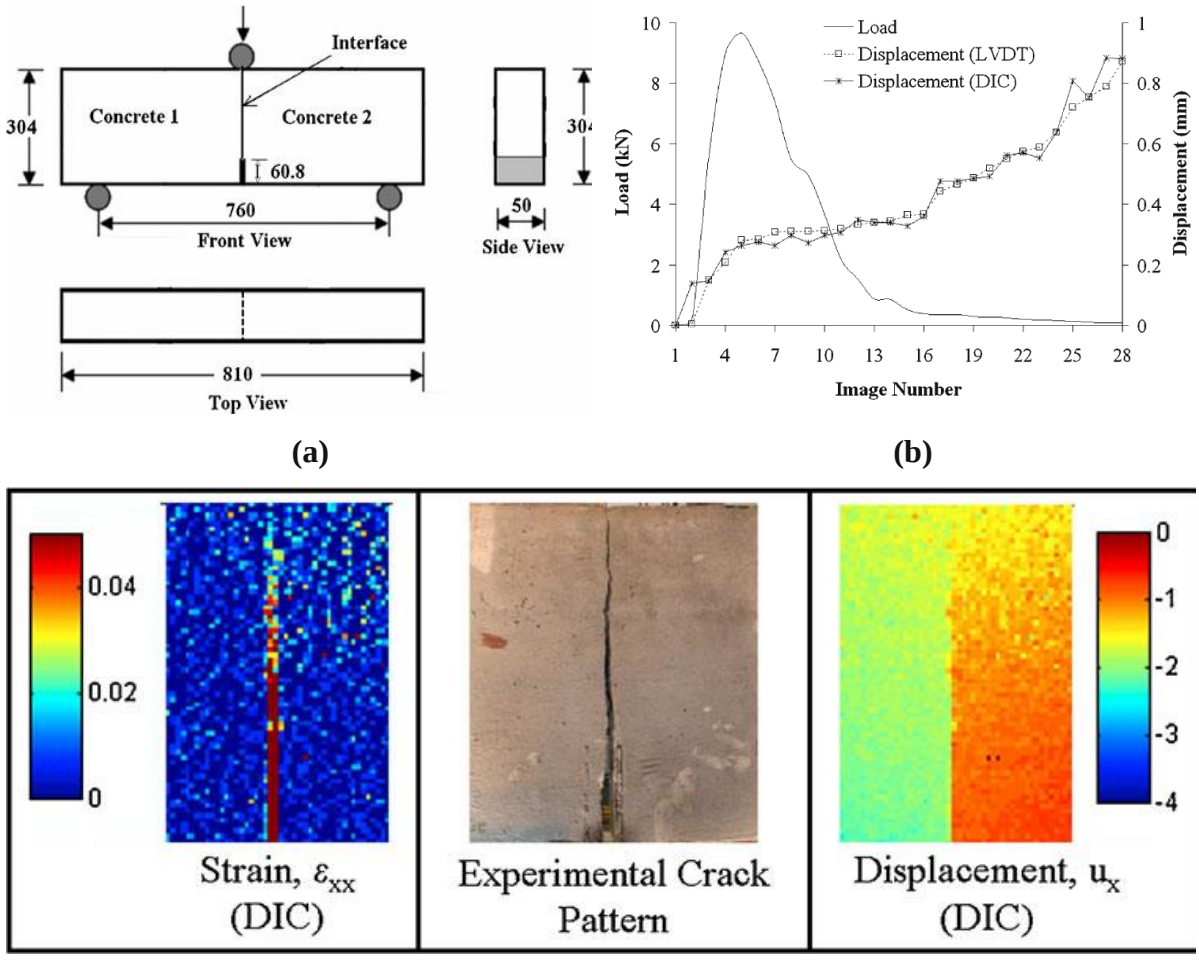

Fig. 3.16: (a) Geometry details of the specimen (b) Vertical load vs midspan displacement (interface beam AB) and (c) Results of strain, crack pattern, and displacement (interface beam AB) (Shah and Kishen, 2010)

Destrebecq et al. (2010) Using a digital image correlation approach, researchers studied the mechanical behavior of a full-scale reinforced concrete beam that was exposed to four-point loads. Three varieties of grade M30 RC beams with total dimensions of 0.160 m width, 0.45 m depth, and 7.840 m length are used in the laboratory. Four 14 mm diameter HYSD steel rods serve as longitudinal reinforcement. In comparison with the digital reference image taken before loading, the author obtains digital photographs at various loading levels. The author evaluated that the detailed information about the cracking process and the flexural behavior were easily derived from the analysis of displacement fields processed from digital photographs of the beam captured at different loading levels. With the help of this technique, the early surface-crack detection and their crack widths were precisely measured as soon as

they appear during the different levels of loading cycles in the tensile region of the RC beam. Furthermore, the displacement longitudinal strain fields provided by the DIC method were used to obtain comprehensive information on the deflection and curvature of the bent RC beam. Values of the mid-span deflection obtained with the DIC technique are in fair correlation with values measured by the LVDT.

Shih and Sung (2012) for studying the process of fracture formation in an RC beam, a digital image correlation approach is used by the authors. The study's major aim is to find the potential of using DIC monitoring as a non-contact approach in reinforced concrete structures. Experiments are conducted in the laboratory utilizing RC beams of grade M30 with overall dimensions of 0.15m and 0.25 m i.e. width and depth, and 1.5 m length, as well as longitudinal tension reinforcement of 2%, and three-point loading. The main parameter investigated in this article were surface strain and surface displacement fields. The DIC approach, according to the authors, can detect and identify early crack formation, whereas the conventional process cannot do so until a particular threshold of loading reached which already has caused breaking or rupture of the specimens.

Fayyad and Lees (2014) under three-point loading, the fracture monitoring of steel-reinforced concrete specimens was investigated. Digital image correlation (DIC) is utilised for a laboratory test to monitor the fracture control of the loaded steel RC beam. The study's main goal is to use DIC to analyze mode-I fracture propagation in reinforced concrete structures **(see Fig. 3.17**). In laboratory tests, two types of RC beams were utilized, with concrete compressive strengths of 36 and 46 N/mm2, overall dimensions of 0.1m width, 0.12m depth, and 0.84m length, and two distinct longitudinal tension reinforcement ratios of 0.5 percent. The displacement vectors of the DIC analysis findings were used to calculate the CMOD values for the investigated samples, which was the major parameter addressed in this research. The DIC analysis was carried out using an open-source tool called GeoPIV, and the simulations were run on a personal computer. CMOD was made on the basis of the DIC analysis and the concrete strength was revealed to have minimal effect on the opening of cracks; but the binding stresses between the reinforcement and the concrete seemed to have a role in the propagation of fractures and the breaking through of cracks. Researchers may also view and evaluate the fracture characteristics of RC beams using the DIC method..

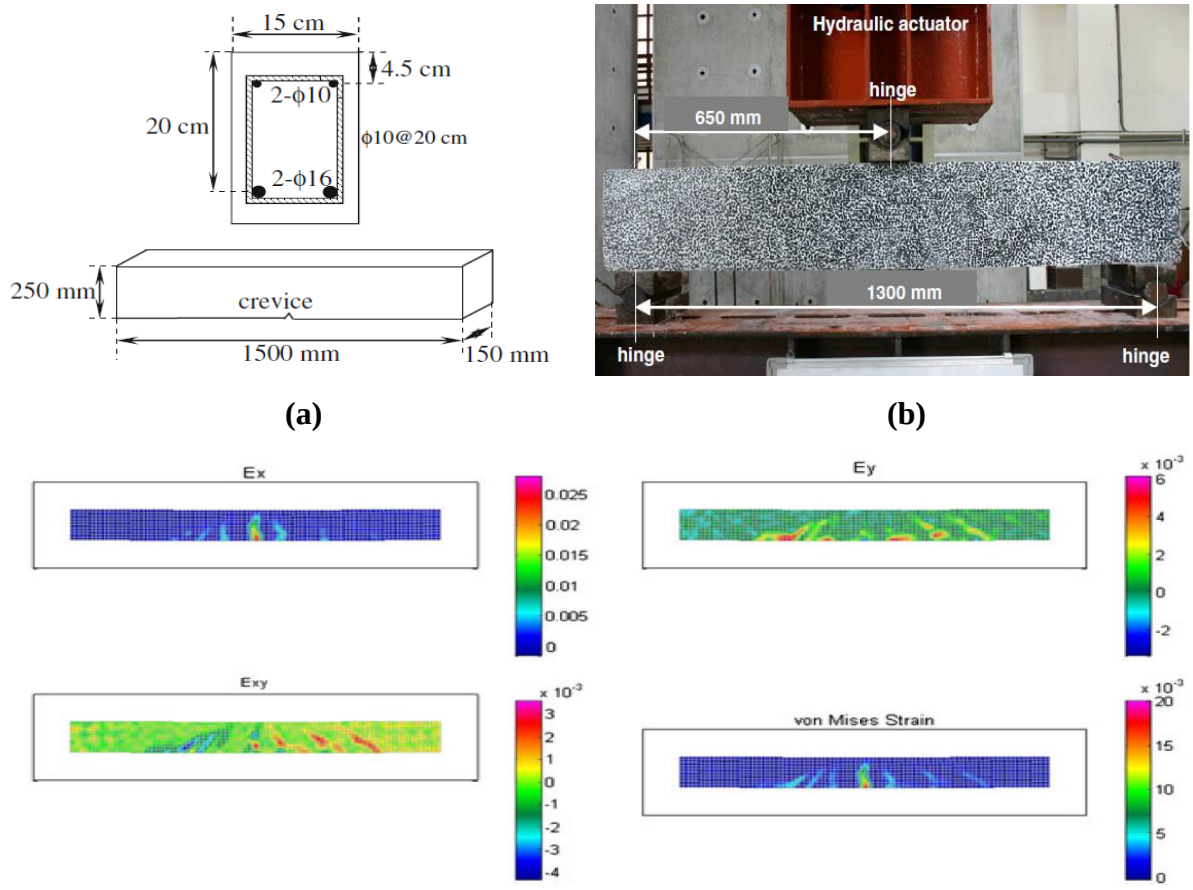

Fig. 3.17: (a) RC Beam dimensions of specimen 0.5% (b) Simple three-point loading set-up and (c) Strain diagram for specimen 0.5% subject to 107 kN loading (Fayyad and Lees, (2014)

Using the DIC technique, **Hamrat et al. (2015)** examine cracking behaviour of both conventional and high-force concrete and high-force fibre concrete beams. Three flexural reinforcement ratios of 1.22%, 1.77%, and 2.42% were used for each series of beams. The beams were 1.5m long and had a cross-section of 0.1m x 0.16m. Beams were subjected to a symmetric loading composed of 4p-loading. The main parameters investigated in this article were crack detection, crack development, crack width measurements, and surface strain. The load-carrying capacity of concrete beams improves as the percentage of tensile reinforcement and compressive strength increases, according to the author. The comparison between standard measuring techniques (strain gauges, LVDT sensors) and the DIC approach was assessed by the author. The measurement of strains and displacements at or near failure, according to the author, is generally not feasible using normal methods, because of the safety risk and damage to equipment. In addition, the good agreement between the two metering methods shows that

the DIC methodology is an effective tool for monitoring displacement and stress areas throughout loading from beginning to failure.

Tambusay et al. (2018) under three-point bending, study the shear fracture mechanism of RC beams is investigated by the author. DIC analysis is used to visualize the formation and propagation of shear cracking behavior in an RC beam in a laboratory test. In the lab, three types of M30 RC beams with overall dimensions of 0.1m width, 0.125m effective depth, and 1.0m length are evaluated against a balanced-section with longitudinal tension reinforcement of 2.4 percent. The concrete's 28-day compressive strength was 43.4 N/mm^2. According to the author, the suggested DIC system has enough resolution to monitor the onset and development of shear cracking in an RC beam. Furthermore, DIC findings revealed that concrete cracking appears as a succession of thin, high-strain strips. With increasing loading, the amount of strain increases, suggesting an increase in fracture width. In this work, hand-drawn crack maps and nonlinear finite element analysis strain fields ($\boldsymbol{\varepsilon}_{xx}$) compare favourably to strain fields ($\boldsymbol{\varepsilon}_{xx}$) created using the DIC approach, in this study. According to the author, DIC is also proving to be a useful technique for studying many aspects of the shear failure process in RC.

The surface strain characteristics in reinforced asphalt concrete beams exposed to four-point loads were studied using the DIC method by **Sudarsanan et al. (2019).** The author uses different types of geo-synthetic products such as woven geotextile; Coir geotextile; and Synthetic geotextile used for reinforcing the AC and compare it with unreinforced samples at 10 and 30-degree temperatures. The strain or displacement field over an ROI may be measured using DIC analysis of successive digital pictures recorded throughout the test. For the DIC analysis, an open-source code called Geo-PIV-RG was utilized, and the simulations were run on a personal computer. The main parameters investigated in this article were horizontal surface strain and vertical surface strain fields. None of the available approaches, according to the author, are capable of assessing the strain generated over a large area. The DIC method, on the other hand, aids in the understanding of the stresses that have evolved inside an ROI. The strains created were estimated using an algorithm based on the pictures collected at regular intervals throughout the test. The horizontal strains ($\boldsymbol{\varepsilon}_{xx}$) produced under four-point loading demonstrated that, as compared to UR samples over the same number of cycles, the reinforcement reduces strain mobilization at the fracture tip, extending fatigue life.

Bhowmik et al. (2019) under the influence of static loading, a variety of small, medium, and large concrete beams were tested. The DIC method has been used to study concrete fracture mechanisms and crack development characteristics. Three distinct types of concrete beams with concrete compressive strength of 34.50 N/mm^2 and total dimensions of

400 mm span, 550 mm length, 20 mm notch size, and 100 mm depth is tested in the lab. Surface displacements, surface strains, CMOD, and crack tip position are calculated using VIC-2D software to examine digital pictures. Digital images corresponding to peak load, 90% post-peak load, 70% post-peak load, 50% post-peak load, 30% post-peak load, and 15% post-peak load were selected for the beam specimens under static loading. The vertical displacements produced from the 2D-DIC analysis were compared to experimental data under static loading conditions at various percentages of post-peak load. Vertical displacements produced by 2D-DIC have also been compared to experimental results in fatigue loading scenarios. The authors discovered a strong correlation between the findings of the DIC analysis and the experimentally observed values.

Johansson et al. (2020) studied the residual capacity in RC beams subjected to impact loading under three-point loading. DIC analysis is used to visualize and study the structural response of impact-loaded concrete beams. The main idea was to study the residual plastic deformation capacity of RC beams first subjected to impact loading, and this was done with high accuracy using DIC analysis. Drop-weight impact tests of 12 beams were carried out and the residual capacity were tested; out of which six beams were statically tested as references. With a span of 1000 mm and dimensions of (0.1 x 0.1 x 1.18) m, the beams were simply supported. The drop weight had a mass of 10 kg and was dropped from heights 2500 mm. A high-speed resolution camera, with 5000 fps, was used during the impact tests. From the digital images obtained, (DIC) analyses were conducted, and deformations and crack propagation of the RC beams were measured. The author observed that the deformations

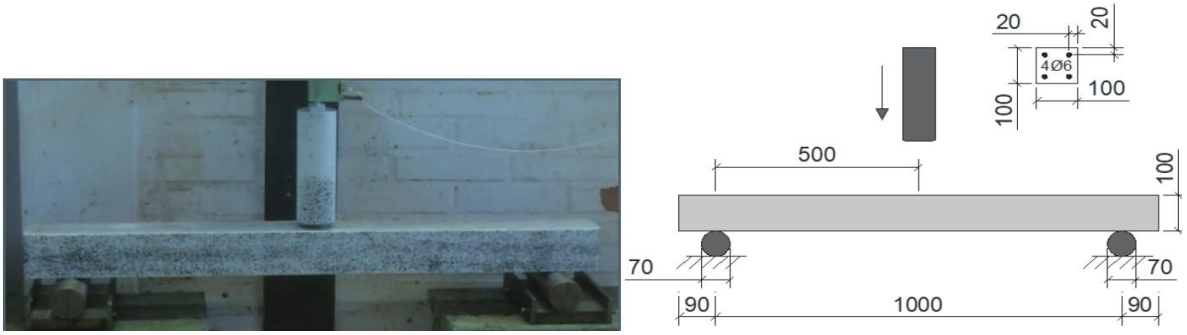

(a)

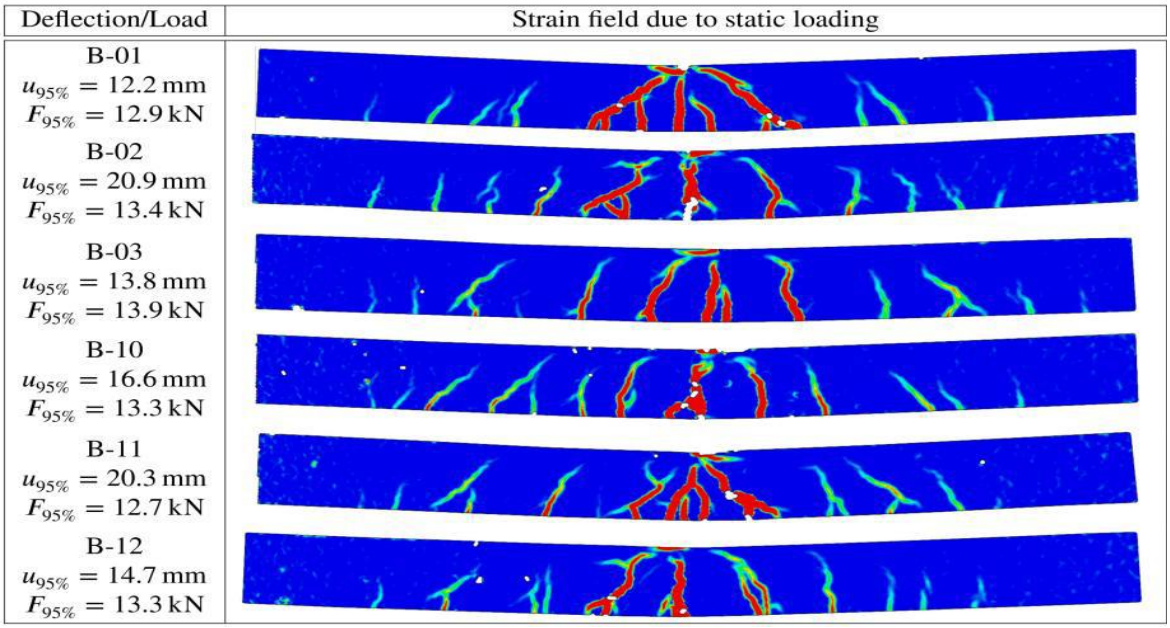

(b)

Fig. 3.18: (a) Experimental setup for drop weight tests and (b) Initial and final crack pattern of RC beam subjected to four-point loading (Bhowmik et al. 2019)

were obtained well, and the largest cracks were acceptably captured, but the smaller cracks were not observed using DIC as shown in **Fig. 3.18.** Furthermore, DIC analysis can detect and identify early crack deformations as well as crack propagation in RC beams.

3.6 CLOSING REMARKS

The processes and principles of AE and DIC, as well as testing methodologies, are presented in detail in this chapter. In addition, comprehensive literature review was conducted independently on AE and DIC flexural monitoring in RC structures. The review established the efficacy of AE and DIC for bending/damage/fracture monitoring in RC structures is carried out. But still need to be investigated before it can be practically employed in civil engineering structures.

CHAPTER 4

EXPERIMENTAL PROGRAM & METHODOLOGY

4.1 GENERAL

In this research endeavor, it is proposed to examine the flexural performance and mechanical behavior of steel-reinforced concrete and GFRP reinforced concrete beams under flexural loading. The primary objective was to study the variation in the mechanical behavior and structural performance of steel-reinforced concrete & GFRP reinforced concrete beams under flexural loading using advanced Non-Destructive Testing (NDT) using Acoustic Emission (AE) and Digital Image Correlation (DIC) under four-point flexural loading. This chapter presents the experimental program and methodology in details of the work done in this thesis including the monitoring the flexural performance of steel and GFRP reinforced concrete beams.

4.2 EXPERIMENTAL PROGRAM AND METHODOLOGY

The experimental program of the present research consists of flexural testing of steel RC & GFRP RC beams with 150mm x 230mm cross-section and a span of 2100 mm. In the present study, Two types of beams were cast in this investigation, one reinforced with conventional steel bars of Fe500 grade and the other strengthened with Glass Fibre Reinforced Polymer (GFRP) bars with increasing tensile reinforcement percentages. Each RC beam is identified with two codes series, the letters S and G identify RC beams as being reinforced with steel and GFRP bars, respectively. The numeric characters 1, 2, and 3 refer to tension reinforcement ratio (A_{st}) of ~0.33%, ~0.52%, and ~1.11% of RC beam specimen respectively as shown in **Fig. 4.1.**

These tension reinforcement ratios roughly correspond to the predicted failure mode respectively, steel yielding or flexural failure in case steel reinforced concrete beam and tension reinforcement rupturing, balanced failure, and concrete crushing in case of GFRP reinforced concrete beam. It is important to note that S-series beams had both longitudinal as well as shear reinforcement made of Fe500 steel bars whereas G-Series beams had both longitudinal as well as transverse reinforcement entirely made of GFRP bars.

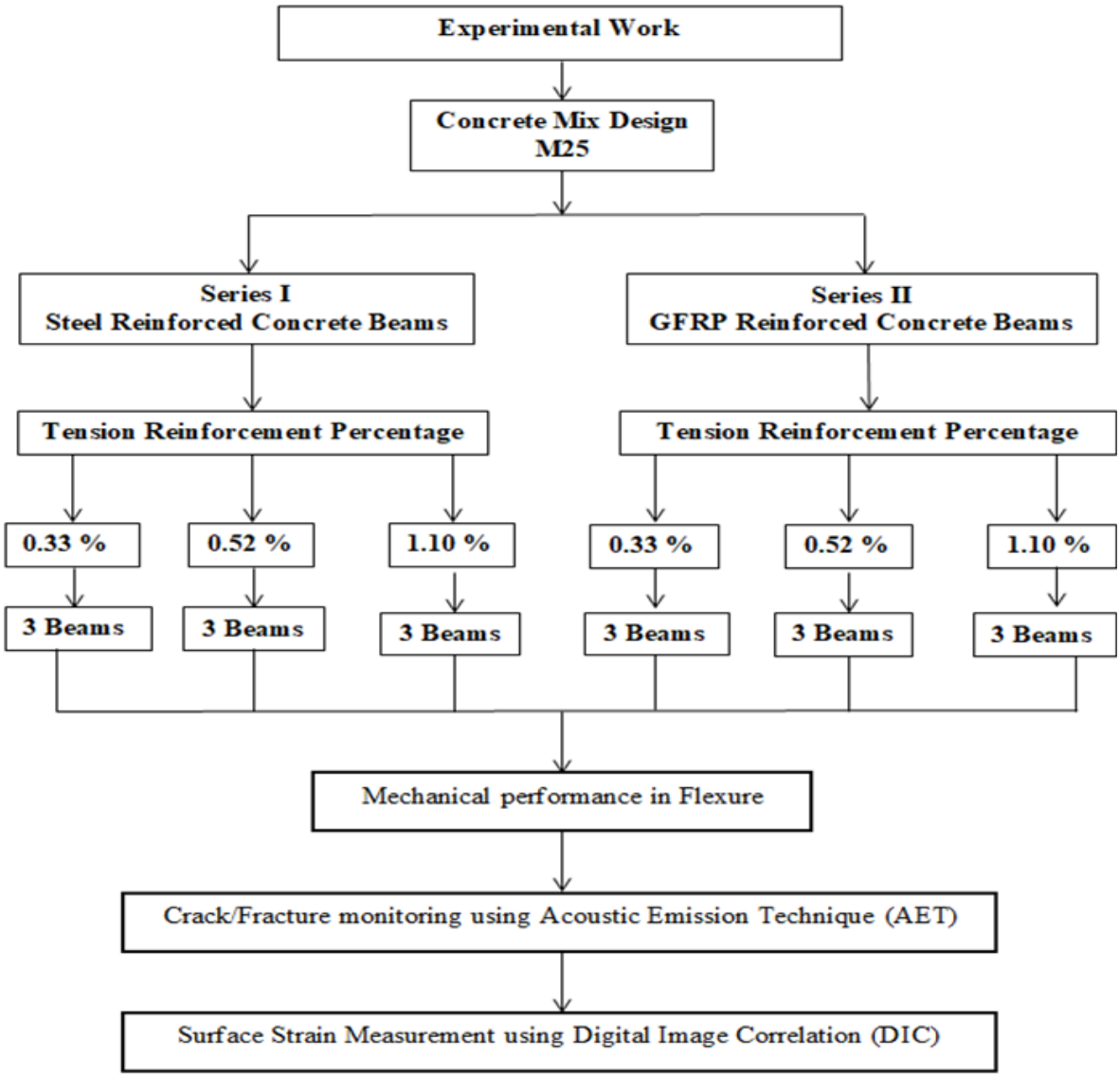

Fig. 4.1: Schematic plan for an experimental program

The ACI codes **ACI (2019)** and **ACI (2015)** are used to design RC beams. **ACI (2019)** was used to design steel-RC beams, whereas **ACI (2015)** was used to design GFRP-RC beams. The reinforcement ratio ($\rho = 100A_{st}/bd$ %) for each set of beams was varied as ~0.33%, ~0.52% and ~1.11% based on volumetric calculations. The reinforcement details of both S and G-series are given in **Table 4.1**. Three specimens of each beam series were cast in order to ensure repeatability of results and the schematic plan for the experimental program is shown in **Fig. 4.1.**

FRP RC beams should have higher reserve strength to account for the lack of ductility and hence they are recommended to be designed as over-reinforced sections according to ACI Committee 440 (2015). The balanced reinforcement ratio value for the GFRP RC beam is 0.00308 or 0.3% (calculated using Equation 2.2) and hence a percentage of 0.33%, 0.52%, and 1.11% (100 Ast /bd %) were chosen corresponding to reinforcement details given in Table 4.1 to make GFRP reinforced section as over reinforced and steel reinforced sections as under-reinforced. (Balanced reinforcement ratio value for steel RC beam is 2% calculated according to Equation 2.15).

These differently reinforced steel RC & GFRP RC beams were subjected to flexural testing along with simultaneous AE and DIC monitoring while undergoing flexural testing. During flexural testing the mechanical performance of the steel and GFRP reinforced beams were compared by studying load-deflection characteristics, failure modes, ultimate moment carrying capacity, energy absorption capacity and pre-and-post cracking bending stiffness, etc. It was corroborated by analysis of the bending behavior of steel-reinforced concrete and GFRP reinforced concrete beams using Acoustic Emission Technique (AET) for internal defect detection and Digital Image Correlation (DIC) for surface cracking. Various AE parameters of cumulative AE hits, Average Frequency (AF) in (kHz), Rise Angle (RA), etc. along with DIC results of the mid-point vertical displacement and surface strain have been used to study the variation in bending and failure pattern of steel-RC and GFRP-RC beams.

Table 4.1: Reinforcement details in the beams

Series Code	**Reinforcement Condition**	**ρ (%)**	Compression Reinforcement (Asc)	Tension Reinforcement (Ast)
S1	Under-Reinforced	0.33	2-8 mm Ø	2-8 mm Ø
S2	Under-Reinforced	0.52	2-8 mm Ø	2-10 mm Ø
S3	Under-Reinforced	1.11	2-8 mm Ø	3-12 mm Ø
G1	Over-Reinforced	0.33	2-8 mm Ø	2-8 mm Ø
G2	Over-Reinforced	0.52	2-8 mm Ø	2-10 mm Ø
G3	Over-Reinforced	1.11	2-8 mm Ø	3-12 mm Ø

***Under-reinforced section designed as per ACI 2019 and over reinforced section designed as per ACI 2015**

Furthermore, analysis of the fracture patterns of these differently reinforced beams was also investigated using AET and DIC. The AE parameters of cumulative AE hits, Cumulative Signal Strength (CSS), Amplitude, Average Frequency (kHz), rise time (RT), and Duration (us) of AE hits and damage localization were used for the same. Moreover, the results of AE

XY-plots and longitudinal surface strain (ε_{xx}) profile were compared with actually cracked images of the steel-reinforced and GFRP reinforced concrete beam specimens. In this chapter, the experimental program, and methodology used in the study as well as the test results of basic materials used in the study are detailed including properties of concrete, tensile test properties of steel reinforcement, and GFRP reinforcement bars.

4.3 MATERIALS USED

Cement (C), Fine Aggregate (FA), Coarse Aggregates (CA), water, chemical, and mineral admixtures are the primary ingredients of the concrete mix. Reinforcing bars and other reinforcing fibers may be utilized in constructing concrete. The quality of the ingredients, their proportions, and the way they are mixed all affect the strength of the concrete. The materials fulfilled the conditions outlined in the appropriate Indian Standard (I.S 10262-2009) Code in general. The following properties were found in the materials used to make steel RC & GFRP RC specimens.

4.3.1 Cement

Cement is a binder, a substance used in construction to bind materials together by setting, hardening, and adhering to them. Ultra-tech Pozzolana Cement (PPC) of 43rd grade was employed in the experiment and complied with the criteria of India's standards IS 8112-1989 Code. It was fresh and free of lumps, which adds to the appeal. Table 4.2 shows

Table 4.2: Physical characteristics of cement used

S. No	Properties	Observation	As per IS:8112-1989 (Part 1)
1	Fineness (90 micron IS Sieve)	5 %	10% (Maximum)
2	Specific gravity	2.88	2.89
3	Soundness	2 mm	5 mm
4	Initial setting time	65 minutes	30 (Minimum)
5	Final setting time	370 minutes	600 (Maximum)
6	Standard consistency	29.5 percent	
	3-days compressive strength	24.70 MPa	23MPa (Minimum)

7	7-days compressive strength	35.90 MPa	33MPa (Minimum)
	28-days compressive strength	44.85 MPa	43MPa (Minimum)

the results of standard tests on Ultra-Tech Pozzolana Cement (PPC) to determine various physical properties such as fineness, specific gravity, soundness, compressive strength of cement, and initial and final setting time, as well as their calculated and recommended values by Indian Standards. Cement was properly kept to avoid its characteristics from deteriorating due to moisture interaction. The cement used in the study met all the standards set by **IS: 8112-1989 (Part 1).**

4.3.2 Fine Aggregates (FA)

Fine Aggregates (FA) are natural sand or crushed stone that is required in the production of concrete. Fine aggregate is granular material that passes through a 4.75mm screen and is used to make concrete or mortar. As a fine aggregate, natural river sand was employed. Table 3.3 shows the fine aggregates' particle size distribution and other physical characteristics. Before being used in concrete, lumps of clay and other extraneous materials were eliminated. Fine aggregates used in the experimental study belonged to Zone III are reported in **Table 4.3**

Table 4.3: Sieve Analysis of Fine Aggregates (as per IS: 383- 1970)

S.No	I.S. Sieve (mm)	Weight Retained	Cumulative retained	Percentage Cumulative Retained	Percentage passing	Limit
1	10	----	----	----	100	100
2	4.75	52	52	2.6	97.40	90-100
3	2.36	60	112	5.6	94.4	85-100
4	1.18	192	304	15.2	84.8	75-100
5	600 µ	212	516	25.8	74.2	60-79
6	300 µ	992	1508	75.4	24.6	12-40
7	150 µ	444	1952	97.6	2.4	0-10
8	Pan	48	2000	----	$\sum$ 2.22	
Fineness Modulus of fine sand = 2.22						

4.3.3 Coarse Aggregate (CA)

The aggregate that is retained after passing through a 4.75mm screen is known as coarse aggregate. The coarse aggregate utilized in the experimental investigation for casting steel and GFRP reinforced beams was a 50:50 mixture of two crushed stones with sizes of 10 mm and 20 mm. The sieve analysis and physical parameters of coarse aggregates with sizes of 10 and 20 mm fulfilled the criteria of IS: 383-1970, as shown in Tables **4.4, 4.5, 4.6, and 4.7** respectively**.**

Table 4.4: Sieve Analysis for C.A 10mm (as per I.S: 383-1970)

S.NO	Sieve size (mm)	Weight Retained (gm)	Cumulative Retained (gm.)	Percentage Cumulative	Percentage passing	IS: 383-1970
1	80	Nil	Nil	Nil	100	-------
2	40	Nil	Nil	Nil	100	-------
3	20	Nil	Nil	Nil	100	-------
4	10	350	350	17.5	82.5	85-100
5	4.75	1500	1850	92.5	7.5	0-20
6	PAN	150	2000	100	0.0	0-5
Total weight of 10mm aggregates = 2000gms						

Table 4.5: Sieve Analysis for C.A 20mm (as per I.S: 383-1970)

S.No	Sieve size (mm)	Weight Retained (gm)	Cumulative Retained(gm)	Percentage Cumulative	Percentage passing	IS: 383-1970
1	80	Nil	Nil	Nil	100	100
2	40	Nil	Nil	Nil	100	100
3	20	55	55	2.75	97.25	85-100
4	10	1940	1995	99.75	.25	0-20
5	4.75	2.5	1997.5	99.8	.2	0-5
6	Pan	2.5	2000	100	0.0	------
Total weight of 20mm aggregates = 2000gms						

Table 4.6: Proportioning of Coarse aggregates

S.No	Sieve size (mm)	Cumulative Percentage passing of 10mm aggregates	Cumulative Percentage passing of 20mm aggregates	Proportion 50:50 (10mm:20mm)	IS:383-1970
1	80	100	100	100	100
2	40	100	100	100	100
3	20	100	97.5	98.75	95-100
4	10	82.5	0.25	41.375	25-55
5	4.75	7.5	0.2	3.85	0-10

Table 4.7: Aggregate physical characteristics

S.No	Physical Properties	Values
1	Water Absorption of Fine Aggregates	2.60
2	Water Absorption of Fine Aggregates	1%
3	Specific Gravity of Coarse Aggregates 10 mm	2.65
4	Specific Gravity of Coarse Aggregates 20 mm	2.65
5	Free Moisture Content of Coarse Aggregates	Nil
6	Water Absorption of Coarse Aggregates	0.5%
7	Fineness modulus (10mm)	6.1

4.3.4 Mix Design Proportions

Concrete is a composite material made up of fine and coarse aggregates that are linked together by fluid cement (cement paste) that hardens (cures) over time. A portable concrete roller mixer produced the concrete for the steel & GFRP reinforced concrete beams utilized in the study. For casting beams, the design mix proportions of cement, fine, and coarse aggregates (crushed gravel with a max size of 20 mm) were 1:1.47:2.54 with a w/c ratio of 0.46 as indicated in **Table 3.8**. These design mix proportions were used for casting of standards 150mm sized cubes and the average 28 days concrete compressive strength was determined as 35.9 N/mm^2 at 28 days **(IS 10262 2009).** The concrete mix designs are presented in **Table 4.8**. The concrete had a slump of 100 mm.

Table 4.8: Concrete Mix Design Proportions

S.No	Material	Quantity
1	Cement	428.60 kg
2	Sand	632.74 kg
3	Coarse Aggregates	1088.71 kg
4	Water	197.16 kg
C : W : FA : CA 1: 0.46: 1.47 : 2.54		

4.3.5 Water

Concrete is produced by mixing binding and inert materials with water. As a result, water and its purity are crucial in defining the quality of concrete. The water-to-cementitious-materials ratios influence the strength and durability of concrete to a considerable extent. The concrete work was done with potable water from the Concrete Structures Laboratory at the **Thapar Institute of Engineering and Technology** (TIET). The water used for mixing and curing was devoid of harmful quantities of oils, alkalis, salt, and sugar, as well as other organic substances that might harm concrete. Potable water is typically regarded as adequate for mixing

and curing concrete, according to Indian Standard 456-2000. As a result, all concrete samples were prepared using potable water.

4.4 TENSILE TESTING OF REINFORCING BARS

Material characteristics such as tensile strength, modulus of elasticity, and rupture strain were determined by preliminary material testing of steel and GFRP reinforcing bars. **Table 4.9** demonstrates the data of mechanical properties tests on steel and GFRP reinforcement bars, using the tensile testing procedure described in **(IS 2008)** for steel bars and **(ASTM D7205 2006)** for Glass Fibre Reinforced Polymer Bars.

Steel rebar purchased from **NAV DURGA STEELS PRIVATE LIMITED** located in Mandi Gobindgarh, Punjab, India. To strengthen the steel RC specimens in this

Table 4.9: Mechanical characteristics of reinforcing bars

Reinforcing bar diameter (mm)	Ultimate Tensile Strength (MPa)		Elastic Modulus (GPa)		Ultimate Strain	
	Steel	GFRP	Steel	GFRP	Steel	GFRP
8	530	866	201	41.3	0.0049	0.021
10	544	1092	205	43.7	0.0048	0.025
12	566	1219	210	41.20	0.0048	0.0296

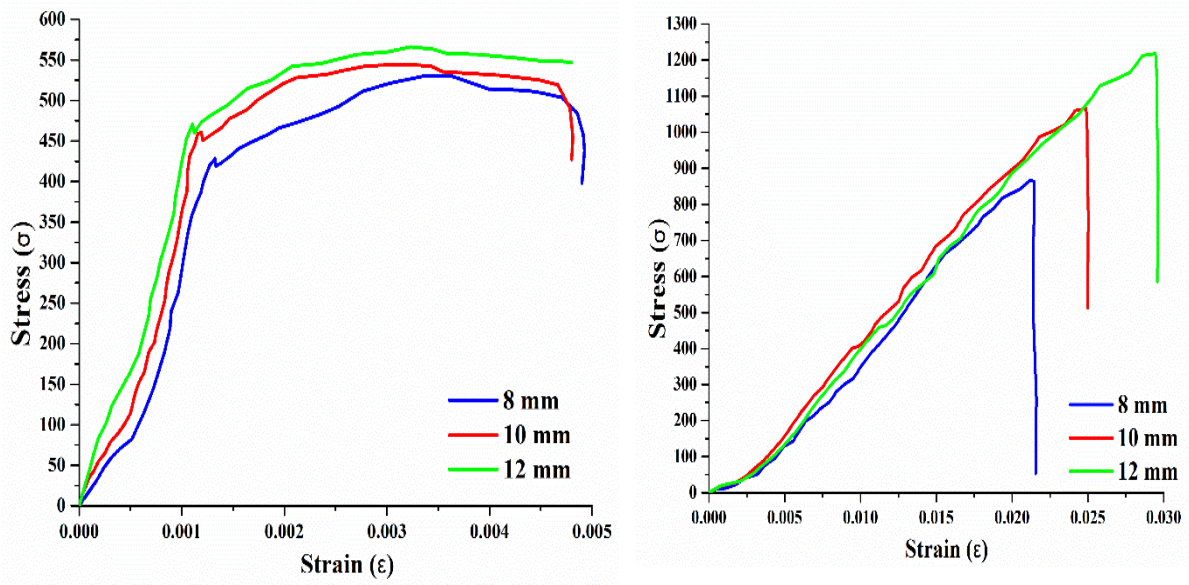

(a) **(b)**

Fig. 4.2: Stress-Strain Plot for (a) steel bars and (b) for GFRP bars

investigation, three types of reinforcing steel bars were used: For longitudinal reinforcement, a deformed steel bar with nominal diameters of 8mm, 10mm, and 12mm is used **(IS, 2008)**. Deformed steel bar of 8mm diameter served as shear reinforcement. As illustrated in **Fig. 4.2,** the steel reinforcing bar failed owing to **"cup and cone"** failure within the free length. **Fig. 4.2a** depicts the stress-strain conduct of steel reinforcing bars. The stress-strain response was linear until the yield point, and then plastic until maximum tensile strength was reached, with necking causing failure.

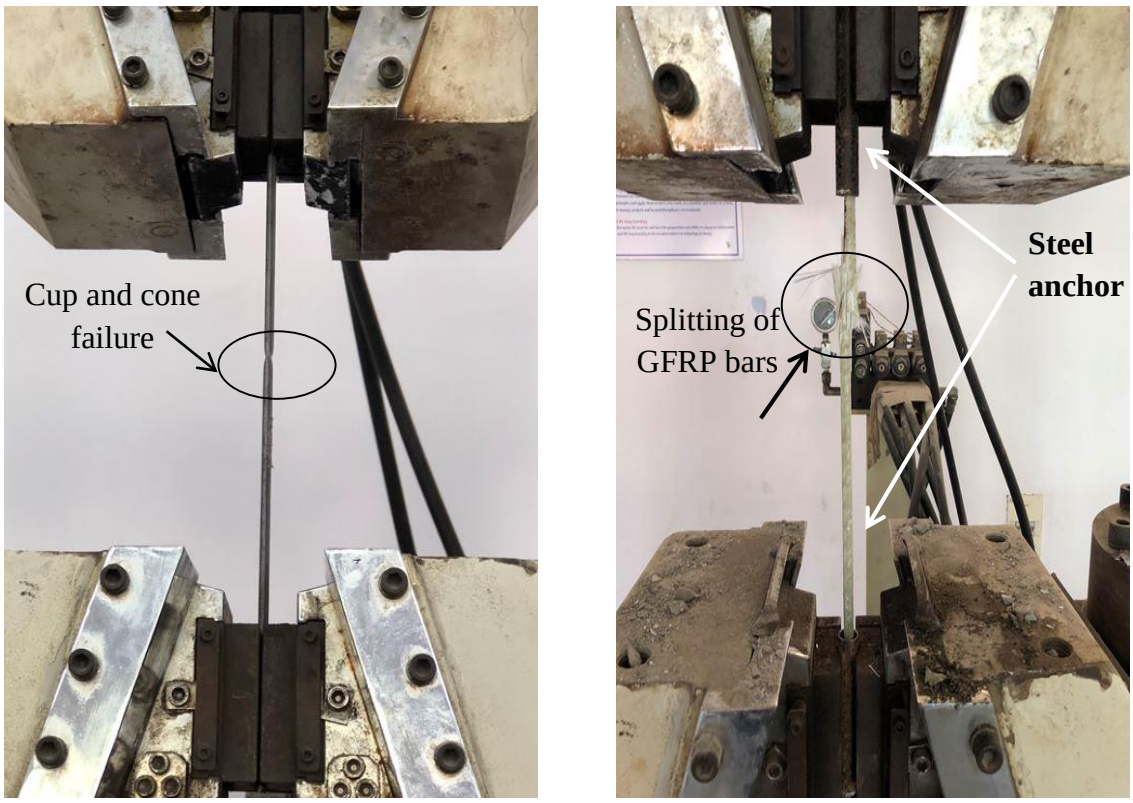

(a) (b)

Fig. 4.3: Tensile testing of reinforcing bars (a) Tensile (cup and cone) failure of steel bars and (b) splitting failure of GFRP bars

Similarly, three types of reinforcing GFRP bars Purchased from **KC CONTECH Private Limited** which is a leading GFRP Rebar manufacturer based in Chennai, Tamil Nadu, and India. In this thesis, to reinforce the GFRP reinforced concrete specimens: GFRP bar of a nominal diameter of 8mm, 10mm, and 12mm was used as longitudinal reinforcement and 8mm diameter bars served as shear reinforcement **(ASTM, 2006).** The stress-strain conduct of the GFRP reinforcement bars is presented in **Fig. 4.2b**. Tensile testing for GFRP bars is more challenging as compared to the strength **(Goldston et al. 2017)**. A GFRP bar specimen tends to crush due to jaw pressure during tensile testing. To overcome this problem, GFRP bars were

capped with cylindrical steel anchors using epoxy. A steel anchor prevents slip and uniformly distributes the pressure on the GFRP bar. The GFRP bars with steel anchors were placed in the jaws of the UTM and the specimen was clamped using a pressurized hydraulic system **(Fig. 4.3).** Two specimens corresponding to each diameter for steel and Glass FRP bars obtained are presented in **Fig. 4.2** and **Table 4.9.** There is a clear distinction between the modes of failure of steel and a GFRP bar, Steel bars undergo a typical **"Cup and Cone"** failure **(Fig. 4.3a),** whereas failure occurs outside the anchor and was primarily due to **"Rupture and Splitting"** of the fibers in GFRP bars **(Fig. 4.3b).**

4.5 FABRICATION OF THE STEEL-RC AND GFRP-RC SPECIMENS

Fabrication of reinforced concrete structural members plays a vital role in their performances. Steel and GFRP reinforcement cages were assembled as presented in **Fig. 4.4 (a) and (b).** The formwork used to fabricate the beams was structural steel sections. Steel forms were used to keep all the specimens in a horizontal position. The sides were 18mm

(a) (b)

Fig 4.4: Formwork and (a) steel and (b) GFRP Reinforcement Cages Before Concrete Pouring

thick, and the bottom was 150mm wide. The forms were oiled, and then steel and GFRP reinforcement cages were placed in the formwork as presented in **Fig. 4.4.** The cage in the formwork was supported by concrete spacers along the side as well as the bottom to ensure the required concrete cover of 20 mm. To replicate typical construction practices with beams, all-

steel RC and GFRP RC beams were cast horizontally. After oiling the forms, steel & GFRP reinforcing cages were placed in the formwork as presented in **Fig. 4.4**. The cage in the formwork was supported by concrete spacers along the side as well as the bottom to ensure the required concrete cover of 20 mm. An electrically driven concrete mixer machine with a capacity of 400 liters was used to make the concrete. Directly from the concrete mixer machine, the concrete was poured into the beam forms. To consolidate the concrete and eliminate air spaces, an electric vibrator was employed. Beams are covered with a jute bag and cured for 28 days. Three standard cubes of 150 mm diameter were prepared and cured in the same situations as the beam samples. On the day of specimen testing, a concrete cube is tested, then the maximum and minimum values are excluded, and the average strength value is computed to ensure that the required strength is achieved. As mentioned the average cube compressive strength of the mix used for casting was obtained as 35.9 Mpa.

4.6 FLEXURAL TEST SET-UP DETAILS

The steel and GFRP reinforced concrete beams were situated in the experimental test setup for static loading between two beams of the steel I section, with a total span of 2100 mm and an effective span of 2.0 m with overhang of 50 mm on both sides. The Steel RC & GFRP-RC beams were simply supported (SS), with a pined support at one end and roller support at the other end were tested under 4-point bending, **see Fig. 4.5,** using a spherical steel ball positioned in the center of the steel I-beam to provide two equally concentrated loads at 667 mm from either support. During testing, a 1000 kN hydraulic controlled load cell was employed. In order to quantify the beam deflection up to failure, a linear differential transformer with a range of 50 mm and precision of 0.01 mm/sec has been linked to the bottom centre of the beams. Until failure, all beams were subjected to 1 mm/min displacement control loads. All statistics, including load and deflection, were recorded using a high-speed data collecting system. **Fig. 4.5** shows the typical flexural test setup for the research. Mechanical performance of the steel RC & GFRP RC beams were compared by studying load-deflection characteristics, modes of failure, the progression of visible cracking patterns, moment carrying capacity, energy absorption capacity pre-and-post cracking bending stiffness, etc.

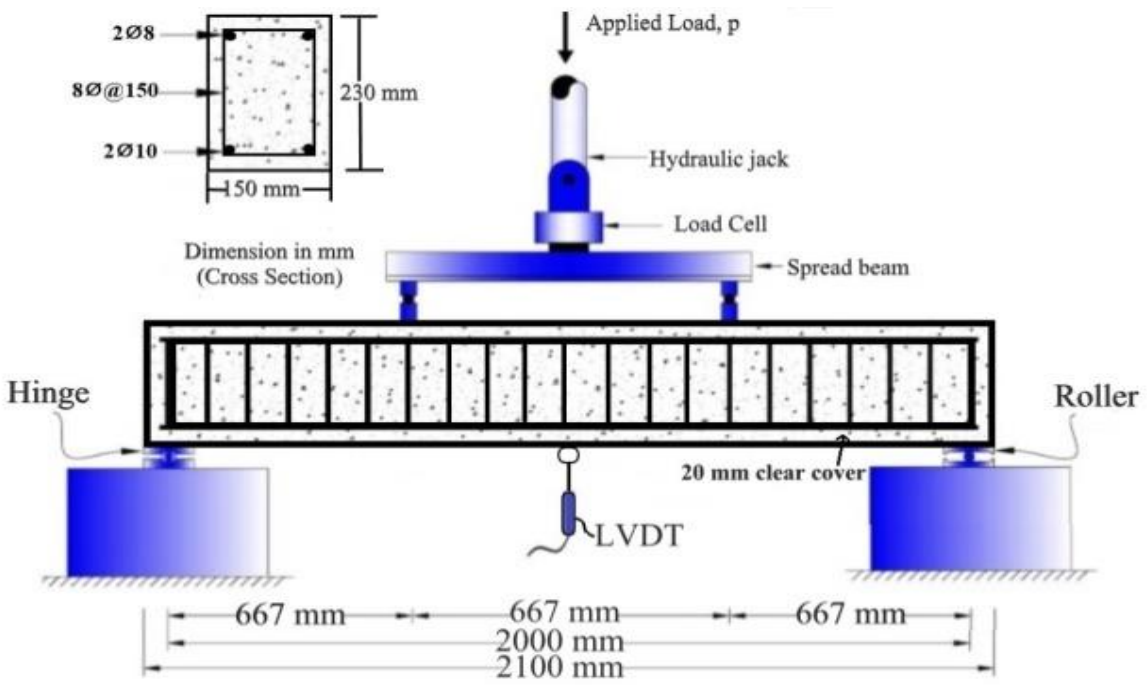

Fig. 4.5: Flexural test set with reinforcement details

4.7 ACOUSTIC EMISSION SET-UP

During flexural testing, the concrete beams were also subjected to simultaneous AE and DIC monitoring. A Micro-II digital AE data acquisition system with AE sensors (PAC, USA), pre-amplifiers, and filters was used to monitor the AE of the steel & GFRP RC beams. When steel & GFRP reinforced concrete beams are subjected to flexural loading, AE sensors detect signals created by micro and macro cracks that arise as a result of flexural and shear cracks. Six AE sensors (Physical Acoustics Corp, (PAC) manufacture) with a resonant frequency of 60 kHz were surface attached on the surface of steel RC & GFRP RC beams to explicitly cover an area where substantial damage and failure was expected. Three sensors were mounted on the front-face of the RC beam in-between-area, which was covered with a DIC speckle pattern, and the other three were mounted on the back-face. The AE sensors were mounted using a vaseline cream and held in position using cello adhesive tapes until the completion of the test. The experimental setup for AE data acquisition is shown in **Fig. 4.6**. AE-signals were recorded continuously until the completion of the experiment. AE-Win software was used for extracting the data providing various characteristics of AE-signal such as cumulative AE hits, amplitude (dB), Rise Angle (RA), Cumulative Signal Strength (CSS), Average Frequency (kHz), duration (μs), and Rise Time (RT), etc. Prior to the real AE monitoring, the Pencil Lead Break (PLB) test was conducted to check the sensitivity of the AE sensor. Following a successful PLB test,

the wave velocity of concrete was determined to be $3.5x10^6$ mm/s (average of six measurements)by a pencil lead break test **(Lee & Oh, 2016 and Sharma et al. 2018)**. To gather acoustic emission signals, a threshold of 45 decibels was first set with a preamplifier gain of 40 dB as input. The signals arising from bending and subsequent breaking of steel & GFRP RC beams were acquired using the AE-win software.

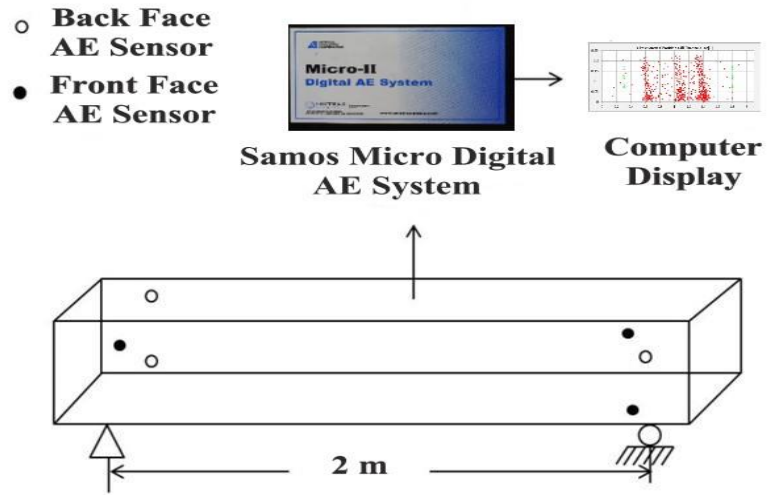

(a) Schematic

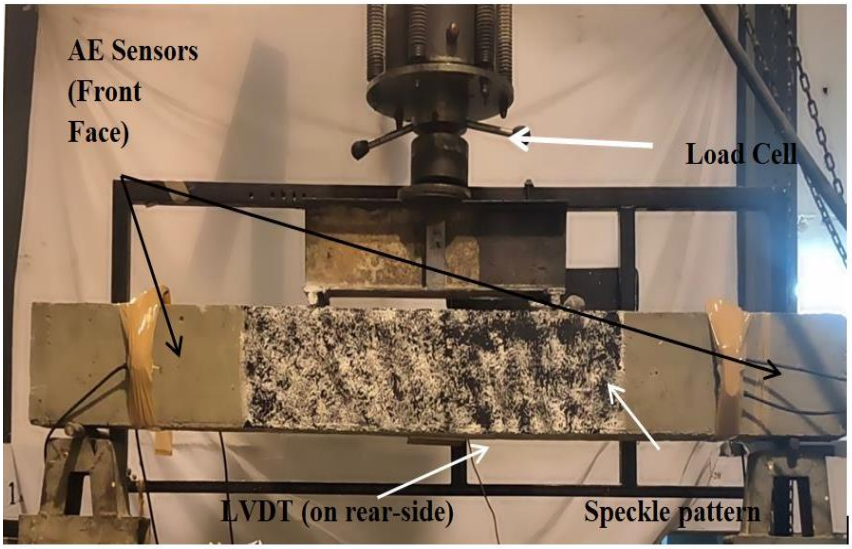

(b) Actual Beam with AE sensors

Fig. 4.6: Acoustic Emission monitoring set up

AE signals were recorded continuously during the entire duration of the loading of the steel RC & GFRP RC beams. From the recorded AE signals, numerous AE waveform parameters of cumulative AE hits, amplitude (dB), Rise Angle (RA) Cumulative Signal Strength (CSS), Average Frequency (kHz), duration and Rise-Time (RT), etc., their expanse and spread obtained using AE X-Y maps have been used to study the variation in initiation and progression

of damage classification of cracking (micro-and-macro cracks) and fracture and failure mode of steel & GFRP RC beams.

4.8 DIGITAL IMAGE CORRELATION (DIC) SET-UP

For DIC monitoring, a speckle pattern comprising of a white backdrop with black dots and measuring 1 meter in length is placed at the mid-span of steel-reinforced concrete and GFRP reinforced concrete beams, and it is referred to as the "Region of Interest" (ROI) **(Fig. 4.7a).** Throughout the testing, pictures of the front surface of the beam were captured using a digital camera (Sony Exmor RV100 model) with a high-resolution image acquisition (5232 x 3488 pixels). The camera was positioned on a tripod stand at a distance of 400 mm. The

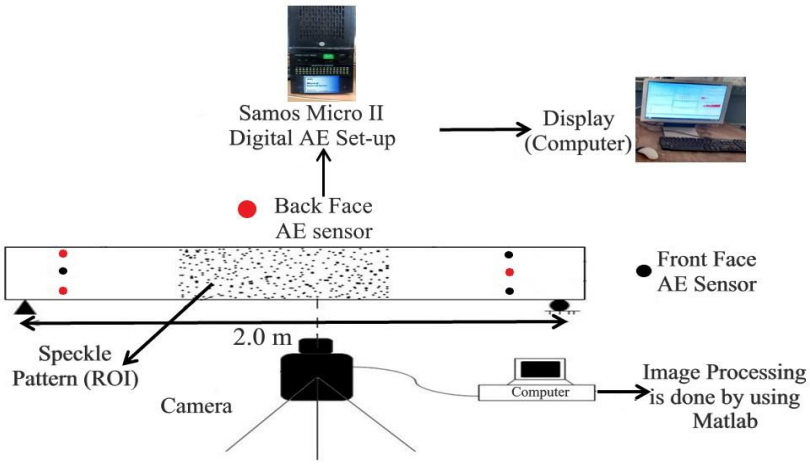

(a) Schematic

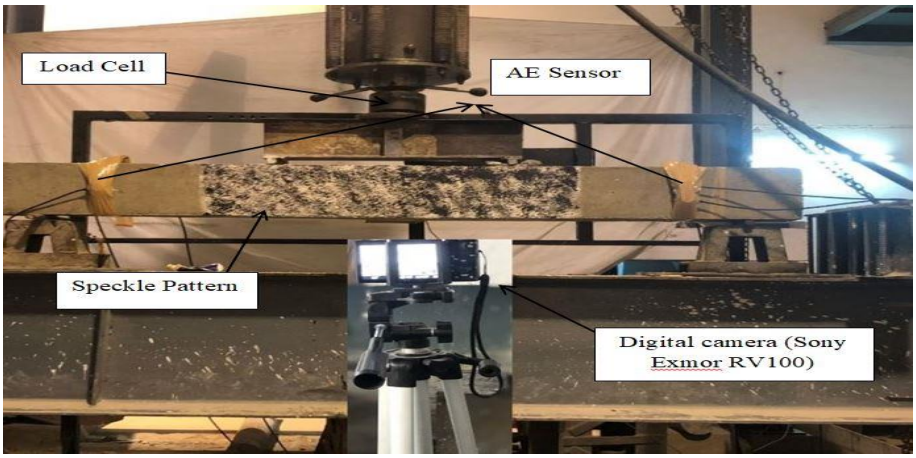

(b) Actual

Fig. 4.7: DIC monitoring set up

camera's focal length was set to 37 mm, the aspect ratio was set to 3:2, and the viewing direction was set to normal to the front surface of the beam. To eliminate any shaking and to maintain the same distance between the camera lens and the specimen, the digital photos are captured

using a remote control. The digital photos were manually modified to improve image quality before being loaded into the freeware 2D-DIC Ncorr V.1.2.1.

It's worth noting that the DIC analysis was only performed on the zone indicated as ROI in **Fig. 4.7.** The flexural performances of steel RC & GFRP RC beams were compared using DIC parameters of mid-point vertical displacement and surface strains. On a UTM Machine, the beams were evaluated under four-point loading with the setup illustrated in **Fig. 4.7b.** However, very limited research has used AE and DIC methods to assess the mechanical/fracture behavior of steel RC & GFRP RC beams. The load was assessed using a data-gathering system, and the mid-span deflections were measured using Linear Variable Differential Transducers (LVDT). The structural response of the steel & GFRP RC beams was studied by investigating the load-deflection behavior as well as AE and DIC parameters to understand the initiation and progression of damage and eventually resulting in unique cracking patterns. AE waveform parameters like cumulative AE hits, amplitudes, average frequency, signal duration, and rise angle were considered in the AE analysis. DIC was primarily employed to compute the vertical displacement at and surface strains at the mid-span. Moreover, the longitudinal strain field (ε_{xx}) so obtained from DIC was compared with AE X-Y event plots and actual photographic images obtained during testing.

4.9 CLOSING REMARKS

The experimental program and testing details of the work is carried out in this work in detail. The test findings of fundamental materials, like cement, fine aggregates, coarse aggregates, steel reinforcement and GFRP enforcement bar water test features and manufacturing details for specimens of steel-RC and GFRP-RC are also discussed. All the steel reinforced & GFRP reinforced concrete beams were subjected to flexural loading along with AE and DIC testing and the details are also presented in this chapter.

CHAPTER 5

FLEXURAL PERFORMANCE OF STEEL AND GFRP RC BEAMS

5.1 GENERAL

In this chapter, the flexural performance and mechanical behavior of differently reinforced steel RC and GFRP RC beams are examined and compared. As already discussed in Chapter 4, two types of steel-reinforced concrete and GFRP reinforced concrete beams were cast with an effective length of 2.0 m and an overhang of 50 mm on each side of 150 mm x 230 mm cross-sectional dimensions using concrete design mix proportions of 1:1.47:2.54 of cement, sand, and coarse aggregates and a w/c ratio of 0.46. Two sets of beams were cast reinforced by conventional Fe500 grade (S-series) and GFRP bars (G-series) respectively. It is important to note that S series beams had both longitudinal as well as shear reinforcement made of Fe 500 steel whereas G Series beams had both longitudinal as well as transverse reinforcement entirely made of GFRP bars. Steel reinforced concrete beams were designed as under reinforced **(ACI 2019);** whereas GFRP reinforced concrete beams were designed as over reinforced (**ACI 2015).** The reinforcement ratio ($\rho = 100A_{st}/bd$ %) for each set of RC beams was varied as ~0.33%, ~0.52%, and ~1.1% based on volumetric calculations. The reinforcement details of both S and G-series are presented in **Table 4.1.**

In this chapter, the comparison of the flexural performance of different reinforced steel & GFRP RC beams is investigated in detail. The influence of different percentages i.e. ~0.33%, ~0.52%, and ~1.1% of longitudinal reinforcement ratios with the same concrete compressive strength (35.9 N/mm^2), on load-deflection behavior and variation in their failure modes is explored during testing (tension failure in under-reinforced beams and shear concrete crushing in over-reinforced beams). Various parameters like mid-span deflection, theoretical moment carrying capacity (M_{th}) and experimental moment carrying capacity (M_{exp}), energy absorption capacity, and pre and post-cracking bending stiffness of steel and GFRP reinforced concrete beam are compared with different reinforcement type as well with different percentages of reinforcements.

5.2 FLEXURAL PERFORMANCE AND MECHANICAL BEHAVIOUR

5.2.1 Steel Reinforced Concrete Beams

Table 5.1 shows load-deflection tables for steel RC beams with varying percentages of tension reinforcement ratio. For each S1, S2, and S3 beam with reinforcement ratios of 0.33%, 0.52%, and 1.11%, etc., three samples are examined to ensure the repeatability of results **(Fig. 5.1)**. The representation of the plot with varying percentages of tension reinforcement is presented in **Fig. 5.2.**

The load-deflection plot of steel-reinforced concrete beams is broadly classified into 3 regions Un-Cracked Elastic, Cracked-Elastic, and Plastic Zones (**Fig. 5.2**). Initially, the applied loads as well as deflection are small and follow a linear relationship. This zone I is named an **Un-cracked elastic zone**. With further increase in loading, a significant change and reduction in stiffness of the steel-RC beam is observed with the development or formation of hairline cracks at cracking load (P_{cr}) of 5.58 kN, 7.65 kN, and 9.54 kN with a deflection (δ_{cr}) of 0.61mm, 0.56mm and 0.43mm for S1, S2, and S3 beam respectively (**Table 5.1**). These cracks proceed along the sides of the steel-RC beam with reducing stiffness. The cracks tend to appear and start becoming visible at a load of 16 kN, 20 kN, and 30 kN for S1, S2, and S3 beam respectively, in the tensile zone of the steel-RC beam. As the load increases, the cracks starts propagating and appear in the form of scattered flexural and shear cracks causing the steel to yield under load (P_y) of 28.93 kN, 45.85 kN, and 75.09 kN with a deflection (δ_y) of 6.27mm, 6.85 mm and 4.94mm in S1, S2, and S3 beams respectively. This part of the load-deflection plot from P_{cr} to P_y is termed as **Cracked-Elastic Zone II.**

Table 5.1 Load-deflection Results for Steel reinforced concrete beams

Beam Series	P_{cr} (kN)	δ_{cr} (mm)	P_{peak} (kN)	P_u (kN)	δ_u (mm)
S1	5.58	0.61	35.18	33.43	55.51
S2	7.65	0.56	50.80	47.10	43.10
S3	9.54	0.43	88.94	82.75	30.90

The concrete section in Zone III, also known as the Plastic Zone, is cracked and ineffective in resisting loads, and the entire load is taken on by steel bars, which yields. It is noticeable by an increase in the mid-span deflection 23.22 mm, 14.47mm, and 12.48 mm respectively, with a minor rise in load up to a peak load (P_{Peak}) of (35.18 kN, 50.80 kN, and 88.94 kN, pointing towards a larger strain at the level of steel and increase in curvature of the

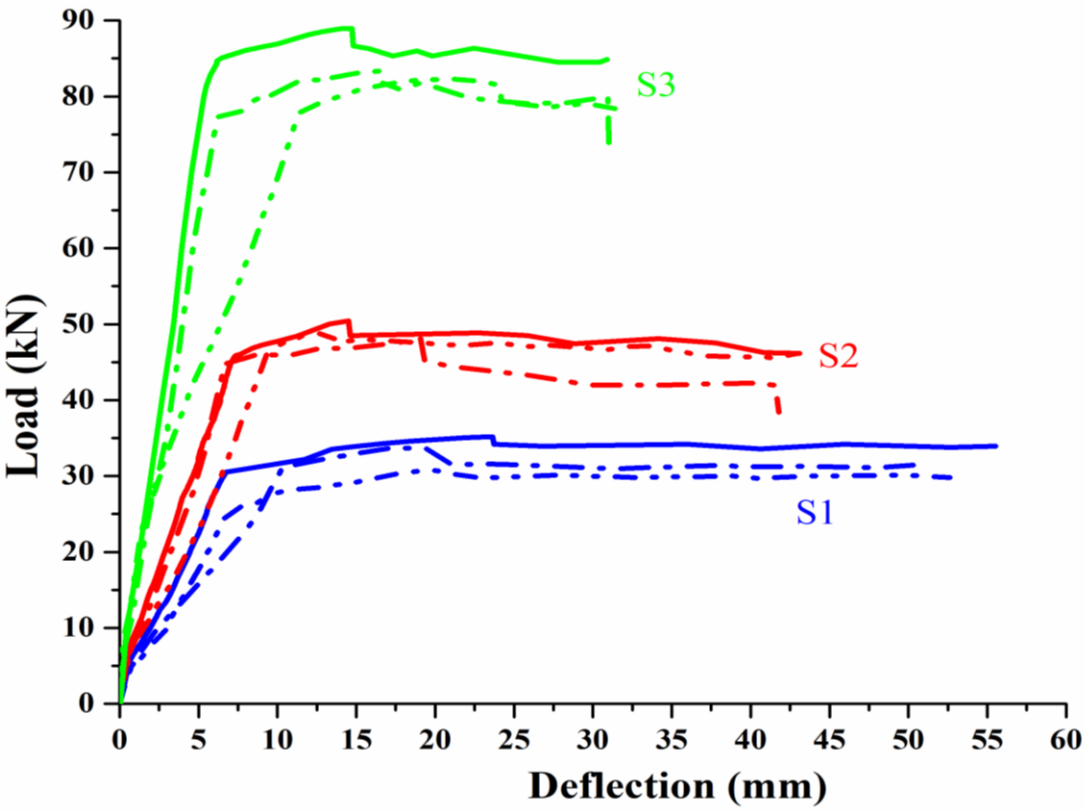

Fig. 5.1: Load v/s Deflection plots for S-series beams

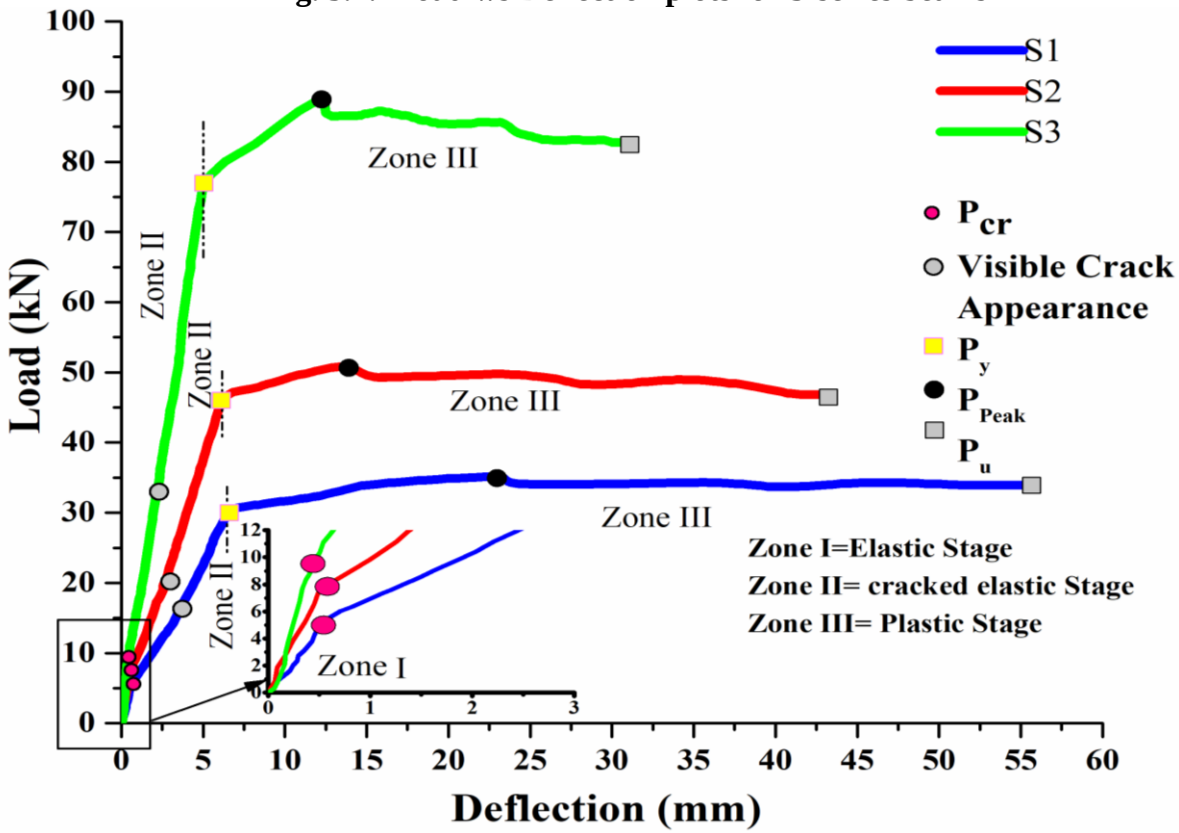

Fig. 5.2: Generalized load v/s Deflection plots for S-series beams

cracked section with an increase in reinforcement ratio. Furthermore, the beams fail at an ultimate load (P_u) of (33.43, 47.10, and 82.75) kN owing to the strain hardening of steel with a

deflection (δ_u) of (55.51, 43.10, and 30.9) mm in for S1, S2, and S3 beams respectively as shown in **Table 5.1**.

In general, as the reinforcement's ratio increases, the ultimate load-carrying capacity of S2 and S3 beams improves by roughly 34% and 42%, respectively, as compared to S1, indicating higher load carrying capacity with increased tensile reinforcement. Another noteworthy finding is a significant increase in the area under the load-deflection plot as the reinforcement ratio is increased. It is also observed that Plastic Zone III reduces drastically with an increase in steel. The failure takes place at the much lower strain in the S3 beam. All S-series RC beams specimens failed by steel yielding and followed by concrete crushing.

5.2.2 GFRP Reinforced Concrete Beams

Similarly, the load-deflection plots of GFRP reinforced concrete beams with varying ratios of tension reinforcement ratio are detailed in **Table 5.2**. Three samples are tested for each G1, G2, and G3 beam with reinforcement ratios of 0.33 percent, 0.52 percent, and 1.11 percent, respectively, to ensure that the results are repeatable **(Fig. 5.3).** The representation of the plot with varying percentages of tension reinforcement is shown in **Fig. 5.4.**

The mechanical behavior of GFRP reinforced beams in flexure is visibly different from steel-reinforced concrete beams (**Fig 5.3**). Broadly, the behavior of GFRP reinforced beams exhibits bi-linear load-deflection characteristics up to the failure without any yielding or ductility as experienced by steel reinforced beams. Initially, the load-deflection curve is perfectly linear and this zone is **Un-cracked Elastic Zone I**.

Table 5.2 GFRP reinforced concrete beams load deflection results

Beam Series	P_{cr} (kN)	δ_{cr} (mm)	P_{peak} (kN)	P_u (kN)	δ_u (mm)
G1	7.89	1.37	51.32	48.94	68.68
G2	8.01	0.91	60.47	60.47	60.09
G3	10.31	0.39	83.71	83.71	34.47

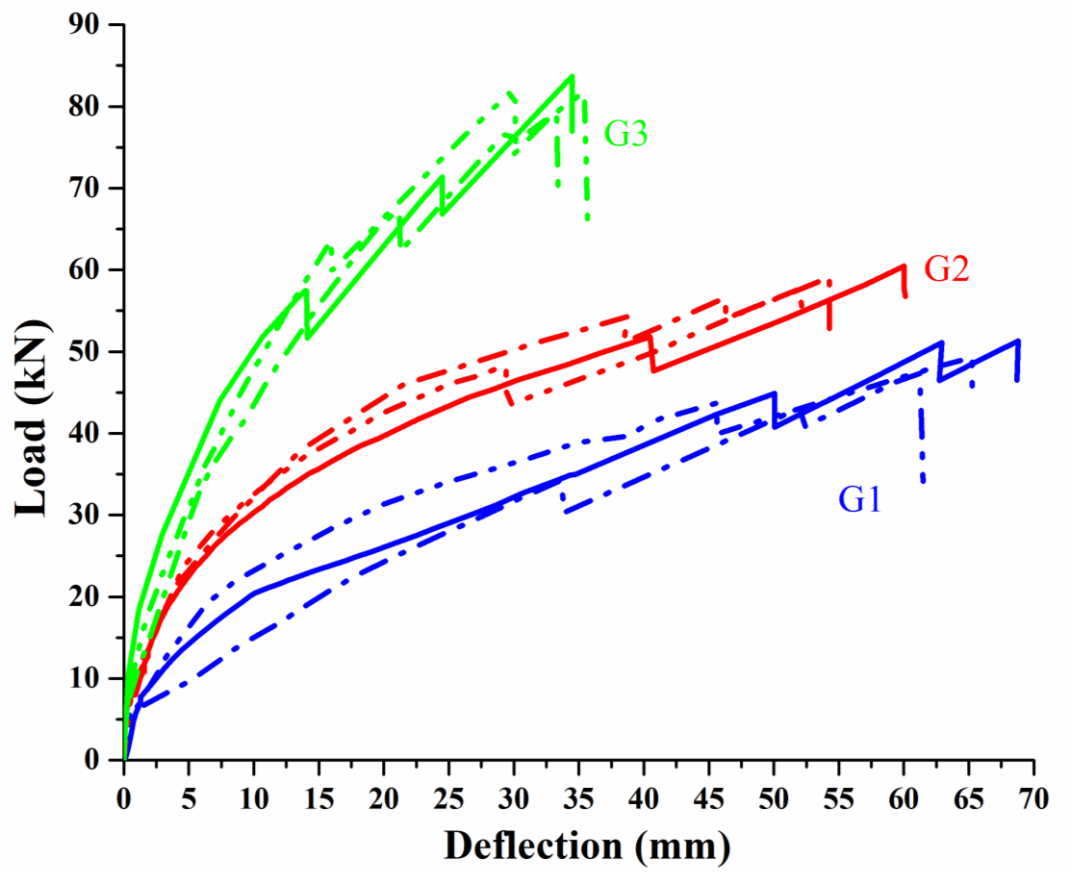

Fig. 5.3: Load v/s Deflection plots for G-series beams

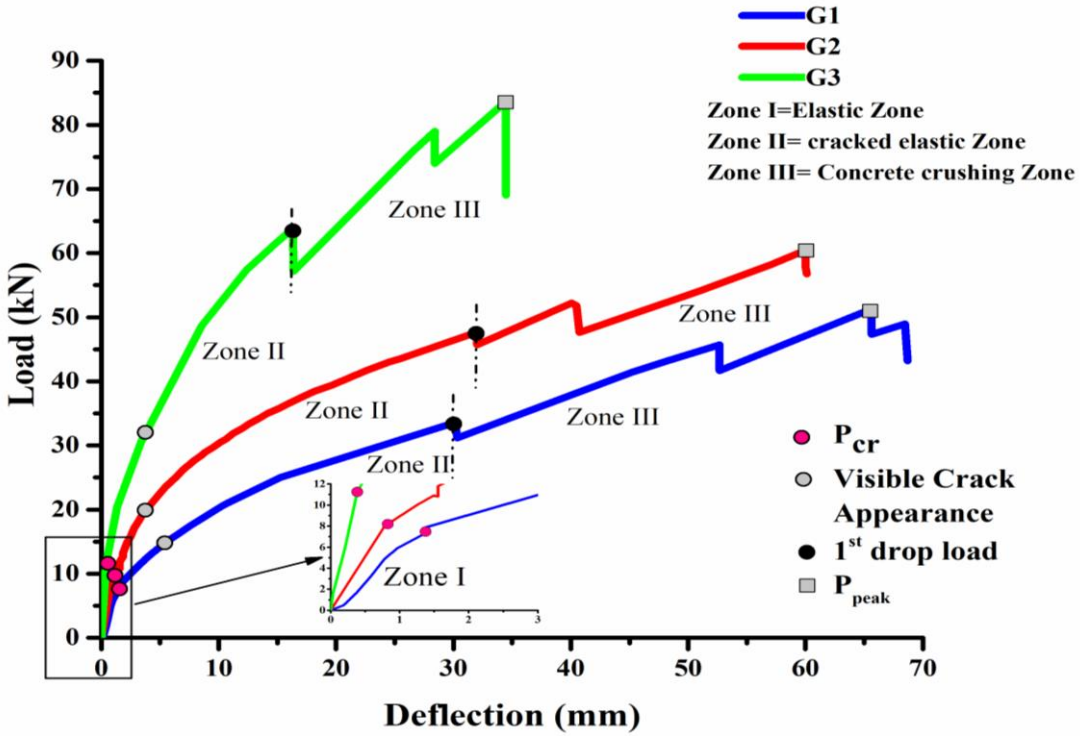

Fig. 5.4: Generalized load v/s Deflection plots for G-series beams

At a load (P_{cr}) of 7.89 kN, 8.01 kN and 10.31 kN, the enlargement of hairline cracks causes a significant reduction in the beam's stiffness with a deflection (δ_{cr}) of 1.37 mm, 0.91 mm and 0.34 mm in G1, G2, and G3 RC beams respectively (**Fig. 5.4 and Table 5.2**). These minor cracks propagate along the beam's sides at a constant stiffness. The initial bending stiffness increases as the reinforcement ratio is increased. At loads of 15 kN, 20 kN, and 33 kN for G1, G2, and G3 RC beams in the pure bending zone, cracks begin to form and become visible. Further with the increase in loading, cracks progress towards the compression zone, and this **Zone II** is named as **Cracked-Elastic Zone**.

With the development of flexural cracks, GFRP beams demonstrate elastic action in this zone. This pattern continues until the load-carrying capacity drops for the 1st time at 33.6 kN, 48.10 kN, and 63.57 kN with a deflection of 30.33 mm, 32.01 mm, and 16.37 mm with increasing reinforcement ratio, pointing towards initiation of concrete crushing. The failure is a typical flexural failure in the form of vertical flexural cracks in the pure bending zone along with their simultaneous spreading across the entire length of the beam. Concrete crushing continues to develop, with a significant increment carrying capacity in Zone III (Concrete Crushing Zone). The beam continuous to carry load linearly with a rise in deflection until the second drop in load is observed at 41.7 kN, 47.63 kN, and 73.99 kN with a deflection of 52.68 mm, 40.74 mm, and 28.41 mm in G1, G2, and G3 RC beams respectively. The effective concrete section is highly reduced due to cracking and ineffective in resisting the tensile load and the beam fail at peak load of (P_{Peak}) 51.32 kN, 60.47 kN, and 83.71 kN for G1, G2, and G3 RC beam with the ultimate deflection (δ_{ult}) 68.68 mm, 60.09 mm and 34.47 mm as shown in **Fig. 5.4.**

All GFRP reinforced beams generally fail typically in shear followed by concrete crushing since they are designed as over-reinforced beams to avoid GFRP rupture, which is frequent in under-reinforced Glass FRP beams. Furthermore, Pre-and post-cracking bending stiffness behavior also was observed in GFRP reinforced beams. Initially, all of the beams would have a high bending stiffness, however, this decreased after cracking due to the reduced elastic modulus of the Glass FRP bars. The post-cracking bending stiffness improves slightly as the reinforcement ratio is increased, owing to an increase in load-carrying capacity and higher stiffness of the highly reinforced GFRP beams. Overall, in comparison to S1 and S2, the ultimate load-carrying capacity for G1 and G2 beams improves by about 34% and 42%, respectively, as the longitudinal reinforcement ratio increases. It's pointing towards higher tensile strength of GFRP bars in comparison to steel bars. But as the reinforcement ratio

increases from 0.52 percent to 1.1 percent there is a slightly 5.2 percent decrease in load-carrying capacity in the G3 beam as compared to the S3 beam. It points towards a lower modulus of elasticity of Glass FRP bars as compared to steel bars.

5.3 COMPARISON OF STEEL AND GFRP REBARS IN CONCRETE

5.3.1 Load deflection characteristics

The load-deflection plot is used to assess the mechanical response and performance of steel & GFRP RC beams under a four-point loading and **Fig. 5.5** shows such plots for one typical specimen beam each. The load-deflection plots of steel-reinforced beams typically exhibit three stages viz. Elastic, Cracked-Elastic, and Plastic Stage. GFRP RC beams exhibit bi-linear response up to the collapse which can also be broadly divided into three stages i.e. Elastic, Cracked-Elastic, and Concrete Crushing Stage as shown in **Figs. 5.5 (a), (b) and (c).**

In the initial phase of the loading, both steel and GFRP-RC beams exhibit perfectly linear behavior up to a cracking load (P_{cr}) in S1, S2, and S3 RC beams and G1, G2, and G3 RC beams respectively. This is classified as an **Elastic Stage** which corroborates to **Damage Level-I** in the beams. Thereafter, a drop in the stiffness of both beams is noticed; this can be ascribed to the initiation of cracking in both the beams, and the load corresponding to this is termed as cracking load P_{cr} **(Fig. 5.5).** With a further increase in the loading, a substantial reduction in stiffness is noticed in both beams. But the rate of the reduction in stiffness of the G-series beam is far higher than the S-series beam owing to the lower modulus of elasticity of Glass FRP bars. During this stage, cracks progress along the sides of the beam at consistent rigidity. Thereafter, the cracks travel up to the surface and become visible (appearance of the visible crack) in the tensile zone of the beam in steel & GFRP reinforced concrete beams respectively.

As the load increases, these cracks progress and reveal them as dispersed flexural and shear cracks. This trend continues in the S1, S2, and S3 RC beam until steel yields (P_y), whereas in G1, G2, and G3 RC beam, this trend precedes until the 1st drop-in load is observed at (P_y). This portion of the load-deflection plot is characterized as **Cracked-Elastic Stage** and the damage is classified as **Damage Level II.** Although the yield loads in both types of beams are comparable, the GFRP-RC beam exhibits a considerable increase in mid-span deflection when compared to the steel RC beam, indicating the linear elastic behavior of Glass FRP reinforcing bars.

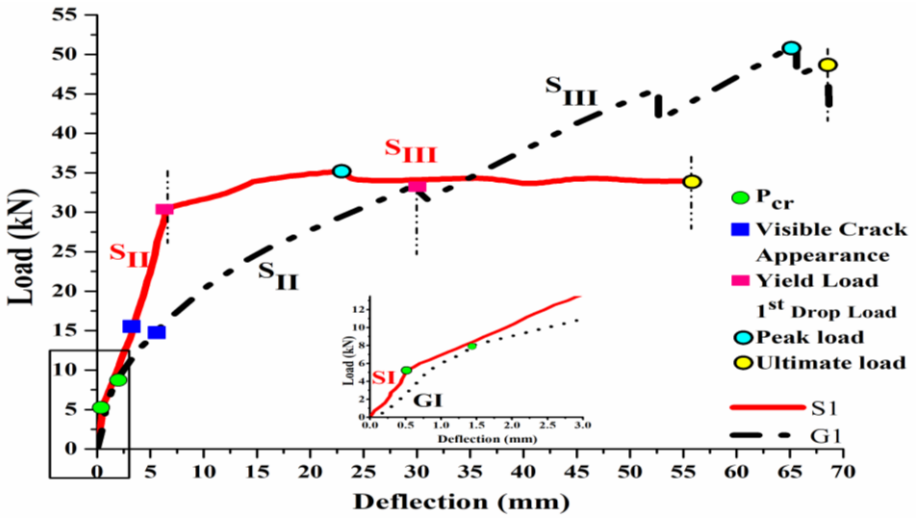

(a) S1 and G1 RC beams

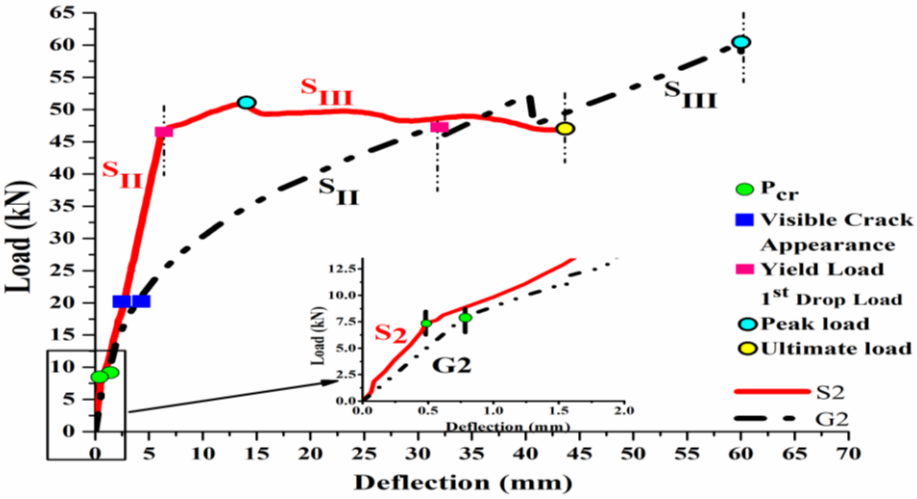

(b) S2 and G2 RC beams

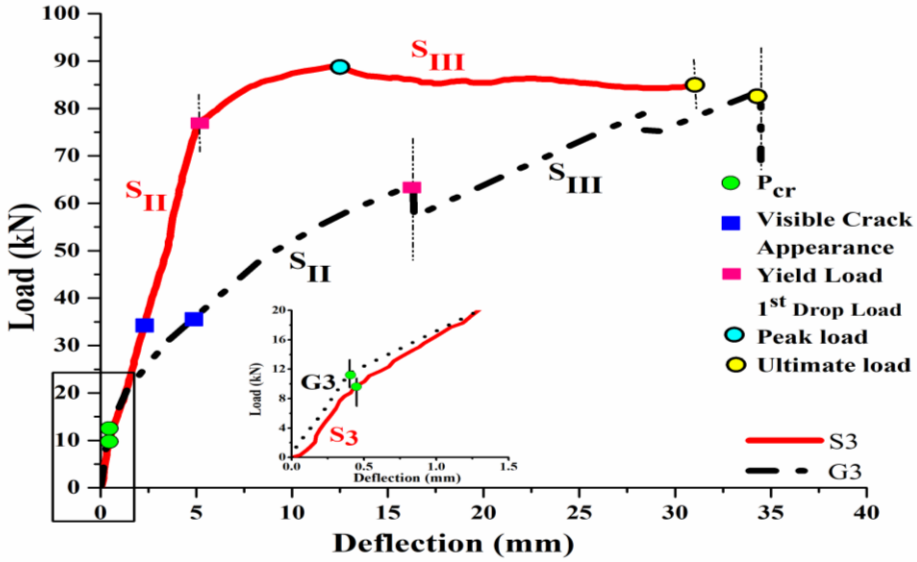

(c) S3 and G3 RC beams

Fig. 5.5: Comparative of load-deflection characteristics

With further loading, a marked increase in the mid-span deflection is observed in S1, S2, and S3 RC beam is observed in the s-series beam with a minor increase in load up to a peak load (P_{peak}), pointing towards larger strain at the level of steel. This part of the curve is characterized as **Plastic Stage** and is named as **Damage Level III** in steel-RC beam and points towards the ductility of the steel-reinforced beams. The concrete is cracked during this stage and the entire load is carried by steel and ultimately steel yields. Furthermore, the beams collapse at an ultimate load (P_{ult}) in S1, S2, and S3 RC beams owing to steel strain hardening. Hence, the steel RC beam fails by steel yielding and is followed by concrete crushing as shown in the steel-RC beam in **Figs. 5.6, 5.8, and 5.10.**

On the contrary, in the case of the GFRP RC beam, the crushing of the concrete progresses with a sharp increase in the load-carrying capacity after the 1st drop of load in the **Concrete Crushing Stage (Damage Level III)**. The beam continues to carry load linearly with an increase in deflection until the 2nd drop-in load is observed and this trend continues up-to-the-peak load. In the end, the beam finally fails at an ultimate load of (P_{ult}) and the failure observed in the GFRP reinforced beam is brittle in the form of concrete crushing as shown in **Figs. 5.6, 5.8, and 5.10.**

5.3.2 Analysis of Damage

From the load-deflection plots of steel RC & GFRP RC beams, as revealed in **Fig. 5.6-5.11,** the development of cracking patterns in the two beams can be classified as:

- **Damage Level I** refers to the phase when the invisible cracking occurs. The development of visible hairline cracks distinguishes this damage zone from the undamaged condition, as does a noticeable drop in the beam's stiffness.
- **Damage Level II** refers to the phase between the formation of hairline cracks and the stage of steel yielding in the case of the steel-RC beams and 1st drop-in load in case of GFRP RC beam and further leading to the formation of distributed flexural and shear cracks.
- **Damage Level III** refers to the phase between the steel yielding and final failure caused due to concrete crushing in the steel beam. In the case of GFRP RC beams, this refers to the phase between 1st drop in load and the final failure due to the crushing of compressive concrete. The formation of crack patterns at different levels of loading and the development of the different damage levels in steel-RC (**Figs. 5.6, 5.8, and 5.10)** and GFRP-RC beam are shown in **Figs. 5.7, 5.9, and 5.11** respectively.

S1 Beam **G1 Beam**

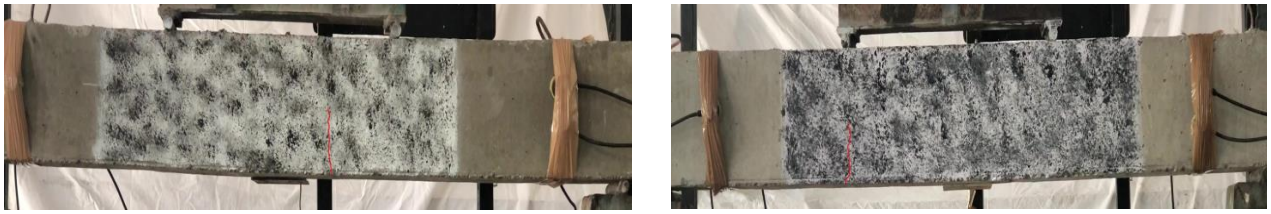

(a) **Damage Level I**

(b) **Damage Level II**

(c) **Damage Level III**

Fig. 5.6: Typical crack patterns

S1 Beam **G1 Beam**

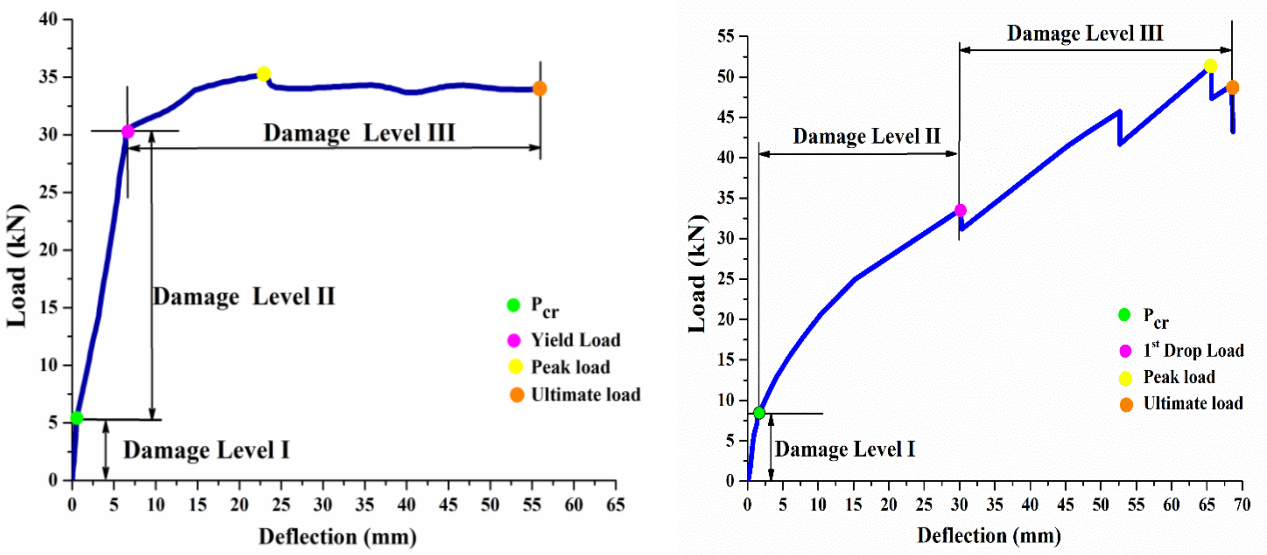

Fig. 5.7: Damage Level Classification

S2 Beam **G2 Beam**

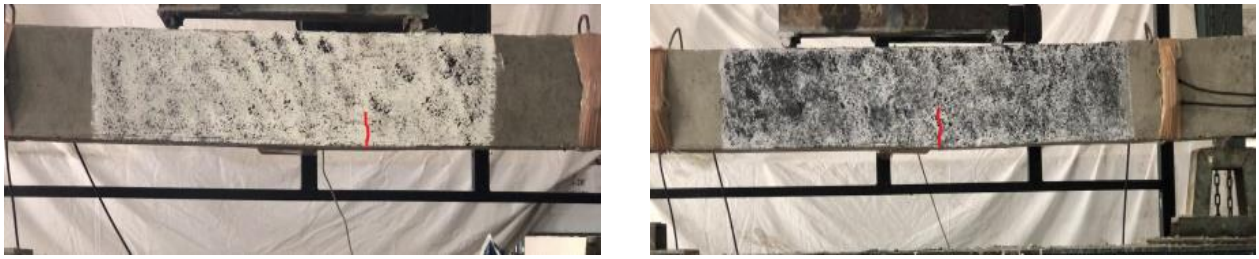

(a) **Damage Level I**

(b) **Damage Level II**

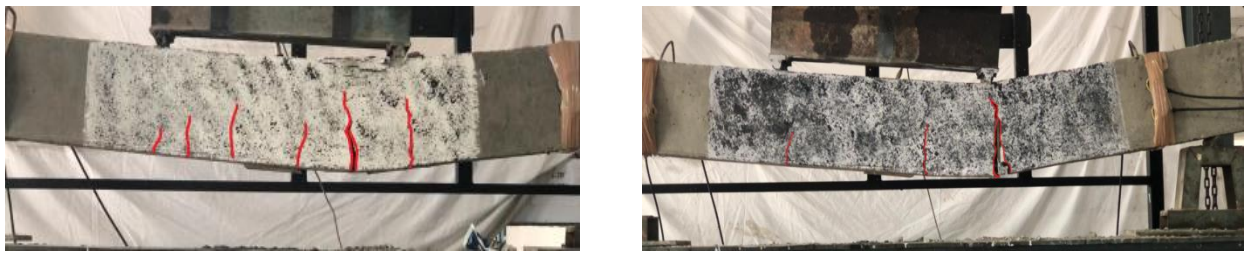

(c) **Damage Level III**

Fig. 5.8: Typical crack patterns

S2 Beam **G2 Beam**

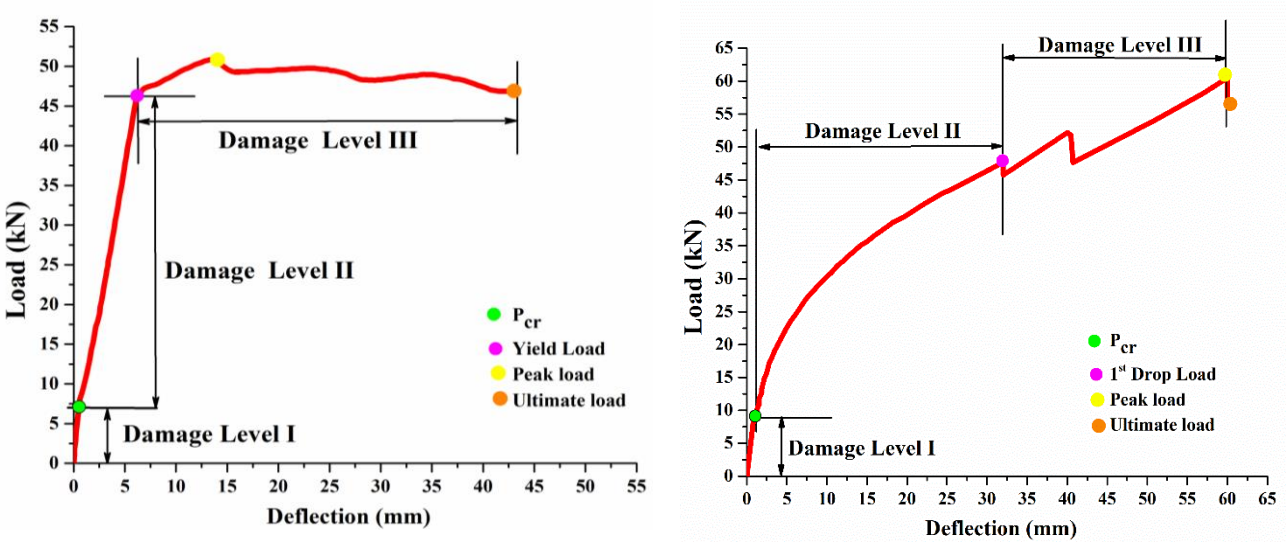

Fig. 5.9: Damage Level classification

S3 Beam **G3 Beam**

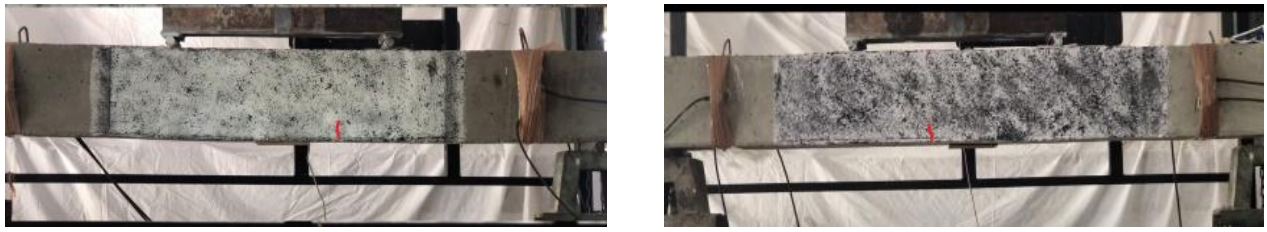

(a) **Damage Level I**

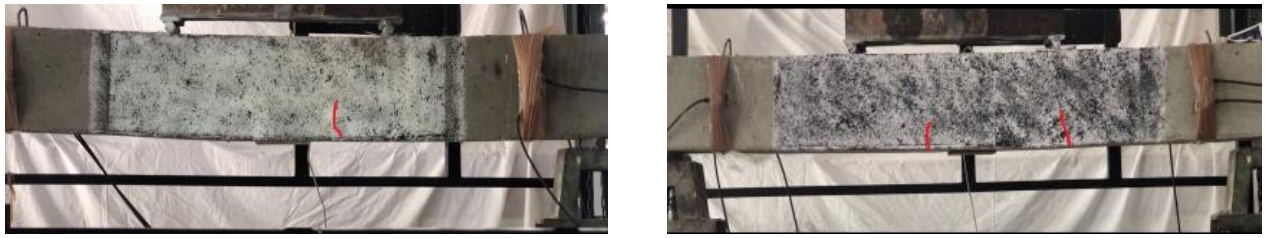

(b) **Damage Level II**

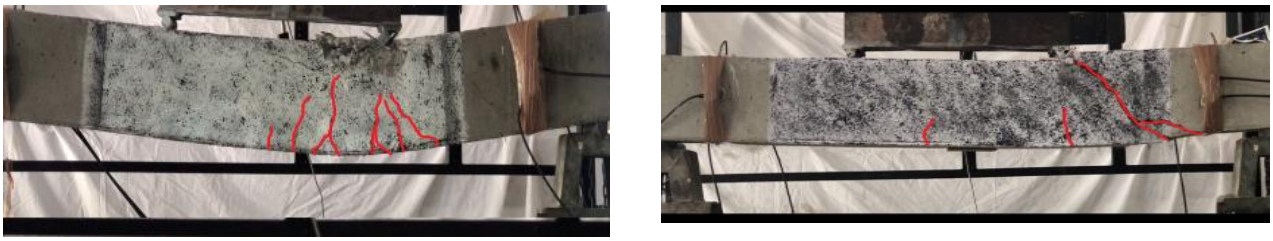

(c) **Damage Level III**

Fig. 5.10: Typical crack patterns

S3 Beam **G3 Beam**

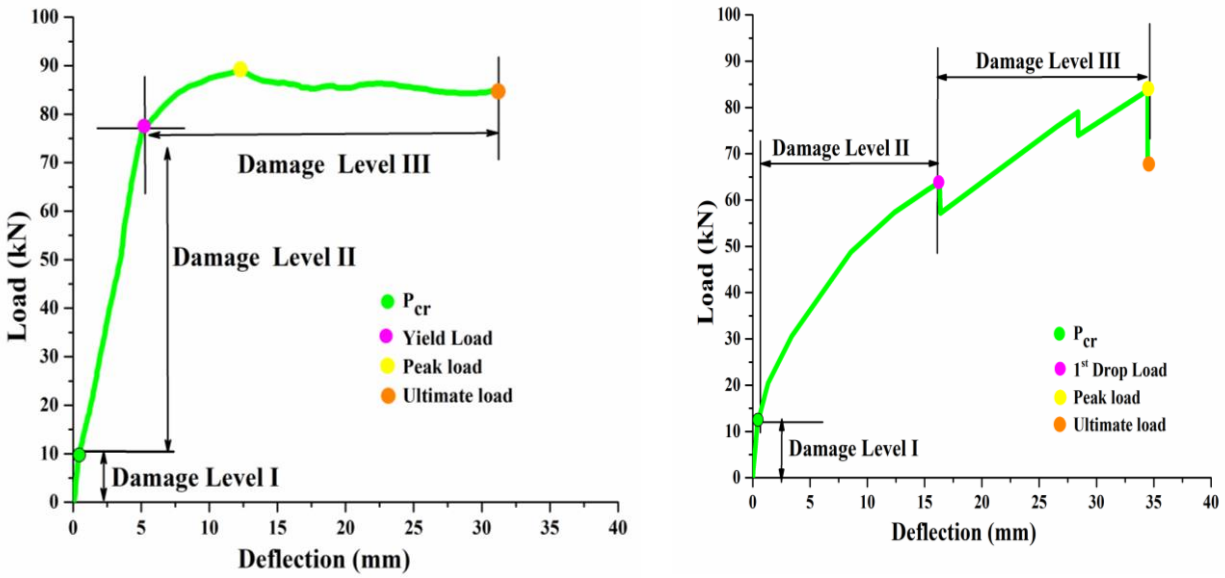

Fig. 5.11: Damage Level classification

5.3.3 Mid-Span deflections

The term deflection is used in structural engineering to describe the displacement of a body from its original position due to a force, load, or weight applied by the body itself. The effect of mid-span deflection with the same concrete strength is intrinsically related to the longitudinal tension reinforcement ratio (ρ). The mid-span deflection in both steel and GFRP RC beams decreases when the longitudinal tension reinforcement ratio (ρ) varies from 0.33 percent to 0.52 percent to 1.1 percent. For instance in the case of steel RC beams, increasing the longitudinal reinforcement ratio changes from 0.33%, 0.52%, and 1.1% decreases the mid-span deflection by 55.51 mm, 43.1 mm, and 30.9 mm. On the contrary, in the case of GFRP reinforced concrete beams decrease by 68.68 mm, 60.09 mm, and 34.43 mm. Hence the overall comparison of steel and GFRP reinforced beams under static flexural loading is widely different. GFRP RC beams exhibit higher deflections in comparison to steel reinforced beams at the same reinforcement ratios **(Fig. 5.12 and Table 5.1 and 5.2).** The deflections are 23.72%, 39.41%, and 11.32% higher in G1 G2 and G3 RC beams in comparison to S1, S2, and S3 RC beams. This is because Glass FRP bars have a low elastic modulus than steel bars.

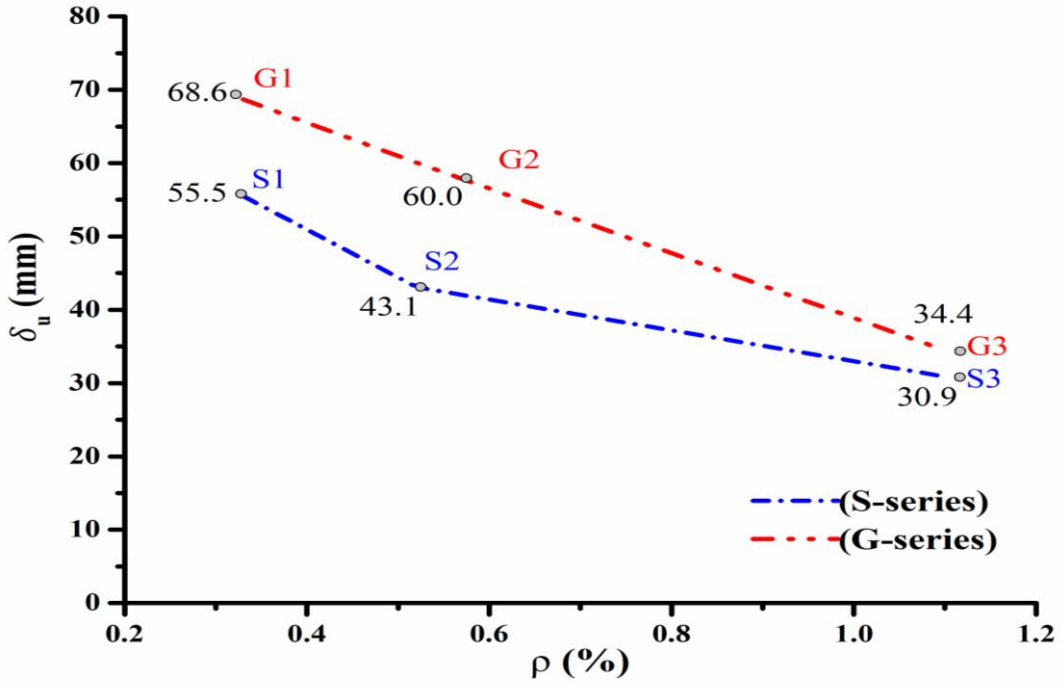

Fig. 5.12: Maximum mid-span deflection Vs 'ρ'

5.3.4 Moment Carrying Capacities

The experimental moment carrying capacity is the maximum bending moment that can be resisted by a beam or any other structural member before it fails in bending. The effect of experimental moment carrying capacities with the same concrete strength is essentially related to the longitudinal tension reinforcement ratio (ρ). As the longitudinal reinforcement ratio changes from 0.33%, 0.52%, and 1.1% the experimental moment carrying capacity increases in both steel and well as GFRP reinforced concrete beams **(Sharma et al., 2021).** For example in the case of steel-reinforced concrete beams, increasing the longitudinal tension reinforcement ratio (ρ) changes from 0.33%, 0.52%, and 1.1% increases the experimental moment carrying capacity by 11.73 kN-m, 16.82 kN-m, and 29.66 kN-m. On the contrary, in the case of GFRP reinforced concrete beams increases by 16.32 kN-m 20.16 kN-m, and 27.61 kN-m as shown in **Fig. 5.13 and Table 5.3.**

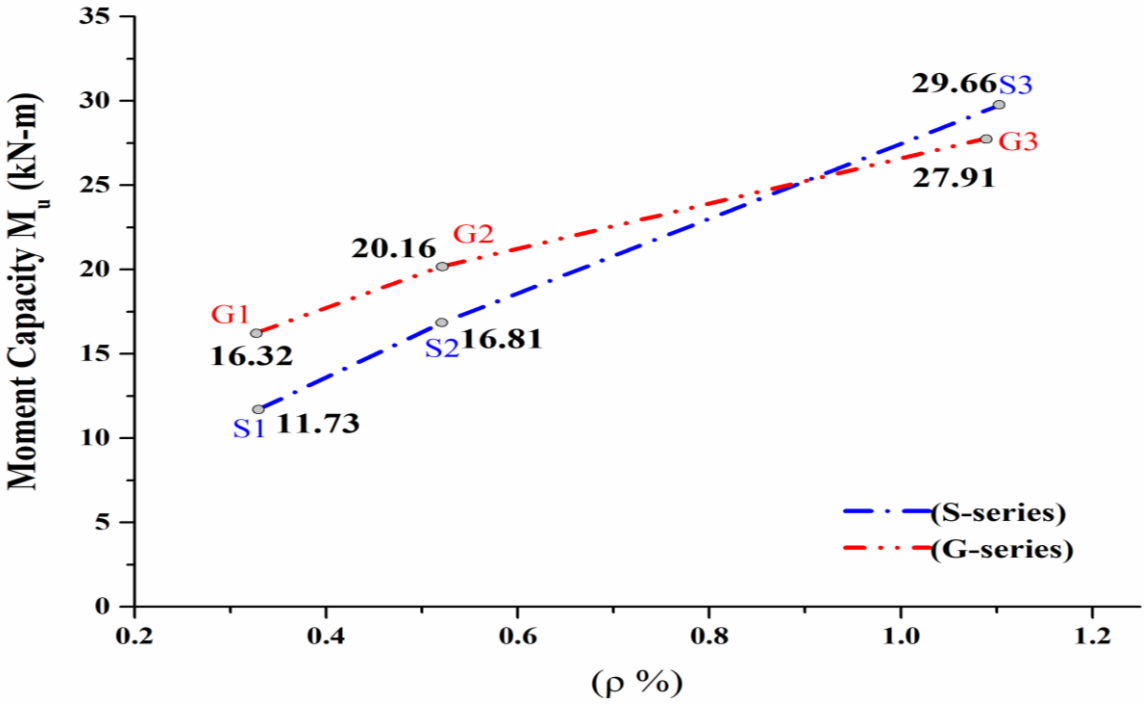

Fig. 5.13: Variation in an experimental moment carrying capacities

Overall, it's worth noting that as the longitudinal reinforcement ratio increases, so does the ultimate load-carrying capacity by 34% in G1 and 42 % in G2 beams in comparison to S1 and S2 (approximately). It's pointing towards higher tensile strength of Glass FRP bars in comparison to steel bars. However, as the reinforcement's ratio increases from 0.52 % to 1.1 % there is a slightly 5.09% decrease in load-carrying capacity in the G3 beam as compared to the S3 beam due to increase brittleness with higher ρ. It indicates that Glass FRP bars have a

lower modulus of elasticity than steel bars. Comparison of theoretical and experimental moment carrying capacities of steel & GFRP beams are presented in **Table 4.3.** The theoretical moment of resistance (M_{th}) in the case of the GFRP-RC beam is calculated by Equation (5.1) **(ACI 2015).**

$$M_{th} = \rho_f f_f \left[1 - 0.59 \rho_f \frac{f_f}{f'_c} \right] bd^2 \quad (5.1)$$

On the other hand, the theoretical moment of resistance (M_{th}) in case of the steel-RC beam is calculated by the formula given in Equation (5.2) **(ACI 2019)**

$$M_{th} = \rho_f f_y \left[1 - 0.59 \rho_f \frac{f_y}{f'_c} \right] bd^2 \quad (5.2)$$

where M_{th} = theortical bending moment resistance, ρ_f = reinforcement ratio, b= width of the beam, d= effective depth of the beam, f'_c = Design characteristic concrete compressive strength, f_f = stress in the FRP reinforcement and f_y = tensile strength of steel reinforcement.

The ratio of M_{th}/M_{exp} is less than 1 for both steel-reinforced as well as GFRP reinforced beams. Thus, for design determinations, the strength reduction factor (Ø) for over reinforced GFRP reinforced beams is calculated by equation (5.3) as given in (**ACI 2015):**

$$\emptyset = 0.65 \text{ for } \rho_f \geq 1.4 \rho_{fb} \quad (5.3)$$

Where ρ_{fb} = balanced reinforcement ratio, ρ_f = actual reinforcement ratio, and On the other hand, for the under-reinforced steel-reinforced RC beams, the strength reduction factor is taken as 0.9 (**ACI 2019).**

Table 5.3: Moment capacities of steel and GFRP reinforced beams

Beam	**M_{exp} (kN-m)**		**M_{th} (kN-m)**		**M_{th}/M_{exp}**		**E (Joules)**	
	S	**G**	**S**	**G**	**S**	**G**	**S**	**G**
0.33%	11.73	16.32	7.83	15.33	0.66	0.93	1753.01	2308.66
0.52%	16.81	20.16	12.63	18.92	0.75	0.93	1895.34	2561.17
1.11%	29.66	27.91	23.95	24.83	0.80	0.88	2383.33	2019.41

5.3.5 Energy absorption capacity

Energy absorption capacity is also known as toughness is a term used to describe the region under a flexural load-deflection curve. Another important significant variation is the Total Energy Absorption Capacities (E) of steel RC & GFRP RC beams divided into E_1 and E_2 **(Fig. 5.14 and Table 5.3).** For steel reinforced beams, E_1 is the area under the load-deflection curve up to Cracked-Elastic Zone II and E_2 is the area under the load-deflection curve in Plastic Zone III.

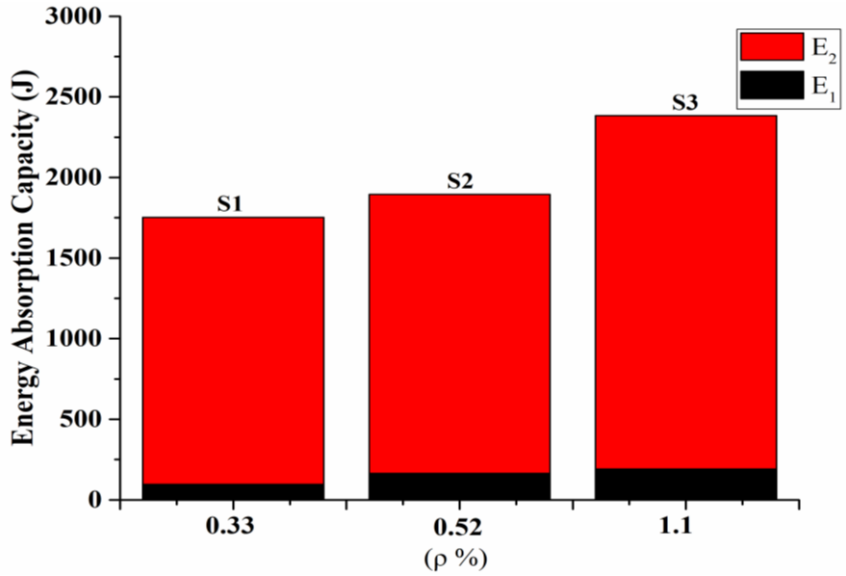

Fig. 5.14: Energy absorption capacity of steel RC beams

On the other hand, in the case of G-series beams, it is also evaluated as the area under the load-deflection curve reported as E_1&E_2 **(Fig. 5.15 and Table 5.3).** E_1 is the area under the load-deflection curve up to Cracked-Elastic Zone II and E_2 is the area under the load-deflection curve after the first load drop i.e. concrete crushing zone III. All the G-series beams continue to resist load after cracking and display 'Reserve post-cracking strength' or ductility E_2 up to collapse. With the increase in the reinforcement's ratio, the reserve strength or ductility reduces. It is because the increase in reinforcement's ratio leads to lower deflection with a higher load carrying capacities leading to the overall reduction in the area under the load-deflection curve. Steel reinforced beams exhibit very low E_1 values in comparison to G series. A drop of E1 values of 90.58%, 88.93%, and 86.34% is observed in S1, S2, and S3 in comparison to G1 G2 and G3 RC beams as shown in **Fig. 5.15.** It points towards larger large cracked area in GFRP reinforced beams. On the other hand, E_2 values in GFRP reinforced beams depicting post-cracking behavior are 29.14%, 60.74%, and 252% lower in G1 G2 and

G3 RC beams as compared to S1, S2, and S3 RC beams as presented in **Fig. 5.15.** GFRP RC beams experience bi-linear conduct up-to-the-final collapse without showing any significant yielding like steel causing larger E_2 values in steel-reinforced beams.

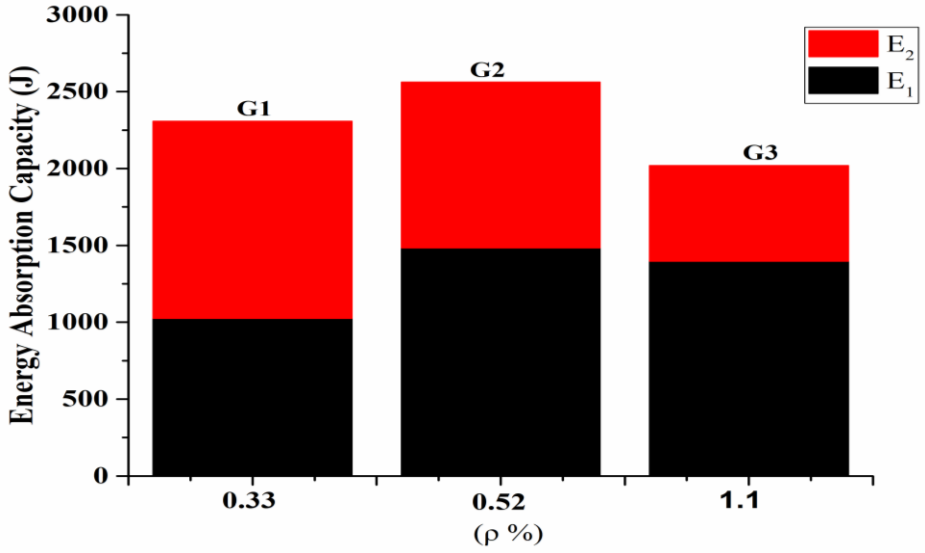

Fig. 5.15: Energy absorption capacity of GFRP RC beams

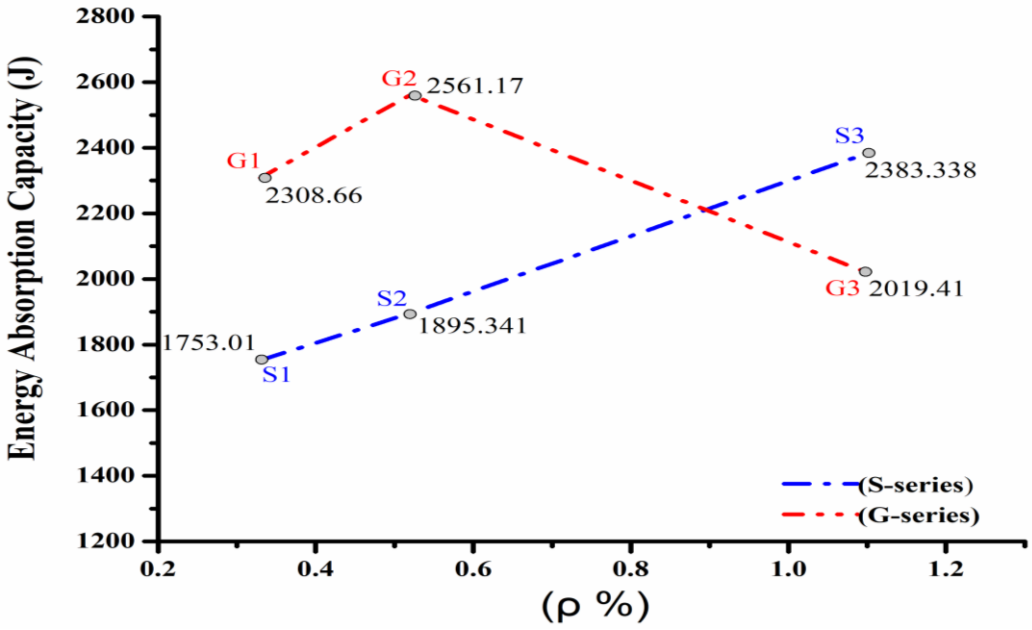

Fig. 5.16: Total energy absorption capacities Vs 'ρ'

The overall comparison of energy absorption capacities of the two types of beams is shown in Fig. 5.16. In general GFRP reinforced beams exhibits 31.69% and 35.12% higher resilience in comparison to steel reinforced beams at ρ= 0.33% and ρ = 0.52%. But at ρ=1.1%

a drop of 15.27% resilience is observed in the G3 RC beam as compared to the S3 RC beam due to reduced ductility at a larger reinforcement ratio in GFRP reinforced beams as presented in **Fig 5.16.**

5.3.6 Pre- and Post-cracking bending stiffness

As shown in **Table 5.4,** all steel and GFRP reinforced beams have a typical pre- and post-cracking bending stiffness. Initially, all of the beams showed high pre-cracking bending stiffness (E_cI_g), which ranged from 1299.14 kNm^2 to 3150.89 kN-m^2 in steel RC beams and to comparatively lower values from 817.91 kNm^2 to 4158.68 kN-m^2 in GFRP RC beams. The post-cracking stiffness (E_cI_e) reduces in both steel RC & GFRP RC beams in comparison to pre-cracking stiffness. However, increasing the reinforcement ratio increases post-cracking bending stiffness in both steel & GFRP reinforced beams **(Fig. 5.17).**

Table 5.4: Pre and post-cracking bending stiffness

Reinforcement ratio	Pre-Cracking Bending Stiffness (E_cI_g) (kNm^2)		Post-Cracking Bending (E_cI_e) (kNm^2)	
	S	G	S	G
0.33%	1299.14	817.91	655.29	146.09
0.52%	1796.57	1262.41	915.98	202.78
1.11%	3150.89	4158.68	2158.78	496.07

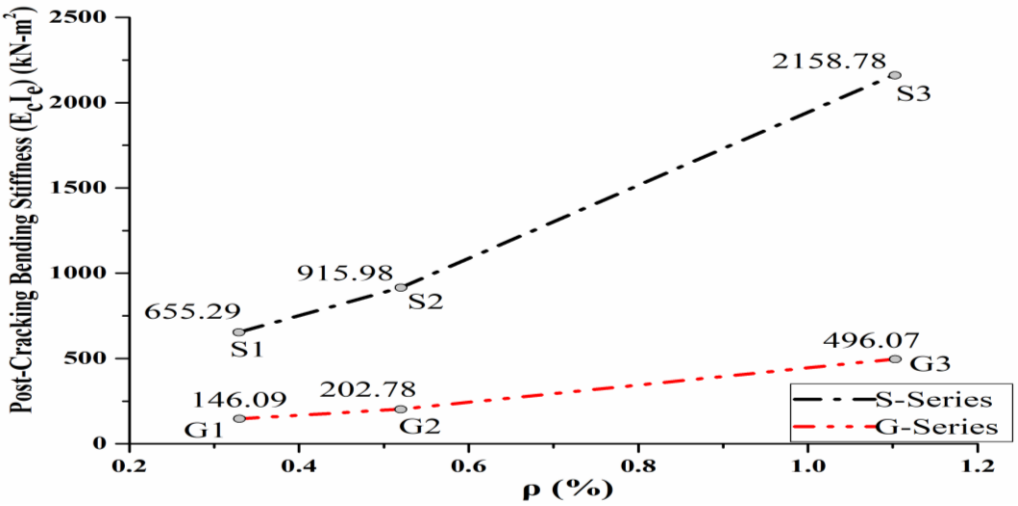

Fig. 5.17: Post cracking bending stiffness Vs 'ρ'

For steel reinforced beams, the pre cracking bending stiffness was estimated up to the yield load, and for GFRP reinforced beams, up to the first drop. Post cracking bending stiffness in G1, G2, and G3 RC beams is 77.70%, 77.86%, and 77.02% lower as compared to S1, S2, and S3 RC beams. This is because GFRP bars have a low elasticity modulus than steel bars. As a result, GFRP RC beams are preferably designed as over-reinforced to avoid failure by the sudden rupture of GFRP bars which can be catastrophic. They're made to fail by concrete crushing, or brittle failure, which is preferable for GFRP reinforced members. To compensate for the lack of ductility in GFRP beams, a higher margin of safety in design is advised in comparison to steel reinforced beams.

5.4 MODES OF FAILURE

The design of both steel & GFRP concrete beams is based on **ACI (2019) & ACI (2015).** The GFRP RC beams were designed as over-reinforced beams with reinforcement's ratio of (0.0033, 0.0052, and 0.0111) (**ACI 2015)** which was greater than the balanced reinforcement ratio of 0.00308. The steel RC beams were designed as under-reinforced beams

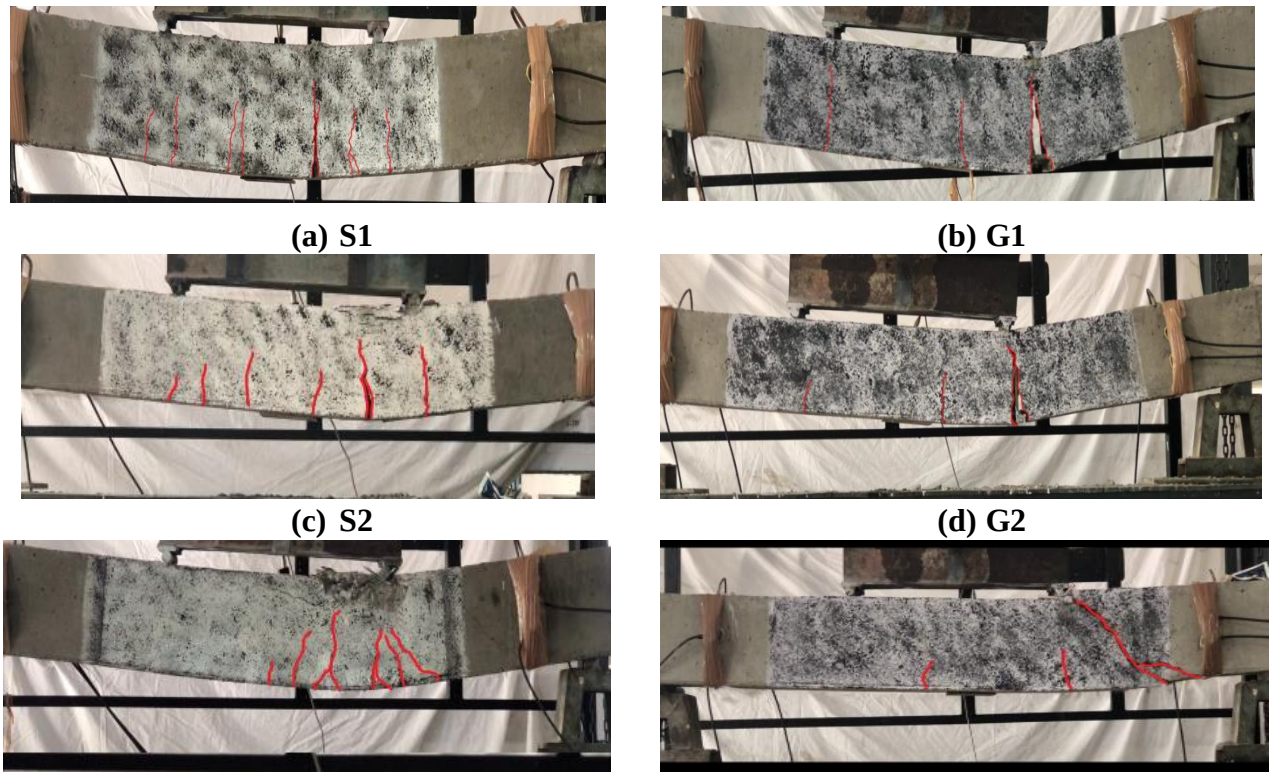

(a) S1 **(b) G1**

(c) S2 **(d) G2**

(e) S3 **(f) G3**

Fig. 5.18: Failure modes in Steel and GFRP-RC beams

having a reinforcement ratio (0.0033, 0.0052, and 0.0111) less than the balanced reinforcement ratio of 0.02 **(ACI 2019).** During flexural testing, compression failure along with concrete

crushing for the GFRP-RC beams and tension failure along with concrete crushing for the steel beams were expected. The failure modes of steel RC & GFRP RC beams are shown in **Fig. 5.18.** Steel-RC beam failed by the crushing of concrete after the tension reinforcement yielded as shown in **Figs. 5.18 (a), (c), and (e)** whereas the GFRP-RC beam failed typically in shear followed by concrete crushing as shown in **Figs. 5.18 (b), (d), and (f), s**ince they are designed as over-reinforced beams to prevent their failure by GFRP rupture. This indicates that even though both Steel-RC and GFRP-RC beams have the same area of tension reinforcement (A_{st}) ratio, GFRP-RC beams experience a different mode of failure as compared to the steel-reinforced concrete beam.

5.5 CLOSING REMARKS

The flexural response of steel reinforced & GFRP reinforced concrete beams under 4-point loading along with the varying percentage of tension reinforcement (~0.33%, ~0.52%, and ~1.11%) is discussed. Moreover, failure modes in steel reinforced and GFRP reinforced concrete beams are also discussed in chapter. The load-deflection plot of steel & GFRP reinforced beams show contrasting profiles. The experimental results shows that as the percentage of reinforcement ratio increases, the performance parameters such as the load carrying capacity, moment carrying capacity, energy absorption capacity, pre and post cracking bending stiffness also increases.

CHAPTER 6

DAMAGE MONITORING USING AE AND DIC

6.0 GENERAL

In this chapter, the damage monitoring in steel RC & GFRP RC beams is studied by comparing the deformation and crack pattern during flexural loading with AE parameters to relate to the initiation and progression of damage. Various AE waveform parameters like cumulative AE hits, AE amplitudes, Average Frequency (kHz), and signal duration (μs), and Rise Angle (RA) are investigated. Additionally, AE-XY plots are compared to longitudinal strain profiles generated by Digital Image Correlation (DIC) to provide a real-time depiction of increasing AE activity and surface strains. The AE approach explains the onset and progression of a cracking pattern and failure mechanism in beams whereas the DIC method is utilised to visualise the displacement and strain fields while emphasising discontinuities in the field of displacement.

The goal of the research is to create an in-situ, non-invasive health monitoring approach for RC beams with steel or GFRP bars that can offer a real-time pre-emptive warning and prevent catastrophic failures. Flexural results for all samples (steel & GFRP RC beam) are shown in **Fig. 5.1 and 5.3** and the results were found to be within reasonable repeatable limits. AE and DIC plots were also generated for all three test sets, but only one such set is presented considering the similarity and avoiding duplications.

6.1 ACOUSTIC EMISSION (AE) MONITORING

As already outlined, during the flexural loading of steel & GFRP RC beams, the initiation and progression of damage were also picked up by AE sensors mounted on these steel RC & GFRP RC beams. Various AE waveform parameters of cumulative AE hits and their corresponding amplitudes, average frequency, signal duration, and rise angle are picked up and further analyzed. The detailed study and analysis of results of various AE waveform parameters are detailed below in the next section.

6.1.1 Cumulative AE Hits & Amplitude

Variations of the cumulative AE hits and their corresponding amplitudes with time indicate the progression of damage in S-series and G-series beams right up till the failure of beams when subjected to a constant loading rate of 0.01 mm/sec. An increase in AE hits is

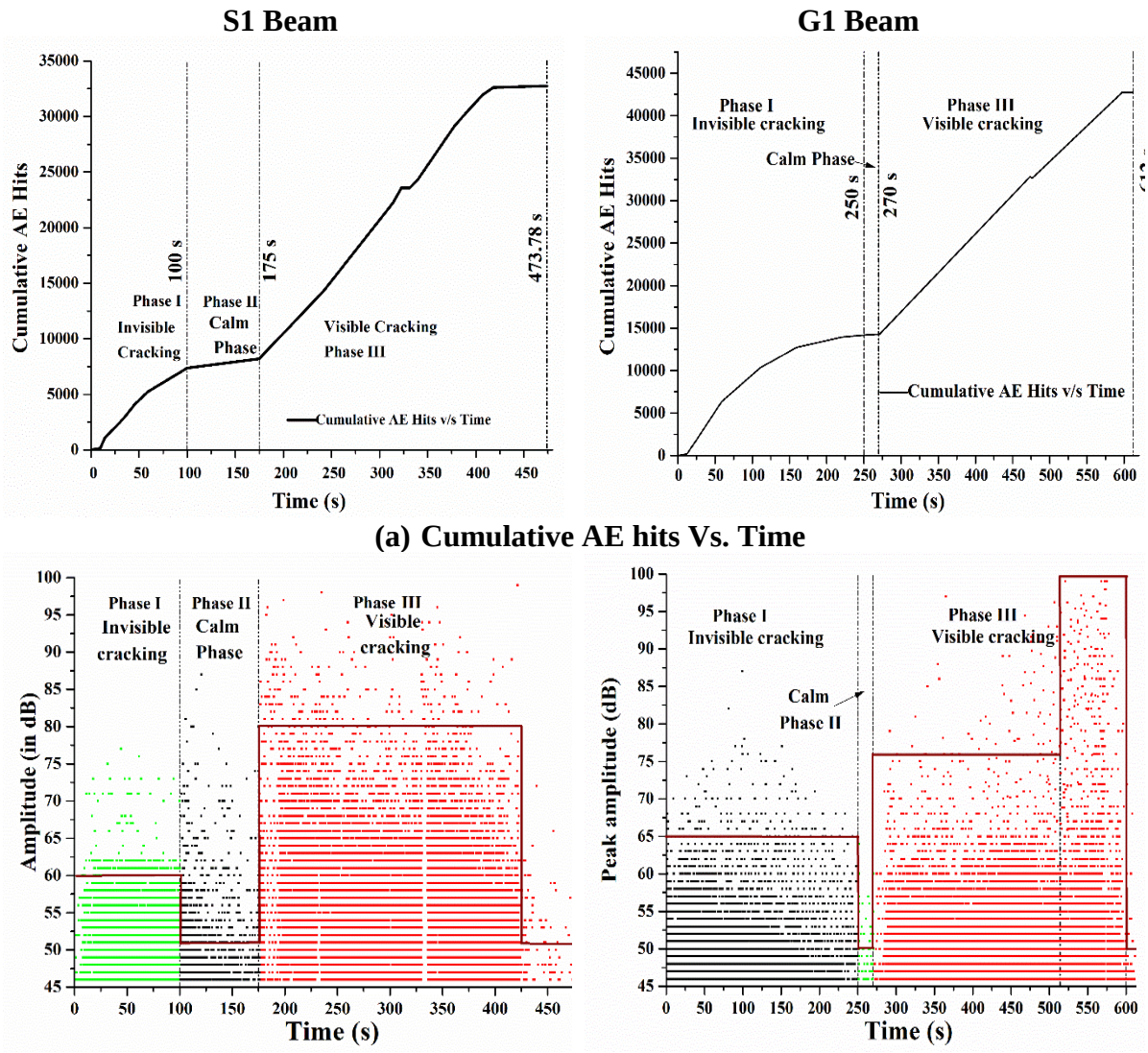

Fig. 6.1: AE Activity in S1 and G1 RC beams

observed in both the steel RC & GFRP RC beams, indicating the initiation of AE activity in the form of invisible cracking. This lasts till 100s, 125s, and 225s in S1, S2, and S3 RC beams and 250s, 300s, and 396s in G1, G2, and G3 RC beams respectively as shown in **Figs. 6.1(a), 6.2(a) and 6.3(a).** The amplitude of AE hits in this phase is about 55-60 dB, 61-64 dB, and 65-68 dB in S1, S2, and S3 RC beams and 60-65 dB, 63-67 dB, and 64-67 in G1, G2 and G3 RC beams as shown in **Figs. 6.1(b), 6.2(b), and 6.3(b).** This phase is called **"Invisible Cracking"** and is very much prolonged in GFRP RC beam due to the longitudinal high tensile strength of Glass FRP bars as compared to steel bars. This phase I of AE activity corroborates well with the **"Cracked Elastic Stage II"** in the load-deflection curve. It's worth noting that no large surface cracks and only minor hairline cracks are seen on the surface of the beams during this phase. As a consequence, even when substantial effects are not visible on the surface, the graph

of cumulative AE strikes and their related amplitudes initially gives a good indicator of the beginning and evolution of cracking inside the concrete.

Furthermore, with a drop in average amplitude of hits to below 50dB, the cumulative AE hits remain constant in **"Calm Phase II"** of activity for about 75s, 100s, and 125s in the S1, S2, and S3 RC beams and about 20s, 30s and 76s in the G1, G2 and G3 RC beam. The linear elastic behavior of GFRP bars is primarily responsible for the calm phase reduction in the GFRP RC beam. This phase is a transition phase in which the invisible cracks coalesce to form visible cracks in **"Visible -Cracking Phase III"** for about 473.78s, 747.7s, and 878.78s for S1, S2, and S3 RC and 612s, 623.85s and 996.96s for G1, G2, and G3 RC beams.

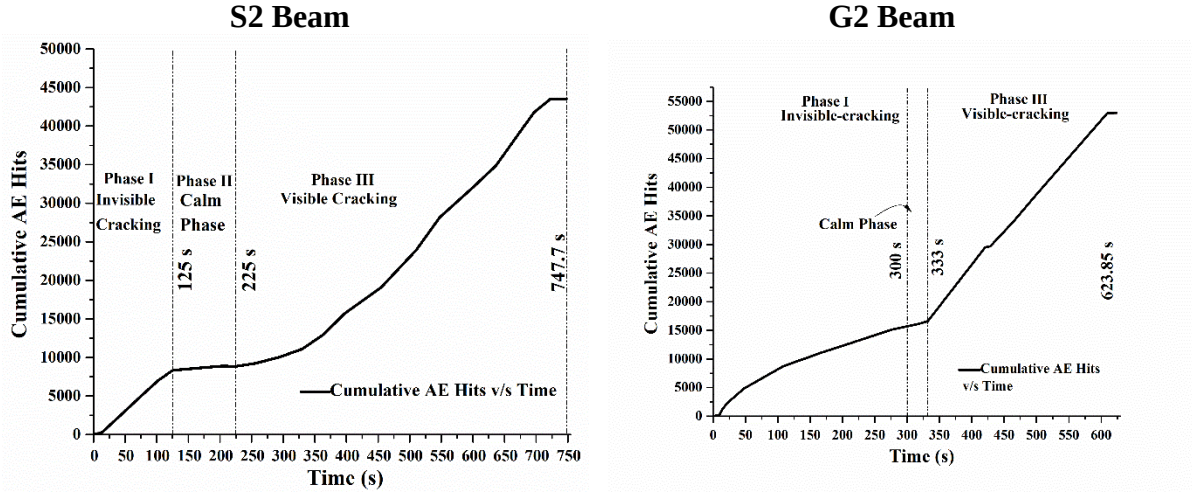

(a) Cumulative AE hits Vs. Time

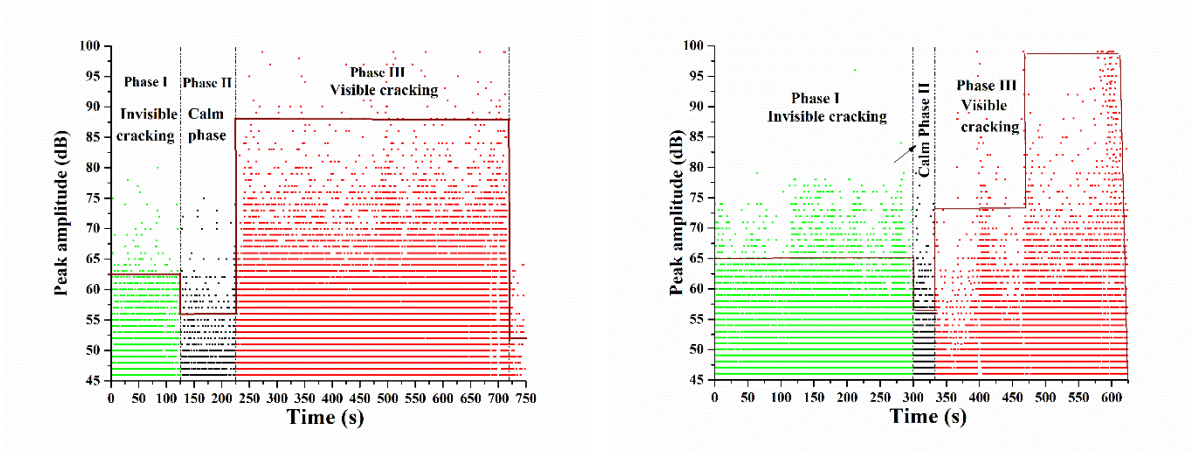

(b) Amplitude of AE hits

Fig. 6.2: AE Activity in S2 and G2 RC beams

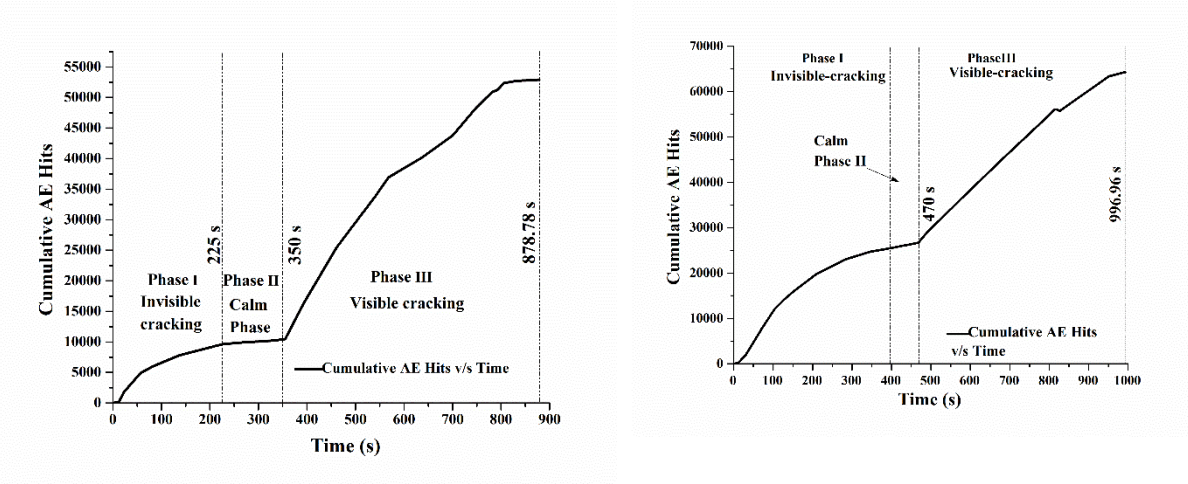

(a) Cumulative AE hits Vs. Time

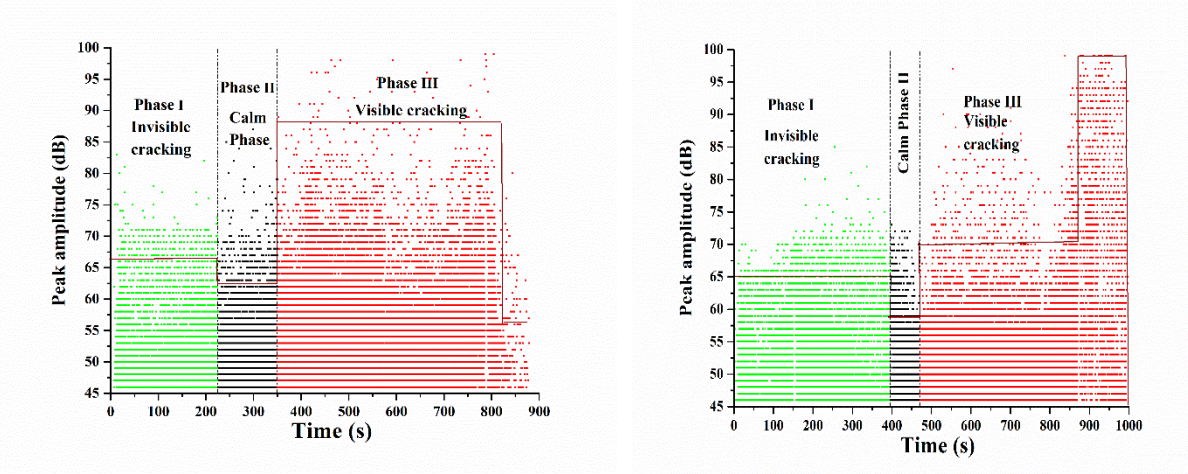

(b) Amplitude of AE hits

Fig. 6.3: AE Activity in S3 and G3 RC beams

On the other hand, a similarly steep rise in AE hits is observed in G1, G2, and G3 RC beams in Phase III with amplitude in the range of 70-75 dB which continues till the failure of the G-series RC beam towards the end of Phase III as shown in **Figs. 6.1, 6.2, and 6.3**. A notable finding is a significant and abrupt increase in high-amplitude AE hits in the range of 95-100dB in G1, G2, and G3 RC against the S1, S2, and S3 RC beam is observed followed by its sudden failure. It is well corroborated by the shear dominant failure of the G-series RC beam followed by concrete crushing as shown in **Figs. 5.18 (b), (d) and (f) respectively.**

During this phase, a sharp rise in cumulative AE hits of higher amplitudes between 80-90 dB, 85-90 dB, and 85-90 dB is observed in S1, S2, and S3 RC beams pointing toward major AE activity leading to visible cracking in the s-series beam. It is well supported by the appearance of profuse flexural and shear cracks appearing in the steel RC beam during flexural testing. Finally, in the steel RC beam no further significant increase in cumulative AE hits is

observed with the average amplitude of AE hits as 45-50dB pointing towards attenuation of AE signals by already cracked S-series RC beam. It is in coherence with the plastic stage of the steel RC beam pointing towards the failure of the steel RC beam initiated by steel yielding and followed by concrete crushing **Figs. 5.18 (a), (c) and (e) respectively.**

At the same reinforcement ratio, it is observed that damage under flexural loading in steel RC beam progresses from slow initiation in the form of invisible cracking of low amplitudes to visible cracking of larger amplitude due to steel yielding. On the contrary, in the case of GFRP RC beams, the AE activity is mostly consisting of invisible and visible cracks of larger amplitudes. GFRP reinforced beams experience much wider and well-distributed cracks as compared to steel reinforced beams throughout the progress of loading as confirmed visually **(Ascione, Mancusi, & Spadea, 2010).** It's presumably because GFRP bars have a low elasticity modulus and a higher tensile strength than steel-reinforced bars which consequently results in a steep rise in AE activity of very higher amplitudes towards the failure, pointing towards sudden cracking and failure of the GFRP RC beam. As a result, AE hits and their amplitudes are key indicators of failure and cracking development in both steel & GFRP RC beams.

6.1.2 Average Frequency (AF) and Rise Angle (RA)

Using moving averages and over 100 AE hits, a parametric comparison was done between AF and RA values **(Ohno & Ohtsu, 2010 and Prem & Murthy, 2017).** The proportions of AF and RA values are also set to 1:200 in this scenario. The plot of Average Frequency (AF) and Rise Angle (RA) values for all three damage levels, for S-series and G-series RC beams, is shown in **Figs. 6.4, 6.5, and 6.6** respectively. AF-RA value plot gives a fair indication of the cracking modes in steel & GFRP reinforced concrete beams and is used for crack classification. The diagonal line is utilized as a crack classification reference line because it indicates the transition between tensile and shear cracks.

In **Damage Level I**, the plot of AF-RA for the S1, S2, and S3 RC beam **(Figs. 6.4(a), 6.5 (a) and 6.6(a).** shows the development of cracks initially due to tensile cracking whereas for the G1, G2, and G3 RC beam it is in shear cracking mode **(Figs. 6.4(a), 6.5(a) and 6.6(a).** A high average AF value of 32.2 kHz, 53.73 kHz, and 50.64 kHz with a lower RA value of 579.9 μs, 398.78 μs, and 205.0 μs values were noticed in the S1, S2, and S3 RC beam as against lower average AF value of 15.0 kHz, 16.20 kHz and 26.73 kHz and a higher RA value of 6432.5 μs, 7324.80 μs, and 10752.52 μs for the G1, G2 and G3 RC beam (Tables 5.2, 5.3 and

5.4) respectively. These values indicate that the steel RC beams can resist and bridge the cracks better owing to the perfect bond between concrete and steel and the high modulus of elasticity of steel bars as compared to GFRP reinforced concrete beams. At this damage level, the hairline cracks were clearly visible in both beams.

With the increasing load in **Damage Level II**, invisible cracking is observed in the steel RC beam at higher AF and smaller RA value indicating tensile cracking mode whereas, in the case of the GFRP-RC beam, a reversed trend is observed with a slight increase in average AF value and drop in RA value pointing towards a shift from shear to tensile cracking in the GFRP-RC beam **Figs. 6.4(b), 6.5 (b) and 6.6(b).** Further in **Damage Level III,** a slight decrease in the average AF value of 37.3 kHz, 40.99 kHz, and 47.41 kHz with a minute increase in the RA value of 1327.0 μs, 1225.25 μs, and 454.92 μs value was noticed in the S1, S2, and S3 RC beam. A plausible explanation for this can be attributed to the reduction in the cross-sectional area due to the yielding of steel bars in the steel RC beam.

Table 6.1: Variation in RA and AF values in S1 and G1 beams

Damage Level	Rise Angle		Average Frequency	
	S1	G1	S1	G1
I	579.9	6432.5	32.2	15.0
II	427.9	5157.2	41.1	25.5
III	1327.0	3317.6	37.3	42.2

Table 6.2: Variation in RA and AF values in S2 and G2 beams

Damage Level	Rise Angle		Average Frequency	
	S2	G2	S2	G2
I	398.78	7324.8	53.73	16.20
II	315.21	5956.17	56.72	27.65
III	1225.257	5130.68	40.99	43.66

Table 6.3: Variation in RA and AF values in S3 and G3 beams

Damage Level	Rise Angle		Average Frequency	
	S3	G3	S3	G3
I	205	10752.52	50.64	26.73
II	238.79	7829.34	50.71	26.81
III	454.922	5255	47.41	39.4

S1 Beam **G1 Beam**

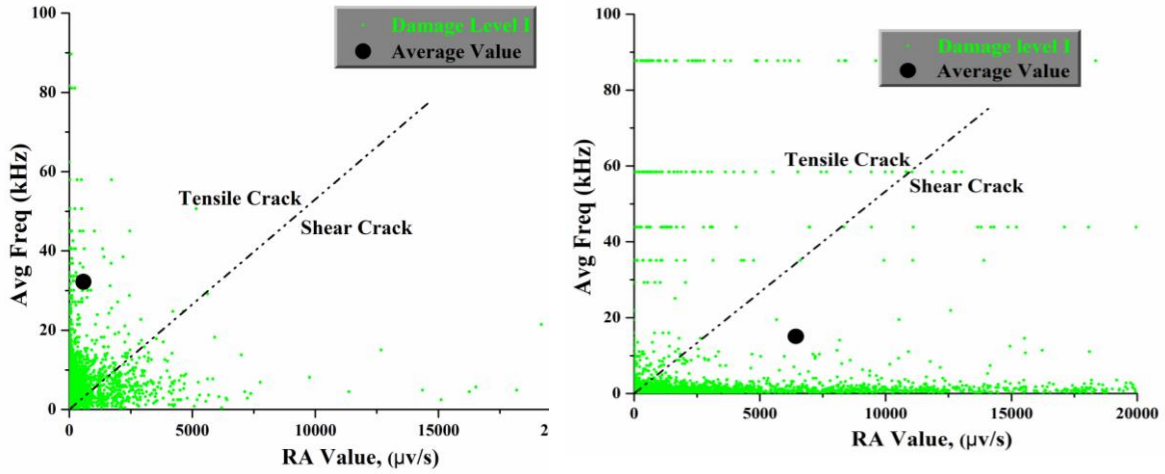

(a) Damage Level I

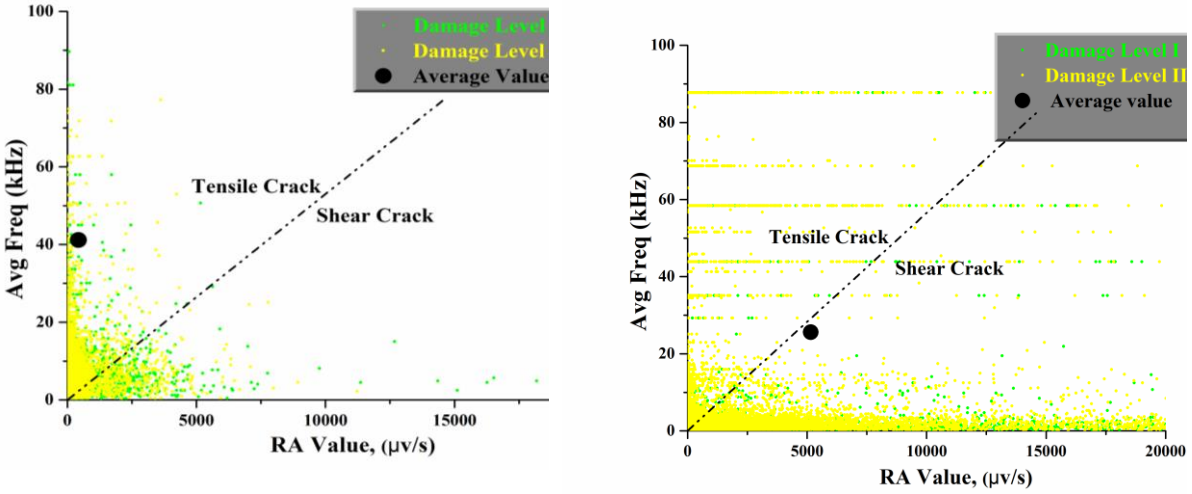

(b) Damage Level II

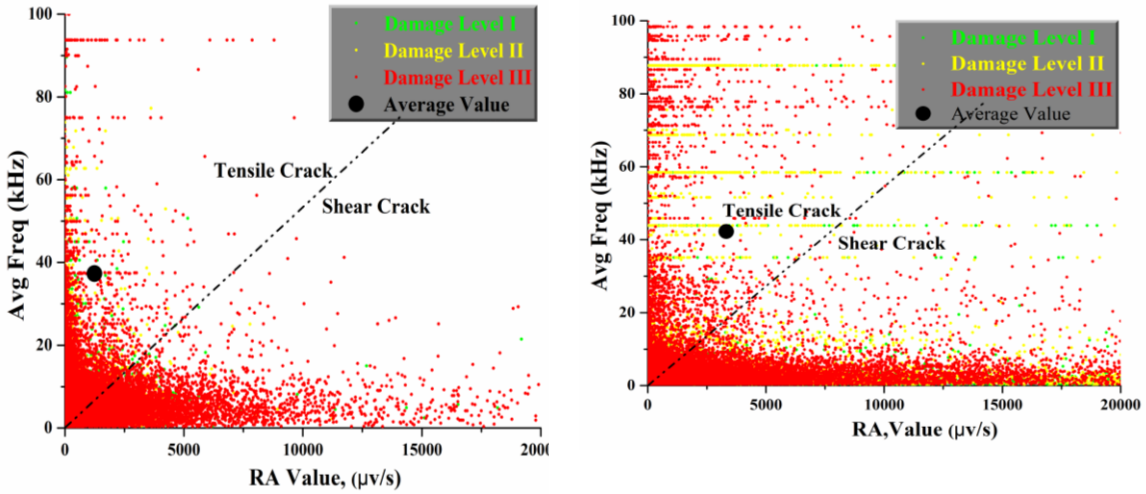

(c) Damage Level III

Fig. 6.4: Variation in AF Vs RA values at different levels of damages

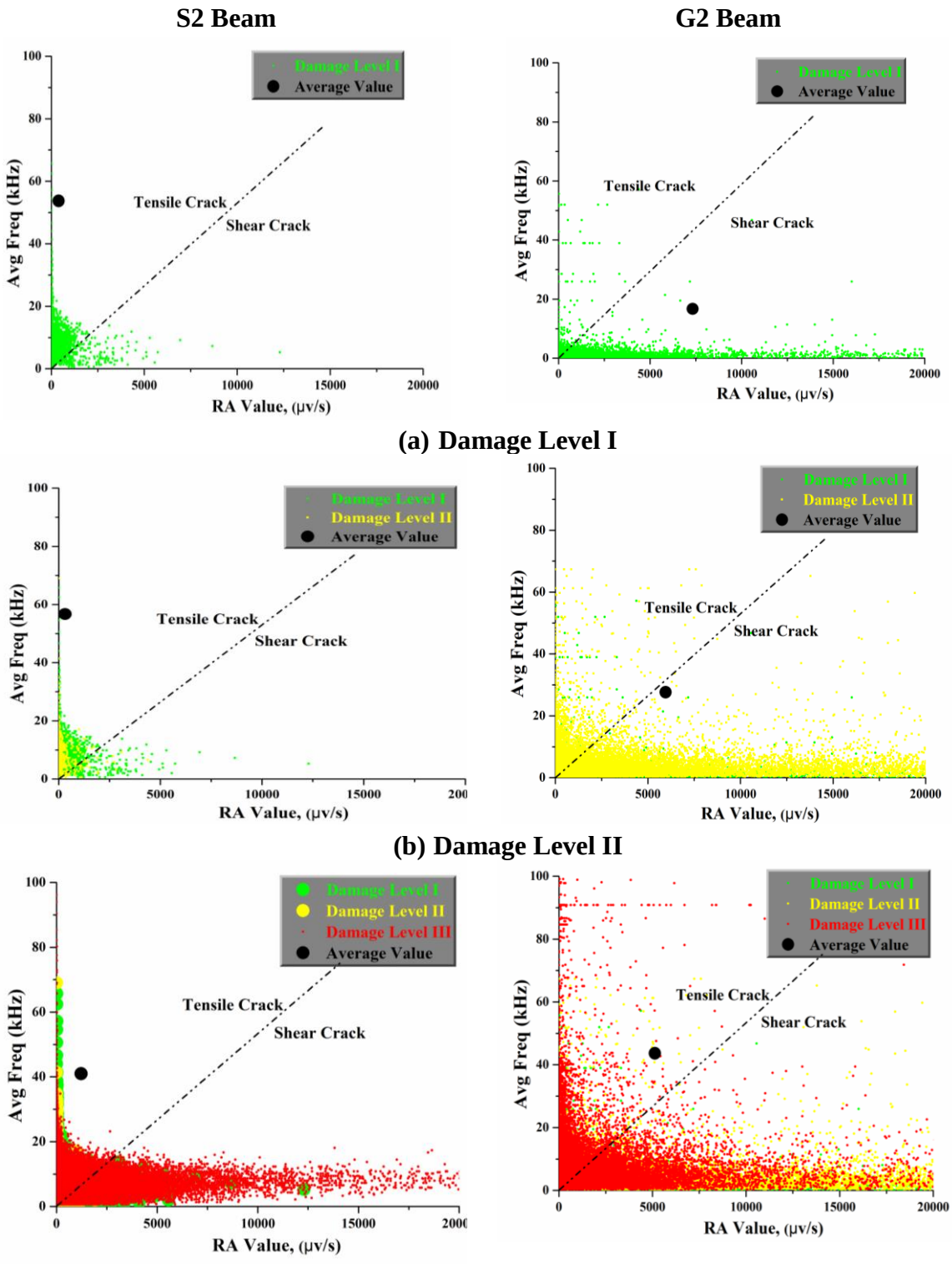

(a) Damage Level I

(b) Damage Level II

(c) Damage Level III

Fig. 6.5: Variation in AF Vs RA values at different levels of damages

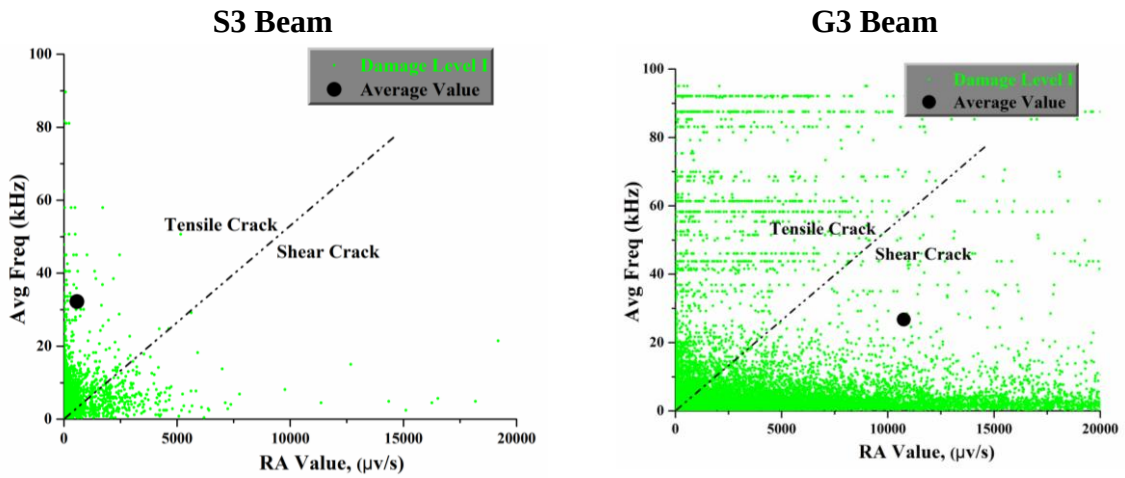

(a) Damage Level I

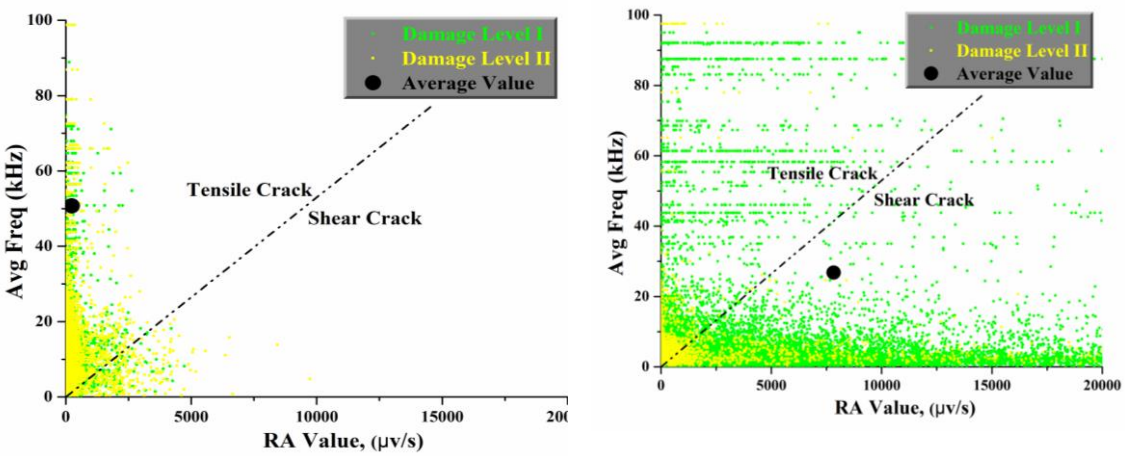

(b) Damage Level II

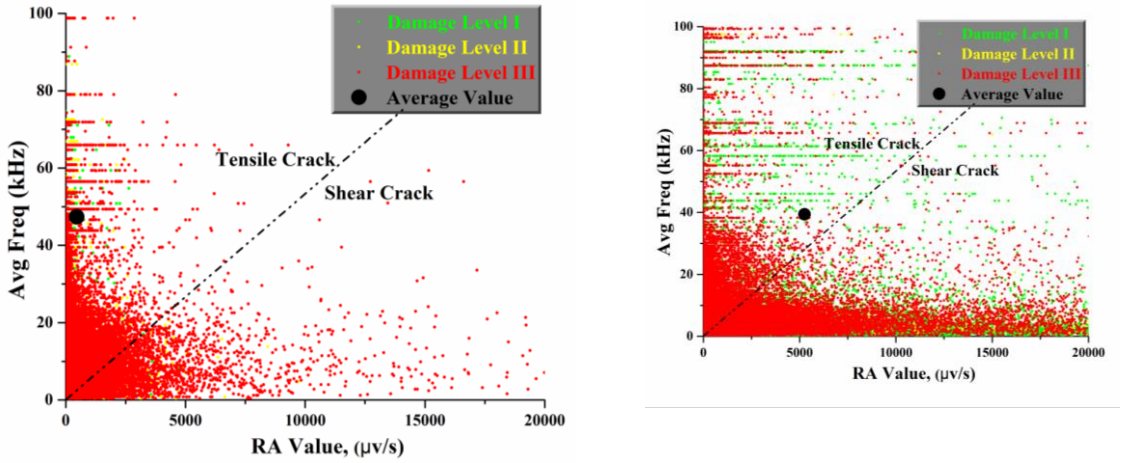

(c) Damage Level III

Fig. 6.6: Variation in AF Vs RA values at different levels of damages

On the contrary, a continuous increase in AF value of 42.2 kHz, 43.66 kHz and 39.40 kHz with a significantly lower RA value of 3317.6 μs, 5130.68 μs and 5255 μs was noticed in the GFRP-

RC beam (**Figs. 6.4(c), 6.5 (c) and 6.6(c).** AF-RA plots at the failure point suggest that the steel RC beam experiences flexural cracks localization, while the Glass FRP reinforced concrete beam experiences shear cracking as also observed visually as shown in **Figs. 6.2, 6.4, and 6.6.**

Hence, AF-RA plots can be exploited to predict the initiation and progression of invisible and visible crack formation in concrete as indicated by the density of dots in the plot of the AF-RA value. As a result, the AE plot of AF and RA value can effectively demonstrate the variation in initiation and progression of damage, classification of cracking and failure modes in steel as-well-as GFRP reinforced beams.

6.1.3 Average Frequency (AF) and Duration (μs)

Besides from cumulative AE hits and AF and RA value analyses, the average frequency (AF) and duration (μs) of AE hit over time might provide useful information. The moving average of the last 100 AE hits is represented by the solid line. While the data is well spread across various average frequency levels, the moving-average line depicts variations at various points in time, as indicated by the numbers in the graph.

For the steel RC beam **Figs. 6.7(a), 6.8(a), and 6.9(a)**, at point 1, AF drops by 40 kHz, 40 kHz, and 38 kHz, which coincides with the P_{peak} of 35.18 kN, 59.32kN, and 88.94 kN sustained by the S1, S2, and S3 RC beam. Further, there is another drop in AF of 35 kHz, 39 kHz, and 29 kHz at point 2 where a minor drop in load is also observed in S-series RC beams. Furthermore, with time as load increases, there is again another drop load in AF of 36 kHz, and 18 kHz were observed in S2 and S3 RC beams. These significant drops in AF values point towards significant AE activity in the form of a shift in the damage mechanisms which are the cause of the emissions. At the moments of load drop, the failure mechanism may be related to the de-bonding of the reinforcing bars from the surrounding concrete which leads to local cracking owing to stress redistribution **(Aggelis, Mpalaskas, & Matikas, 2013).**

On the other hand, AF drops are more significant, sharp, and illustrative as compared to the S-series beam and closely match with the load drops at 1, 2, 3, and 4 in the G-series beam (**Figs. 6.7(a), 6.8(a) and 6.9(a)**. A drop in a load of (2.4 kN and 3.99 kN) in G1, (2.9 kN and 5.1 kN) in G2 and (7.12 kN and 5.99 kN) is observed at points 1 and 2 in the AF curve with average frequency drops of (5 kHz and 20 kHz) in G1, (29.8 kHz and 30.1 kHz) in G2 and (40.19 kHz and 27.98 kHz) in G3 RC beams approximately. At point 3, a drop in AF of 45 kHz, 17 kHz, and 10 kHz is observed in G1, G2, and G3 RC beams, which coincides with the

P_{peak} load of 51.32 kN, 60.47 kN, and 83.71 kN. Finally, the G1 RC beam fails at a load of 48.94 kN at AF of 25 kHz at point 4.

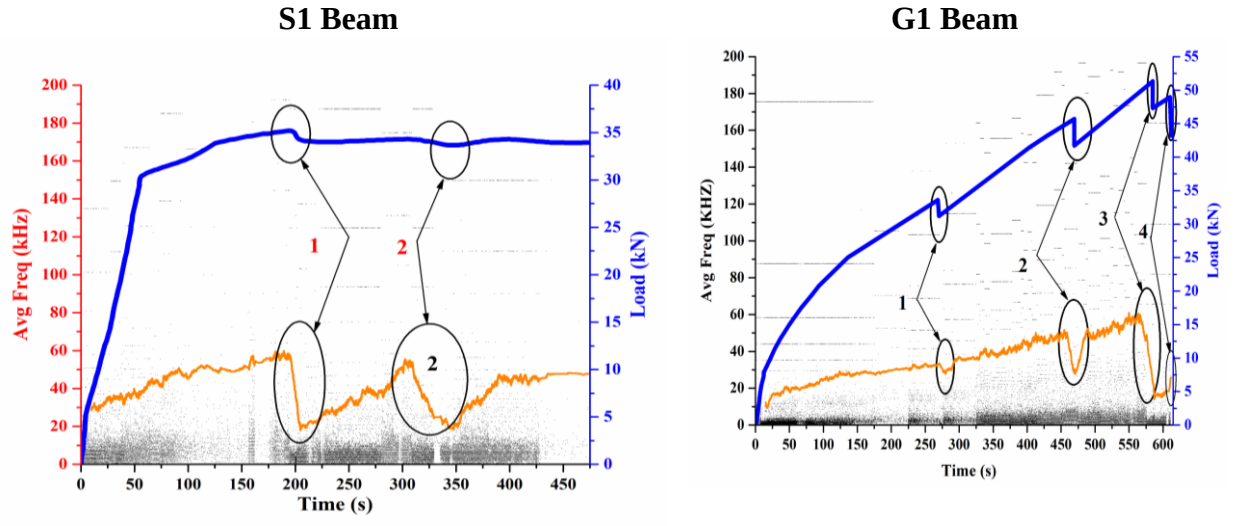

(a) Average frequency (AF)

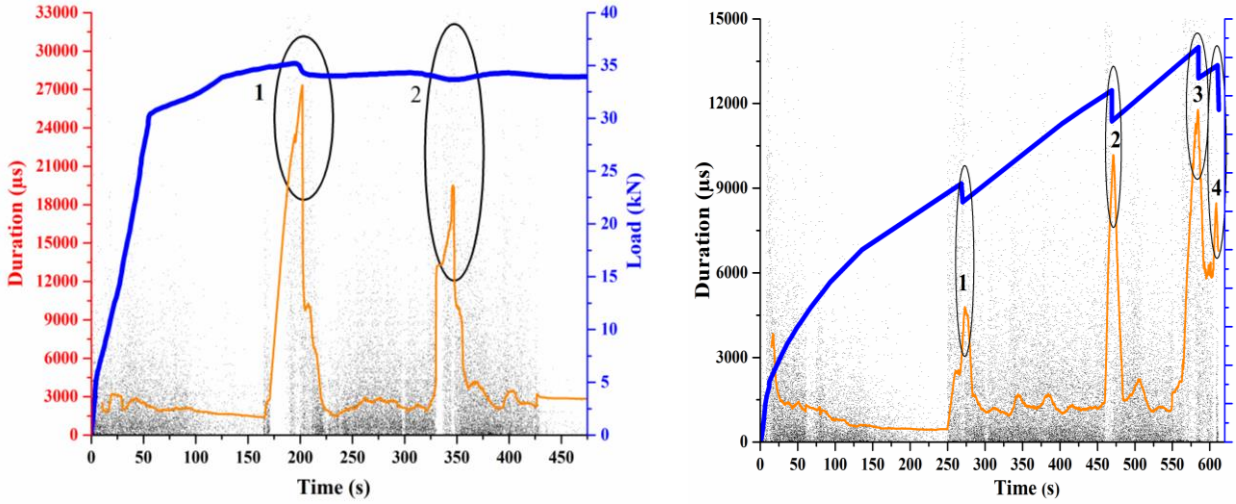

(b) Duration of AE signals

Fig. 6.7: Variation of AF and Duration of AE signals

It is important to note that at instants of loads and AF value drops, a corresponding significant jump in the duration of AE signals is observed and shown in **Fig. 6.7(b), 6.8(b), and 6.9(b)**. The fact that substantial variations are documented in the AE behavior evidenced the shift of the damage mechanisms, which are the source of the emissions. At the moments of load drop, the failure mechanism may be connected to the de-bonding of the reinforcing bars from the surrounding concrete which also leads to local cracking owing to stress redistribution **(Aggelis, Mpalaskas, & Matikas, 2013; Yan, Lin & Yang, 2016).** It is also observed that the moving average line of AF was high and the duration line was low in the GFRP RC beam in comparison to the steel RC beam. The reason for this is that GFRP bars have different bond

characteristics, have a lower elastic modulus, and deflect more than steel bars, causing AE activity to accumulate **(Yoo & Yoon, 2017)**. As a result, a drop in average frequency and significant jump AE duration at the same time indicate critical failure points in steel RC and GFRP RC beams. These changes are much more illustrative than those in load-deflection curves and can go a long way in developing real-time damage monitoring and evaluation tools for RC structures.

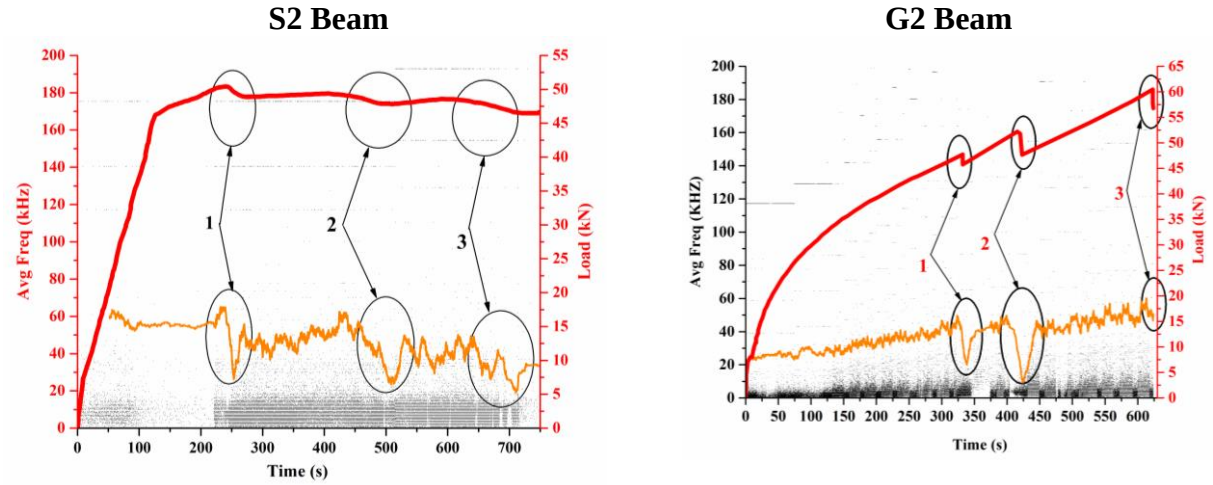

(a) Average frequency (AF)

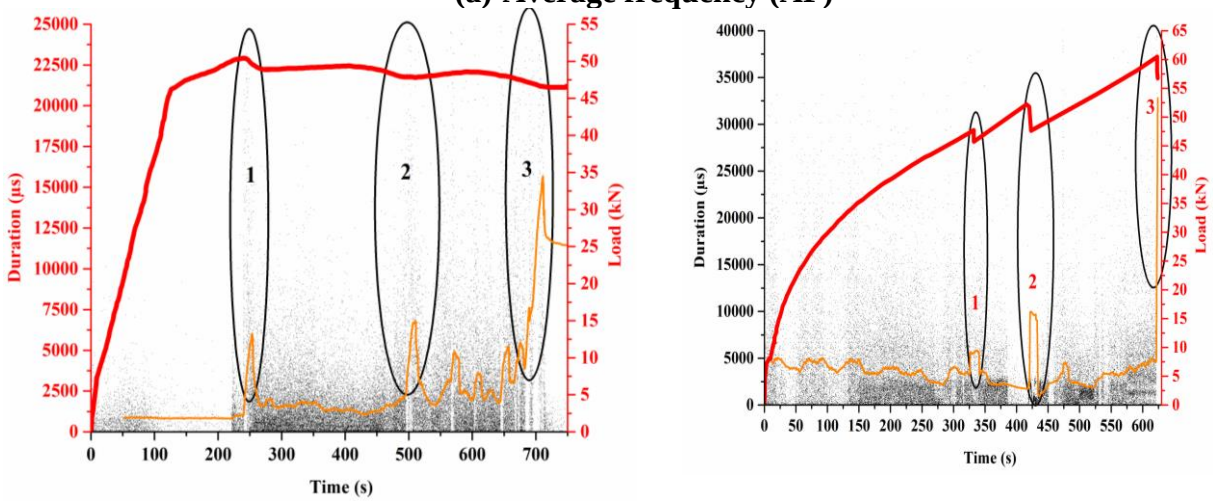

(b) Duration of AE signals

Fig. 6.8: Variation of AF and Duration of AE signals

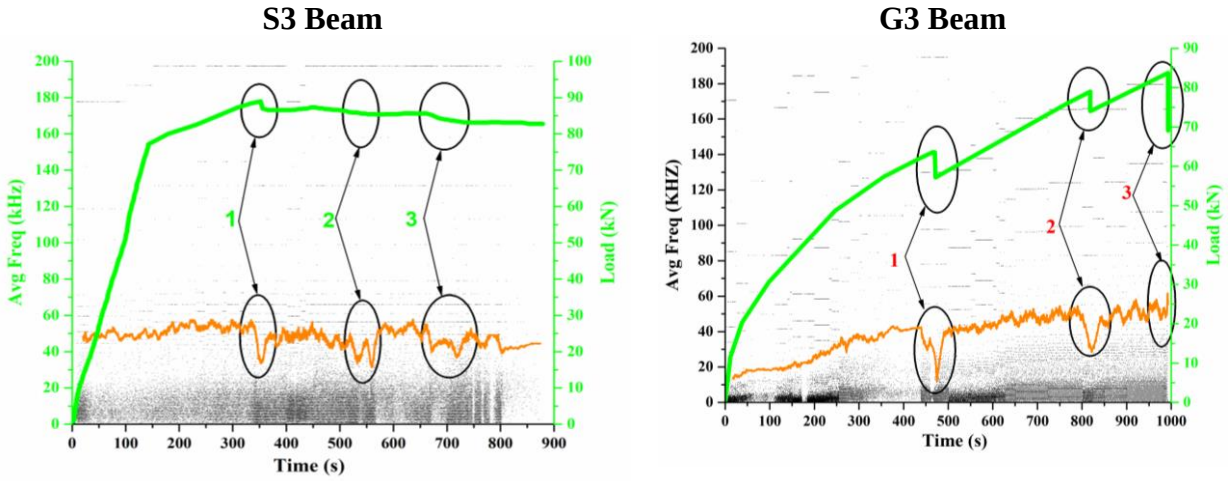

(c) Average frequency (AF)

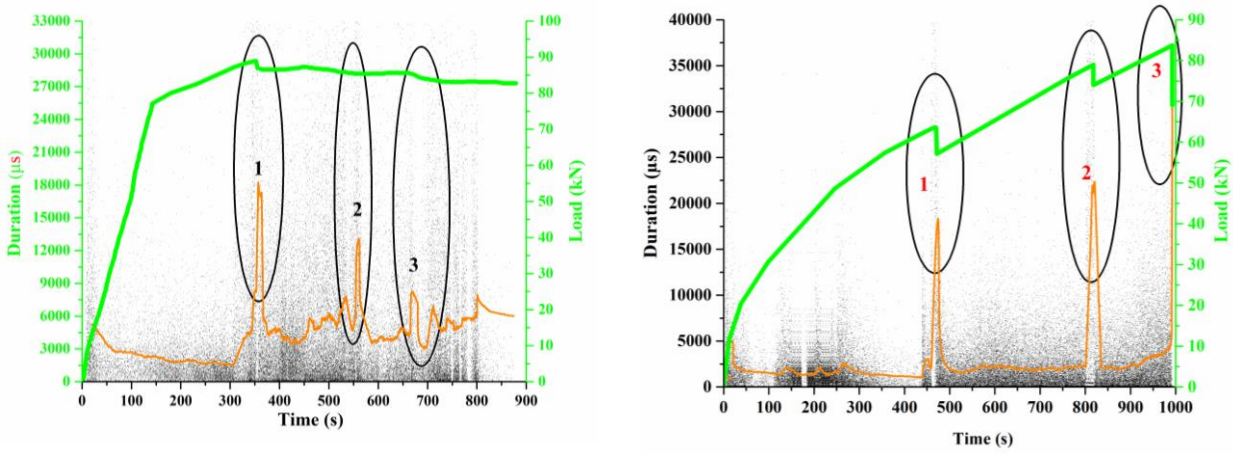

(d) Duration of AE signals

Fig. 6.9: Variation of AF and Duration of AE signals

6.5 DIGITAL IMAGE CORRELATION (DIC) MONITORING

An algorithm (NCORR) is used to correlate the digital pictures captured throughout the experiment for the steel RC & GFRP RC beam specimens **(Blaber et al. 2015).** The results of a four-point bending test on steel RC & GFRP RC beams are shown and analyzed in **Figs. 6.10-6.18.** The present study shows that 2 Dimensional-DIC, as a full-field method, is very well capable of capturing strain localization, which also enables visualization of crack development i.e. (invisible and visible cracking) at very low strain levels. Besides the qualitative representation of results, this method can be also used for the quantification of displacements.

An open-source 2D-DIC is used to assess the surface strain of each point in the speckle pattern. An open-source can give full-field longitudinal strain data at the bottom mid-point location of the RC beam. **(Figs. 6.10-6.18)** show the pictorial description of the longitudinal strain fields (ε_{xx}) obtained from the 2D-DIC analysis of the selected images in both S-series and G-series beams. The dark blue color symbolizes a zero strain field (ε_{xx}) and as the color

evolves more towards the red tone, the strain becomes higher. The red zones, representing a strain (ε_{xx}) of 1 percent or higher, indicate the cracks.

For effective damage monitoring and localization in the steel RC & GFRP RC beams using AE and DIC techniques, the longitudinal surface strain (ε_{xx}) profiles obtained using DIC are plotted along with the AE XY- event plots **(Figs. 6.10-6.18).** The red spawn in AE plots signifies the position of each AE event recorded and the crack mapping of DIC strain profiles indicate the frontal surface condition of the steel RC & GFRP RC beams at different stages of damage under flexural loading. Both of these approaches are intended to improve structural inspection efficiency by showing the beginning and development of cracking, as well as surface strains, in the two types of beams respectively.

It is apparent from **Figs. 6.10(a), 6.13(a), and 6.16(a)** that, during the Damage Level I i.e.at cracking loads of ~5.58 kN, 6.99 kN and 9.54 kN for S1, S2, and S3 RC beam and ~7.89, 8.01, and 10.31 kN for G1, G2 and G3 RC beam respectively, the DIC plot shows little development of strain localization at the bottom of the beam. It is indicated by a light bluish color of longitudinal strain (ε_{xx}) profile at the 1.2 m, 1.2 m, and 1.1 m for S1, S2, and S3 RC beam and 0.67 m, 1.0 m, and 0.85m for G1, G2, and G3 RC beam from the left support **Figs. 6.10(b), 6.13(b) and 6.16(b).** The DIC plot depicts the variation in the value of the longitudinal surface strain (ε_{xx}) scale and indicates the possible locations of crack since there is no clear discontinuity. It is well confirmed by the appearance of AE events in the XY- plot at the same instant which suggests the formation of invisible cracks in Steel RC & GFRP RC at the same location as presented in **Figs. 6.10(c), 6.13(c), and 6.16(c).** Hence, it can be concluded that invisible cracking which is not visible to the human eye can be reliably displayed by DIC longitudinal strain profile images and AE XY- event plots.

Further, with an increase in loading, it is visually observed that at a yield load (P_y) of ~28.93 kN, 45.85 kN, and 81.44 kN in S1, S2 and S3 RC beam the earlier invisible crack starts to become visible and eventually coalesce together to form visible cracks propagating vertically upwards. This indicates the progression of damage to Level II as shown in **Figs.6.11(a), 6.14(a), and 6.17(a)**. The DIC longitudinal surface strain (ε_{xx}) profile changes from light bluish to light yellow color at the same location at a longitudinal surface strain (ε_{xx}) value of 0.10, 0.07, and 0.06 (approx.) These cracks do not result in sudden failure of the beam as their propagation is arrested by the presence of shear stirrups. On the contrary, in GFRP RC beams, owing to the elastic behavior of GFRP bars, the beam continues to carry load linearly and invisible cracking is observed at a load of ~33.6 kN, 51.80 kN, and 57.46 kN and a

corresponding longitudinal strain value of 0.12, 0.1 and 0.03 (approx.,) as shown by dark yellow DIC plot as shown in **Figs.6.11(b), 6.14(b) and 6.18(b)**. This is in a close match with the actual cracked beam. On the contrary, the AE event plot clearly shows the congregation of red dots pointing towards the coalescence of invisible cracks into visible cracks at approximately (1.2, 1.2, and 1.1) m and (1.3, 1.2, and 1.1) m distance from the left support for S1,S2 and S3 and G1, G2 and G3 RC beams. The same can also be noted in the actual beam sample and compared with the DIC images and AE X-Y plots **Figs. 6.11(c), 6.14(c) and 6.18(c)**.

With further loading i.e. Damage Level III, steel bars yield leading to flexural failure followed by concrete crushing **Figs. 6.12(a), 6.15(a) and 6.18(a)**. And the same is also confirmed by the dark red color band in the DIC image at an ultimate load of ~33.93 kN, 46.10 kN and 84.85 kN and corresponding longitudinal surface strain (ε_{xx}) value of 0.15, 0.116 and 0.94 (approx.,).at 1.2, 1.2 and 1.1 m from the left support **Figs. 6.12(b), 6.15(b) and 6.18(b)**. The same can also be confirmed with the actual beam sample. On the other hand, the G1, G2, and G3 RC beam fail typically in shear followed by concrete crushing at Damage level III. The corresponding ultimate load of ~48.94 kN, 56.74 kN, and 76.98 kN and maximum longitudinal strain (ε_{xx}) value of 0.18, 0.1316, and 0.058 (approx.,) in G1, G2, and G3 RC beam and is also depicted in by dark red color in the DIC plot at 1.33, 1.33 and 1.33 m from the left support. The failure and cracking are also well corroborated by extremely dense AE event plots at the same locations **Figs. 6.12(c), 6.15(c), and 6.18(c)**.

A clear trajectory of transverse vertical cracks is also observed from the AE event plot as well as DIC images. This is also validated by the image of the actual cracked beams. Thus, AE events maps and DIC provide a reliable and real-time indication of the initiation and progression of cracking inside concrete in Steel RC and GFRP RC beams undergoing flexural loading.

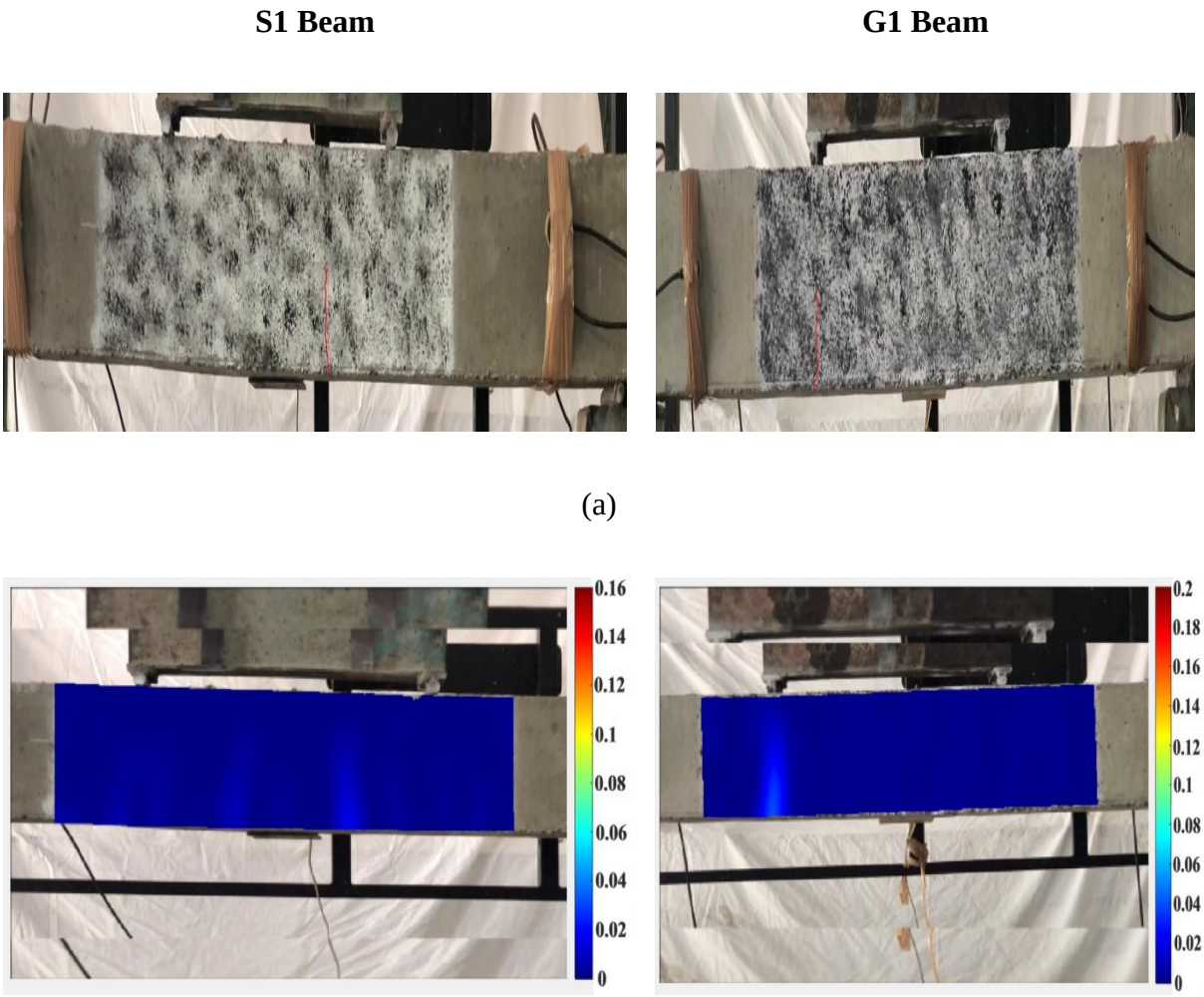

Fig. 6.10: (a) Beam sample (S1&G1) (b) DIC longitudinal strain profiles (c) AE XY plots at Damage Level I

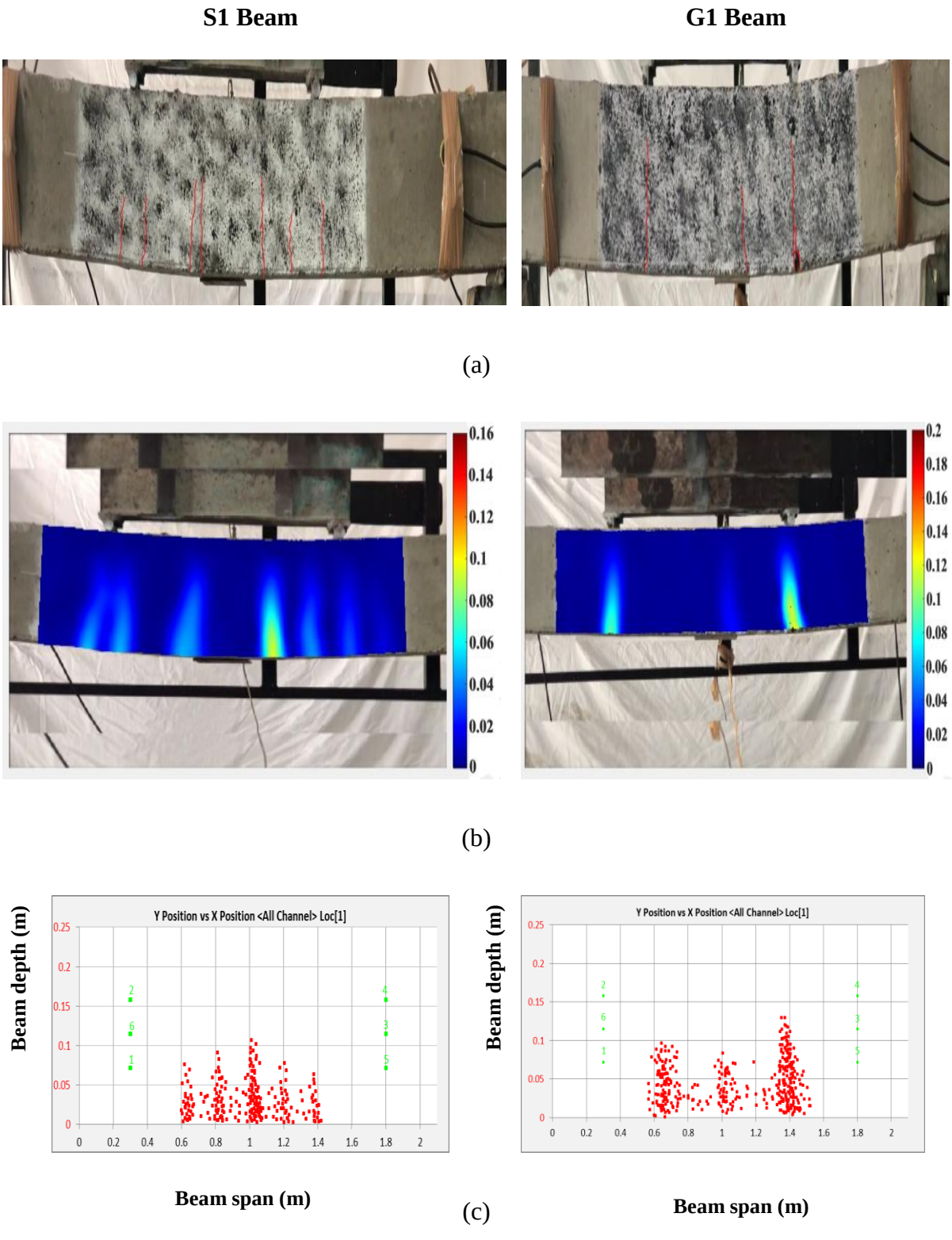

Fig. 6.11: (a) Beam sample (S1&G1) (b) DIC longitudinal strain profiles (c) AE XY plots at Damage Level II

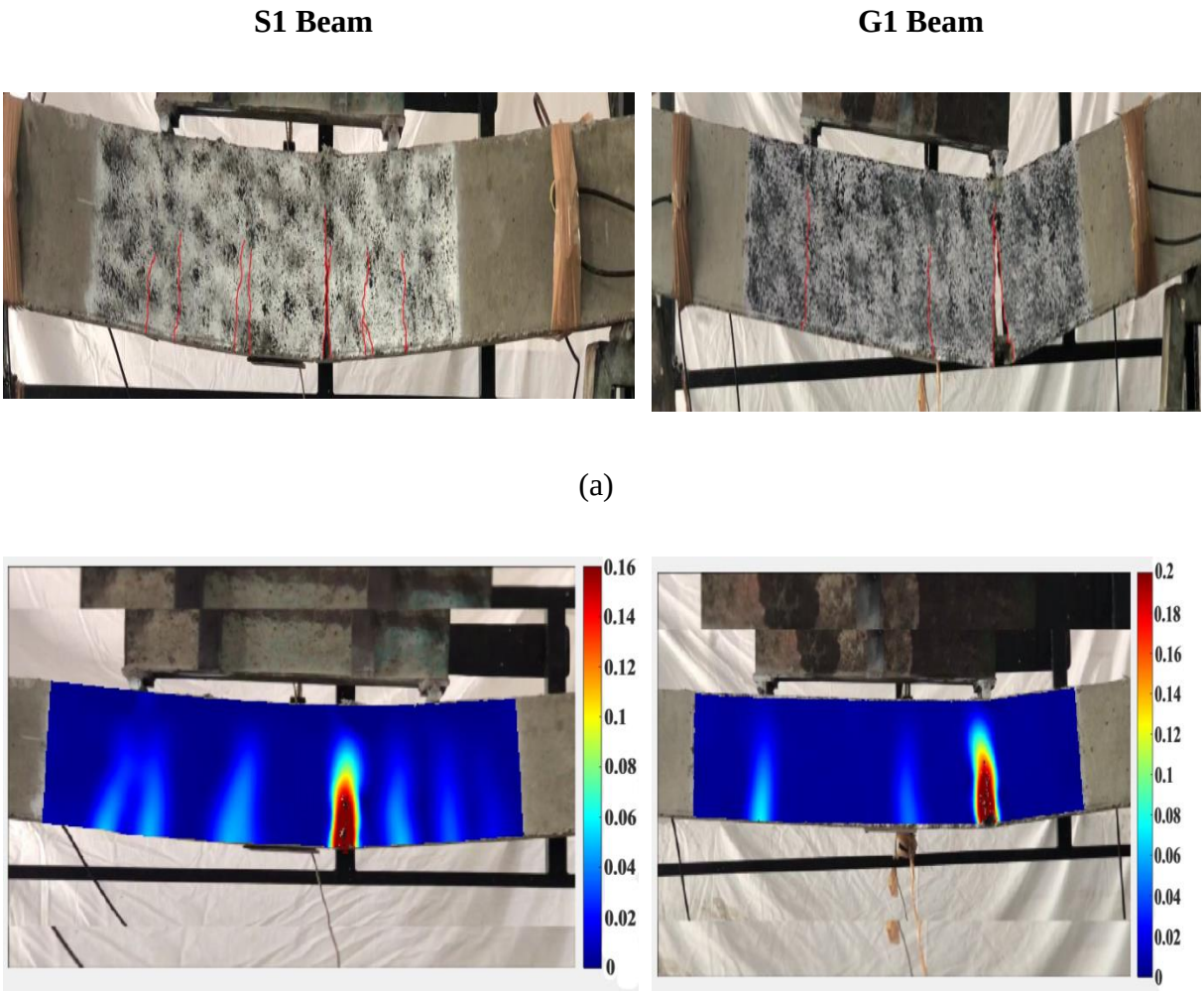

Fig. 6.12: (a) Beam sample (S1&G1) (b) DIC longitudinal strain profiles (c) AE Location-XY plots at Damage level III

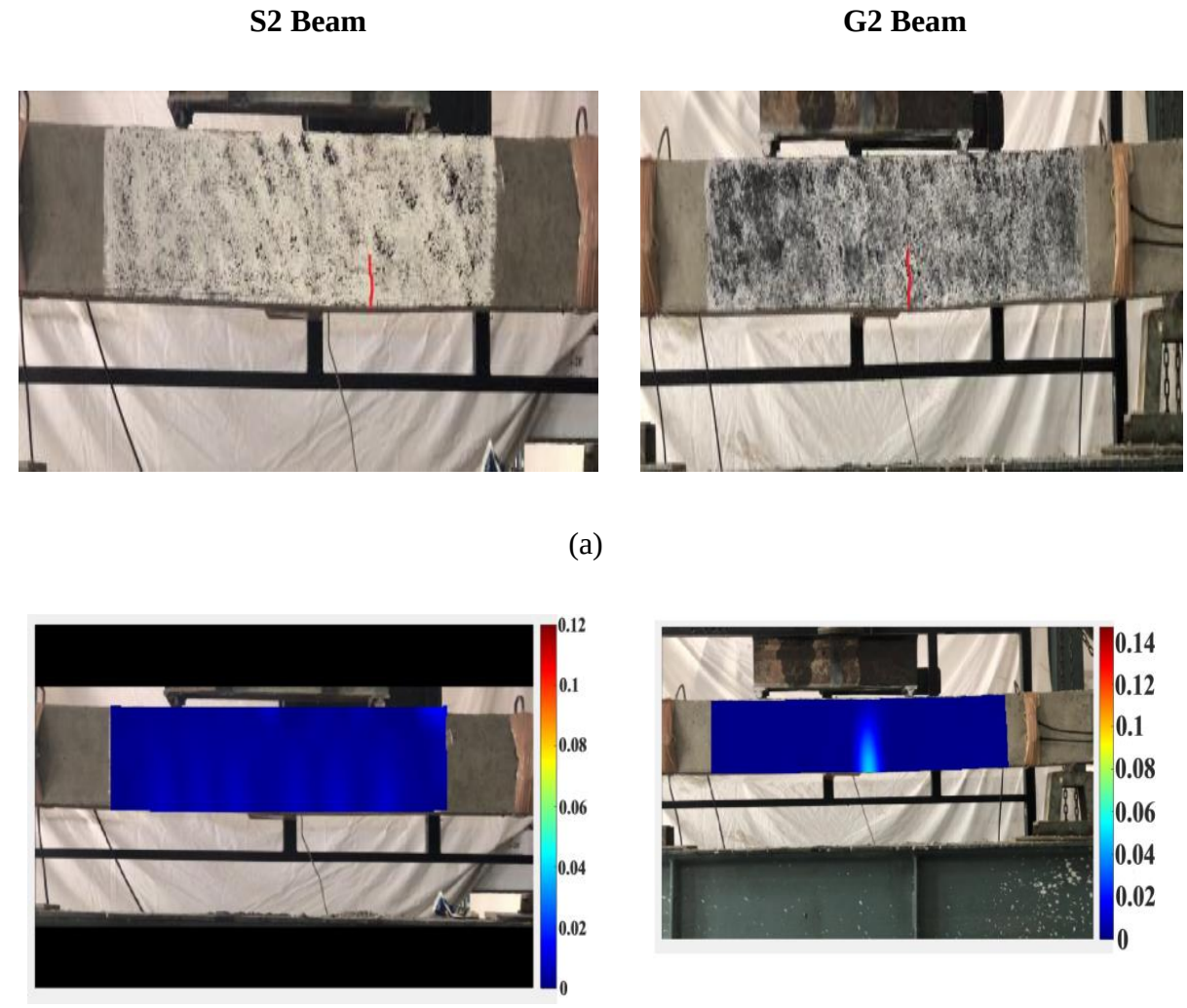

Fig. 6.13: (a) Beam sample (S2&G2) (b) DIC longitudinal strain profiles (c) AE XY plots at Damage Level I

S2 Beam **G2 Beam**

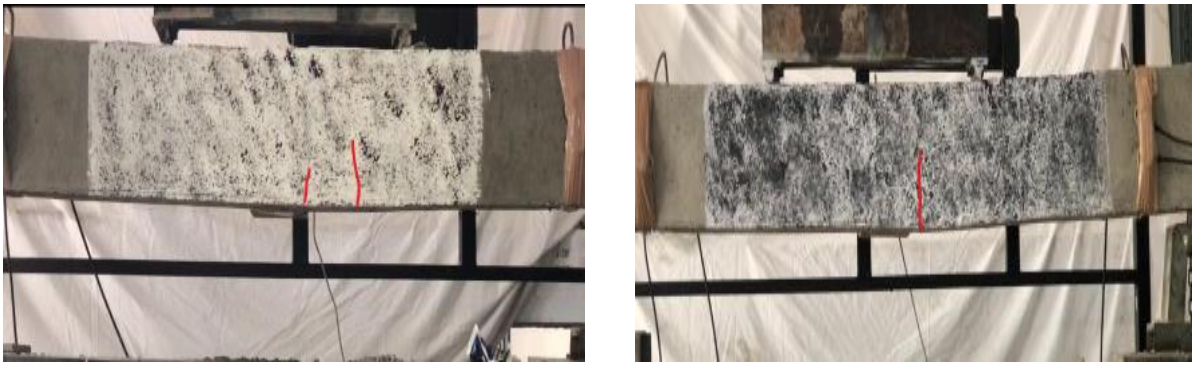

(a)

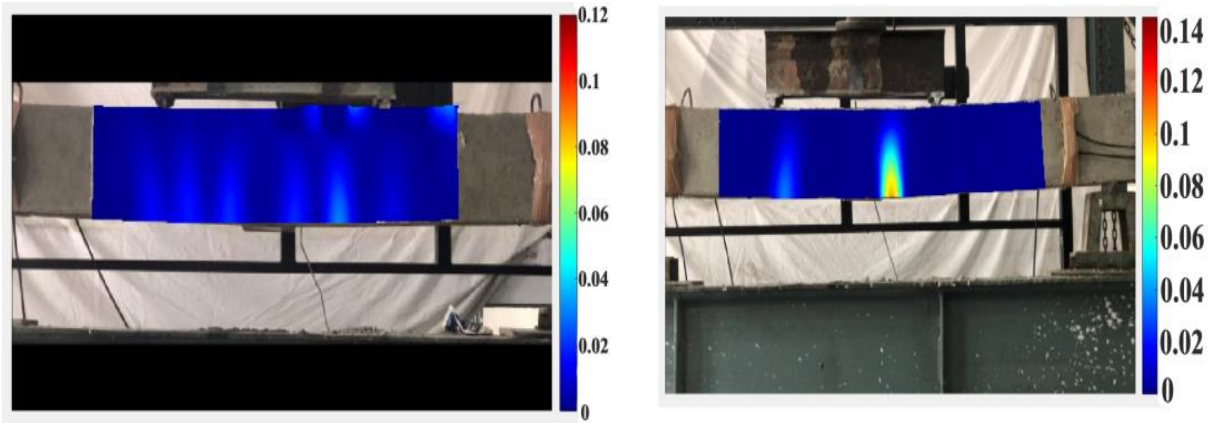

(b)

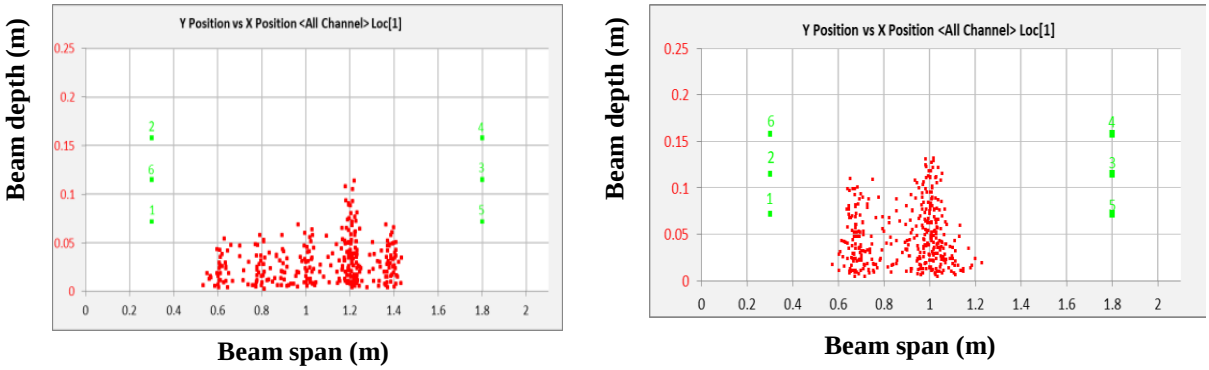

(c)

Fig. 6.14: (a) Beam sample (S2&G2) (b) DIC longitudinal strain profiles (c) AE XY plots at Damage Level II

S2 Beam **G2 Beam**

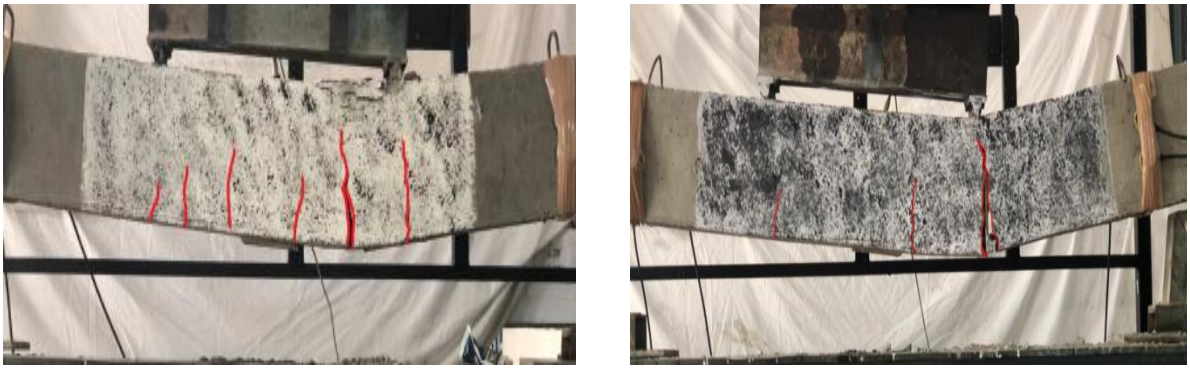

(a)

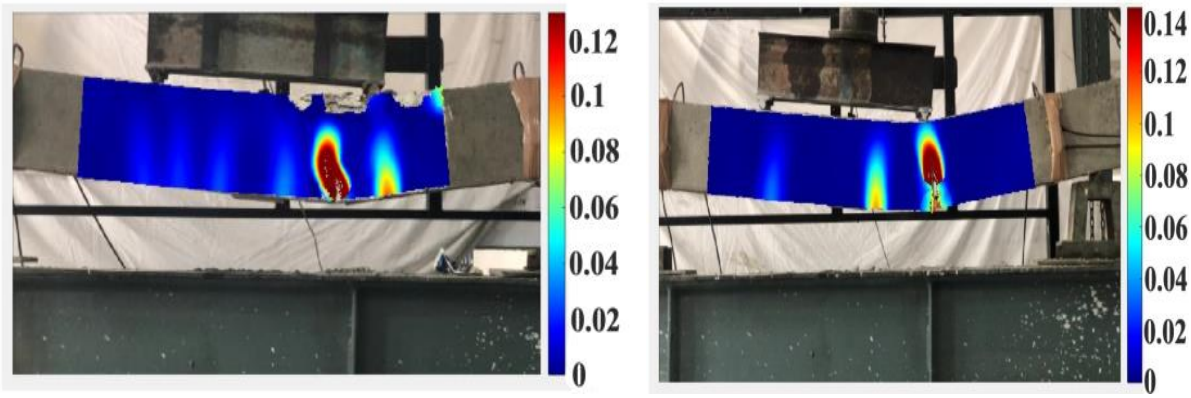

(b)

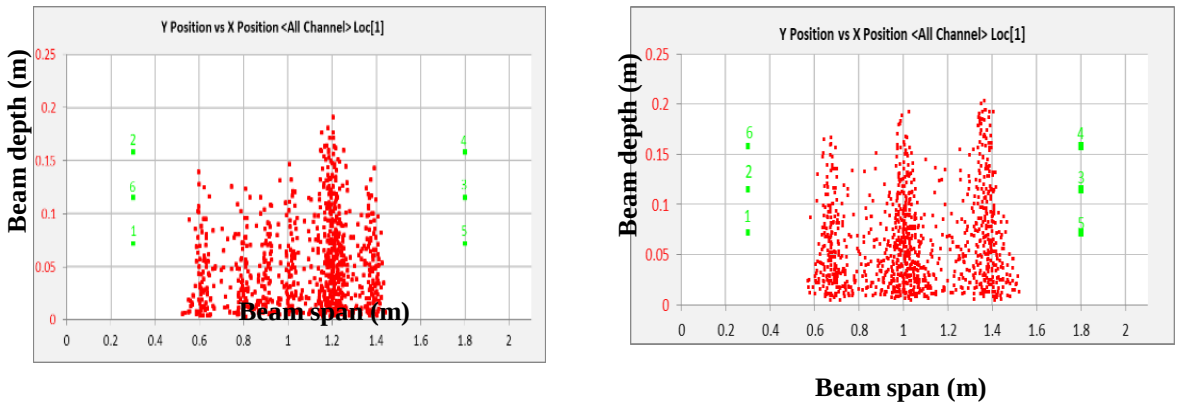

(c)

Fig. 6.15: (a) Beam sample (S2&G2) (b) DIC longitudinal strain profiles (c) AE Location-XY plots at Damage level III

S3 Beam **G3 Beam**

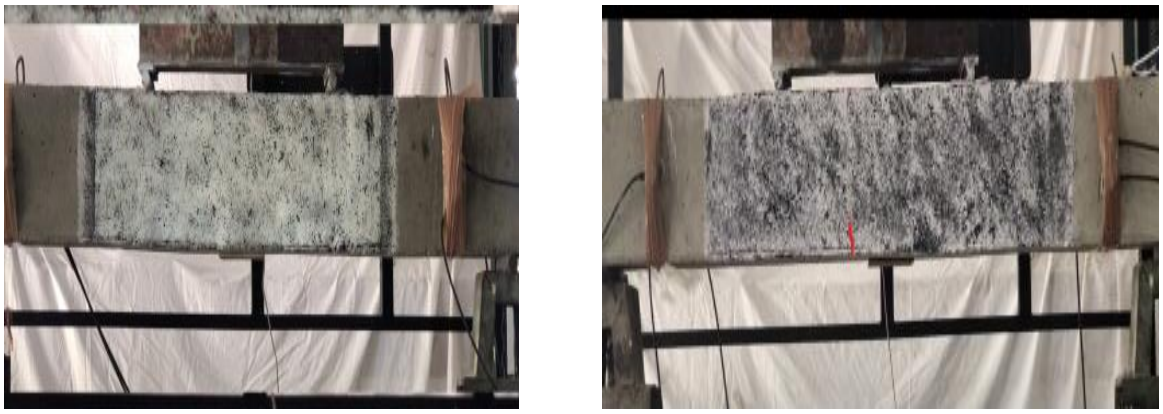

(a)

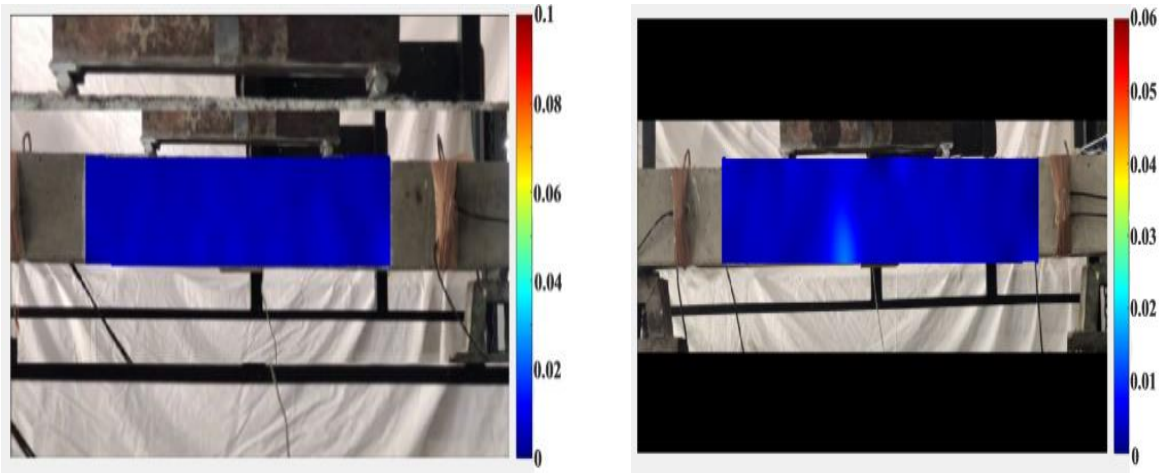

(b)

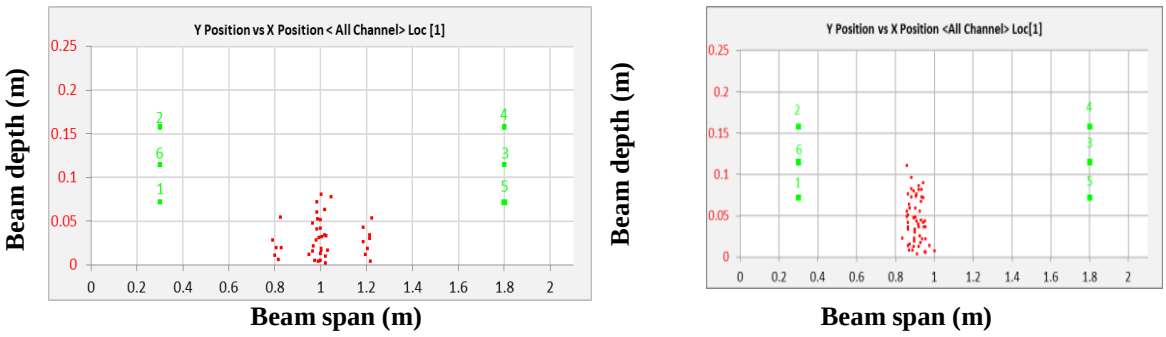

(c)

Fig. 6.16: (a) Beam sample (S3&G3) (b) DIC longitudinal strain profiles (c) AE XY plots at Damage Level I

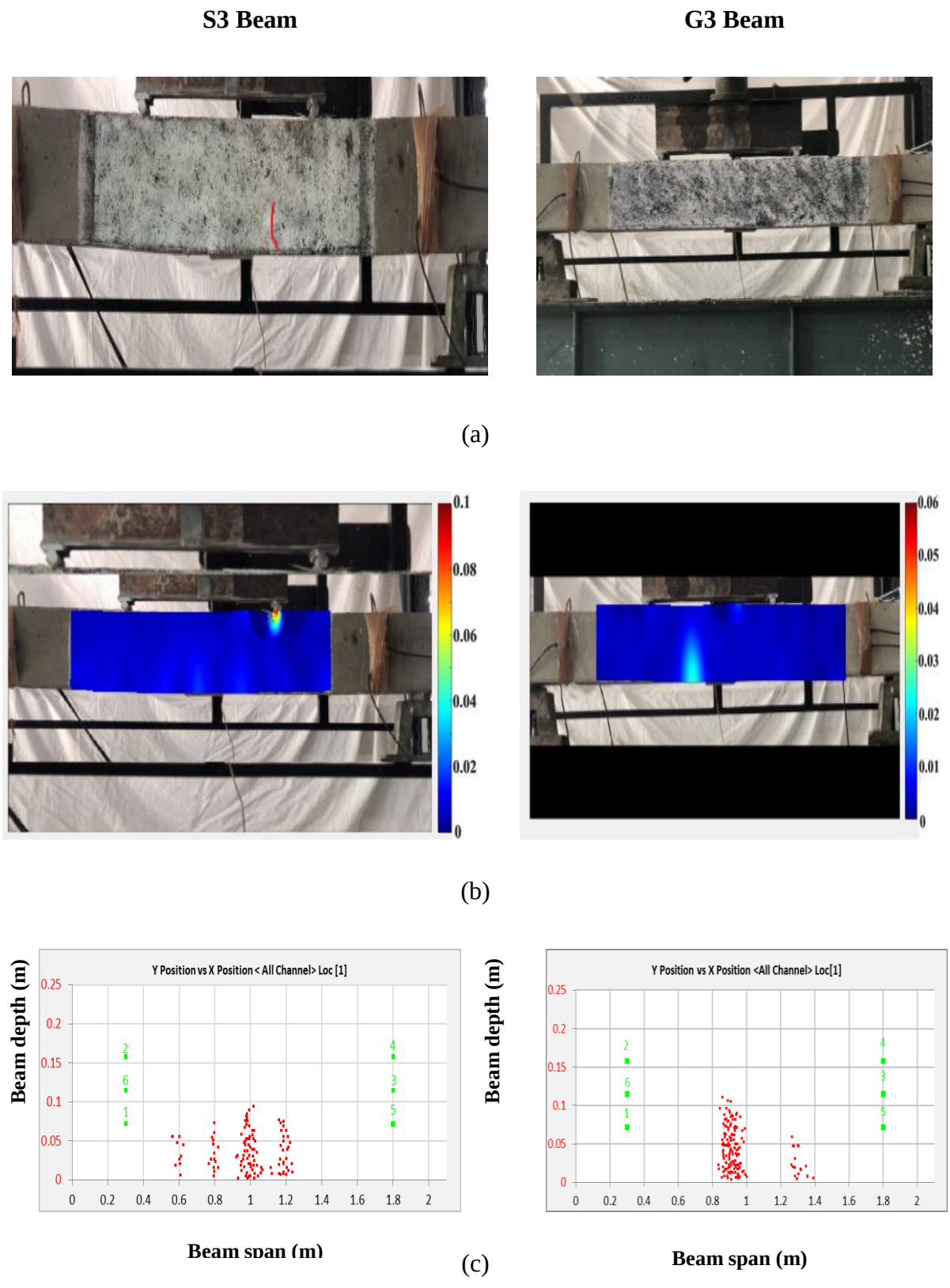

Fig. 6.17: (a) Beam sample (S3&G3) (b) DIC longitudinal strain profiles (c) AE XY plots at Damage Level II

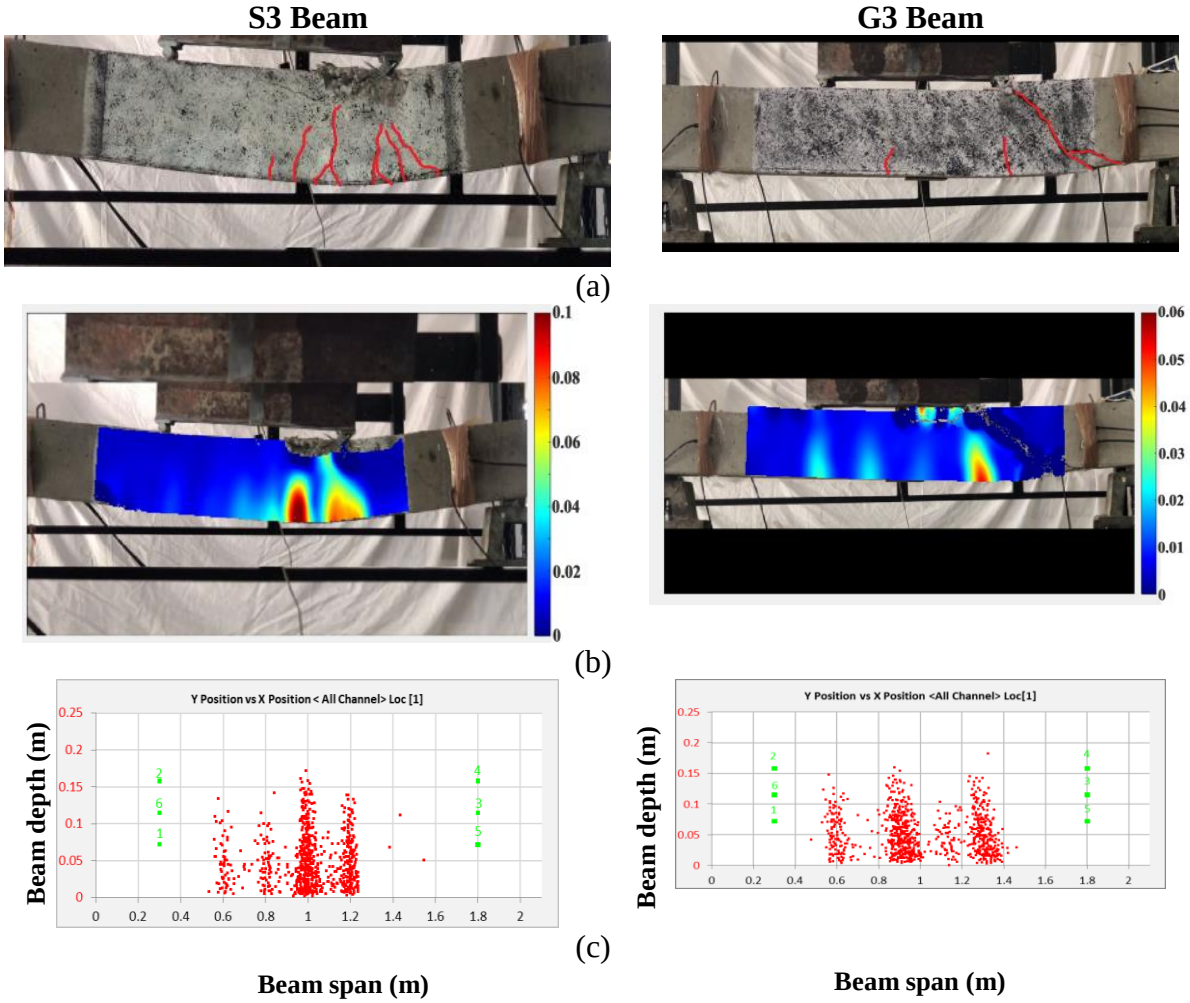

Fig. 6.18: (a) Beam sample (S3&G3) (b) DIC longitudinal strain profiles (c) AE Location-XY plots at Damage level III

The vertical surface displacement of each point of the speckle pattern is also analyzed using an open-source 2D-DIC algorithm. The vertical surface displacement point at the mid-span of Steel RC & GFRP RC beams estimated by 2D-DIC analyses, and the deflection measured with an LVDT are plotted in **Fig. 6.19 (a), (b), and (c)** respectively. It can be noticed that there is a reasonably close match between the deflection measured with LVDT's and the vertical deflection obtained from 2D-DIC. The findings show that DIC is a good replacement for LVDTs, with the extra benefit of being able to offer precise displacement values at any given point **(Shah & Kishen, 2011).**

S1 Beam

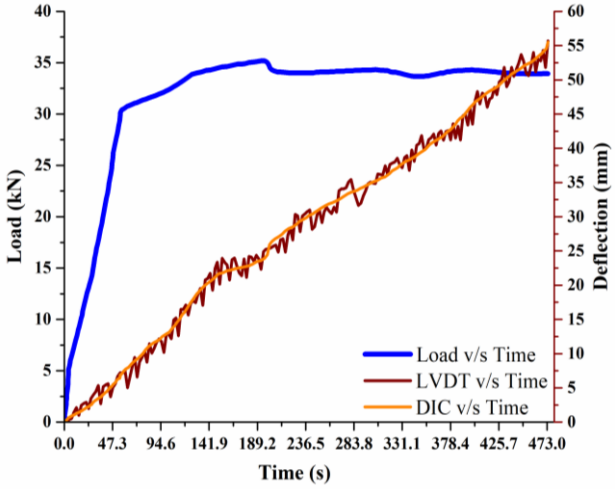

G1 Beam

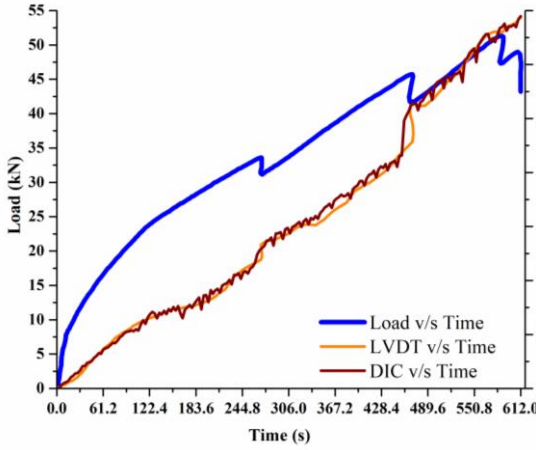

(a)

S2 Beam

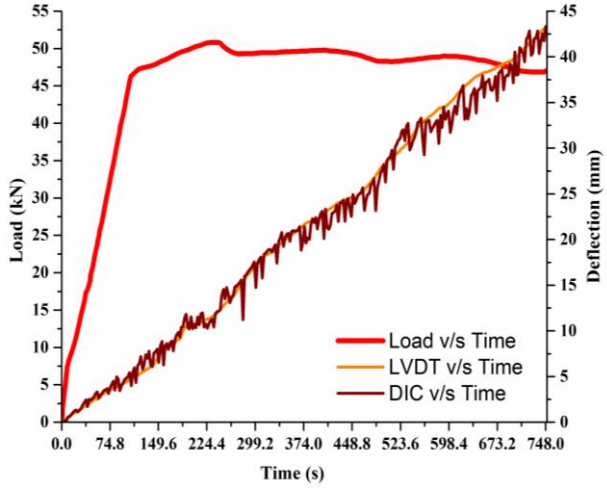

G2 Beam

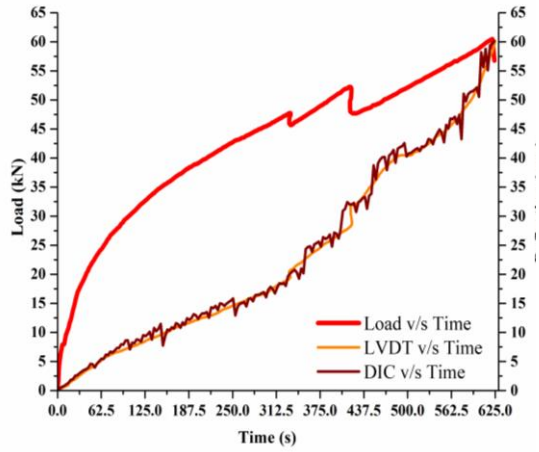

(b)

S3 Beam

G3 Beam

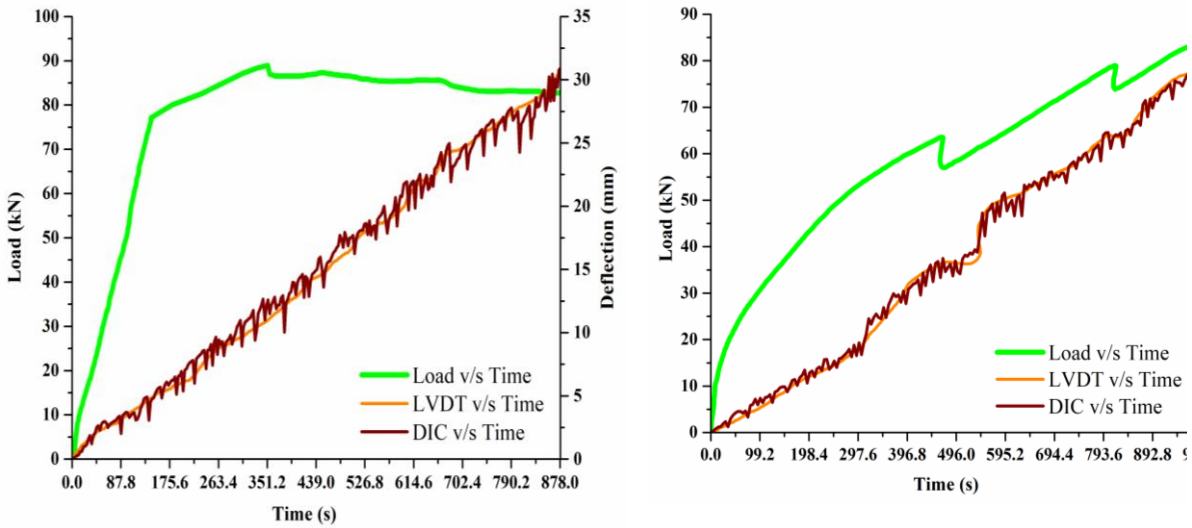

(c)

Fig. 6.19: LVDT and DIC deflection with load

6.6 CLOSING REMARKS

In this chapter, damage monitoring of reinforced concrete beams using steel & GFRP beams under flexural loading utilizing AE and DIC is analysed. Various AE parameters such as cumulative AE hits, amplitudes, average frequency and rise angle not only determine the onset and development of cracking but can also be used to classify the cracking modes in the steel RC and GFRP RC beams. Furthermore, average frequency and signal duration analysis show significant drop in average frequency and significant jump AE duration at the same time indicates critical failure points in steel RC and GFRP RC beams. In the end, AE events maps and DIC longitudinal surface strains (ε_{xx}) and displacements, provide a reliable and real-time indication of the onset and progression of cracking inside concrete in conventional steel RC and Glass FRP RC beams undergoing flexural loading. Both the advanced NDT tools can be effectively used in conjunction with NDE of various types of RC structures incorporating steel as well as GFRP bars.

CHAPTER 7

FRACTURE MONITORING USING AE AND DIC

7.0 GENERAL

In this chapter, the fracture behavior and cracking pattern in steel RC & GFRP RC beams is done by investigating the load versus deflection (P-Δ) behavior with AE and DIC parameters. Acoustic Emission parameters of cumulative AE hits, Cumulative Signal Strength (CSS), Average Frequency (kHz), and Rise Time (RT) were considered for fracture analysis using AE. DIC was primarily employed to compute the vertical displacement and longitudinal strain profiles at the mid-span of the steel & GFRP reinforced concrete beams. In addition, AE-XY plots and DIC longitudinal strain profiles were also utilized to represent increasing AE activity and strains in real-time. While AE is recommended for characterizing the start and propagation of the cracking pattern as well as the cause of failure in beams, DIC assists in localization by visualization the displacement and strain fields while highlighting discontinuities in the displacement field.

7.1. ANALYSIS OF FLEXURAL PERFORMANCE

7.1.1 Load deflection characteristics

The load versus deflection (P-Δ) plots for steel-reinforced & GFRP-reinforced concrete specimens are shown in **Fig. 5.5**. The initial linear segment of both the curves has a very steep slope, which corresponds to the un-cracked condition of these beams. In this region, the vertical deflection is directly proportional to the applied load and the entire concrete section is considered effective in resisting the loads. As can be seen from **Fig. 5.5,** the behavior of both S-series and G-series beams is similar before cracking when both beams are stiff. The end-point of this linear part is an indication of the initiation of cracking in S1, S2, and S3 RC beams and G1, G2, and G3 RC beams respectively, hence it is termed as cracking load (P_{cr}) as shown in **Fig. 5.5 (a)-(b) and (c).**

The second part of the curve that immediately follows this linear segment provides information about the bond quality and tension stiffening effects due to crack spacing. The slope of this part is smaller than the slope of the initial linear segment. This shows that the rate of deflection per unit load is higher after the beam has cracked, which is an indication of the reduction in the stiffness of the cracked beam. It can be seen that the gap between steel & GFRP RC beams widens pointing towards a higher rate of reduction in the stiffness of the GFRP RC

beam with the increase in the applied load as compared to steel reinforced beams. Thereafter, the cracks travel up-to-the surface and become visible in the tensile zone of the steel & GFRP RC beam. This trend continues in the steel RC beam until steel yields in steel-RC beams whereas, in the GFRP RC beam, it continues until the 1st drop-in load. The stiffness was calculated up-to-the yield load for steel RC beams and 1st drop for the GFRP RC beam. The stiffness in the G1, G2, and G3 RC beam is much lower as compared to S1, S2, and S3 RC beams. This can be attributed to the low elastic modulus of the GFRP bars. The reduced stiffness of the GFRP RC beams after cracking has also been reported by various other researchers. The last part of the curve is an indication of a possible failure mechanism in steel and GFRP reinforced beams. As shown in **Fig. 5.5 (a)-(b) and (c)**, the steel RC beam showed a very ductile behavior and failed at an ultimate load (P_{ult}) after undergoing considerable deformation with a very small increase in the load once steel yielded.

On the other hand, in the GFRP reinforced concrete, the crushing of concrete progresses with a sharp increase in the load-carrying capacity after the 1st drop of the load. The beam continues to carry load linearly with an increase in deflection until the 2nd drop and this trend continues up-to-the-peak load (P_{peak}) as well as the ultimate load as shown in **Fig. 5.5 (a)-(b) and (c)**. The failure observed in the GFRP reinforced concrete beam is brittle in the form of concrete crushing as also observed. The ultimate load-carrying capacity of the G1 and G2 RC beams was observed to be around 46.39% and 28.95% higher than S1 and S2 RC concrete beams. This can be attributed to the higher strength of GFRP bars as compared to the yield strength of steel bars **(Table 5.1 and 5.2)**. But as the reinforcement ratio increases from 0.52 % to 1.1 % there is a slightly 5.2% decrease in load-carrying capacity in the G3 beam as compared to the S3 beam. It points towards a lower modulus of elasticity of GFRP bars as compared to steel bars.

7.2 FRACTURE ANALYSIS USING AE

7.2.1 AE Hits & CSS

This section evaluates the crack propagation in terms of micro and macro cracking in Steel & GFRP-RC beams based on AE signals received during flexural testing **(Ohno and Ohtsu 2010 and Ohtsu et al., 2011).** Amplitude and number of AE hits and cumulative signal strength values were calculated using ASCII OUTPUT utility option of AE-win software to identify and relate to crack initiation and progression in steel & GFRP reinforced concrete beams. Various AE parameters such as a change in slope in cumulative AE hits and their corresponding amplitude and

sudden rise in cumulative signal strength (CSS) values commonly known as knee pointing towards micro-and-macro cracking in steel & GFRP reinforced concrete beams.

Figs. 7.1-7.6 present the plots of increase in cumulative-AE hits, a sudden rise in CSS-curve, and variation of the amplitude of AE hits with increasing flexural loading in Steel & GFRP-RC beams along with load-time curve giving an indication of the progression of fracture/cracking in the two types of beams from initiation of cracking to the ultimate failure of these beams.

An increase in the slope of cumulative AE hits is observed in both types of beams pointing towards initiation of AE activity inside in the form of micro-cracking up-to-100s, 125s, and 225s in Steel RC **(Fig. 7.1(a), 7.3(a) 7.5(a)** and 250s, 300s and 396s and GFRP-RC **(Fig 7.2(a), 7.4(a) 7.6(a)**. This is well supported by a sudden rise in the CSS curve called 'Knees' in CSS plots of $1.1x10^9$ pVs, $1.8x10^9$ pVs, and $2x10^9$ pVs ((**Fig. 7.1(b), 7.3(b), 7.5(b)** for steel RC beams and $2.5x10^9$ pVs, $2.2x10^9$ pVs and $5x10^9$ pVs **(Fig. 7.2(b), 7.4(b) 7.6(b)** for GFRP RC beam (approx.) which are also indicators of initiation of micro-cracking. It can also be observed the average amplitude of AE hits in this phase is about 55-60 dB, 61-64 dB, and 65-68 dB (**Fig. 7.1(c), 7.3(c) 7.5(c)** in S1,S2 and S3 RC beams and 60-65 dB, 63-67 dB and 64-67 in G1, G2 and G3 RC beams **(Fig 7.2(c), 7.4(c) 7.6(c)** in the G1,G2 and G3 RC beam. This **Phase-I** is called the **'micro-cracking phase'.**

It is important to note that Phase I is very much prolonged and reports larger values of cumulative AE hits, their amplitudes, and CSS values in the GFRP RC beam as compared to steel reinforced beams due to the high tensile strength of GFRP bars. Another important observation is that no major cracks are observed in this phase and only minor hairline cracks start appearing on the surface of both types of beams. Hence, the plot of cumulative-AE hits, CSS, and their corresponding amplitudes indicates the initiation and progression of micro-cracking inside concrete even when significant effects are not visible on the surface.

Further, with increasing loading on the beams beyond **Phase I**, cumulative-AE hits as well as CSS curve becomes constant with a drop in average amplitude of hits to below 55dB to 60 dB in **"Calm Phase-II"** of activity for about 75s, 100s, and 125s in the S1, S2 and S3 RC beams and about 20s, 30s and 76s in the G1, G2 and G3 RC beam. The calm phase is relatively shorter in GFRP reinforced beam when compared to the steel RC beam primarily due to the linearly-elastic behavior of GFRP bars, hence the GFRP RC beam continues to carry load linearly. During this phase, micro-cracks coalesce to form macro cracks and progress towards **Phase-III** i.e. **Macro-Cracking Phase** for about 298.75s, 522.7s, and 528.78 for the S1, S2, and S3 RC beam and 342s, 299.85s, and 526.96s in the G1, G2, and G3 RC beam.

During this Phase III, a steep rise in cumulative AE hits of larger amplitudes between 80-90 dB, 85-90 dB, and 85-90 dB are observed in S1, S2, and S3 RC beams pointing toward major AE activity leading to macro cracking in the steel-reinforced beam. A similar observation is made in the CSS plot with a sudden rise (2^{nd} Knee) in the CSS curve with high fluctuations of approximately more than $2.1x10^{10}$ pVs, $2.26x10^{10}$ and $4.8x10^{10}$ pVs. On the other hand, in the G1, G2, and G3 RC beam also, a steep rise in cumulative-AE hits, along with the steep fluctuation of magnitude $1.1x10^{10}$ pVs, $1.25x10^{10}$ pVs, and $2x10^{10}$ pVs in CSS curve is observed in this Phase III with average amplitudes of AE hits in the range of 70-80 dB which continues till the failure of GFRP-RC beam towards the end of Phase-III (Figure 6). Finally, a sudden and steep rise in AE hits as well as with a large amplitude as high as 95-100dB is observed along with the sudden rise (2^{nd} Knee) in the CSS-curve with high fluctuations of approximately more than $2.7x10^{10}$ pVs, $2.9x10^{10}$ pVs and $5.3x10^{10}$ pVs with the sudden failure of the G1 G2 and G3 RC beam in Phase-III. It is well confirmed by shear failure followed by concrete crushing in the G series RC beam. Finally, in steel-RC beams, there is no change in cumulative AE hits, and CSS-curve is observed and the amplitude of AE hits drops to 45-50 dB and thereafter becomes constant pointing towards attenuation of AE signals by already existing cracks developed in **Phase II** and **III**. It is in coherence with the plastic zone of steel-reinforced beams, indicating the progression to a failure caused by steel yielding followed by concrete crushing in the steel RC beams.

Hence, it can be concluded that at the same reinforcement ratio, damage initiation, and progression in S-series and G-series reinforced concrete beams is widely differing. In the steel RC beam, it progresses from slow initiation in the form of invisible cracks of smaller amplitudes and smaller CSS values to higher amplitudes visible cracks at later stages due to steel yielding. On the other hand, in the GFRP-RC beam, AE activity mostly consists of initially invisible cracks as well as further visible cracks of larger amplitudes and larger CSS values primarily due to concrete crushing failure. It can be attributed to the lower modulus of elasticity of GFRP as compared to steel resulting in a steep rise in AE activity of very large amplitudes and CSS values leading to its final failure by abrupt cracking and fracture.

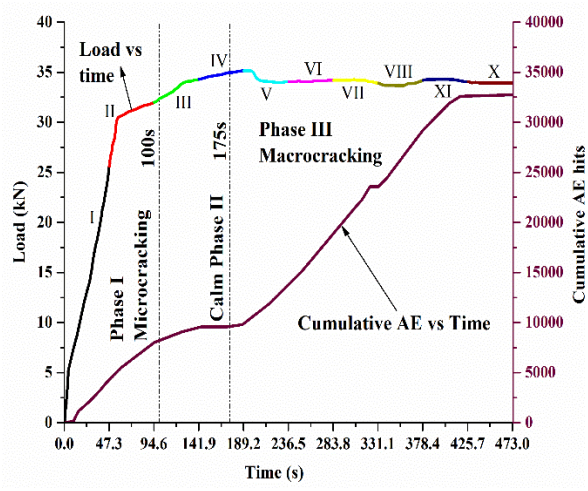

(a) Variation in AE hits with increasing loads

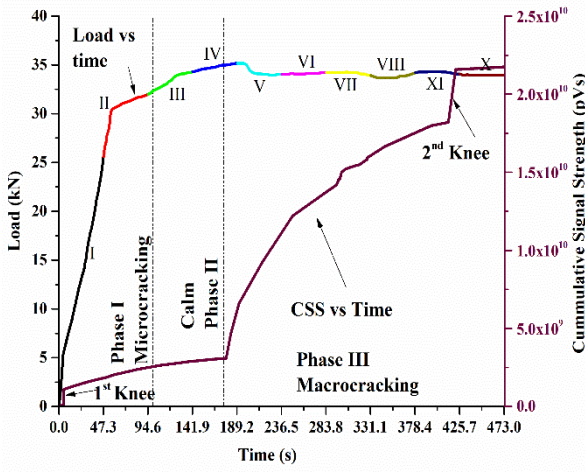

(b) Variation in CSS with increasing loads

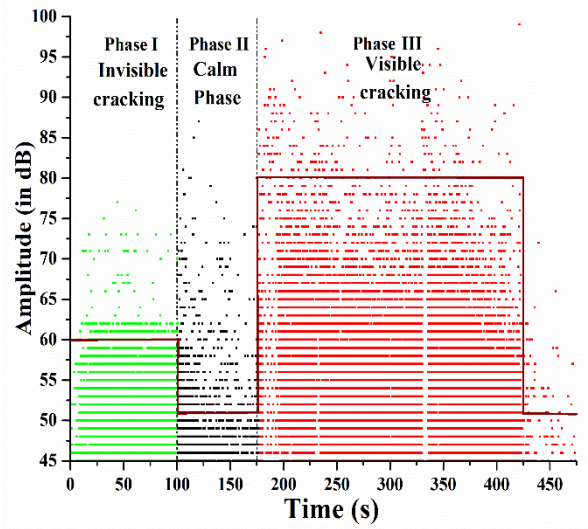

(c)Variation in the amplitude of AE hits

Fig. 7.1: Variation in AE parameters in S1 beam

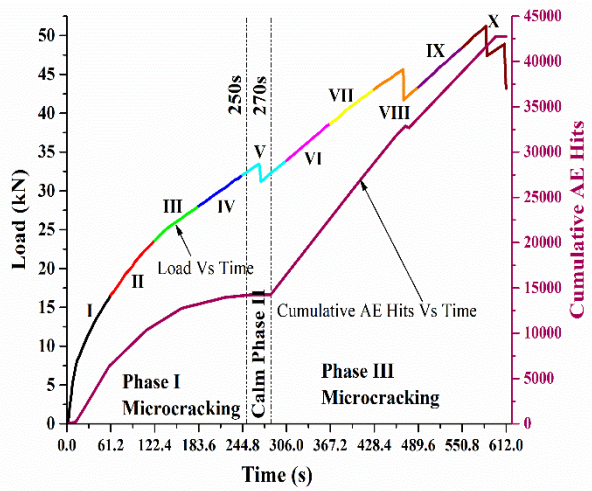

(a) Variation in AE hits with increasing loads

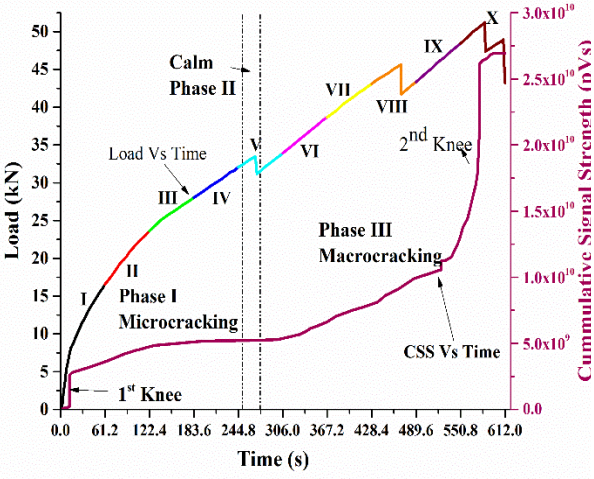

(b) Variation in CSS with increasing loads

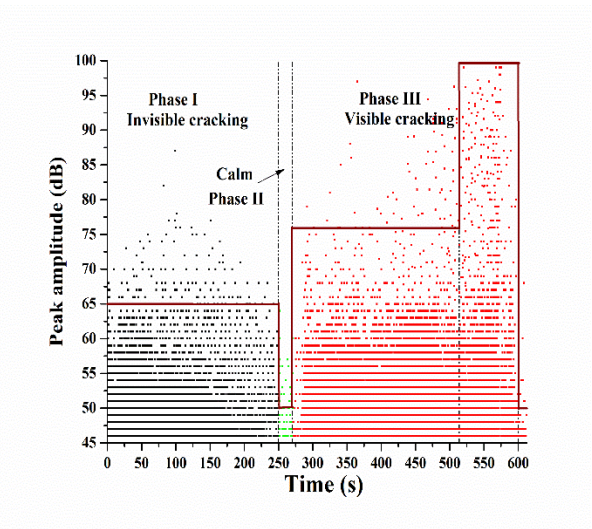

(c) Variation in the amplitude of AE hits

Fig. 7.2: Variation in AE parameters in G1 beam

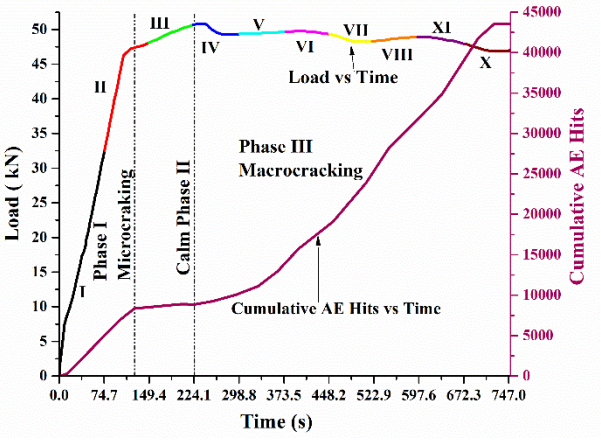

(a) Variation in AE hits with increasing loads

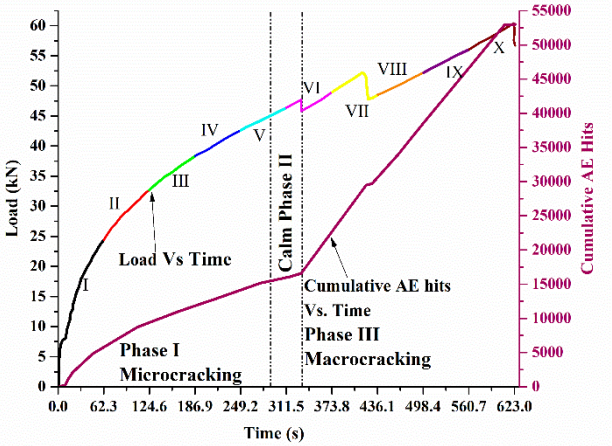

(a) Variation in AE hits with increasing loads

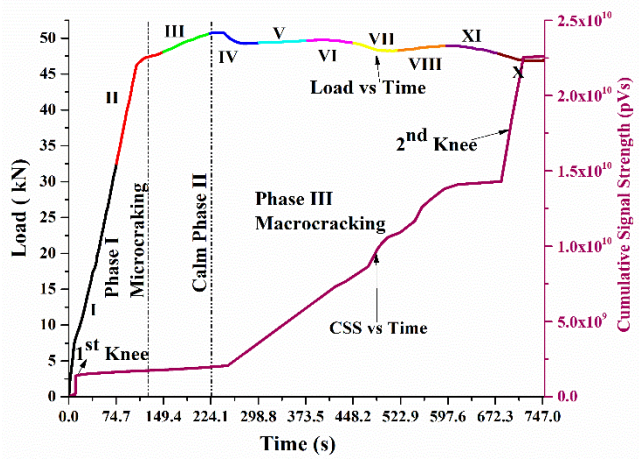

(b) Variation in CSS with increasing loads

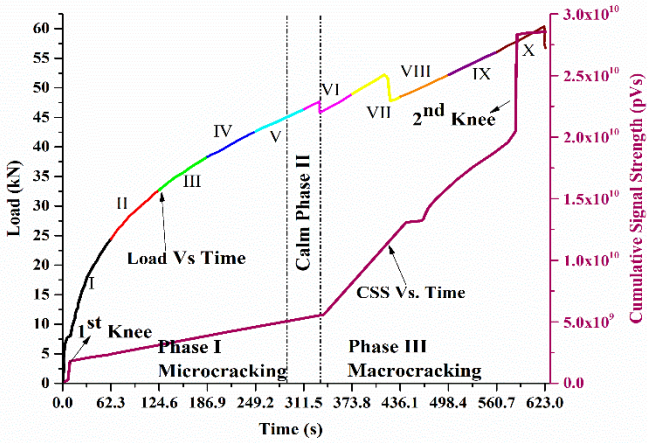

(b) Variation in CSS with increasing loads

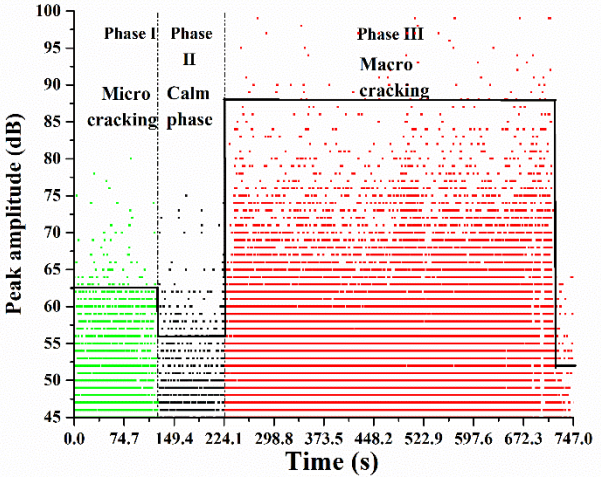

(c) Variation in the amplitude of AE hits

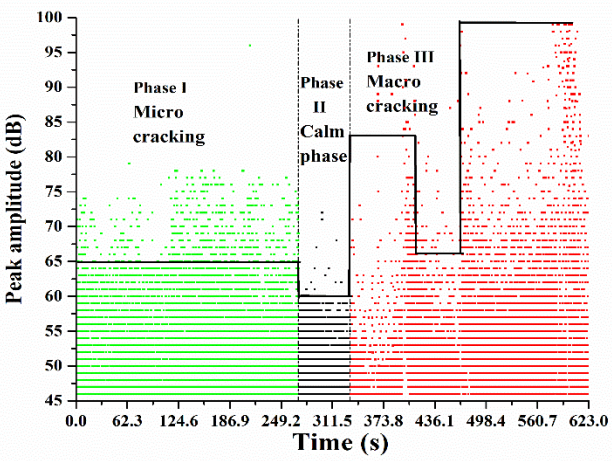

(c) Variation in the amplitude of AE hits

Fig. 7.3: Variation in AE parameters in S2 beam

Fig. 7.4: Variation in AE parameters in G2 beam

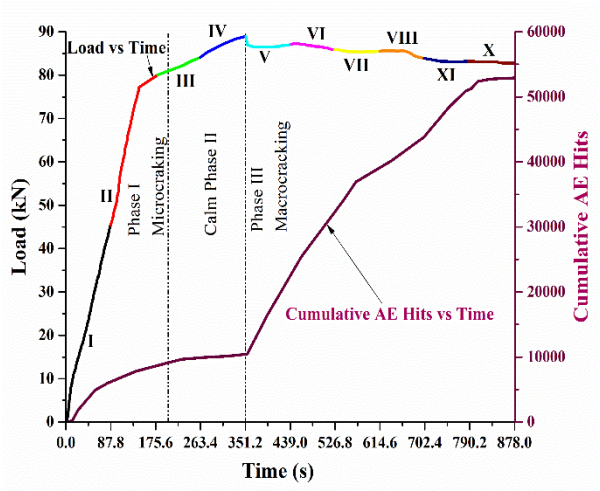

(a) Variation in AE hits with increasing loads

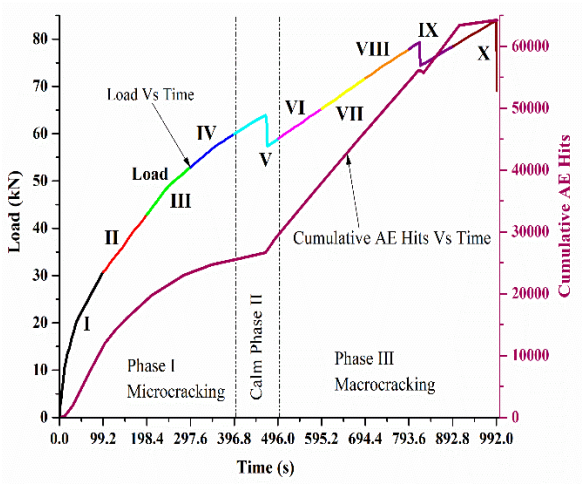

(a) Variation in AE hits with increasing loads

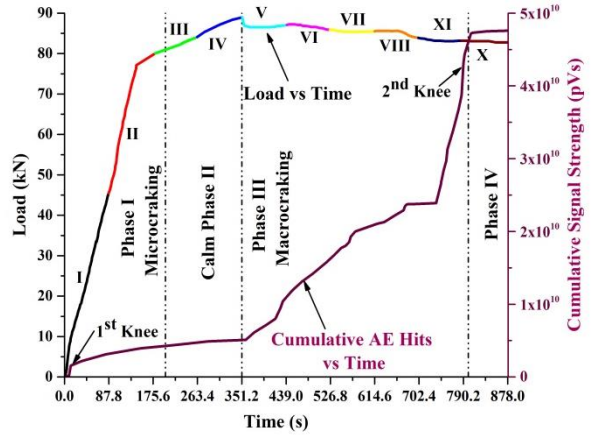

(a) Variation in CSS with increasing loads

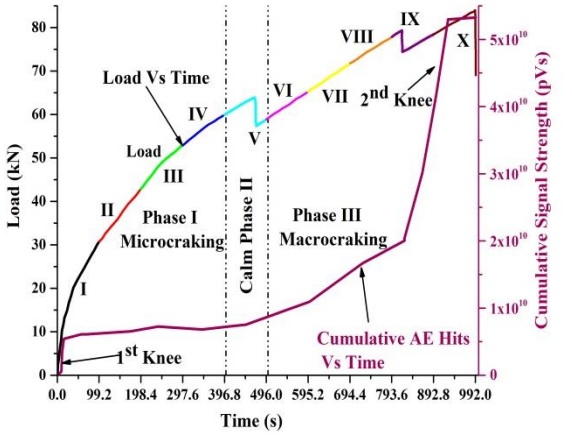

(b) Variation in CSS with increasing loads

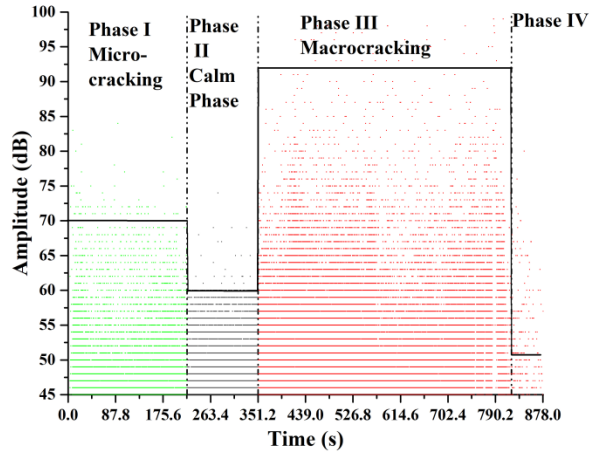

(c) Variation in the amplitude of AE hits

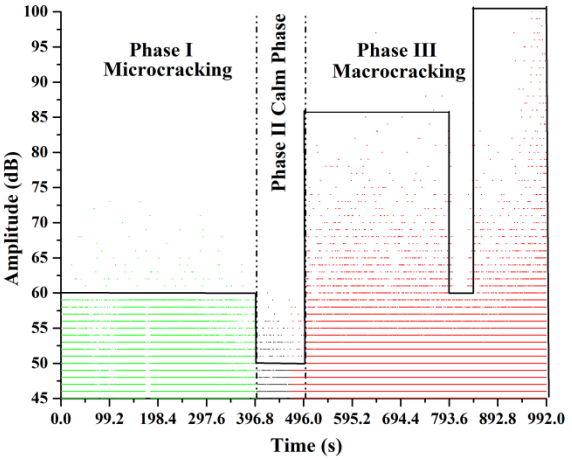

(c) Variation in the amplitude of AE hits

Fig. 7.5: Variation in AE parameters in S3 beam

Fig. 7.6: Variation in AE parameters in G3 beam

7.2.2 Average Frequency (AF) and Rise Time (RT)

The early AE-activity in terms of the number of cumulative AE-hits and their amplitudes and CSS along with the load history is separated into ten different zones (multi-color line) as shown in **Figs 7.7-7.12.** Expressing AE activity as a number of hits is quite common. Additionally, it is well-known that this AE activity is correlated to the rate of cracking and the number of active sources **(Mpalaskas et al. 2015, Sutter et al. 2018 & Sharma et al. 2021).** However, to focus on the possibility to characterize the widely different damage mechanisms in steel & GFRP reinforced beams, AE parameters of Average Frequency (AF) and Rise Time (RT) are also studied in detail in addition to AE hits, CSS, and AE hit amplitudes.

To assist in the fracture analysis, the entire time duration of the experiment is divided into ten equal parts (**Figs. 7.7-7.12**). Stage-I (initial) refers to low load steps, Stages (II to IX) indicate intermediate stages of loading leading to activity at peak load, and Stage X is recorded after the load drop (and thus after RC beam failure) while the deflection was still increasing. For these X stages, a value of the AE parameters of AF and RT are averaged and helps to differentiate the cracking modes in steel & GFRP reinforced concrete beams. **Figs. 7.7, 7.9, and 7.11** represent the data for steel RC beam where, initially at the micro-cracking Stage (I and II), a higher AF with shorter RT signal value is observed, representing the tensile-cracking mode for the steel-reinforced beam. On the other hand, low AF with a longer RT value is observed up to stage-III in the case of the GFRP-RC beam which represents shear-crack mode for GFRP reinforced beam (**Figs. 7.8, 7.10, and 7.12**). This behavior may be due to the ability of the steel beam to resist and bridging the crack, owing to the perfect bonding between concrete and steel and higher modulus of elasticity of steel bars as compared to GFRP bars. It shows that the AF Vs RT plots can be used to predict the occurrence of the micro-crack formation in two differently reinforced concrete beams very efficiently.

With further increase in load, the progression of micro-cracking at P_{peak} load of (35.18, 50.80, and 88.94) kN is observed in S1, S2, and S3 RC beams, which also coincides with the highest value of AF (59.94 kHz, 56.35, and 54.65) kHz and low RT (2.63, 2.72 and 3.58) μs value in Stage-IV in S1 RC beam and Stage-III in the S2 and S3 RC beam. Due to the strain hardening behavior of the steel RC beam, load-carrying capacity slightly reduces with time. On further increasing the load, a slight shift is observed with marginally lower AF and slightly longer RT value. This is because strain hardening behavior of steel RC beam

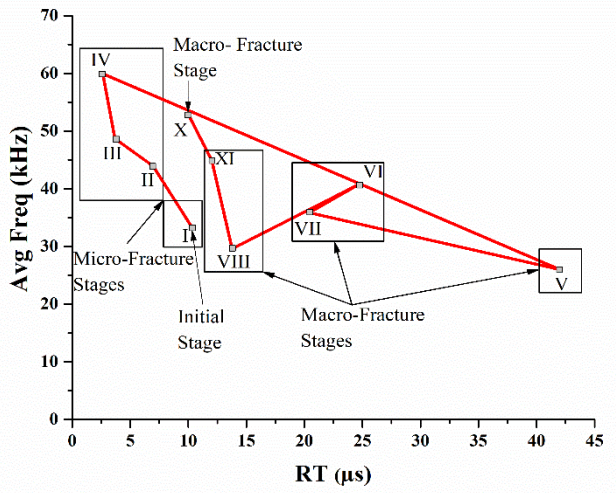

Fig. 7.7: Average Frequency versus Rise time for S1 RC beam

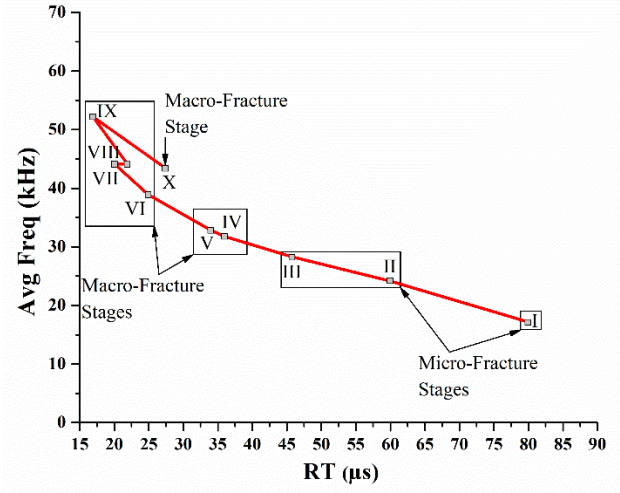

Fig. 7.8: Average Frequency versus Rise time for G1 RC beam

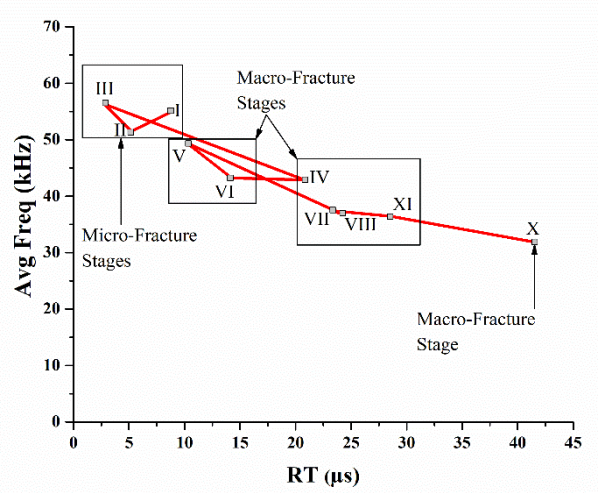

Fig. 7.9: Average Frequency versus Rise time for S2 RC beam

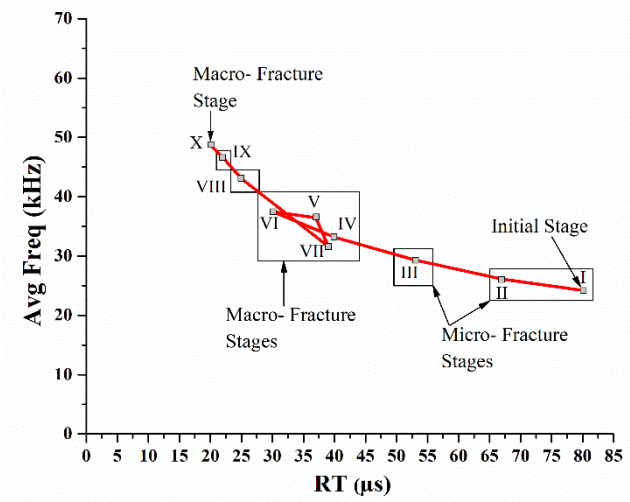

Fig. 7.10: Average Frequency versus Rise time for G2 RC beam

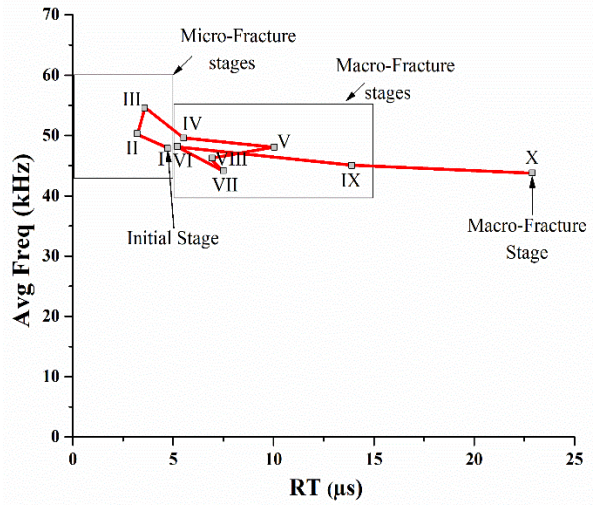

Fig. 7.11:- Average Frequency versus Rise time for S3 RC beam

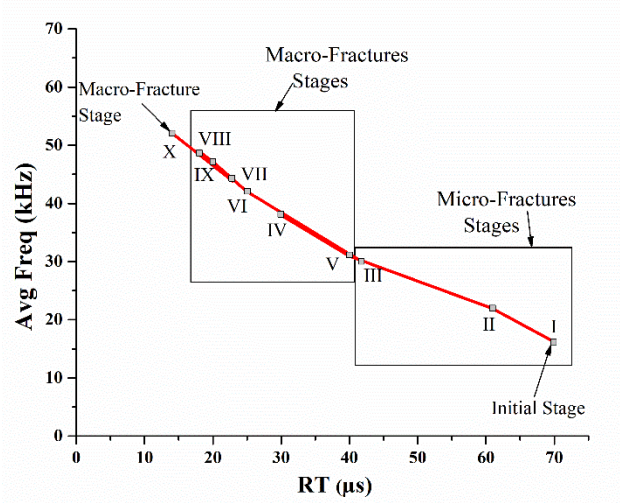

Fig. 7.12: Average Frequency versus Rise time for G3 RC beam

load-carrying reduces with time, which represents the shift in cracking mode from tension progressing marginally towards shear cracking up to the stage-IX. In the last stage-X, which

refers to final failure at an ultimate load of (33.43, 47.01, and 82.75) kN represents slightly longer-RT signal (10.02, 41.63, and 22.89) μs and lower-AF (52.83, 31.83 and 43.74) kHz. This signifies the macroscopic collapse of the beams, indicating that the steel beam experiences tensile cracks localization; leading to flexural failure followed by concrete crushing as shown in **Figs. 5.18 (a), (c) and (e)**

On the other hand, in GFRP reinforced concrete beams, it is observed that AF continuously increases, and RT-value continuously decreases with time as the load increases up to stage-X. It might be due to linearly-elastic behavior and the high tensile strength of GFRP bars. It is also noticed that at two stages i.e. IV and IX there is a slight decrease in frequency and an increase in rise-time value is observed. It might be due to the improper **bonding and slippage between concrete and GFRP bars leading to** a certain level of fluctuation between the successive stages, indicating that the failure mechanics do not follow a smooth succession as in the case of the steel RC beam. In the last Stage-X, which refers to final failure at peak load of (51.32, 60.47, and 83.71) kN, a lower RT (16.96, 20.12, and 14.01) μs value and highest AF value of (52.18, 48.74, and 52.10) kHz) is observed in G1, G2, and G3 RC beams. This signifies the macroscopic collapse of the beams also coincides with the macro-cracking phase at P_{peak} load. This indicates that the beam experiences shear-crack; leading to over-reinforced shear failure followed by concrete crushing as shown in **Figs. 5.18 (b), (d) and (f)**. Hence, the AE plot of AF and RT value can be effectively demonstrate the variation of failure modes in steel as well as GFRP reinforced concrete beams.

7.3 DAMAGE LOCALIZATION USING AE AND DIC

In structural health monitoring, an important step in damage diagnosis and prognosis is crack localization which can guide engineers to the most sensitive zone so that appropriate strengthening can be effectively applied **(Tan et al. 2009 & Behnia et al. 2014).** In this study, an attempt has been made to localize and pictorially represent stages of cracking in steel RC & GFRP RC beams using AE-XY plot and longitudinal strain (ε_{xx}) profiles using DIC. AE-XY plot give the online record of the events (red dots) from six AE-sensors that trace back the origin of the event. The origin and accumulation of crack events detected with AE-XY plots are compared with DIC longitudinal strain (ε_{xx}) profile images. These longitudinal strain fields are important in the sense that they represent the displacement of every point in the imaging zone which easily enables them to locate crack due to displacement discontinuity. The blue color represents a

Time Actual Cracked Image DIC image AE XY Plot

0 s

(a)

47.37s

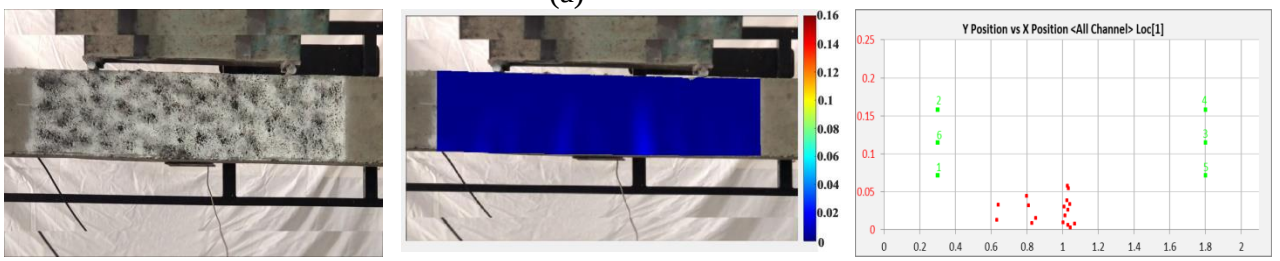

(b)

94.75s

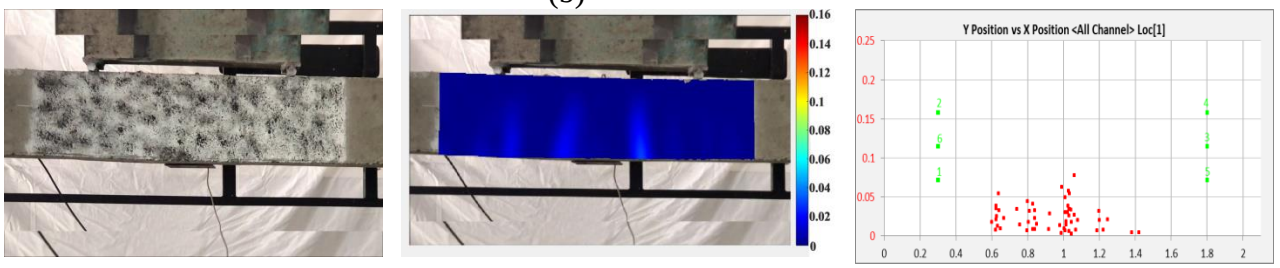

(c)

142.13s

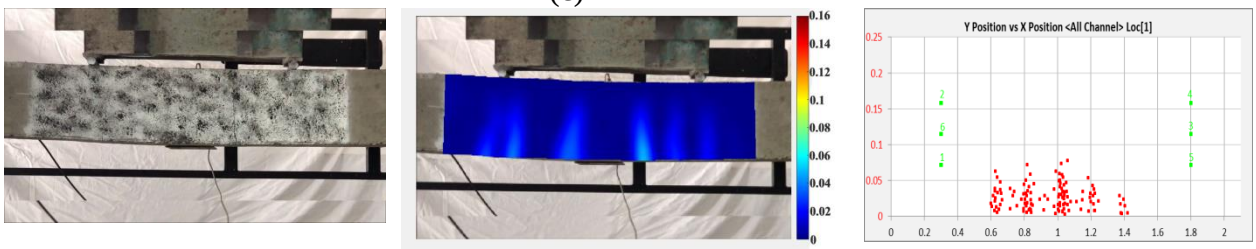

(d)

189.51s

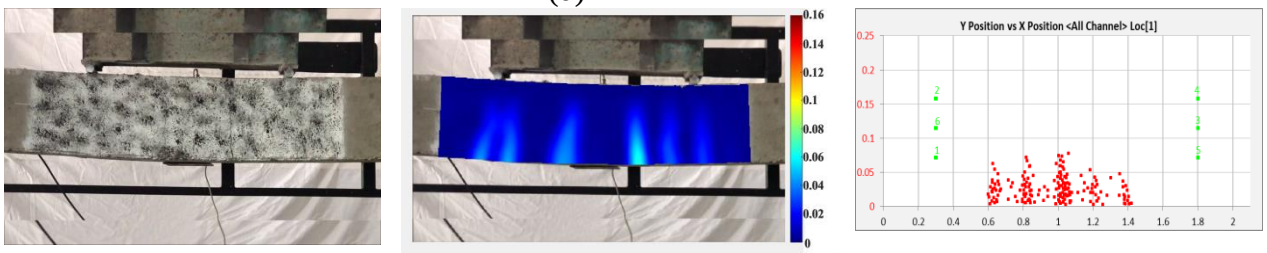

(e)

236.89s

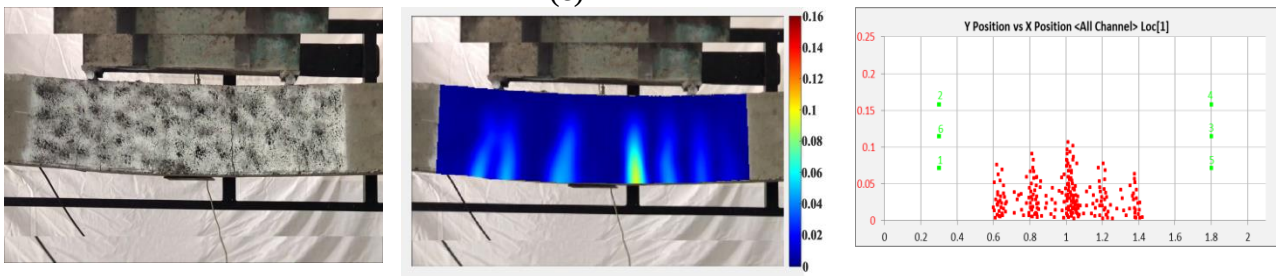

(f)

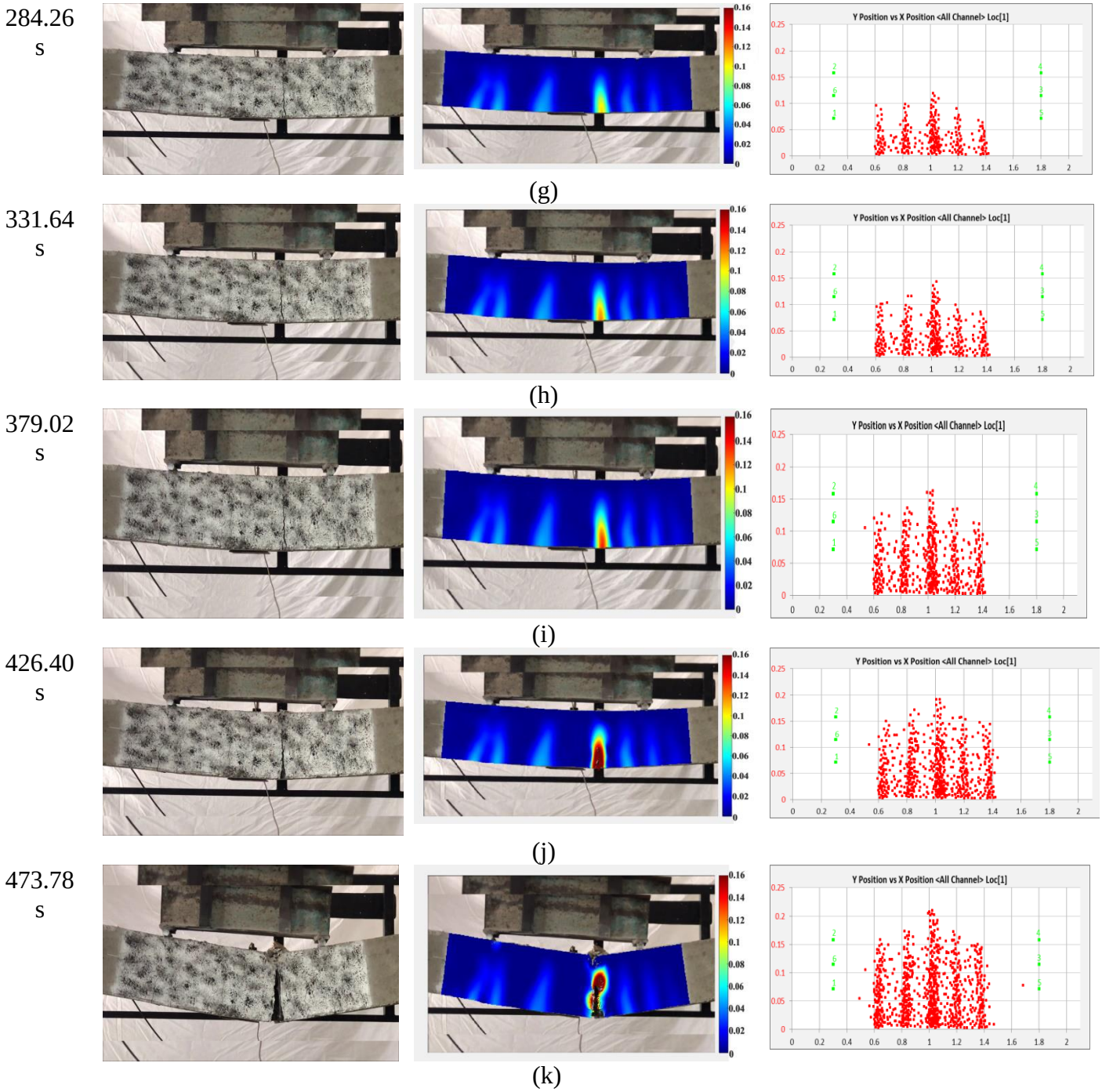

Fig. 7.13: Actual cracked images of S1 RC beam, DIC longitudinal strain profile, and AE events plots (a-k). The red spawn indicates the locations of the AE events: (a) Zero loading stage, (b-c) Initiation of microcracking, (d-j) crack propagation, and (k) final failure.

Time	Actual Cracked Image	DIC image	AE XY Plot
0 s		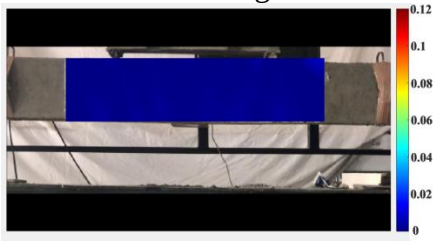	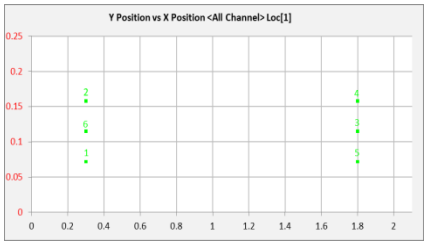
	(a)		
74.79 s			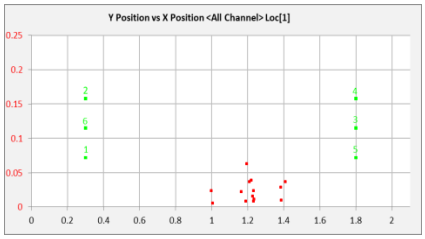
	(b)		
149.58 s			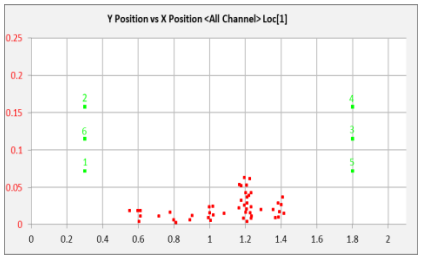
	(c)		
224.37 s		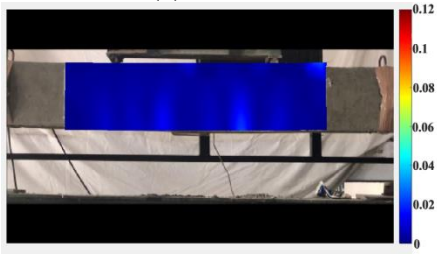	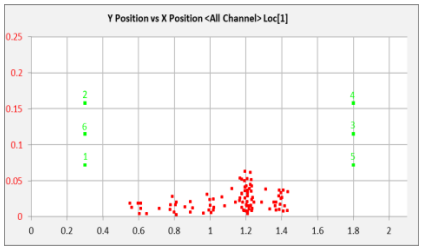
	(d)		
299.16 s	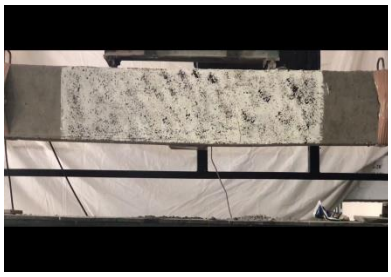	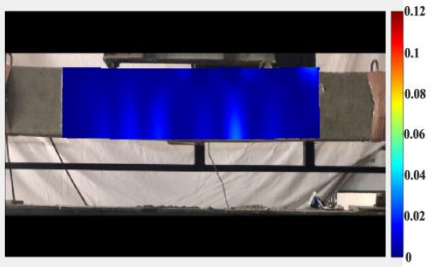	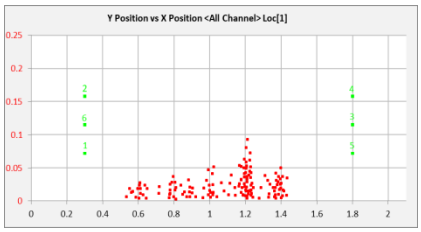
	(e)		
373.95 s		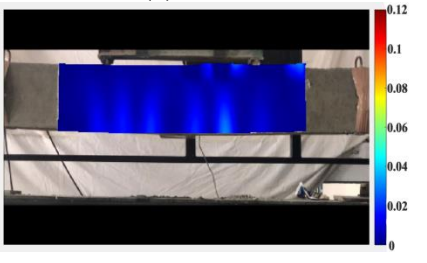	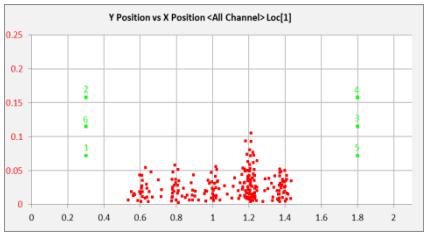
	(f)		

448.74 s

(g)

523.53 s

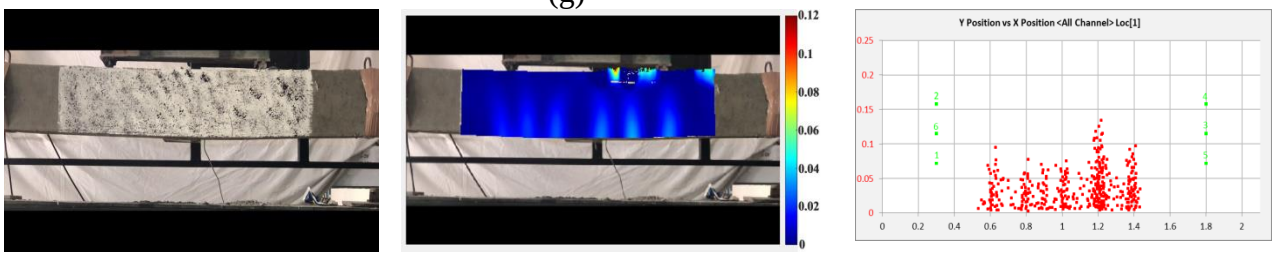

(h)

598.32 s

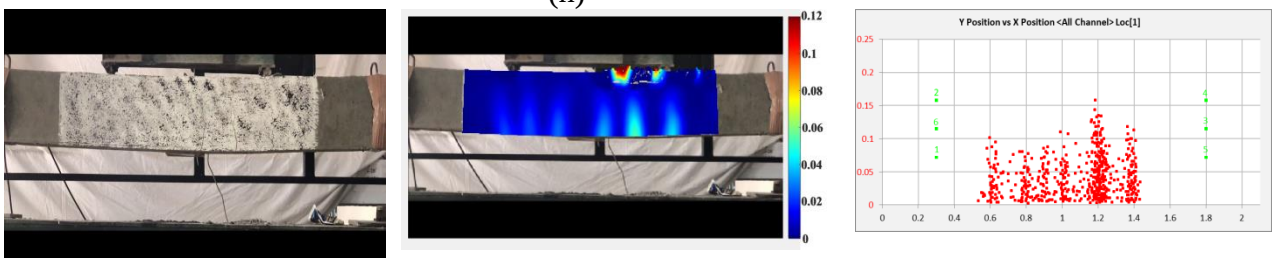

(i)

673.11 s

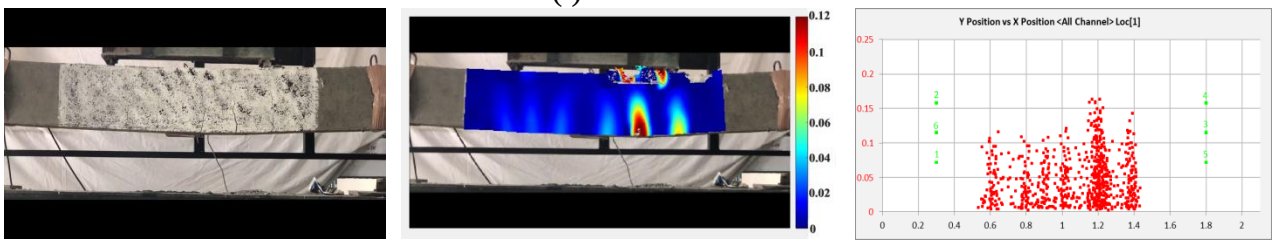

(j)

747.99 s

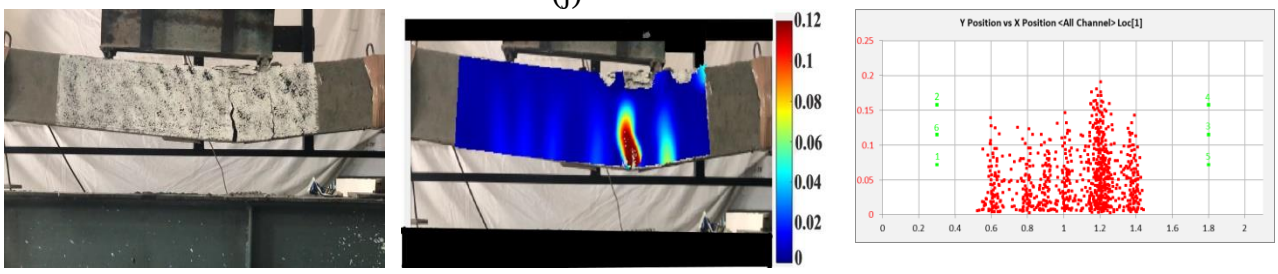

(k)

Fig. 7.14: Actual cracked images of S2 RC beam, DIC longitudinal strain profile, and AE events plots (a-k). The red spawn indicates the locations of the AE events: (a) Zero loading stage, (b-c) Initiation of microcracking, (d-j) crack propagation, and (k) final failure.

Time Actual Cracked Image DIC image AE XY Plot

0 s

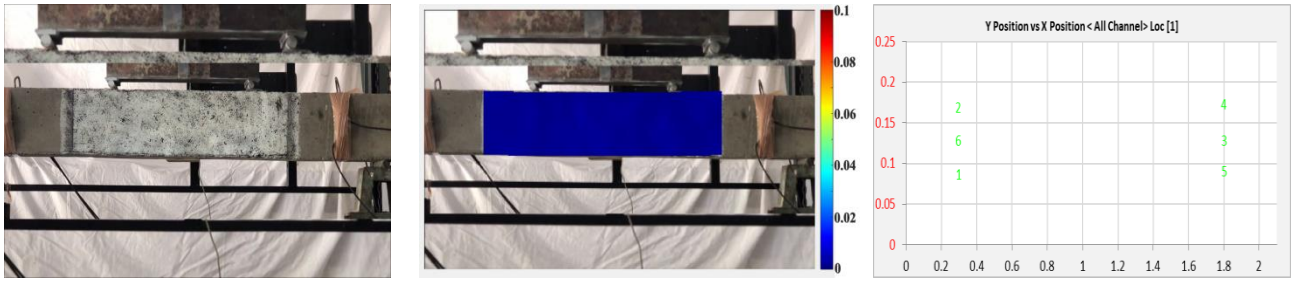

(a)

87.8 s

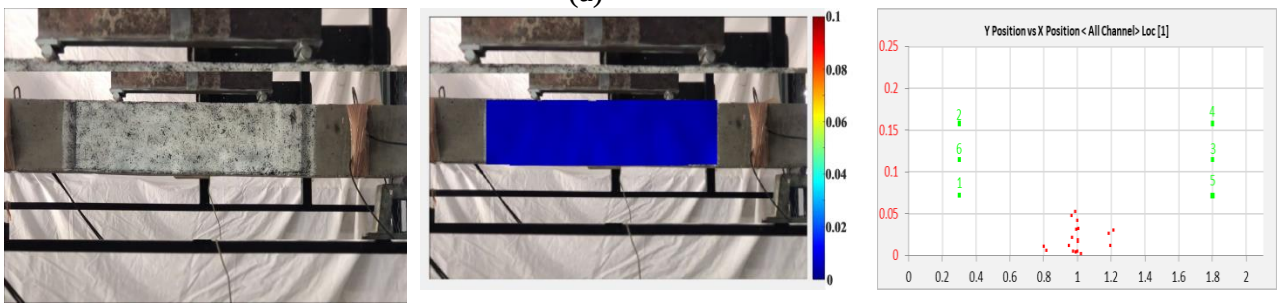

(b)

175.6 s

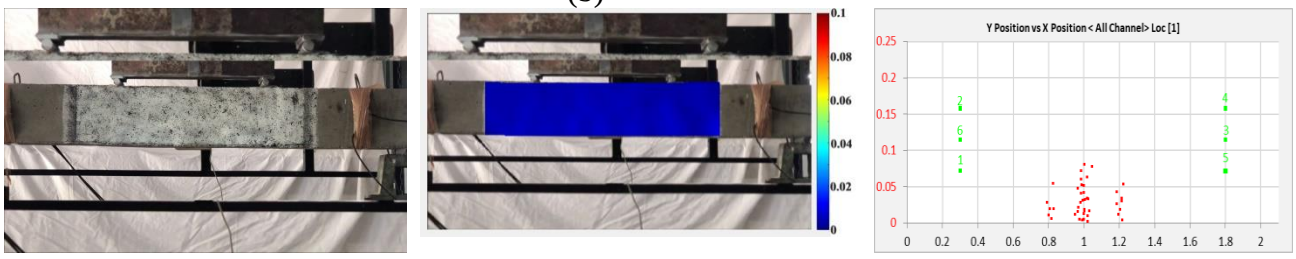

(c)

263.4 s

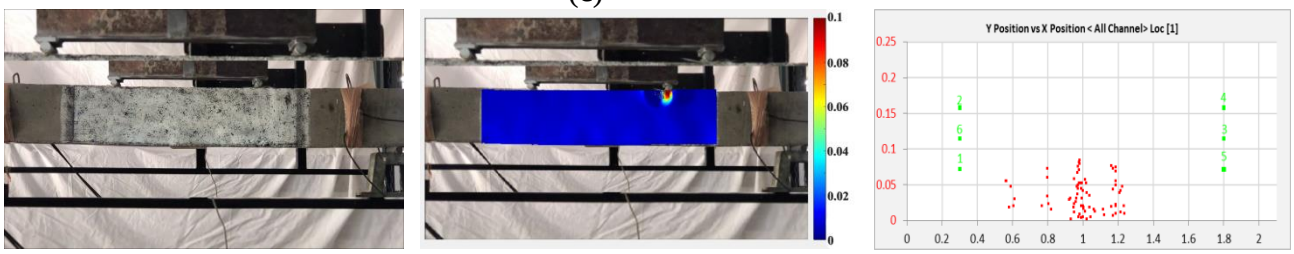

(d)

351.2 s

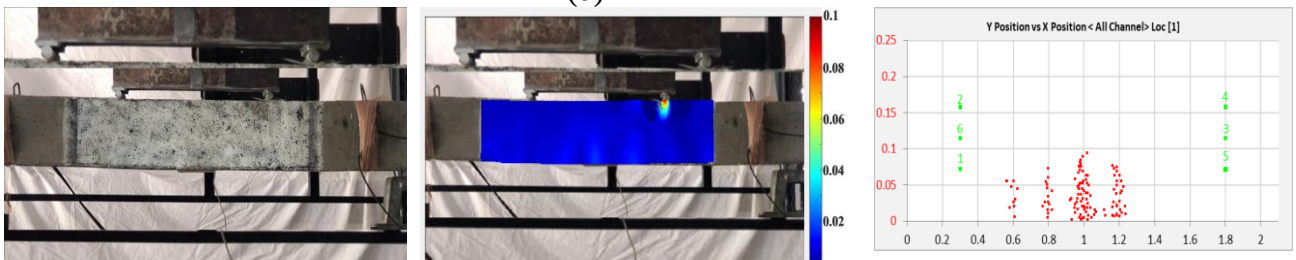

(e)

439 s

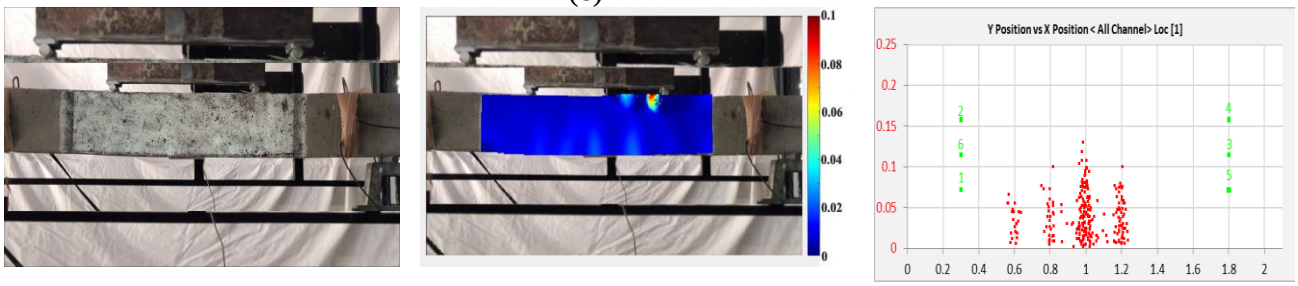

(f)

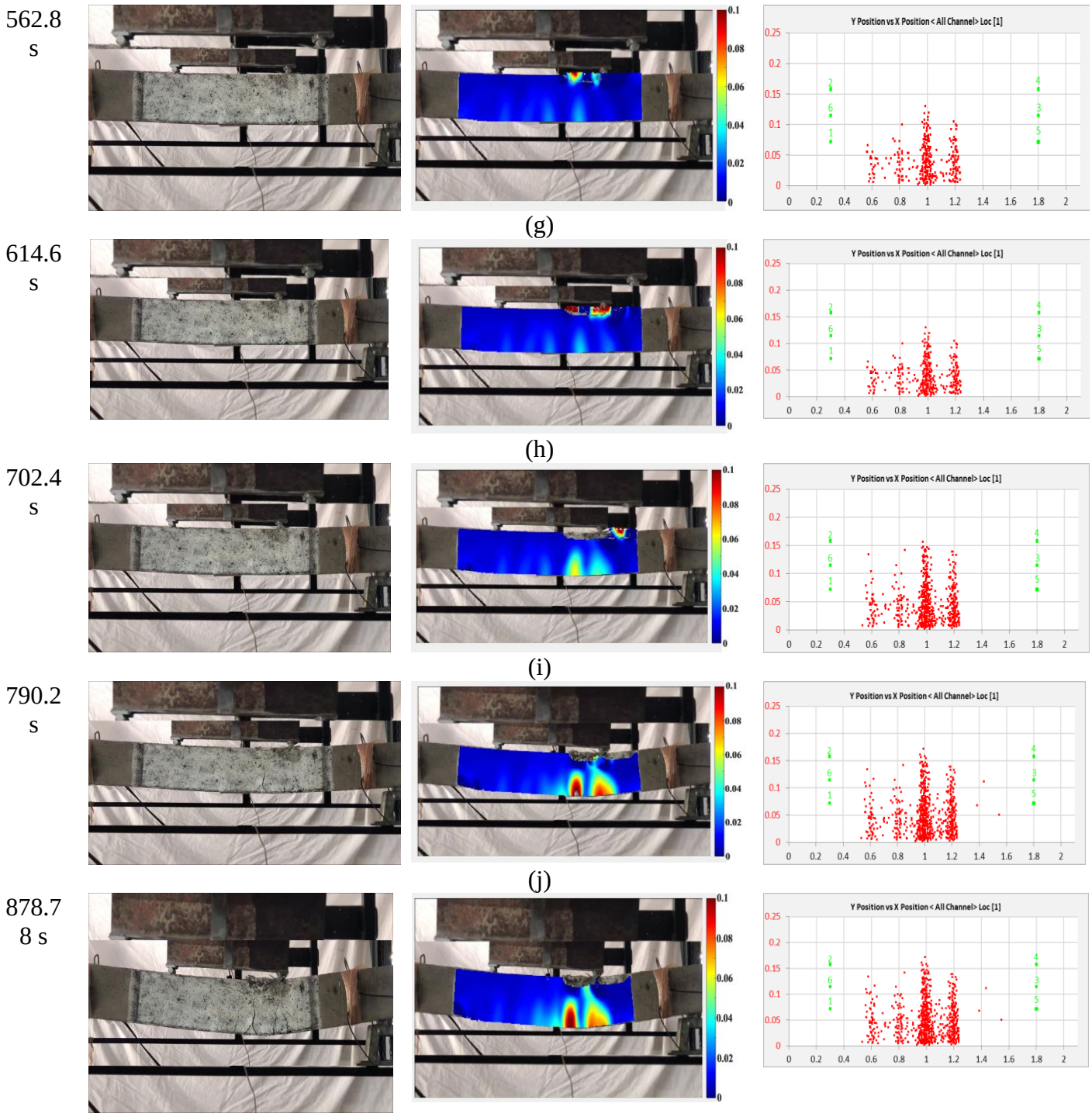

Fig. 7.15: Actual cracked images of S3 RC beam, DIC longitudinal strain profile, and AE events plots (a-k). The red spawn indicates the locations of the AE events: (a) Zero loading stage, (b-c) Initiation of microcracking, (d-j) crack propagation, and (k) final failure.

negative-or-zero strain field (ε_{xx}); as the color evolves more towards the red tones, the strain becomes higher. The red zones, representing a strain (ε_{xx}) of 1% or higher, indicate the presence of cracks **(Hwang et al. 2008 & Ivanov et al. 2014)**. A close matching and coherence are observed between AE-XY plots and DIC longitudinal strain profiles in the form of micro-and macro-

cracking leading to final failure as observed visually in the actual beams at various stages of loading initiation-to-final failure.

Figs 7.13(a), 7.14(a) and 7.15(a) and Figs 7.16(a), 7.17(a) and 7.18(a) shows 2D-DIC analyzed the digital-images for steel RC & GFRP-RC beams initially, showing minimum/zero longitudinal surface strain (ε_{xx}) value, which is indicated by the dark blue color at the surface of the beam. On the other hand, it is also seen that no AE events were recorded on the XY plot at the same time which is further visually validated by the actual image of the beam (**Sharma et al. 2020).**

As the load increases, the 2D-DIC longitudinal strain (ε_{xx}) profile shows diminishing light bluish color at the 1.2 m (Approx.,) for S1, S2, and S3 RC beams in **Figs. 7.13 (b-c), 7.14(b-c) and 7.15 (b-c)** and 0.67m 1.1m and 0.88 m for G1, G2 and G3 RC in **Figs. 7.16 (b-c), 7.17(b-c) and 7.18(b-c)** from the left support. This depicts the variation in the value of longitudinal surface strain (ε_{xx}) values and points towards the possible location of crack since there is no clear discontinuity. This is in coherence with the AE events recorded in the XY plot which can be attributed to the formation of micro-cracking at the bottom of the steel-reinforced & GFRP reinforced concrete beam, at the same location. Hence, both AE-XY event plots and DIC longitudinal strain profiles can very well indicate the cracking initiation process in steel as well as GFRP reinforced concrete beams. The micro-cracking initiates at a load of (~ 5.58, 7.65, and 9.54) kN for S1, S2, and S3 reinforced concrete beams (**Figs. 7.13 (b-c), 7.14(b-c) and 7.15 (b-c)** and (~ 7.89, 8.01, and 10.31) KN for G1, G2, and G3 RC beams as observed in **Figs. 7.16 (b-c), 7.17(b-c) and 7.18(b-c)**. Hence, micro-cracking in two beams which is invisible to the naked eye can be easily picked up by AE-XY event plots and DIC longitudinal strain profiles.

With further increase in loading, it is observed that these micro-cracks open up leading to the formation of macro-cracks indicating crack propagation **(Figs. 7.13 (d-j), 7.14(d-j) and 7.15 (d-j)** for steel RC, **(Figs. 7.16(d-j), 7.17(d-j) and 7.18(d-j)** for GFRP-RC beam. These cracks propagate vertically towards the height of the RC beam as indicated by DIC longitudinal surface strain (ε_{xx}) profile images which change color from light bluish to dark red color at the same location. AE events recorded at the same instants also show the spawn of red dots moving towards the loading region indicating the appearance of a major crack across the height of the steel RC beam at 1.2m and for the GFRP-RC beam at 1.15m from the left support. **Figs. 7.14 (d), 7.15(d) and 7.16 (d)** represent the macro-cracking at a P_{peak} load of (~35.18, 50.80 and 88.94) kN and longitudinal surface strain (ε_{xx}) value of 0.02, 0.050, 0.020 (approx.) in S1, S2, and S3 RC beams as shown by a light bluish color. In the Steel RC beam, the propagating cracks

Time Actual Cracked Image DIC image AE XY Plot

0 s

(a)

61.2 s

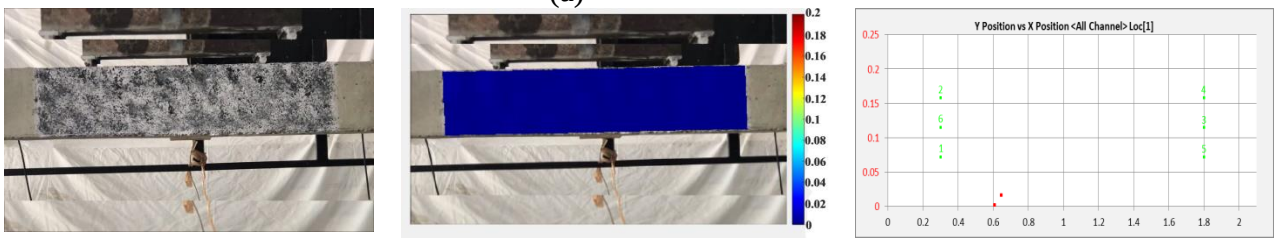

(b)

122.4 s

(c)

183.6 s

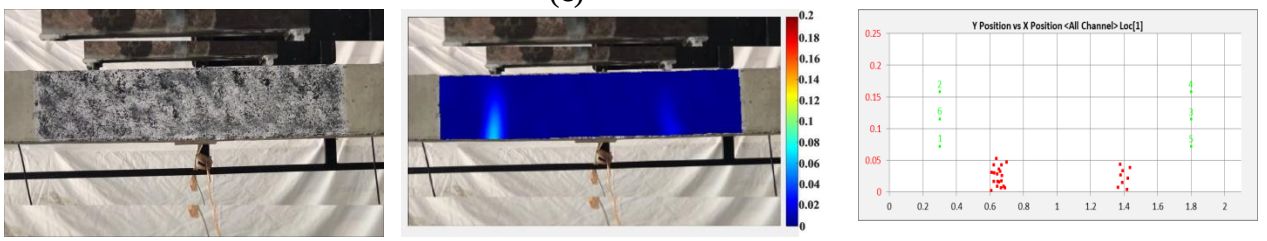

(d)

244.8 s

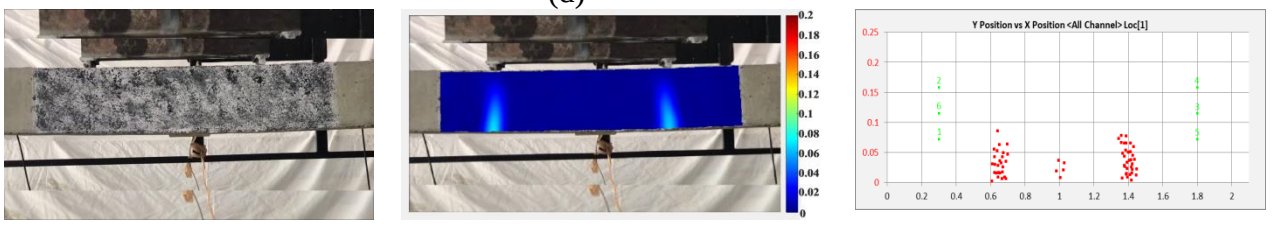

(e)

306 s

(f)

367.2 s

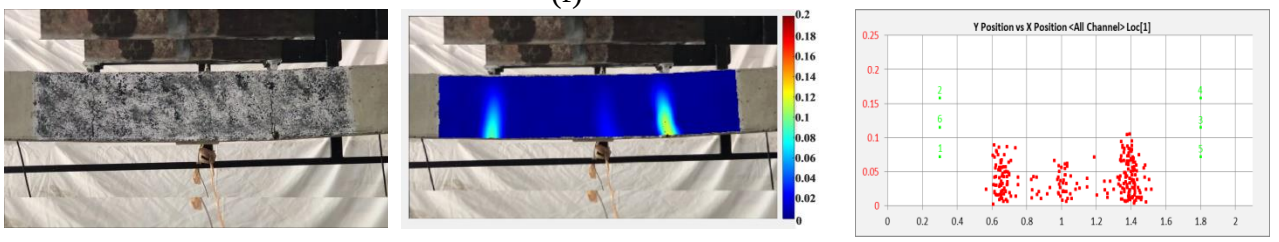

(g)

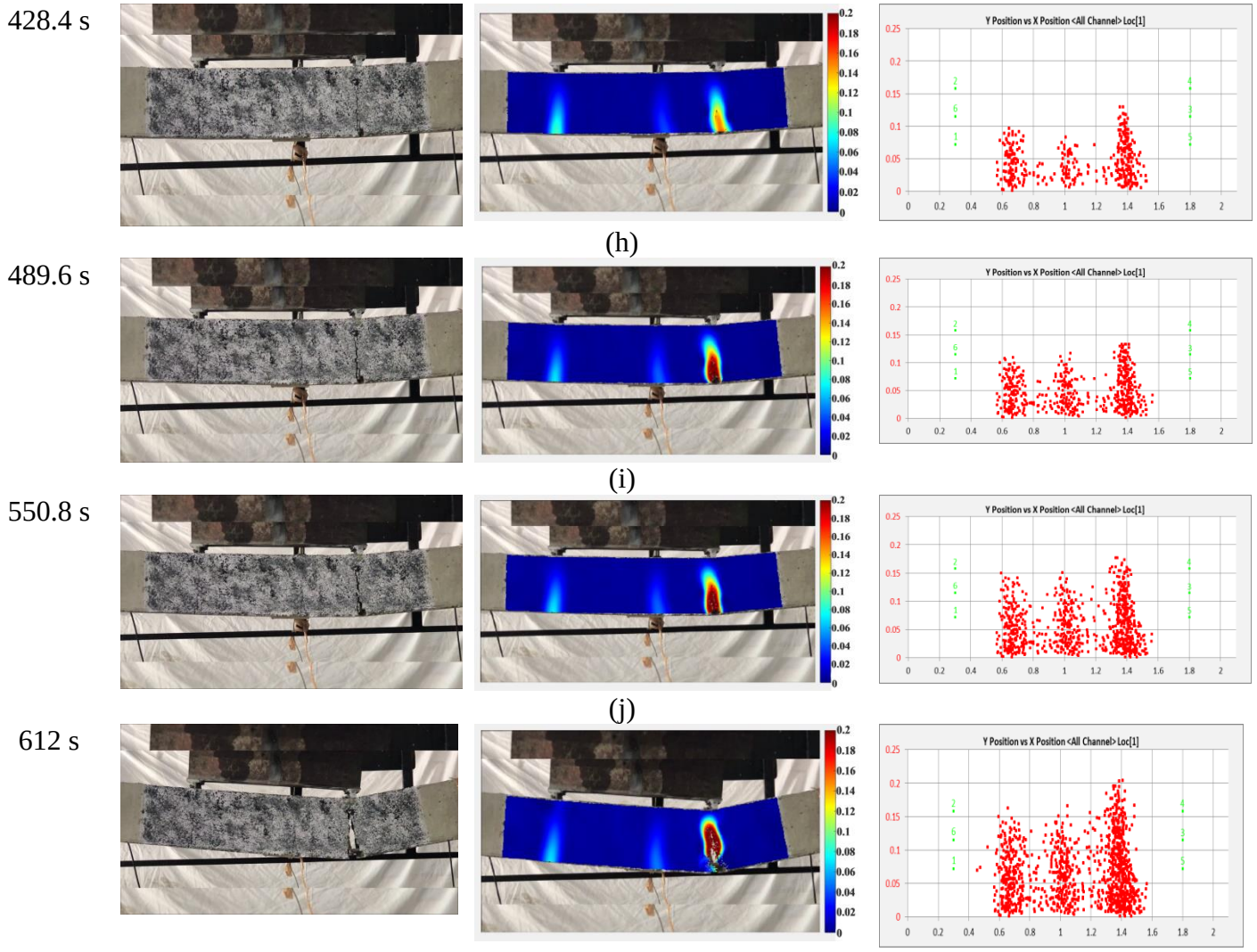

Fig. 7.16: Actual cracked images of G1 RC beam, DIC longitudinal strain profile, and AE events plots (a-k). The red spawn indicates the locations of the AE events: (a) Zero loading stage, (b-c) Initiation of microcracking, (d-j) crack propagation, and (k) final failure.

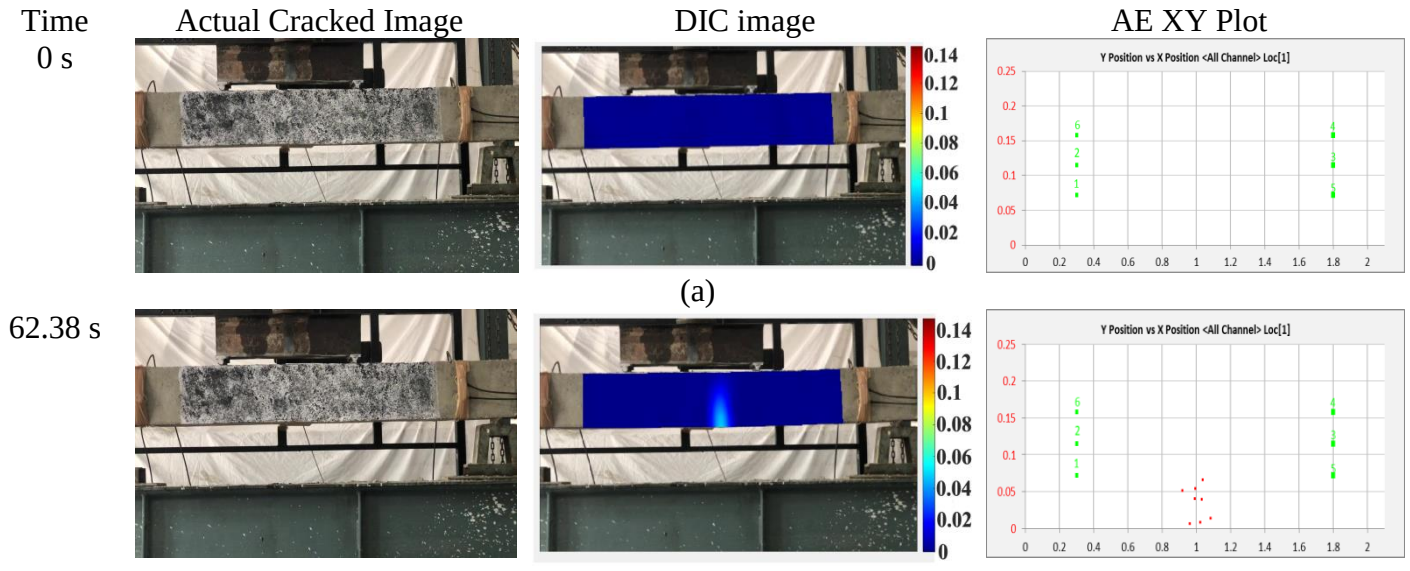

(b)

124.76 s

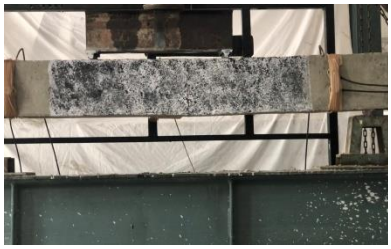

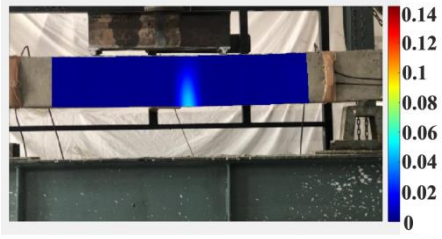

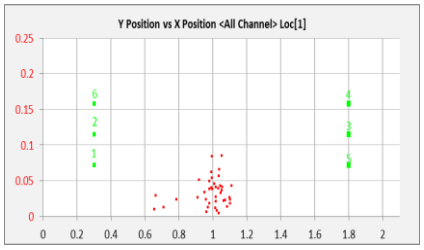

(c)

187.14 s

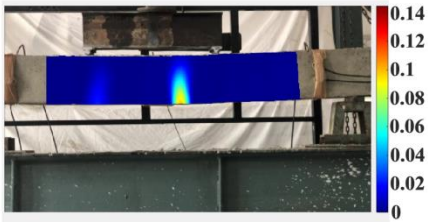

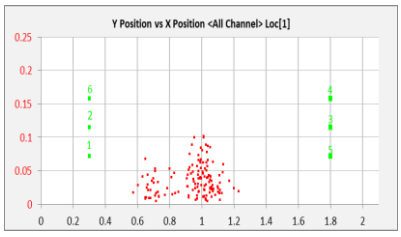

(d)

249.52 s

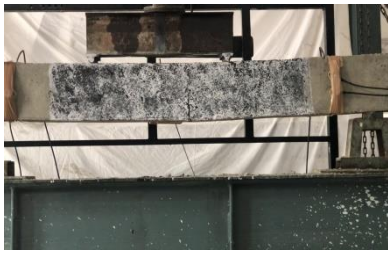

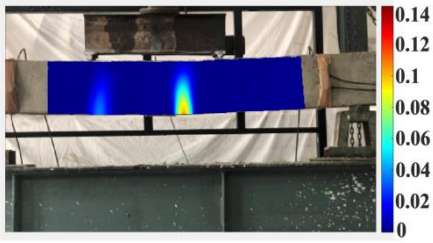

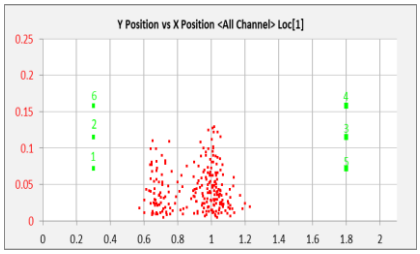

(e)

311.9 s

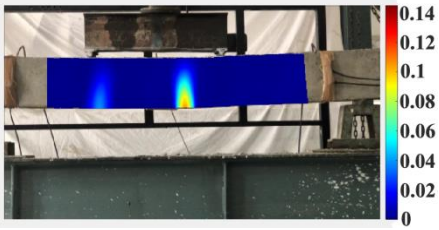

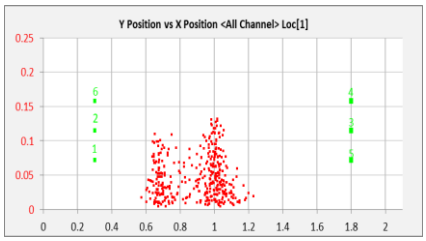

(f)

374.28 s

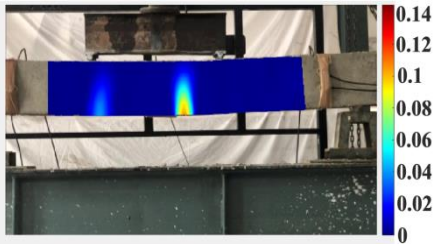

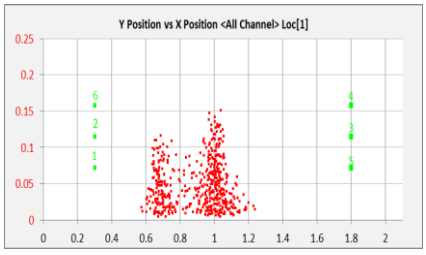

(g)

436.66 s

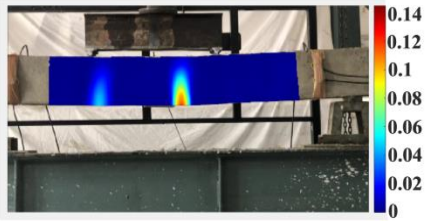

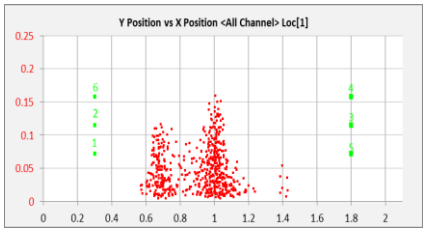

(h)

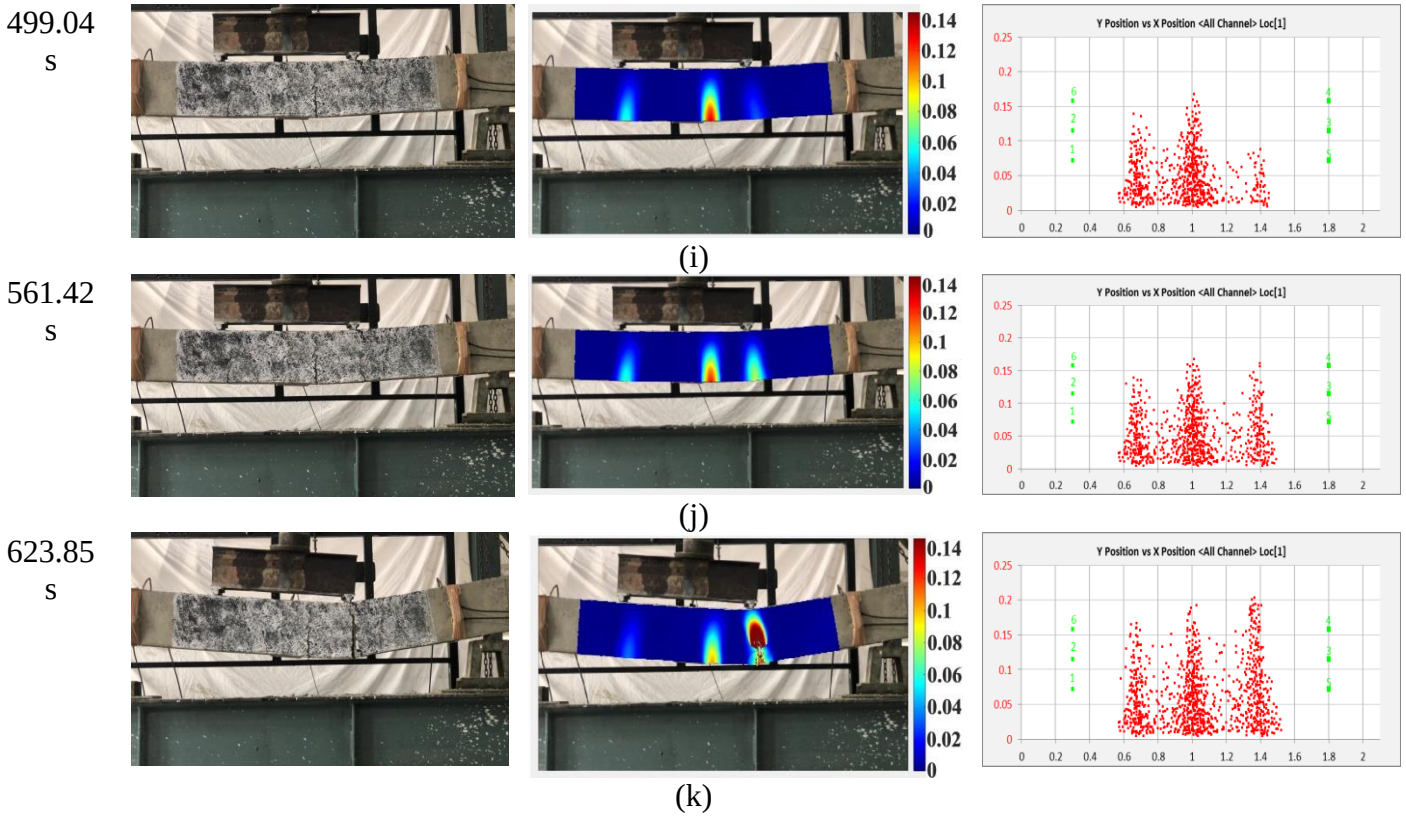

Fig. 7.17: Actual cracked images of G2 RC beam, DIC longitudinal strain profile, and AE events plots (a-k). The red spawn indicates the locations of the AE events: (a) Zero loading stage, (b-c) Initiation of microcracking, (d-j) crack propagation, and (k) final failure.

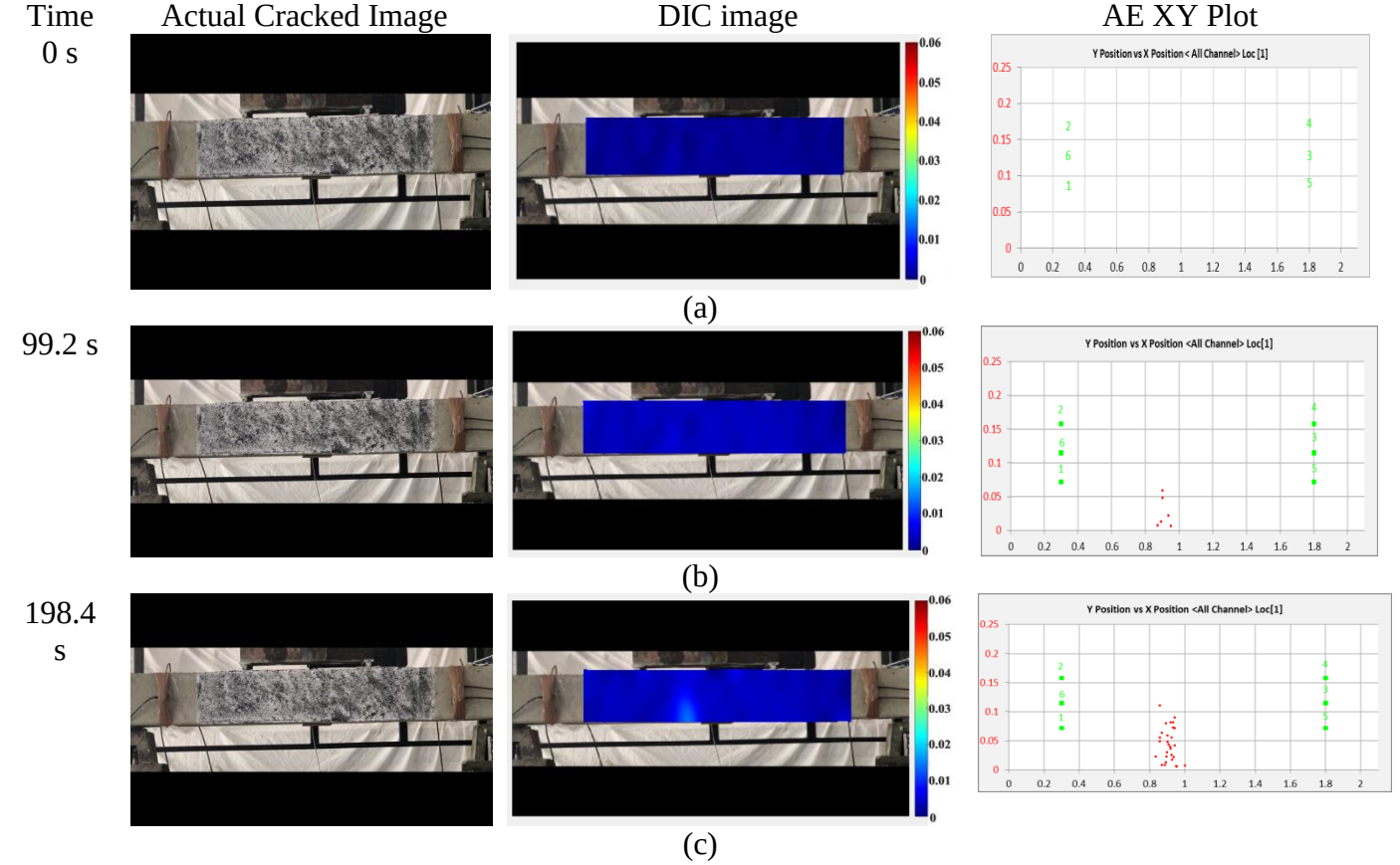

297.6 s

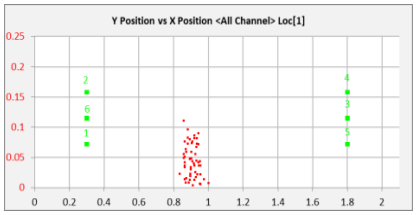

(d)

396.8 s

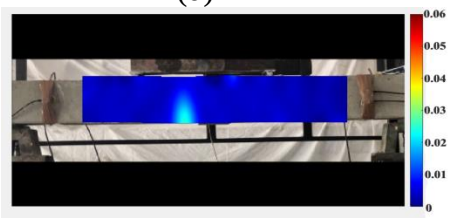

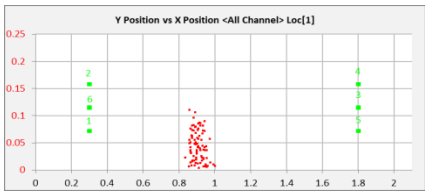

(e)

496.0 s

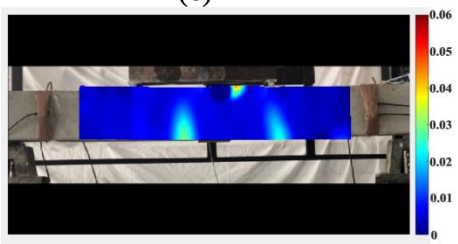

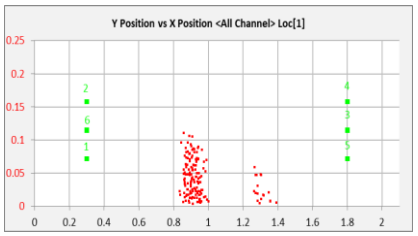

(f)

595.2 s

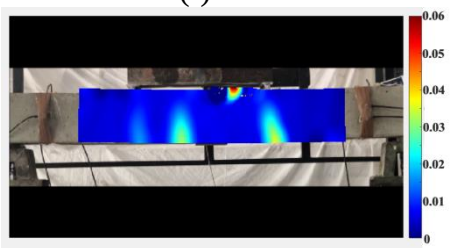

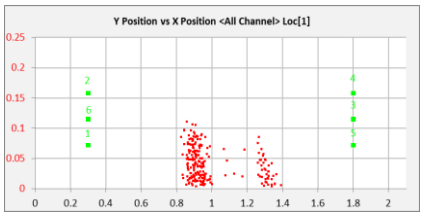

(g)

694.4 s

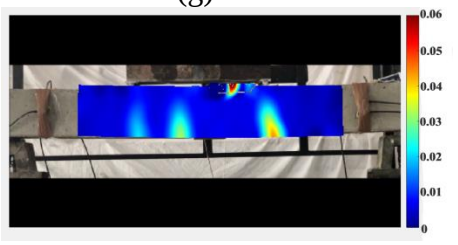

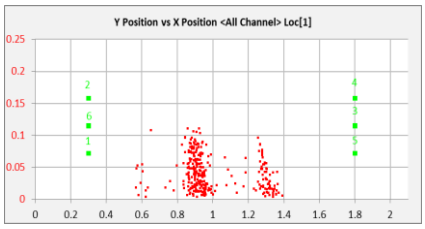

(h)

793.6 s

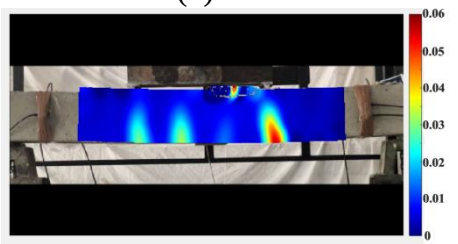

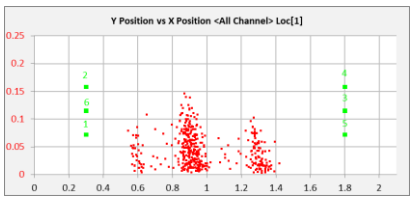

(i)

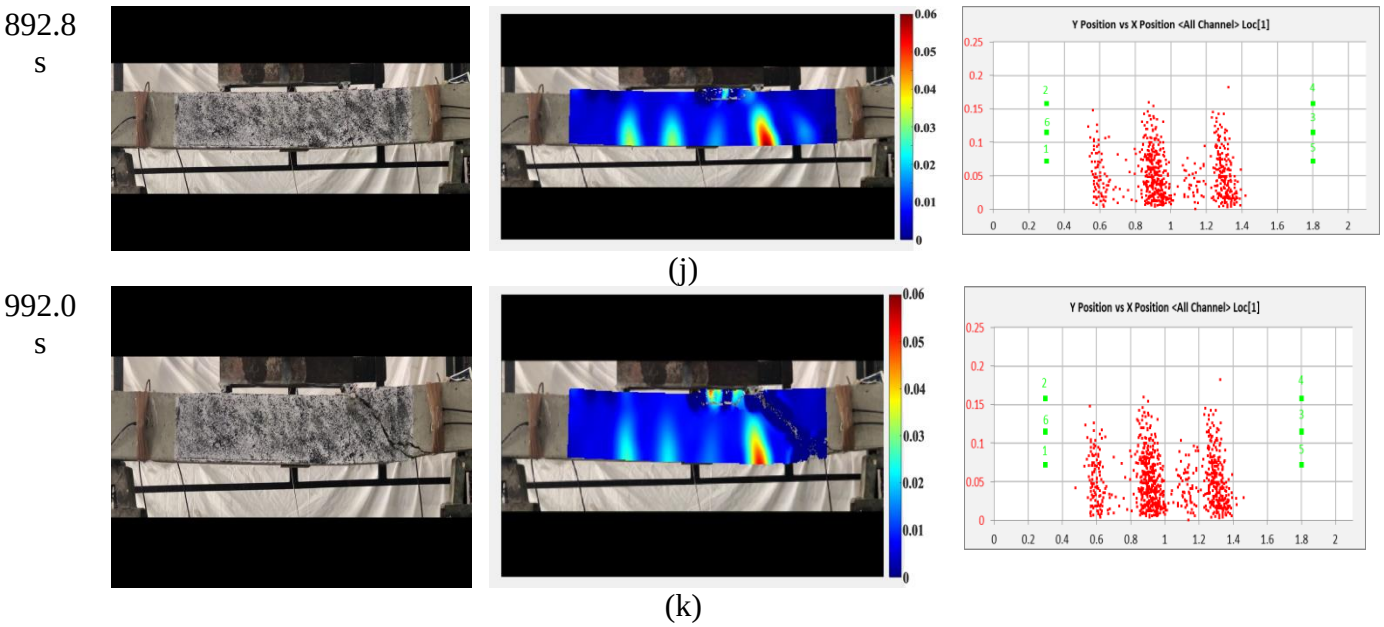

Fig. 7.18: Actual cracked images of G3 RC beam, DIC longitudinal strain profile, and AE events plots (a-k). The red spawn indicates the locations of the AE events: (a) Zero loading stage, (b-c) Initiation of microcracking, (d-j) crack propagation, and (k) final failure.

do not lead to sudden failure of the beam as they are intercepted by the presence of stirrups and show steel yielding leading to flexural failure followed by concrete crushing. **Figs. 7.13 (k), 7.14(k), and 7.15 (k)** show the digital-image at an ultimate load of (~33.43, 47.01 and 82.75) kN and maximum longitudinal surface strain (ε_{xx}) value of 0.15, 0.1116, and 0.091 (approx.) in S1, S2 and S3 RC beams at failure indicated by dark red color which occurs at 1.2 m from the left support and is also confirmed visually by the dense spawn of AE events in AE-XY plots in S-series RC beams.

On the other hand, in GFRP reinforced concrete beam, due to the elastic behavior of GFRP bars, the beam continues to carry load linearly. GFRP reinforced beam fails typically in shear followed by concrete crushing as they are designed as over-reinforced beams to prevent the failure by GFRP rupture**. (Figs. 7.16 (k), 7.17(k), and 7.18(k)** show the digital-image at a P_{peak} as well as an ultimate load of (~51.32, 60.47 and 83.71) kN and maximum longitudinal strain (ε_{xx}) value of 0.180, 0.1316, and 0.058 (approx.) at failure indicated by dark red color which occurs at 1.33 m from the left support and is also confined visually as well as by AE-XY plots in G-series RC beams. It is also observed that the G1 and G2 reinforced concrete beams indicates 20% and 17.92% more longitudinal surface strain (ε_{xx}) and exhibits more central deflection as compared to the S1 and S2 reinforced concrete beam. But as the reinforcement ratio increases to 1.1 % there is a slightly 36.26% decrease in longitudinal

surface strain (ε_{xx}) in the G3 RC beam as compared to the S3 RC beam. It points towards a lower modulus of elasticity of GFRP bars as compared to steel bars.

7.4 CLOSING REMARKS

This chapter presents an insight into the effectiveness of AE and DIC techniques as health monitoring strategies of RC structures. AE parameters of cumulative AE-hits with their amplitudes and cumulative signal strength are well indicative of different damage initiation modes and failure progression in steel RC and GFRP RC beams. Moreover, AE parameters of Average Frequency (AF) and Rise Time (RT), in the form of AF/RT signal values are averaged to distinguish the fracture behavior in steel and GFRP RC beams. Additionally, a pictorial representation of different stages of fracture in steel and GFRP reinforced beams using AE X-Y event maps and longitudinal strain (ε_{xx}) profiles using DIC is presented. As a result, wide scatter in AE event plots and longitudinal surface strain (ε_{xx}) profiles in DIC provide a real-time visual plot of initiation and progression of micro-and-macro cracking inside concrete due to flexural loading in steel as well as GFRP reinforced concrete beams, which is well-validated by actual cracked images of the beams.

CHAPTER 8

CONCLUSIONS

8.0 GENERAL

This research effort investigates the flexural behavior and mechanical performance, damage, and fracture monitoring in steel RC and GFRP RC beams along with AE and DIC techniques. The sudden brittle failure in GFRP RC structures calls for an effective and real-time health monitoring strategy to evaluate its integrity, structural performance, and crack evolution before the damage reaches catastrophic levels.

The focus of the present research is to critically investigate and differentiate between the mechanical behavior and flexural efficacy of steel and GFRP RC beams under 4-point loading with varying percentage of reinforcement ratios and the conclusion drawn from the study have been listed in **Section 8.1.**

Due to the sudden brittle failure in GFRP-reinforced concrete structures, it is essential to evaluate the damage behavior of steel RC and GFRP RC beams using a combination of passive Acoustic Emission technique and non-contact Digital Image Correlation technique is presented and the major conclusion drawn from the study are outlined in **Section 8.2.**

Further, AE and DIC methods have been used to study the fracture monitoring of steel and GFRP bars reinforced concrete beams in flexure. Much before it is evident to the naked eye, AE-XY plots and longitudinal strain profiles produced by DIC provide an early, online, and real-time depiction of increasing AE activity and stresses inside the concrete. The micro-and macro fracture development and progression in steel-RC and GFRP-RC at various stages of loading were effectively depicted by AE in combination with DIC, and the conclusions are presented in **Section 8.3.**

8.1 FLEXURAL PERFORMANCE

- The load-deflection plot of steel reinforced and GFRP reinforced concrete beams show contrasting profiles. With increasing reinforcement ratio, steel-reinforced beams typically show an increase in ultimate load-carrying capacity, shrinking plastic zone with reduced ductility, and failure taking place at the much lower strains by steel yielding followed by concrete crushing. On the other hand, GFRP reinforced beams exhibit bi-linear load-deflection response up to the failure without any yielding and exhibit higher ultimate load-carrying capacities and deflections due to their low elastic modulus as compared to steel reinforced beams indicating enhanced ductility and ultimate strength.

- An increase in reinforcement ratio resulted in lesser deflections at ultimate loads in both types of the beams. Because of the low elastic modulus of the GFRP bars, GFRP RC beams deflect more as compared to steel RC beams and the mid-span deflections observed in GFRP reinforced beams were 23.72%, 39.41%, and 11.32% more than in steel-reinforced concrete beams at 0.33%, 0.52%, and 1.1% reinforcement ratio. Furthermore, the ultimate moment carrying capacity of GFRP reinforced beams was 34.35 % 10.08 % more as compared to steel reinforced beams at 0.33%, and 0.52% reinforcement ratio due to the high tensile strength of GFRP bars. But when the reinforcement ratio increases to 1.1%, the ultimate moment carrying capacity decreases by 5.2% as compared to steel reinforced beams due to the sudden over-reinforced shear failure.
- With an increasing reinforcement ratio in GFRP RC beams, the post-cracking bending stiffness improves slightly due to an increase in the load-carrying capacity leading to higher stiffness. But reserve strength or ductility reduces since the increase in GFRP reinforcement leads to reducing deflections at higher load carrying capacities leading to the overall reduction in the area under the load-deflection plot, when compared to steel reinforced concrete beams. The post cracking bending stiffness of GFRP reinforced beams was 28.06%, 85.04%, and 41.61% less as compared to steel reinforced beams at the same reinforcement ratios 0.33%, 0.52% and 1.11%. The average energy absorption capacity (E) of GFRP reinforced beam was observed to be 26.33% and 22.94% more when compared with steel reinforced at 0.33% and 0.52% reinforcement ratio. When the reinforcement ratio increases to 0.52% to 1.1% for GFRP reinforced beams the energy absorption capacity reduces by 7.85 % when compared to steel reinforced concrete beams due to the sudden over-reinforced shear failure of GFRP reinforced concrete beams.
- The failure mode of steel and GFRP reinforced concrete beams may be reliably predicted using sectional analysis, which is used for conventional RC beams. The ratio of beam reinforcement to calculated balanced reinforcement can be utilized as a failure mode which is indicative of typical failures in steel as well as GFRP reinforced beams. All the steel RC beams failed in flexure due to steel yielding, while all GFRP RC beams failed in shear due to concrete crushing irrespective of reinforcement ratio.

8.2 DAMAGE MONITORING USING AE AND DIC

- Various AE parameters not only determine the onset and development of cracking but can also be used to classify the cracking modes in the steel-reinforced and GFRP reinforced concrete beams. Progressive increase in cumulative AE hits and their varying amplitudes

directly point towards increasing damage levels experienced by steel and GFRP reinforced beams at different stages of flexural loading observed in the form of invisible and visible cracking in concrete. GFRP reinforced concrete beams exhibited increased number of cumulative AE hits of higher amplitudes as compared to steel reinforced beams due to their low elastic modulus and different bond characteristics. It is also well supported by the larger number of **Knees** indicated by a steep rise/jump in the CSS plot. Cumulative AE hits observed in GFRP reinforced beams were 26.47%, 17.97%, and 22.64% more than in steel-reinforced beams with reinforcement ratios of 0.33%, 0.52%, and 1.11%. This is due to the low elastic modulus of the GFRP bars as compared with steel bars.

- The Average Frequency (AF) and Rise Angle (RA) value plots can be used to predict the type of cracks experienced by steel-reinforced and GFRP reinforced concrete beams. The change in these values of AE parameters correspond well to the actual damage mechanisms in the two differently reinforced concrete beams as below:
  - ✓ High AF and low RA value indicate pure bending cracks in steel-reinforced beams at the microcracking level, whereas low AF and high RA value point towards shear cracks in GFRP reinforced beams initially.
  - ✓ At the macro cracking level, a marginal increase in RA and the drop of AF indicates flexure-failure by steel yielding followed by concrete crushing in steel-reinforced beams. On the other hand, in the GFRP RC beam, a significant increase in AF value and a decrease in RA value indicate sudden shear failure followed by concrete crushing.
- It is also demonstrated that the behaviour of differently reinforced beams under flexural loading is well categorized by the AE parameters of the Average frequency (AF) and Duration (μs) with time. This analysis show significant drop in average frequency and significant jump AE duration at the same time indicates critical failure points in steel RC and GFRP RC beams. These changes are better indicative of damage than the load-deflection plots. It is also observed that the moving average line of AF was high and the duration line was low in the GFRP RC beams in comparison to the steel RC beams. This is due to the fact that GFRP bars have different bond characteristics, and a lower elastic modulus, and deflect more than steel bars, causing AE activity to accumulate leading to the high frequency of hits. It can go a long way in developing real-time damage monitoring and evaluation tools for differently reinforced concrete beams.
- AE and DIC have the potential to serve as an online non-destructive monitoring tool that can map the development of cracking in RC structures. A clear trajectory of transverse

vertical cracks is also observed from AE XY event plots as well as DIC images. This is also validated by the actual images of the cracked beams.

- AE technique offers a qualitative insight into the fracture/damages process in concrete by studying variations in the amplitude of AE hits, AE XY events map and DIC strain gives a pictorial representation of cracking in terms of longitudinal surface strains (ε_{xx}) and displacements, and much before the actual cracking is visible to the naked eye. Thus, AE events plot and DIC provide a reliable and real-time indication of the initiation and progression of cracking inside concrete in steel-reinforced and GFRP reinforced concrete beams undergoing flexural loading, much before these are visible to the naked eye.

8.3 FRACTURE MONITORING USING AE AND DIC

- In two distinct types of RC beams, AE parameters of cumulative AE-hits and their amplitudes and Cumulative Signal Strength (CSS) are well indicative of different damage initiation modes and failure progression mechanisms. GFRP reinforced concrete beams exhibited a larger number of cumulative AE hits of higher amplitudes, as well as a sudden and steep rise in CSS curves with high fluctuations compared to steel reinforced beams.

- The entire duration of the flexural experiment in steel & GFRP reinforced concrete beams is divided into 10 equal portions to aid in fracture analysis. AE parameters of Average Frequency (AF) and Rise Time (RT) values are averaged and help to differentiate the cracking modes in steel & GFRP reinforced concrete beams. The fracture behavior and type of cracking in steel and GFRP reinforced concrete beams may be predicted using AF and RT plots as below:
  - ✓ At the initial stage or low loads steps, the steel-reinforced concrete beam has a high AF and a shorter RT signal, indicating that the fracture is dominated by pure flexural cracks. Due to the low elastic modulus of the GFRP bars, low AF and longer RT signal was observed in GFRP reinforced concrete beams, with fracture dominance towards shear cracks.
  - ✓ At the final stage or high loads steps, a slight longer RT signal and a reduction (low) in AF suggest ultimate flexure failure due to steel yielding followed by concrete crushing in a steel-reinforced concrete beam. On the contrary, a considerable increase in AF value and drop in RT signal value suggests sudden shear failure followed by concrete crushing in the GFRP reinforced concrete beam.
- AE X-Y plots along with AE hit analysis accompanied by DIC strains demonstrate the progressively damaged zones surrounding the cracked section in steel as well as GFRP reinforced concrete beams. The emergence of initial micro-and later stage macro cracking is

well be predicted in AE and DIC monitoring indicative of damage-prone zones in steel and GFRP reinforced concrete beams. The surface strain field (ε_{xx}) calculated using DIC analysis and AE events maps are compared with actual cracked images obtained from the experiment were found to be accurately matching.

Hence, it can be concluded that the combined use of AE and DIC has the potential to serve as an online non-destructive tool to monitor and map the initiation, progression, and localization of damage and cracking in steel, as well as GFRP, reinforced concrete beams. The thesis suggests a judicious combination of AE and DIC techniques for the same. AE can successfully localize the initiation and progression of cracks; it gives limited information about the damage severity as measured by the amplitude of AE hits. Similarly, DIC offers to measure the relative displacement of selected points using virtual extensometers using a camera which reduces the measurement costs by replacing conventional LVDT's and strain gauges. But the adequacy of the outcomes of the DIC systems is dependent on the image quality, presence of dust on the testing surface, and lenses. The combined application of these techniques is attempted to overcome their shortcomings. The information provided by DIC will help in validating AE observations, as visible changes in the strain field can be correlated well with the emissions recorded in AE.

8.4 RECOMMENDATIONS FOR FUTURE RESEARCH

From the research carried out in this work, following is recommended as a future scope of work:

1. Investigate and compare the flexural performance and behavior of differently reinforced concrete structures using steel and other FRP as bar reinforcement like Aramid, Basalt, and Carbon Fibre bars.
2. Characterization of the damage and fracture process in differently reinforced concrete beams subjected to various kinds of loadings (shear, fatigue, and impact) condition using advanced NDT tools of AE, DIC and combined with other advanced NDT tools like thermography, etc.
3. Develop the analysis and design procedure for differently reinforced concrete beams utilizing different reinforcement like Aramid, Basalt, and Carbon fiber bars.
4. Investigate AE and DIC techniques for damage monitoring in FRP reinforced concrete specimens under dynamic or quasi-dynamic loading.

5. Development of Damage Models or Finite Element Models which can be employed in cases where DIC and AE are difficult to apply like in FRP reinforced concrete subjected to extreme loadings.

List of Publications

- ✓ Sharma, G., Sharma, S., & Sharma, S. K. (2020). Monitoring structural behaviour of concrete beams reinforced with steel and GFRP bars using acoustic emission and digital image correlation techniques. ***Structure and Infrastructure Engineering, 1-16. https://doi.org/10.1080/15732479.2020.1836661.***
- ✓ Sharma, G., Sharma, S., & Sharma, S. K. (2021). Fracture monitoring of steel and GFRP reinforced concrete beams using acoustic emission and digital image correlation techniques. ***Structural Concrete. https://doi.org/10.1002/suco.202000650.***
- ✓ Sharma, G., Sharma, S., & Sharma, S. K. (2021). Non-Destructive Evaluation of Steel and GFRP Reinforced Beams using AE and DIC Techniques. ***Structure Engineering and Mechanics.***77 (5), 637-650***. http://dx.doi.org/10.12989/sem.2021.77.5.637.***
- ✓ Detection of Surface Cracking in Steel and GFRP RC beams Using Acoustic Emission and Digital Image Processing Techniques, Submitted to Structures, Elsevier (Under Review)
- ✓ Moment-Curvature behaviour of steel and GFRP reinforced beam by combined used of AE and DIC Techniques (Under Review)

References

- Abbood, I. S., aldeen Odaa, S., Hasan, K. F., & Jasim, M. A. (2021). Properties evaluation of fiber reinforced polymers and their constituent materials used in structures–A review. *Materials Today: Proceedings*, *43*, 1003-1008.
- Abu-Obaida, A., El-Maaddawy, T., & El-Ariss, B. (2020). Numerical simulation of double-sided concrete corbels internally-reinforced with GFRP bars. *Composites Part C: Open Access*, *2*, 100040.
- ACI 318 (2008). Building code requirements for structural concrete and commentary. American Concrete Institute; Farmington Hills, MI, USA.
- ACI 440.1R-06 (2006). Guide for the Design and Construction of Concrete Reinforced with FRP Bar, American Concrete Institute; Farmington Hills, MI, USA.
- ACI Committee. (2015). Guide for the Design and Construction of Structural Concrete Reinforced with Fiber-Reinforced Polymer Bars. ACI440. 1R-15, American Concrete Institute, Farmington Hills, MI, 88(2), 546-565.
- Adam, M. A., Said, M., Mahmoud, A. A., & Shanour, A. S. (2015). Analytical and experimental flexural behavior of concrete beams reinforced with glass fiber reinforced polymers bars. *Construction and Building Materials*, *84*, 354-366.
- Afifi, A. J., & Ashour, W. M. (2012). Image retrieval based on content using color feature. *International Scholarly Research Notices*.
- Ahmed, S. F. U., Maalej, M., & Mihashi, H. (2007). Cover cracking of reinforced concrete beams due to corrosion of steel. *ACI materials journal*, *104*(2), 153.
- Alam, S. Y., Saliba, J., & Loukili, A. (2014). Fracture examination in concrete through combined digital image correlation and acoustic emission techniques. *Construction and Building Materials*, *69*, 232-242.
- Alhozaimy, A., Hussain, R. R., Al-Negheimish, A., Singh, J. K., & Singh, D. D. N. (2018). Protection against Reinforcement Corrosion Using Phosphoric Acid-Based Rust Converter. *ACI Materials Journal*, *115*(6).
- Allahvirdizadeh, R., Rashetnia, R., Dousti, A., & Shekarchi, M. (2011, September). Application of polymer concrete in repair of concrete structures: A literature review. In *The 4th International Conference on Concrete Repair, Dresden, Germany*.

- Almusallam, A. A., Al-Gahtani, A. S., & Aziz, A. R. (1996). Effect of reinforcement corrosion on bond strength. *Construction and building materials*, *10*(2), 123-129.
- Alsayed, S. H. (1998). Flexural behaviour of concrete beams reinforced with GFRP bars. *Cement and Concrete Composites*, *20*(1), 1-11.
- Al-Sunna, R., Pilakoutas, K., Hajirasouliha, I., & Guadagnini, M. (2012). Deflection behaviour of FRP reinforced concrete beams and slabs: An experimental investigation. *Composites Part B: Engineering*, *43*(5), 2125-2134.
- Amran, Y. M., Alyousef, R., Rashid, R. S., Alabduljabbar, H., & Hung, C. C. (2018, November). Properties and applications of FRP in strengthening RC structures: A review. In *Structures* (Vol. 16, pp. 208-238). Elsevier.
- Apostolopoulos, C. A., Koulouris, K. F., & Apostolopoulos, A. C. (2019). Correlation of surface cracks of concrete due to corrosion and bond strength (between steel bar and concrete). *Advances in Civil Engineering*.
- Ascione, L., Mancusi, G., & Spadea, S. (2010). Flexural behaviour of concrete beams reinforced with GFRP bars. *Strain*, *46*(5), 460-469.
- ASTM D7205 (2006), Standard test method for tensile properties of fiber reinforced polymer matrix composite bars, ASTM International; West Conshohocken, Pennsylvania, USA.
- Balendran, R. V., Rana, T. M., Maqsood, T., & Tang, W. C. (2002). Application of FRP bars as reinforcement in civil engineering structures. *Structural Survey*.
- Barile, C., Casavola, C., Pappalettera, G., & Kannan, V. P. (2020). Application of different acoustic emission descriptors in damage assessment of fiber reinforced plastics: A comprehensive review. *Engineering Fracture Mechanics*, *235*, 107083.
- Barris, C., Torres, L., Turon, A., Baena, M., & Catalan, A. (2009). An experimental study of the flexural behaviour of GFRP RC beams and comparison with prediction models. *Composite Structures*, *91*(3), 286-295.
- Batis, G., & Rakanta, E. (2005). Corrosion of steel reinforcement due to atmospheric pollution. *Cement and concrete composites*, *27*(2), 269-275.
- Bazan, P., Nosal, P., Wierzbicka-Miernik, A., & Kuciel, S. (2021). A novel hybrid composites based on biopolyamide 10.10 with basalt/aramid fibers: Mechanical and thermal investigation. *Composites Part B: Engineering*, 109125.

- Behnia, A., Chai, H. K., & Shiotani, T. (2014). Advanced structural health monitoring of concrete structures with the aid of acoustic emission. *Construction and Building Materials*, *65*, 282-302.
- Bhaskaran, R., Palaniswamy, N., Rengaswamy, N. S., & Jayachandran, M. (2005). A review of differing approaches used to estimate the cost of corrosion (and their relevance in the development of modern corrosion prevention and control strategies). *Anti-Corrosion Methods and Materials*.
- Bhowmik, S., Dubey, S., & Ray, S. (2019). Investigation on fracture processes of concrete. *Frattura ed Integrità Strutturale*, *13*(48), 419-428.
- Blaber, J., Adair, B., & Antoniou, A. (2015). Ncorr: open-source 2D digital image correlation matlab software. *Experimental Mechanics*, *55*(6), 1105-1122.
- Bodzak, P. (2019). Flexural behaviour of concrete beams reinforced with different grade steel and strengthened by CFRP strips. *Composites Part B: Engineering*, *167*, 411-421.
- Bonacci, J. F., & Maalej, M. (2000). Externally bonded FRP for service-life extension of RC infrastructure. *Journal of Infrastructure systems*, *6*(1), 41-51.
- Boyle, H. C., & Karbhari, V. M. (1994). Investigation of bond behavior between glass fiber composite reinforcements and concrete. *Polymer-Plastics technology and engineering*, *33*(6), 733-753.
- Bruck, H. A., McNeill, S. R., Sutton, M. A., & Peters, W. H. (1989). Digital image correlation using Newton-Raphson method of partial differential correction. *Experimental mechanics*, *29*(3), 261-267.
- Burud, N. B., & Kishen, J. C. (2021). Response based damage assessment using acoustic emission energy for plain concrete. *Construction and Building Materials*, *269*, 121241.
- Burud, N., & Kishen, J. C. (2020). Damage detection using wavelet entropy of acoustic emission waveforms in concrete under flexure. *Structural Health Monitoring*, 1475921720957096.
- Cadenazzi, T., Dotelli, G., Rossini, M., Nolan, S., & Nanni, A. (2019). Life-cycle cost and life-cycle assessment analysis at the design stage of a fiber-reinforced polymer-reinforced concrete bridge in Florida. *Advances in Civil Engineering Materials*, *8*(2), 128-151.
- Canadian Standards Association (CSA). (2002). "Design and Construction of Building Structures with Fibre-Reinforced Polymers". Canadian Standards Association, S806-02, Ontario, Canada.

- Canadian Standards Association (CSA). (2012). “Design and Construction of Building Structures with Fibre-Reinforced Polymers”. Canadian Standards Association, S806-12, Ontario, Canada.
- Castel, A., François, R., & Arliguie, G. (2000). Mechanical behaviour of corroded reinforced concrete beams—Part 2: Bond and notch effects. *Materials and Structures*, *33*(9), 545-551.
- Chigondo, M., & Chigondo, F. (2016). Recent natural corrosion inhibitors for mild steel: an overview. *Journal of Chemistry*, *2016*.
- Chitsazan, I., Kobraei, M., Jumaat, M. Z., & Shafigh, P. (2010). An experimental study on the flexural behaviour of FRP RC bemas and comparison of the ultimate moment capacity with ACI. *Journal of civil engineering and construction technology*, *1*(2), 27-42.
- Choi, S., & Shah, S. P. (1997). Measurement of deformations on concrete subjected to compression using image correlation. *Experimental mechanics*, *37*(3), 307-313.
- Cope, A., Bai, Q., Samdariya, A., & Labi, S. (2013). Assessing the efficacy of stainless steel for bridge deck reinforcement under uncertainty using Monte Carlo simulation. *Structure and Infrastructure Engineering*, *9*(7), 634-647.
- Corrado, C., Claudio, G., Nicola, L., Vincenzo, P., Joseph, Q., & Gianvittorio, R. (2017). Acoustic Emissions analysis of a four-point bending test on a Reinforced Concrete beam. In *MATEC Web of Conferences* (Vol. 125, p. 05014). EDP Sciences.
- Dai, S., Liu, X., & Nawnit, K. (2019). Experimental study on the fracture process zone characteristics in concrete utilizing DIC and AE methods. *Applied Sciences*, *9*(7), 1346.
- De Sutter, S., Verbruggen, S., Tysmans, T., & Aggelis, D. G. (2017). Fracture monitoring of lightweight composite-concrete beams. *Composite Structures*, *167*, 11-19.
- Destrebecq, J. F., Toussaint, E., & Ferrier, E. (2011). Analysis of cracks and deformations in a full scale reinforced concrete beam using a digital image correlation technique. *Experimental Mechanics*, *51*(6), 879-890.
- Dhawan, S. K., Bindal, A., Bhalla, S., & Bhattacharjee, B. (2019). Expected residual service life of reinforced concrete structures from current strength considerations. *Advances in Structural Engineering*, *22*(7), 1631-1643.
- El Maaddawy, T., Soudki, K., & Topper, T. (2005). Long-term performance of corrosion-damaged reinforced concrete beams. *ACI Structural Journal*, *102*(5), 649.
- El-Hacha, R., Mirmiran, A., Cook, A., & Rizkalla, S. (2011). Effectiveness of surface-applied corrosion inhibitors for concrete bridges. *Journal of materials in civil engineering*, *23*(3), 271-280.

- El-Hassan, H., & El Maaddawy, T. (2019). Microstructure characteristics of GFRP reinforcing bars in harsh environment. *Advances in Materials Science and Engineering*.
- El-Nemr, A., Ahmed, E. A., & Benmokrane, B. (2013). Flexural Behavior and Serviceability of Normal-and High-Strength Concrete Beams Reinforced with Glass Fiber-Reinforced Polymer Bars. *ACI structural journal*, *110*(6).
- El-Salakawy, E., Benmokrane, B., & Desgagné, G. (2003). Fibre-reinforced polymer composite bars for the concrete deck slab of Wotton Bridge. *Canadian Journal of Civil Engineering*, *30*(5), 861-870.
- Elsayed, A., Ahmed, M., & Hassan, H. (2015). Behavior of beams reinforced with different types of bars from glass fiber reinforced polymer (GFRP), Carbon fiber Reinforced Polymer (CFRP) and high tensile steel (HTS) Under Static Load. *IOSR Journal Of Mechanical And Civil Engineering*, *12*(4), 66-97.
- Escórcio, P., & França, P. M. (2016). Experimental study of a rehabilitation solution that uses GFRP bars to replace the steel bars of reinforced concrete beams. *Engineering Structures*, *128*, 166-183.
- Fayyad, T. M., & Lees, J. M. (2014). Application of digital image correlation to reinforced concrete fracture. *Procedia Materials Science*, *3*, 1585-1590.
- Feng, M. (2014). Modern bridges in China. *Structure and Infrastructure Engineering*, *10*(4), 429-442. Knippers, J., & Gabler, M. (2008). The FRP road bridge in Friedberg Germany–new approaches to a holistic and aesthetic design. In *Fourth International Conference on FRP Composites in Civil Engineering (CICE2008)*.
- Flansbjer, M., & Lindqvist, J. E. (2018). Meso-mechanical study of cracking process in concrete subjected to tensile loading. *Nordic Concrete Research*, *59*(1), 13-29.
- Fowler, D. W. (1999). Polymers in concrete: a vision for the 21st century. *Cement and concrete composites*, *21*(5-6), 449-452.
- Francois, R., & Maso, J. C. (1988). Effect of damage in reinforced concrete on carbonation or chloride penetration. *Cement and Concrete Research*, *18*(6), 961-970.
- Frangopol, D., & Tsompanakis, Y. (Eds.). (2014). *Maintenance and safety of aging infrastructure: Structures and infrastructures book series, vol. 10* (Vol. 10). CRC press.
- Garhwal, S., Sharma, S., & Sharma, S. K. (2021). Acoustic emission monitoring of RC beams corroded to different levels under flexural loading. *Arabian Journal for Science and Engineering*, *46*(5), 4319-4335.

- Garhwal, S., Sharma, S., & Sharma, S. K. (2021). Monitoring the flexural performance of GFRP repaired corroded reinforced concrete beams using passive acoustic emission technique. *Structural Concrete*, *22*(1), 198-214.
- Getzlaf, D. D. (2012). *An investigation into the flexural behaviour of GFRP reinforced concrete beams*. University of Toronto (Canada).
- Gholizadeh, S., Leman, Z., & Baharudin, B. H. T. (2015). A review of the application of acoustic emission technique in engineering. *Structural Engineering and Mechanics*, *54*(6), 1075-1095.
- Giannaros, P., Kanellopoulos, A., & Al-Tabbaa, A. (2016). Sealing of cracks in cement using microencapsulated sodium silicate. *Smart Materials and Structures*, *25*(8), 084005.
- Goldston, M. W., Remennikov, A., & Sheikh, M. N. (2017). Flexural behaviour of GFRP reinforced high strength and ultra high strength concrete beams. *Construction and Building Materials*, *131*, 606-617.
- Goldston, M., Remennikov, A., & Sheikh, M. N. (2016). Experimental investigation of the behaviour of concrete beams reinforced with GFRP bars under static and impact loading. *Engineering Structures*, *113*, 220-232.
- Gribniak, V., Rimkus, A., Torres, L., & Jakstaite, R. (2017). Deformation analysis of reinforced concrete ties: Representative geometry. *Structural Concrete*, *18*(4), 634-647.
- Gu, L., & Meng, X. H. (2016). Review on research and application of stainless steel reinforced concrete. In *MATEC Web of Conferences* (Vol. 63, p. 03003). EDP Sciences.
- Gudonis, E., Timinskas, E., Gribniak, V., Kaklauskas, G., Arnautov A.K. and Tamulėnas,V. (2013). FRP reinforcement for concrete structures: A state-of-the-art review of application and design. *Engineering Structures and Technologies*, **5**(4) 147-158.
- Hamrat, M., Boulekbache, B., Chemrouk, M., & Amziane, S. (2016). Flexural cracking behavior of normal strength, high strength and high strength fiber concrete beams, using Digital Image Correlation technique. *Construction and Building Materials*, *106*, 678-692.
- Hansson, C. M. (1995). Concrete: the advanced industrial material of the 21st century. *Metallurgical and materials transactions B*, *26*(3), 417-437.
- Hawileh, R. A., Abdalla, J. A., Al Tamimi, A., Abdelrahman, K., & Oudah, F. (2011). Behavior of corroded steel reinforcing bars under monotonic and cyclic loadings. *Mechanics of Advanced Materials and Structures*, *18*(3), 218-224.
- Hensher, D. A. (2016). *Fiber-reinforced-plastic (FRP) reinforcement for concrete structures: properties and applications* (Vol. 42). Elsevier.

- Hild, F., & Roux, S. (2006). Digital image correlation: from displacement measurement to identification of elastic properties–a review. *Strain*, *42*(2), 69-80.
- Housing and Building National Research Centre. (2005). The Egyptian Code of Practice on the Use of Fibre Reinforced Polymers in the Construction Fields. *Housing and Building National Research Centre*, ECP 208-2005, Egypt.
- Hwang, S. F., Horn, J. T., & Wang, H. J. (2008). Strain measurement of nickel thin film by a digital image correlation method. *Strain*, *44*(3), 215-222.
- Intelligent Sensing for Innovative Structures (ISIS). (2001). Reinforcing Concrete Structures with Fibre Reinforced Polymers. The Canadian Network of Centres of Excellence on Intelligent Sensing for Innovative Structures, Design Manual No. 3. Winnipeg, Manitoba, Canada.
- International Federation for Structural Concrete (fib). (2007). FRP reinforcement in RC Structures. International Federation for Structural Concrete, Bulletin No. 40, Federal Institute of Technology, Lausanne, Switzerland.
- IS 10262 (2009). Indian Standard Code for Concrete Mix Proportioning Guidelines (First Revision), Bureau of Indian Standards, New Delhi, India.
- IS 1708 (2008). High Strength Deformed Steel Bars and Wires for Concrete Reinforcement—Specification, Bureau of Indian Standards, New Delhi, India.
- IS-383. (1970). Specification for coarse and fine aggregates from Natural Sources for Concrete. Bureau of Indian Standards, New Delhi, India.
- IS-8112. (1989). 43 Grade Ordinary Portland Cement - Specification Bureau of Indian Standards, New Delhi, India
- Ivanov, E., Ienny, P., Léger, R., Caro-Bretelle, A. S., & Kotsilkova, R. (2014). Strain localisation in iPP/MWCNT nanocomposites using digital image correlation. *Strain*, *50*(1), 37-47.
- Jakubovskis, R., Kaklauskas, G., Gribniak, V., Weber, A., & Juknys, M. (2014). Serviceability analysis of concrete beams with different arrangements of GFRP bars in the tensile zone. *Journal of Composites for Construction*, *18*(5), 04014005.
- Japan Society of Civil Engineers (JSCE). (1997b). Recommendation for Design and Construction of Concrete Structures using Continuous Fiber Reinforcing Materials. Japan Society of Civil Engineers, Concrete Engineering Series No. 23, Tokyo, Japan.

- Johansson, M., Leppanen, J., & Flansbjer, M. (2019). Residual Capacity of RC Beams Subjected to Impact Loading. *In Proceedings of the 90th Shock and Vibration Symposium, Shock and Vibration Exchange*, www.savecenter.org, Atlanta, Georgia. 1-12.
- Kalpana, V. G., & Subramanian, K. (2011). Behavior of concrete beams reinforced with GFRP bars. *Journal of reinforced plastics and composites*, *30*(23), 1915-1922.
- Koch, G. (2017). Cost of corrosion. *Trends in oil and gas corrosion research and technologies*, 3-30.
- Krasniqi, C., Kabashi, N., Krasniqi, E., & Kaqi, V. (2018). Comparison of the behavior of GFRP reinforced concrete beams with conventional steel bars. *Pollack Periodica*, *13*(3), 141-150.
- Kumar, A., Vishnuvardhan, S., Murthy, A. R., & Raghava, G. (2019). Tensile and fracture characterization using a simplified digital image correlation test set-up. *Structural Engineering and Mechanics*, *69*(4), 467-477.
- Kumar, G. N., & Sundaravadivelu, K. (2017, July). Experimental study on flexural behaviour of beams reinforced with GFRP rebars. In *IOP Conference Series: Earth and Environmental Science* (Vol. 80, No. 1, p. 012027). IOP Publishing.
- Küntz, M., Jolin, M., Bastien, J., Perez, F., & Hild, F. (2006). Digital image correlation analysis of crack behavior in a reinforced concrete beam during a load test. *Canadian Journal of Civil Engineering*, *33*(11), 1418-1425.
- Lee, S. K., Krauss, P. D., & Wiss, J. (2004). *Long-term performance of epoxy-coated reinforcing steel in heavy salt-contaminated concrete* (No. FHWA-HRT-04-090). United States. Federal Highway Administration. Office of Infrastructure Research and Development.
- Lin, X., Zhang, Y. S., & Pathak, P. (2019). *Nonlinear finite element analysis of composite and reinforced concrete beams*. Woodhead Publishing.
- López-Calvo, H. Z., Montes-Garcia, P., Kondratova, I., Bremner, T. W., & Thomas, M. D. A. (2013). Epoxy-coated bars as corrosion control in cracked reinforced concrete. *Materials and Corrosion*, *64*(7), 599-608.
- Maas, H. G., & Hampel, U. (2006). Photogrammetric techniques in civil engineering material testing and structure monitoring. *Photogrammetric Engineering & Remote Sensing*, *72*(1), 39-45.
- Manalo, A. C., Mendis, P., Bai, Y., Jachmann, B., & Sorbello, C. D. (2021). Fiber-Reinforced Polymer Bars for Concrete Structures: State-of-the-Practice in Australia. *Journal of Composites for Construction*, *25*(1), 05020007.

- Manning, D. G. (1996). Corrosion performance of epoxy-coated reinforcing steel: North American experience. *Construction and Building Materials*, *10*(5), 349-365.
- Molina-Viedma, Á. J., Pieczonka, L., Mendrok, K., López-Alba, E., & Díaz, F. A. (2020). Damage identification in frame structures using high-speed digital image correlation and local modal filtration. *Structural Control and Health Monitoring*, *27*(9), e2586.
- Mpalaskas, A. C., Matikas, T. E., Van Hemelrijck, D., Iliopoulos, S., Papakitsos, G. S., & Aggelis, D. G. (2015, March). Acoustic signatures of different damage modes in plain and repaired granite specimens. In *Smart Materials and Nondestructive Evaluation for Energy Systems 2015* (Vol. 9439, p. 94390L). International Society for Optics and Photonics.
- Mufti, A. A., Onofrei, M. B. N. M. J. B. G., Benmokrane, B., Banthia, N., Boulfiza, M., Newhook, J. P., ... & Brett, P. (2007). Field study of glass-fibre-reinforced polymer durability in concrete. *Canadian Journal of Civil Engineering*, *34*(3), 355-366.
- Nair, A. (2006). Acoustic emission monitoring and quantitative evaluation of damage in reinforced concrete members and bridges.
- Nanni, A., De Luca, A., & Jawaheri Zadeh, H. (2019). *Reinforced concrete with FRP bars: Mechanics and design*. CRC Press.
- Nanni, A., Okamoto, T., Tanigaki, M., & Osakada, S. (1993). Tensile properties of braided FRP rods for concrete reinforcement. *Cement and Concrete Composites*, *15*(3), 121-129.
- National Research Council (CNR). (2006). Guide for the Design and Construction of Concrete Structures Reinforced with Fiber-Reinforced Polymer Bars. *National Research Council*, CNR-DT 203/2006, Rome, Italy.
- Ohno, K., & Ohtsu, M. (2010). Crack classification in concrete based on acoustic emission. *Construction and Building Materials, 24*(12), 2339-2346.
- Ohtsu, M., & Tomoda, Y. (2007). Corrosion process in reinforced concrete identified by acoustic emission. *Materials transactions, 48*(6), 1184-1189.
- Ohtsu, M., & Uddin, F. A. (2008). Mechanisms of corrosion-induced cracks in concrete at meso-and macro-scales. *Journal of Advanced Concrete Technology*, *6*(3), 419-429.
- Ohtsu, M., Mori, K., & Kawasaki, Y. (2011). Corrosion process and mechanisms of corrosion-induced cracks in reinforced concrete identified by AE analysis. *Strain*, *47*, 179-186.
- Omondi, B., Aggelis, D. G., Sol, H., & Sitters, C. (2016). Improved crack monitoring in structural concrete by combined acoustic emission and digital image correlation techniques. *Structural Health Monitoring*, *15*(3), 359-378.

- Ou, Y. C., Tsai, L. L., & Chen, H. H. (2012). Cyclic performance of large-scale corroded reinforced concrete beams. *Earthquake Engineering & Structural Dynamics*, *41*(4), 593-604.
- Ouyang, C., Landis, E., & Shah, S. P. (1991). Damage assessment in concrete using quantitative acoustic emission. *Journal of Engineering Mechanics*, *117*(11), 2681-2698.
- Paik, J. K., Lee, J. M., & Ko, M. J. (2004). Ultimate shear strength of plate elements with pit corrosion wastage. *Thin-walled structures*, *42*(8), 1161-1176.
- Pan, B. (2018). Digital image correlation for surface deformation measurement: historical developments, recent advances and future goals. *Measurement Science and Technology*, *29*(8), 082001.
- Pan, B., Qian, K., Xie, H., & Asundi, A. (2009). Two-dimensional digital image correlation for in-plane displacement and strain measurement: a review. *Measurement science and technology*, *20*(6), 062001.
- Pardey, P. G., Alston, J. M., & Ruttan, V. W. (2010). The economics of innovation and technical change in agriculture. *Handbook of the Economics of Innovation*, *2*, 939-984.
- Parvez, A., & Foster, S. J. (2012). Fatigue behaviour of reinforced concrete beams with addition of steel fibres. *From Materials to Structures: Advancement through Innovation*, 333.
- Pendhari, S. S., Kant, T., & Desai, Y. M. (2008). Application of polymer composites in civil construction: A general review. *Composite structures*, *84*(2), 114-124.
- Peterson, A. K. (2005). Introduction to Basic Measures of a Digital Image for Pictorial Collections, Prints & Photographs Division. In *Library of Congress, Washington, DC* (pp. 20540-4720).
- Prashanth, M. H., & Kishen, J. C. (2016). An acoustic emission study of mixed mode crack propagation in reinforced concrete beams. In *Proceedings of the 9th International Conference on Fracture Mechanics of Concrete and Concrete Structures.*
- Prem, P. R., & Murthy, A. R. (2017). Acoustic emission monitoring of reinforced concrete beams subjected to four-point-bending. *Applied Acoustics*, *117*, 28-38.
- Providakis, C. P., Stefanaki, K. D., Voutetaki, M. E., Tsompanakis, Y., & Stavroulaki, M. (2014). Damage detection in concrete structures using a simultaneously activated multi-mode PZT active sensing system: Numerical modelling. *Structure and Infrastructure Engineering*, *10*(11), 1451-1468.
- Rabi, M., Cashell, K. A., & Shamass, R. (2019). Flexural analysis and design of stainless steel reinforced concrete beams. *Engineering Structures*, *198*, 109432.

- Rafi, M. M., & Nadjai, A. (2011). A suggested model for European code to calculate deflection of FRP reinforced concrete beams. *Magazine of concrete research*, *63*(3), 197-214.
- Raj, B., Chellapandi, P., & Mudali, U. K. (2015). Life cycle management of structural components of Indian nuclear reactors and reprocessing plants. *Procedia CIRP*, *38*, 8-13.
- Raupach, M., & Schießl, P. (2001). Macrocell sensor systems for monitoring of the corrosion risk of the reinforcement in concrete structures. *NDT & E International*, *34*(6), 435-442.
- Reichmann, M. (2011). Understanding bit depth. *The Understanding Series Retrieved*, *2*(16), 2011.
- Russ, J.C. (2016). The Image Processing Handbook, 7th Edition, CRC Press and Taylor & Francis Group, Boca Raton, Florida, USA.
- Sagar, R. V. (2017). Acoustic emission characteristics of reinforced concrete beams with varying percentage of tension steel reinforcement under flexural loading. *Case studies in construction materials*, *6*, 162-176.
- Sagar, R. V., & Prasad, B. R. (2012). A review of recent developments in parametric based acoustic emission techniques applied to concrete structures. *Nondestructive Testing and Evaluation*, *27*(1), 47-68.
- Sagar, R. V., & Prasad, B. R. (2012). Damage limit states of reinforced concrete beams subjected to incremental cyclic loading using relaxation ratio analysis of AE parameters. *Construction and Building Materials*, *35*, 139-148.
- Saleh, Z., Goldston, M., Remennikov, A. M., & Sheikh, M. N. (2019). Flexural design of GFRP bar reinforced concrete beams: An appraisal of code recommendations. *Journal of Building Engineering*, *25*, 100794.
- Saleh, Z., Goldston, M., Remennikov, A. M., & Sheikh, M. N. (2019). Flexural design of GFRP bar reinforced concrete beams: An appraisal of code recommendations. *Journal of Building Engineering*, *25*, 100794.
- Sam, A. R. M., & Swamy, R. N. (2005). Flexural behavior of concrete beams reinforced with glass fiber reinforced polymer bars. *Malaysian Journal of Civil Engineering*, 17(1), 49-57.
- Sarfarazi, M. P. (1992). Acoustic emissions and damage constitutive characteristics of paper. Project 3571, final report to the Paper Properties and Uses Project Advisory Committee.
- Sehmi, A., Ouici, H. B., Guendouzi, A., Ferhat, M., Benali, O., & Boudjellal, F. (2020). Corrosion inhibition of mild steel by newly synthesized pyrazole carboxamide derivatives in

HCl acid medium: experimental and theoretical studies. *Journal of The Electrochemical Society*, *167*(15), 155508.

- Shah, S. G., & Kishen, J. C. (2011). Fracture properties of concrete–concrete interfaces using digital image correlation. *Experimental mechanics*, *51*(3), 303-313.
- Shah, S. G., & Kishen, J. C. (2012). Use of acoustic emissions in flexural fatigue crack growth studies on concrete. *Engineering Fracture Mechanics*, *87*, 36-47.
- Shahidan, S., Pulin, R., Bunnori, N. M., & Holford, K. M. (2013). Damage classification in reinforced concrete beam by acoustic emission signal analysis. *Construction and Building Materials*, *45*, 78-86.
- Sharma, A., Sharma, S., Sharma, S., & Mukherjee, A. (2015). Ultrasonic guided waves for monitoring corrosion of FRP wrapped concrete structures. *Construction and Building Materials*, *96*, 690-702.
- Sharma, A., Sharma, S., Sharma, S., & Mukherjee, A. (2018). Investigation of deterioration in corroding reinforced concrete beams using active and passive techniques. *Construction and Building Materials*, *161*, 555-569.
- Sharma, A., Sharma, S., Sharma, S., & Mukherjee, A. (2018). Monitoring invisible corrosion in concrete using a combination of wave propagation techniques. *Cement and Concrete Composites*, *90*, 89-99.
- Sharma, G., Sharma, S., & Sharma, S. K. (2020). Monitoring structural behaviour of concrete beams reinforced with steel and GFRP bars using acoustic emission and digital image correlation techniques. *Structure and Infrastructure Engineering*, 1-16.
- Sharma, G., Sharma, S., & Sharma, S. K. (2021). Fracture monitoring of steel and GFRP reinforced concrete beams using acoustic emission and digital image correlation techniques. *Structural Concrete*.
- Sharma, G., Sharma, S., & Sharma, S. K. (2021). Non-destructive evaluation of steel and GFRP reinforced beams using AE and DIC techniques.
- Sharma, N., Sharma, S., Sharma, S. K., & Mehta, R. (2020). Evaluation of corrosion inhibition and self healing capabilities of nanoclay and tung oil microencapsulated epoxy coatings on rebars in concrete. *Construction and Building Materials*, *259*, 120278.
- Shih, M. H., & Sung, W. P. (2013). Application of digital image correlation method for analysing crack variation of reinforced concrete beams. *Sadhana*, *38*(4), 723-741.
- Stankiewicz, A., Szczygieł, I., & Szczygieł, B. (2013). Self-healing coatings in anti-corrosion applications. *Journal of Materials Science*, *48*(23), 8041-8051.

- Stevens, M., Párraga, C. A., Cuthill, I. C., Partridge, J. C., & Troscianko, T. S. (2007). Using digital photography to study animal coloration. *Biological Journal of the Linnean society*, *90*(2), 211-237.
- Sudarsanan, N., Arulrajah, A., Karpurapu, R., & Amrithalingam, V. (2019). Digital image correlation technique for measurement of surface strains in reinforced asphalt concrete beams under fatigue loading. *Journal of Materials in Civil Engineering*, *31*(8), 04019135.
- Sumarac, D., Sekulovic, M., & Krajcinovic, D. (2003). Fracture of reinforced concrete beams subjected to three point bending. *International Journal of Damage Mechanics*, *12*(1), 31-44.
- Talakokula, V., & Bhalla, S. (2015). Reinforcement corrosion assessment capability of surface bonded and embedded piezo sensors for reinforced concrete structures. *Journal of Intelligent Material Systems and Structures*, *26*(17), 2304-2313.
- Talakokula, V., Bhalla, S., & Gupta, A. (2014). Corrosion assessment of reinforced concrete structures based on equivalent structural parameters using electro-mechanical impedance technique. *Journal of Intelligent Material Systems and Structures*, *25*(4), 484-500.
- Tambusay, A., Suryanto, B., & Suprobo, P. (2018). Visualization of shear cracks in a reinforced concrete beam using the digital image correlation. *International Journal on Advanced Science, Engineering and Information Technology*, *8*(2), 573-578.
- Tan, A. C., Kaphle, M., & Thambiratnam, D. (2009, July). Structural health monitoring of bridges using acoustic emission technology. In *2009 8th International Conference on Reliability, Maintainability and Safety* (pp. 839-843). IEEE.
- Theriault, M., & Benmokrane, B. (1998). Effects of FRP reinforcement ratio and concrete strength on flexural behavior of concrete beams. *Journal of composites for construction*, *2*(1), 7-16.
- Toutanji, H. A., & Saafi, M. (2000). Flexural behavior of concrete beams reinforced with glass fiber-reinforced polymer (GFRP) bars. *Structural Journal*, *97*(5), 712-719.
- Triantafillou, T. C., & Antonopoulos, C. P. (2000). Design of concrete flexural members strengthened in shear with FRP. *Journal of composites for construction*, *4*(4), 198-205.
- Tsangouri E, Karaiskos G, Deraemaeker A, Van Hemelrijck D, Aggelis D. (2016) Assessment of acoustic emission localization accuracy on damaged and healed concrete. Construction and Building Materials. Dec 30; 129:163-71.

- Tsangouri, E., Karaiskos, G., Deraemaeker, A., Van Hemelrijck, D., & Aggelis, D. (2016). Assessment of acoustic emission localization accuracy on damaged and healed concrete. *Construction and Building Materials*, *129*, 163-171.
- Valdez, B., Ramirez, J., Eliezer, A., Schorr, M., Ramos, R., & Salinas, R. (2016). Corrosion assessment of infrastructure assets in coastal seas. *Journal of Marine Engineering & Technology*, *15*(3), 124-134.
- Verbruggen, S., Aggelis, D. G., Tysmans, T., & Wastiels, J. (2014). Bending of beams externally reinforced with TRC and CFRP monitored by DIC and AE. *Composite structures*, *112*, 113-121.
- Verbruggen, S., De Sutter, S., Iliopoulos, S., Aggelis, D. G., & Tysmans, T. (2016). Experimental structural analysis of hybrid composite-concrete beams by digital image correlation (DIC) and acoustic emission (AE). *Journal of Nondestructive Evaluation*, *35*(1), 2.
- Verbruggen, S., Tysmans, T., & Wastiels, J. (2016). Bending crack behaviour of plain concrete beams externally reinforced with TRC. *Materials and Structures*, *49*(12), 5303-5314.
- Vidya Sagar, R., Raghu Prasad, B. K., & Sharma, R. (2012). Evaluation of damage in reinforced concrete bridge beams using acoustic emission technique. *Nondestructive Testing and Evaluation*, *27*(2), 95-108.
- Wang, L., Li, C., & Yi, J. (2015). An experiment study on behavior of corrosion RC beams with different concrete strength. *Journal of Coastal Research*, (73 (10073)), 259-264.
- Wang, Z., Bovik, A. C., & Simoncelli, E. P. (2005). Structural approaches to image quality assessment. *Handbook of image and video processing*, *7*(18).
- Wattrisse, B., Chrysochoos, A., Muracciole, J. M., & Némoz-Gaillard, M. (2001). Analysis of strain localization during tensile tests by digital image correlation. *Experimental Mechanics*, *41*(1), 29-39.
- Wilbur, P. C. (2011). *Damage Identification in Reinforced Concrete Beams using Digital Image Correlation*. University of Windsor (Canada).
- www.googleimages.com
- Yao, Y., Zhu, D., Zhang, H., Li, G., & Mobasher, B. (2016). Tensile behaviors of basalt, carbon, glass, and aramid fabrics under various strain rates. *Journal of Materials in Civil Engineering*, *28*(9), 04016081.

- Yoon, I. S. (2007). Deterioration of concrete due to combined reaction of carbonation and chloride penetration: experimental study. In *Key Engineering Materials* (Vol. 348, pp. 729-732). Trans Tech Publications Ltd.
- Yun, H. D., Choi, W. C., & Seo, S. Y. (2010). Acoustic emission activities and damage evaluation of reinforced concrete beams strengthened with CFRP sheets. *Ndt & E International*, *43*(7), 615-628.
- Zdunek, A. D., Prine, D., Li, Z., Landis, E., & Shah, S. (1995). *Early detection of steel rebar corrosion by acoustic emission monitoring* (No. ITI Technical Report No. 16). Northwestern University (Evanston, Ill.). Infrastructure Technology Institute.
- Zhang, W., Zheng, Q., Ashour, A., & Han, B. (2020). Self-healing cement concrete composites for resilient infrastructures: A review. *Composites Part B: Engineering*, *189*, 107892.
- Zhou, X., & Zhang, X. (2019). Thoughts on the development of bridge technology in China. *Engineering*, *5*(6), 1120-1130.
- Zhou, Y., Gencturk, B., Willam, K., & Attar, A. (2015). Carbonation-induced and chloride-induced corrosion in reinforced concrete structures. *Journal of Materials in Civil Engineering*, *27*(9), 04014245.
- Żyjewski, A., Chróścielewski, J., & Pyrzowski, Ł. (2017). The use of fibre-reinforced polymers (FRP) in bridges as a favourable solution for the environment. In *E3S Web of Conferences* (Vol. 17, p. 00102). EDP Sciences.